IMPERIAL COLLEGE LONDON
ROYAL SCHOOL OF MINES
DEPARTMENT OF EARTH SCIENCE AND ENGINEERING

A THESIS PRESENTED FOR THE DEGREE OF DOCTOR OF PHILOSOPHY

Palaeomagnetic studies of Eyjafjardardalur, northern Iceland: does the geocentric axial dipole exist during 3-7 Ma?

Radchagrit Supakulopas

Supervised by

Dr. Adrian MUXWORTHY (Imperial College London)

Dr. Morten RIISHUUS (University of Iceland)

Prof. Conall MAC NIOCAILL(University of Oxford)

Dr. Arne DØSSING (DTU Space)

27th March 2018

Copyright Declaration

Radchagrit Supakulopas

27th March 2018

Declaration of Originality

I, Radchagrit Supakulopas, confirm that the research presented within this thesis: Palaeomagnetic studies of Eyjafjardardalur, northern Iceland: does the geocentric axial dipole exist during 3-7 Ma?, is the product of my own work under primary supervision of Dr Adrian Muxworthy at Imperial College London.

Radchagrit Supakulopas

27th March 2018

Abstract

The geocentric axial dipole (GAD) hypothesis states that when we average the geomagnetic field over sufficient geological time intervals, the time-averaged field (TAF) behaves like a dipole aligned along the Earth's spin axis and positioned at the Earth's centre. This hypothesis is crucial in palaeomagnetic research, e.g., it is a key to tectonic reconstructions. However, there is some evidence for the persistence of long-term hemispheric asymmetry on time scales of 10^5-10^6 yrs, particularly at high-latitudes. As most palaeomagnetic research is conducted under the GAD hypothesis, this hypothesis needs to be rigorously tested. This thesis investigates the symmetry of the palaeomagnetic field and tests the GAD hypothesis during ~2.6-8.5 Ma using full-vector palaeomagnetic data - including palaeodirection and palaeointensity - from dated lava piles in northern Iceland.

Demagnetisation measurements including alternating field (AF) and thermal were made to determine palaeomagnetic directions. A mean declination and inclination of 354.1° and 71.4° were found in this study, with a 95% confidence limit of only 2.4°. The mean virtual geomagnetic pole (VGP) is located at 80.6°N and 184.6°E, which is tilted ~10° from the geographic north; this VGP position does not agree with the GAD hypothesis. It is argued that this shallow inclination is a result of the non-dipole fields which contribute to the GAD field. This was confirmed by the palaeosecular variation (PSV) model compilation of the global dataset during 0-8.5 Ma. The PSV model suggests that 4% of axial quadrupole and 1% of axial octupole contribute to the TAF during 0-8.5 Ma.

Palaeointensity data reveals a weak mean intensity of 26.9 ± 1.8 μT, which is lower than the intensity of the expected GAD field (55.9 μT) at 65°N for the current day field. This weak intensity equates to a virtual dipole moment (VDM) of 37.4 ± 2.5 $\mathrm{ZAm^2}$. After combining this study data with 1-3 Ma data also from Iceland to improve temporal resolution, a mean VADM of 44.0 ± 2.2 $\mathrm{ZAm^2}$ was obtained. The direct comparison of the VADM between high-northern and high-southern latitudes (37.3 ± 3.8 $\mathrm{ZAm^2}$) was made. This study reveals that there is hemispheric asymmetry of the field between Northern and Southern Hemisphere.

Acknowledgement

Firstly, I must thank the Development and Promotion of Science and Technology Talents Project (DPST), who provides me the funding to pursue the PhD degree in UK. Secondly, I would like to express my appreciation to my supervisor, Adrian Muxworthy who helped me throughout my PhD, with valuable advice and support. I would like to thank my co-supervisor, Morten Riishuus who helped and suggested me through all geological problems, Conall Mac Niocaill who helped me in the fields and Arne Dossing who trained me the techniques in the lab.

While completing the PhD I have received the help from many friends and colleagues. I must thank Dan Barford at the SUERC for teaching me the groundmass preparation and running the 40Ar/39Ar dating which forms part of this thesis. Special thanks would be given to Kathryn Turner and Brendan Cych who helped me in the field in 2015 and performed part of palaeomagnetic experiments. I must thank Dylan Rood for his help in groundmass and XRF preparation at Imperial College. I also thank Sarah Dodd for showing me the dual-blade saw and Thomas Berndt for being a lab buddy. Thank are also due to Graham Nash and Gary Jones for their continued help in the rock preparation room. I also thank Tom Knott at the University of Leicester for running XRF analysis. NMG members Jay Shah, Susie Maidment, Joel Hancock and Sope Badejo would deserve special thank for keeping the lab not so silence. I also thank my English teacher, Su Peneycad who keeps encouraging me to improve my English. I must of course thank Xuanyu for supporting me and travelling with me throughout the PhD. Finally, I must thank my family for their constant love and support.

Content

List of Figures

List of Tables

List of Abbreviations

AF	alternating field
APW	apparent polar wander
CALS	continuous models of archaeomagnetic and lake sediment
CDF	cumulative distribution function
CMB	core mantle boundary
CRM	chemical remanent magnetisation
DG	directional group
DRM	depositional/detrital remanent magnetisation
GAD	geocentric axial dipole
GGP	giant gaussian process
FORC	first-order reversal curve
IGRF	international geomagnetic reference field
IRM	isothermal remanent magnetisation
IZZI	infield/zero field and zero field/infield
LN	lava flow during normal polarity interval
LSN	lava flow and sediment during normal polarity interval
MAD	maximum angular deviation
MAD	median absolute deviation
MD	multidomain
NRM	natural remanent magnetisation
PCA	principal component analysis
PINT	absolute palaeointensity database
PSD	pseudo-single domain
PSV	palaeosecular variation
pTRM	partial-thermoremanent magnetisation

RMS	root mean square
SAA	south Atlantic anomaly
SD	single domain
TAF	time-averaged field
TRM	thermoremanent magnetisation
TWP	true polar wander
VADM	virtual axial dipole moment
VDM	virtual dipole moment
VGP	virtual geomagnetic pole
VRM	viscous remanent magnetisation
VSM	vibrating sample magnetometer
XRF	X-ray fluorescence

List of Symbols

α_{95}	95% confidence limit
B_c	coercivity
B_{cr}	coercivity of remanence
B_{anc}	ancient field
B_{lab}	laboratory field
B_r	radial field
Dec, D	declination
g_1^0	axial dipole
g_2^0	axial quadrupole
g_3^0	axial octupole
g_l^m, h_l^m	Gauss coefficients degree l and order m
Inc, I	inclination
k	Fisher's precision parameter
M_{rs}	remanent magnetisation
M_s	saturation magnetisation
Q_{AD}	adiabat heat flow on the outer core side
Q_{CMB}	CMB heat flow
T_b	blocking temperature
T_{ub}	unblocking temperature
τ	relaxation time
□	vacancies in spinel structure

Chapter 1

Introduction

1.1 Introduction

The Earth's magnetic field has existed for at least 3.47 billion years (Hale and Dunlop, 1984; Smirnov and Tarduno, 2003; Smirnov and Tarduno, 2004; Tarduno et al., 2007) and it is widely accepted that the field is driven by a self-sustaining dynamo within the Earth's core. The Earth's magnetic field plays an important role in protecting living organisms from cosmic radiation (e.g., Merrill et al., 1996), and is thought to be essential for life on Earth (e.g., Tarduno et al., 2014). The field also acts as a navigation aid for species such as birds and bacteria, and indirectly for humans (Blakemore et al., 1980; Hanzlik et al., 2000).

Direct observation of the geomagnetic field started in 16th century. These observations have shown that the geomagnetic field is dynamic in terms of both its direction and intensity. Generally, about 80% of the current day field can be expressed as dipolar spherical harmonics. This dipole position is currently tilted approximately 11.5° from the geographic north, and located over northern Canada (Figure 1.1a), however, over the last 400 years it has been observed to drift west with an average speed of 0.2° per year and the tilt angle varies. Because of this so-called secular variation, it is assumed that if the geomagnetic field is averaged over a sufficient geological time interval, the time-average field will behave like a geocentric axial dipole (GAD); that is, a dipole field aligned with the Earth's rotation axis. The GAD hypothesis is crucial in many aspects of palaeomagnetic research, e.g., it is a key to tectonic studies, from regional rotations to global plate reconstructions.

The time interval over which the geomagnetic field must be averaged to equate to a GAD field is still unclear. It was believed that averaging the field over several thousand years is sufficient to achieve the GAD (Creer et al., 1954); however, subsequent historical and archaeological records have shown that the GAD is invalid over 10,000 year averaged field (Constable et al., 2000; Jackson et al., 2000; Korte and Constable, 2003; Korte and Constable, 2005; Korte et al., 2011; Cai et al., 2014; Cai et al., 2015; Shaar et al., 2015; Cai et al., 2017). Over very long periods of time, i.e., 250 Myrs, the GAD seems to hold (Bloxham, 2000; Aubert et al., 2010). However, for the intermediate time interval of 10^4-10^6 years, there is still some debate as to what sufficient time is needed. Current analysis of the time-averaged field (TAF) is only close to the GAD field hypothesis with ~3-6% of axial quadrupole and axial octupole contributions still existing (e.g., Johnson and Constable, 1997; Carlut and Courtillot, 1998; Kono et al., 2000; Hatakeyama and Kono, 2002; Cromwell et al., 2018). However, there are still key unanswered questions: (1) Given the inhomogeneous temporal and spatial data distributions, how accurate are these models?; (2) does the GAD hypothesis display a latitudinal dependency, as hinted by the current database, that is, does data at low-latitudes support the GAD hypothesis, and not that from high latitudes? And (3) are there differences with respect to the TAF between directional and intensity data; Constable (2007) and Johnson and McFadden (2007) show that intensity data should be more sensitive to high-latitudinal variations at the core-mantle boundary (CMB) than directional data. This thesis attempts to answer all these questions, by undertaking a new high-latitudinal full-vector field study of basalts, aged ~3 to 8 Ma. The latter two questions, are directly addressed in this thesis. The first of these three questions is hard to resolve with a single, albeit large, study; however, the data can be added to the global database.

Iceland is a promising location to test the GAD hypothesis at high-latitudes as Iceland landmass is located above 65°N on the mid-ocean ridge. Icelandic volcanoes usually produce an eruption every 3 to 5 years and 20% of these eruptions produce lava flows (Stanton et al., 2011). The nature of lava flows in Iceland provides discrete palaeomagnetic data spanning ca. 0-16 Ma, which is suitable to test the GAD hypothesis on timescales of 10^4 to 10^6 years. There is also the small effect of plate rotations on Icelandic lava flows which minimises the bias on palaeomagnetic data. Therefore, Iceland is chosen as the study area for this thesis.

1.2 Mathematical description of the Earth's magnetic field

As the Earth's magnetic field is full-vector, measurements of declination, inclination and intensity of the field at different places around the world can be made (Tauxe et al., 2010). From such early measurements, William Gilbert in 1600 proposed that the Earth's magnetic field was like a giant bar magnet, and he proposed that its origin was large piece of lodestone within the Earth (Gilbert, 1600). In 1832 Carl Friedrich Gauss applied spherical harmonic analysis to describe the magnetic field, and concluded that the Earth's field originates from deep within the Earth.

Using spherical harmonic analysis, the scalar potential Ψ of the internal geomagnetic field can be written as (Blakely, 1995)

$$\Psi(r,\theta,\phi) = a\sum_{l=1}^{\infty}\sum_{m=0}^{l}\left(\frac{a}{r}\right)^{l+1} \times (g_l^m \cos m\phi + h_l^m \sin m\phi)P_l^m(\cos\theta) \tag{1.1}$$

where g_l^m and h_l^m are Gauss coefficients with degree l and order m, a is the Earth's radius, r is the radius, θ is co-latitude, ϕ is longitude and P_l^m are the partially normalised Schmidt polynomials. The geomagnetic field at the Earth's surface can be derived in spherical coordinates from (Johnson and McFadden, 2007)

$$B_r = -\frac{\partial\Psi}{\partial r}, \qquad B_\theta = -\frac{1}{r}\frac{\partial\Psi}{\partial\theta}, \qquad B_\phi = -\frac{1}{r\sin\theta}\frac{\partial\Psi}{\partial\phi} \tag{1.2}$$

The relationship of the spherical and cartesian coordinate for the geomagnetic field is (Blakely, 1995)

$$B_x = -B_\theta, \qquad B_y = B_\phi, \qquad B_z = -B_r \tag{1.3}$$

The benefit of using the spherical harmonic expansion of the field is that the magnetic field can be described anywhere on the sphere. The given field is specified by Gauss coefficients g_l^m and h_l^m. The order term $m = 0$ represents non-azimuthal structure of the field, i.e., the field is axially symmetric or zonal (declination is zero). g_1^0, g_2^0 and g_3^0 are the Gauss coefficients representing the axial dipole, axial quadrupole and axial octupole (Figure 1.1). The declination (Dec) and inclination (Inc) of the field can be calculated using the following relation (Blakely, 1995)

$$Dec = \tan^{-1}\left(\frac{B_y}{B_x}\right), \qquad Inc = \tan^{-1}\left(\frac{B_z}{\left({B_x}^2+{B_y}^2\right)^{1/2}}\right) \tag{1.4}$$

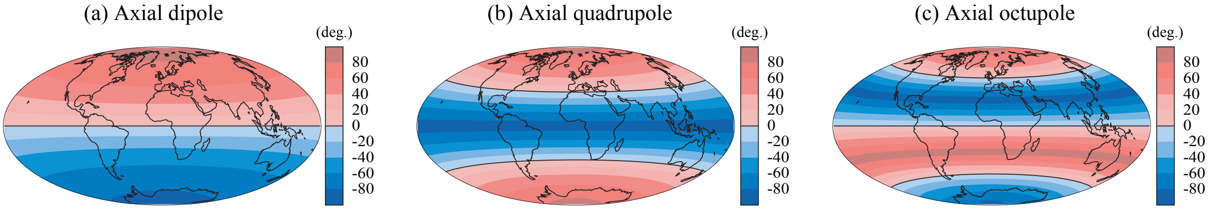

Figure 1.1: The inclinations versus latitudes due to (a) axial dipole field, (b) axial quadrupole field and (c) axial octupole field. The blue tones represent negative inclination while red tones show positive inclination.

1.3 The geocentric axial dipole (GAD) hypothesis

According to the GAD hypothesis, the TAF is a dipole field with its geomagnetic pole aligned with the spin axis (Figure 1.2b). For a GAD the declination of the field is always zero degree everywhere on the Earth's surface while the field inclination varies with latitudes (Figure 1.2b) by (Tauxe et al., 2010)

$$\tan I_{GAD} = 2\tan\lambda \tag{1.5}$$

where I_{GAD} is the GAD inclination and λ is geographic latitude. Therefore, the deviation of the geomagnetic field from the GAD hypothesis can be determined from (Johnson and McFadden, 2007)

$$\Delta I = I - I_{GAD}, \Delta D = D \tag{1.6}$$

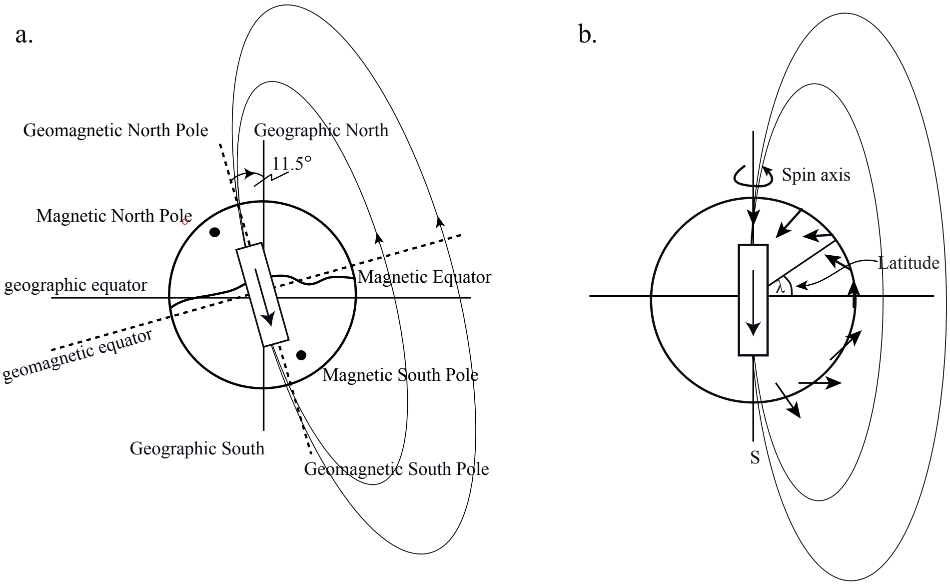

Figure 1.2: Schematic diagrams of (a) the current day's dipole field and (b) the geocentric axial dipole field.

The first order approximation of the TAF is the GAD hypothesis. Opdyke and Henry (1969) were the first group to test the deviation of the field inclination from the GAD hypothesis. They examined the inclinations using 52 marine cores from various localities around the world. They concluded that the GAD hypothesis holds true over the past 2.5 Ma. However, the GAD does not need to be valid as some individual palaeomagnetic studies also show the non-dipole fields which contribute to the GAD field. For example, Mejia et al. (2005) sampled the Pliocene-Holocene lava flows from the Trans-Mexican Volcanic Belt (TMVB) areas in Mexico. Their results show significant departure from the GAD hypothesis with 5% of axial quadrupole field, which contributes to the TAF during 0-2 Ma. Opdyke et al. (2006) also showed that 5% of the axial quadrupole contribute to the TAF during 0-2.6 Ma at Ecuador.

1.4 Long-term field strength

As the palaeomagnetic data are non-linear functions of the radial field (B_r) at the core-mantle boundary (CMB), Johnson and McFadden (2007) linearized data kernel for declination, inclination and intensity (Figure 1.3). These kernels show how the components of the geomagnetic field at the Earth's surface respond to the changes of the B_r at the CMB. These kernels can be used to observe declination and inclination anomalies at the Earth's surface. The kernels vary with geographical latitudes of the sampling locations (Figure 1.3). Declination data are influenced by the B_r along the east and west of the sampling locations. Inclination data at low latitudes are influenced by the B_r beneath the sampling locations while data at high latitudes are less influenced by the B_r. Therefore, a lot of inclination data from high-latitudes are required to detect the inclination anomalies at high-latitudes. With regards to intensity, data at high-latitudes is sensitive to the B_r at the CMB beneath the sampling locations. As can be seen from Figure 1.3, the high-latitude field behaviour at the CMB, arguably the most interesting region, is best studied using intensity data.

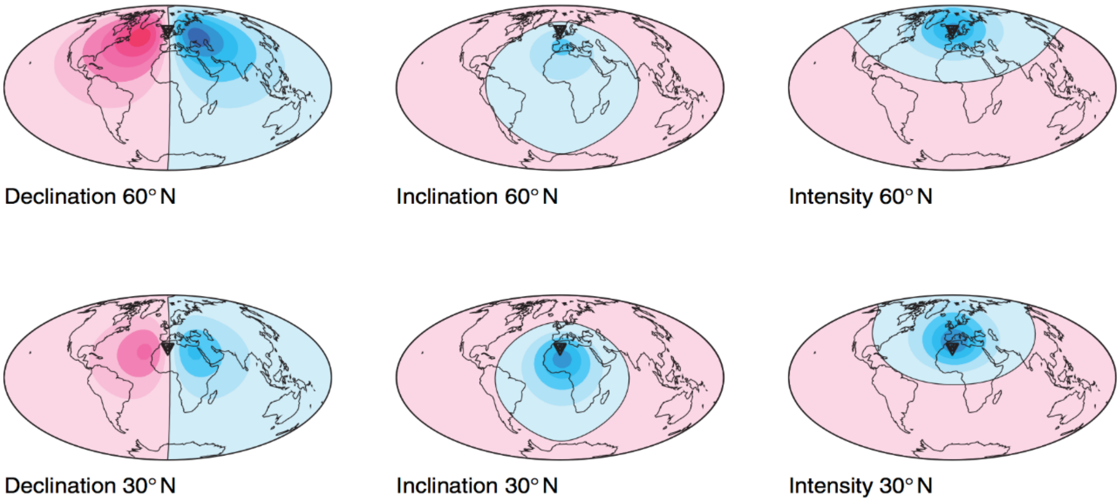

Figure 1.3: Sampling kernels show how observations of the declination, inclination and intensity at the Earth's surface sample the B_r at the CMB. Color scale shows relative sampling: darker areas are sampled more heavily than lighter areas. Positive (negative) scale is shown in red (blue). Observed declinations provide the longitudinal information while observed inclinations preferentially sample the B_r at the CMB. Palaeointensity data are sensitive to the radial field (B_r) beneath the sampling locations at high-latitudes. Figure from Johnson and McFadden (2007).

The deviations of the TAF from the GAD hypothesis are also expressed in the ancient field intensity (palaeointensity) record (Tauxe et al., 2010). The GAD field intensity predicts that the intensity at the pole is twice as strong as the intensity at the equator (Tauxe et al., 2010) (Equation 1.7 and Figure 1.4).

$$B = g_1^0(1 + 3\cos^2\theta)^{1/2} \tag{1.7}$$

where g_1^0 is the axial dipole in the spherical harmonic expansion of the geomagnetic field and θ is the site co-latitude in degree.

The palaeointensity is not often determined in palaeomagnetic investigations, because, whilst palaeo-directional information is relatively easy to robustly determine, palaeointensity analysis is very slow, often yields low success rates (~20-50%) and the data quality is variable. Currently, not many palaeointensity studies of the GAD field at high latitudes have been reported. The existing palaeointensity data at high-latitudes from the literature mostly deviate from the GAD hypothesis. For example, Lawrence et al. (2009) measured the field strength during 0-5 Ma recorded in Erebus Volcanic Province, Antarctica (~78°S). They found weak palaeointensity of 31.5 μT, compared to the GAD field intensity at the Antarctic sites (59 μT, predicted from Equation 1.7 using the current day g_1^0 of 30 μT).

While the ancient fields at high-southern latitudes are weaker than the GAD field, the ancient fields at high-northern latitudes show significantly higher intensities than the GAD field. For example, Stanton et al. (2011) measured palaeointensity during the Holocene Epoch recorded in Icelandic basalt. They found a high field strength of 59 μT during 10 ka and the field during the Holocene epoch was more dynamic than the current day field. The GAD intensity for Iceland is ~56 μT predicted from Equation 1.3. Cromwell et al. (2013b) sampled the ancient field at higher latitudes than Iceland. They found the palaeointensity of 57 μT during 0-0.5 Ma recorded in Jan Mayen, Norway (~71°N). Their intensity is relatively high when compared to the Antarctic data of Lawrence et al. (2009) during the same time interval. Cromwell et al. (2013b) proposed that there is a long-term hemispheric asymmetry in the palaeomagnetic field between the Arctic and Antarctic. To confirm the hemispheric asymmetry assumption, Cromwell et al. (2015) re-investigated palaeointensity during 11 ka to 3.35 Ma recorded in rapid-cooled lava basalts in Iceland. They found the weak palaeointensity of 33 μT, which is weaker than the data from the Arctic site during the same time interval (Cromwell et al., 2013b) and also weaker than the GAD intensity in Iceland. Cromwell et al. (2015) suggested that there might not be a significant difference between Arctic and Antarctic palaeointensity. However, because of the paucity of both high-northern and high-southern latitude palaeointensity, they suggested that this assumption cannot be excluded. With regard to equatorial palaeointensity, Wang et al. (2015) sampled the palaeointensity during Pliocene-Pleistocene from Galapagos lavas (~1°N). The weak intensity of ~21.6 ± 11 μT was found and is nearly twice lower than McMurdo data. Their result supports that the time-averaged field intensity is the GAD during ca. 5 Ma.

Since 2015, the current palaeointensity data for low- to mid-latitudes from the Palaeointensity (PINT15) Database (Biggin et al., 2009) should be sufficient for studying long-term field strength. However, palaeointensity data from high-latitudes are still sparse in the database. I plot palaeointensity data (grey dot) from PINT Database against latitudes for the past 8.5 Ma and present in Figure 1.4. Selected data pass the per cent standard deviation ≤ 15%. The PINT15 database does not include recent palaeointensity data from high-latitude studies published after 2015 such as Døssing et al. (2016) and Tanaka and Yamamoto (2016). Data were grouped into 10° latitude bin in order to improve spatial resolution. Mean intensity for each latitudinal bin was calculated and plotted as black circles with its standard error. It is seen that the palaeointensity data highly deviate from the GAD field intensity at high latitudes, especially at ~65°N and ~78°S. However, temporal and spatial coverage of the data might not be sufficient, and more data at high latitudes are needed for comparing between the field in the Northern and Southern Hemispheres.

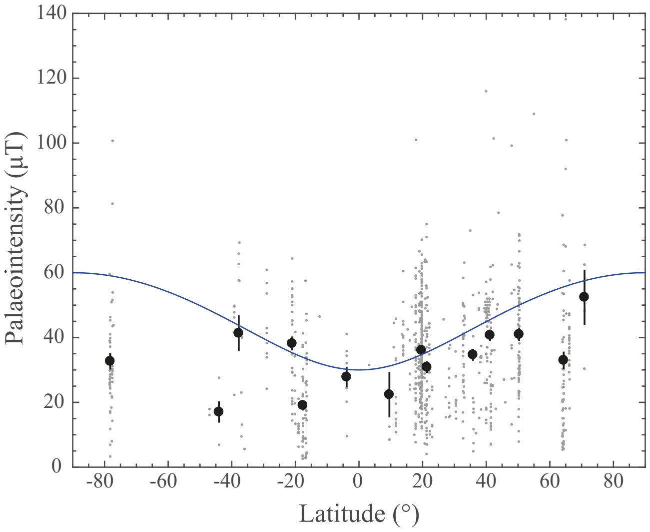

Figure 1.4: The plot of palaeointensity data during 8.5 Ma from the PINT15 database (grey points) (Biggin et al., 2009) versus latitudes. Data were binned into 10° latitude bands and the mean intensity of each band was calculated and represented as black circles with the standard errors. Blue line shows the GAD field intensity varying with latitudes for $g_1^0 = -30\ \mu T$.

1.5 Essentials of the GAD hypothesis

Direct application of the GAD hypothesis is to reconstruct the plate tectonics. A pole position that is observed from the rocks during a single observation is referred to as virtual geomagnetic pole (VGP). Averaging several VGPs would yield a mean VGP that coincides with the Earth's rotation axis. This seems to work for the rocks younger than 5 Ma as not much tectonic movements occur during this period. However, rocks older than ca. 5 Ma show significant deviations of the palaeomagnetic pole from the spin axis due to tectonic movements (Figure 1.5). An example is represented in Figure 1.5a. Four palaeomagnetic poles during mid-Cretaceous were derived from four localities in North America: 1) Arkansas intrusion (Globerman and Irving, 1988), 2) lamprophyric dykes, Newfoundland (Lapointe, 1979; Prasad, 1981), 3) igneous intrusions, Monteregian Hills, Quebec (Foster and Symons, 1979) and 4) Niobrara Formation, Colorado, Kansas and Wyoming (Shive and Frerichs, 1974). The mean palaeomagnetic pole calculated from four palaeomagnetic poles significantly deviates from the true north with no overlap of the 95% confidence limit. If the GAD hypothesis holds true, the mean palaeomagnetic pole which is fixed with North America can be adjusted to the geographic north. Then, North America is moved northward and eastward to the its palaeolocations during mid-Cretaceous (Figure 1.5b). It is seen that the position of North America during mid-Cretaceous was located at higher latitude than the current day location of North America. As can be seen from Figure 1.5, the palaeomagnetic pole illustrates the past spin axis of the Earth with respect to the continents, i.e., the pole does not move over geological time, but the continent does. To construct the palaeomagnetic pole for a particular time as a reference, high-quality and sufficient palaeomagnetic data are required to remove secular variation out.

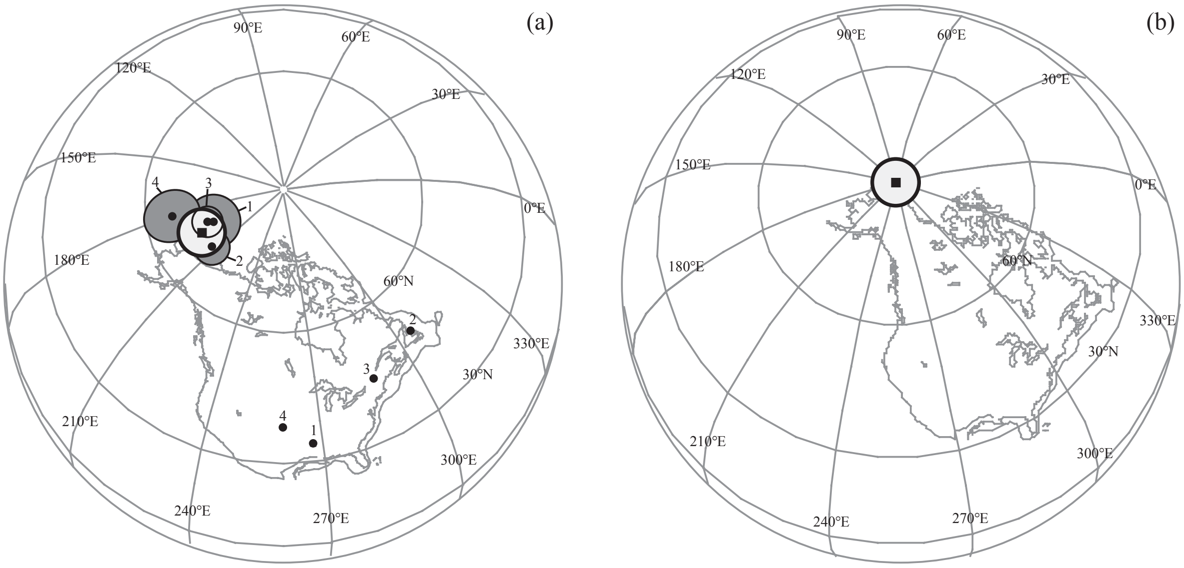

Figure 1.5: The mean palaeomagnetic pole (black square with light grey error ellipse) during mid-Cretaceous observed in North America (a) prior to tectonic reconstruction and (b) after the mean pole position is adjusted to the Earth's rotation axis. The mean palaeomagnetic pole was calculated from four mean VGPs (black circle with dark grey error ellipse) from four localities in North America including 1) Arkansas intrusion (Globerman and Irving, 1988), 2) lamprophyric dykes, Newfoundland (Lapointe, 1979; Prasad, 1981), 3) igneous intrusions, Monteregian Hills, Quebec (Foster and Symons, 1979) and 4) Niobrara Formation, Colorado, Kansas and Wyoming (Shive and Frerichs, 1974). It is clear that the position of North America is located at higher latitudes than the present position. Figures from Butler (1992). Butler (1992) modified the figures from Globerman and Irving (1988).

In palaeomagnetic community, the apparent polar wander (APW) path, which is the sequential positions of the palaeomagnetic poles, is constructed for each continent to assist tectonic reconstructions (Creer et al., 1954). Each APW path is considered to result from the moving continent sliding on a fix plate around the palaeomagnetic Euler pole (Tauxe et al., 2010). Each continent has its own Euler poles according to their APW paths (e.g., Torsvik et al., 2008a). The APW paths are used as a reference poles for a sequential time interval. For example, an individual palaeomagnetic study during 150 Ma in Europe should yield the palaeomagnetic pole that coincides with the 150 Ma pole from the APW path for Europe. The disadvantage of using the APW paths is that the paths can yield reconstruction mismatch if the paths are derived from poor quality of palaeomagnetic dataset or the GAD hypothesis does not hold true, e.g., 5° departure of the mean palaeomagnetic pole from the Earth's spin axis due to the non-dipole fields leads to 500 km reconstruction mismatch.

The bias that is commonly found in the palaeomagnetic research is shallow inclination. There are several causes of shallow inclination in lava flows, e.g., 1) local magnetic anomalies generated by strong magnetisation in underlying lava flows (e.g., Baag et al., 1995; Valet and Soler, 1999; Speranza et al., 2006); 2) shape anisotropy and magnetic refraction (e.g., Castro and Brown, 1987; Tanguy, 1990); 3) block movements when lava flows formed; 4) local tectonic movements and tectonic complications; 5) insufficiently averaged secular variation; 6) bias from overprint (McElhinny and McFadden, 1997); 7) averaging of unit vectors (Creer, 1983); 8) permanent non-dipole field. For example, there has been the controversy over the "A-type" Pangea reconstruction (Domeier et al., 2011). Using the palaeomagnetic data compiled by Torsvik et al. (2008a), the locations of the 250 Ma mean palaeomagnetic pole between Laurussia and Gondwana are ~20° apart (Figure 1.6a). Domeier et al. (2011) sampled palaeomagnetic field during the Late Permian (~264 Ma) from Upper Choiyoi Group and Early to Middle Triassic (~245 Ma) from Puesto Viejo Group. The mean palaeomagnetic pole from Upper Choiyoi Group does not overlap with 260 Ma mean pole from Gondwana (Figure 1.6a) but overlaps with the 265 Ma global mean pole derived from Laurussia and Gondwana (Figure 1.6b). With regards to the Puesto Viejo Group, the mean palaeomagnetic pole from volcanic rocks after anisotropy magnetic susceptibility (AMS)-tilt corrections overlaps with both 245 Ma mean pole from Gondwana and global mean pole. In the case of volcaniclastic data from Puesto Viejo Group (Figure 1.6), the mean palaeomagnetic pole after the AMS-tilt correction is located near the north pole (red diamond). Further anisotropy corrections were made with the factors of $f = 0.8$ and $f = 0.71$; the palaeomagnetic pole positions were adjusted to lower latitudes. It is seen that the mean palaeomagnetic pole from volcaniclastic site moves closer to the global APW paths after the anisotropy correction (Figure 1.6b). According to these mean pole data, Domeier et al. (2011) noticed that the incongruity between the independent Laurussian and Gondwana APW paths is a result of the bias in the palaeomagnetic data from Gondwana, i.e., shallow inclinations. Typically, the bias due to shallow inclination causes the reconstruction mismatch leading the continent moving toward low-latitudes area.

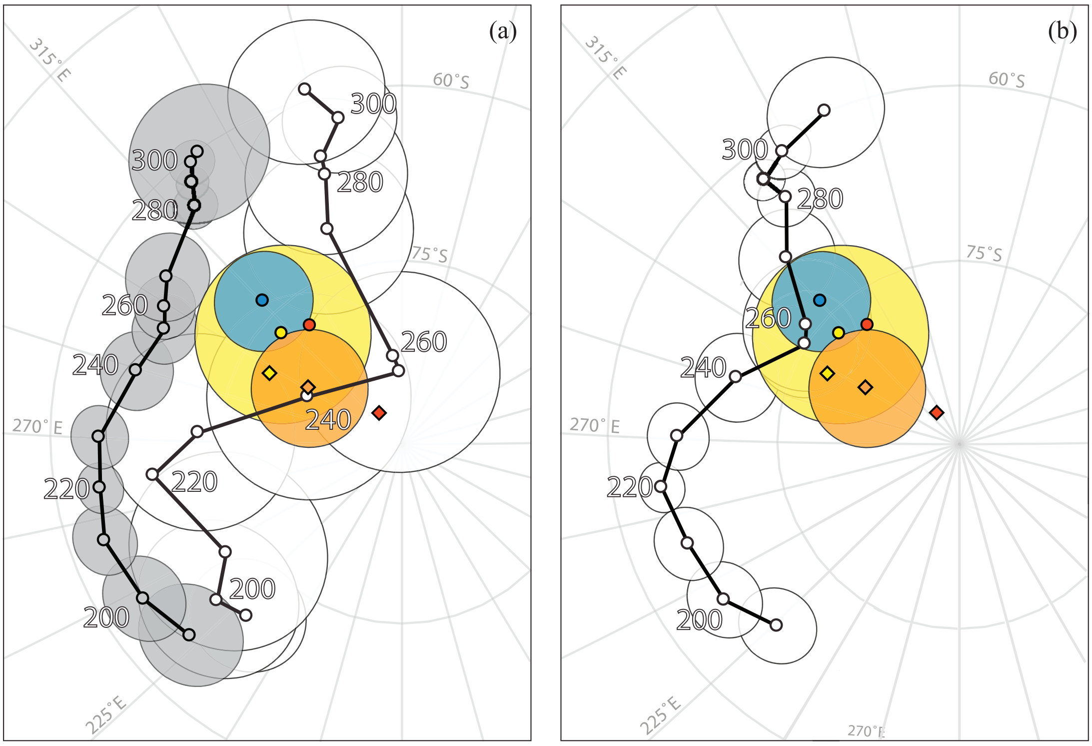

Figure 1.6: The mean palaeomagnetic poles during Late Permian (~264 Ma) from Upper Choiyoi Group and Early to Middle Triassic (~245 Ma) from Puesto Viejo Group (Domeier et al., 2011) are plotted against (a) the APW paths of Laurussia (grey) and Gondwana (white) and (b) the mean APW paths derived from Laurussian and Gondwana data (Torsvik et al., 2008b). The pole from Upper Choiyoi group after AMS-tilt correction is represented as blue circle with 95% error ellipse (blue circle). Red and yellow circles represent anisotropy-corrected poles from volcanic rocks from Puesto Viejo Group after AMS tilt and raw tilt corrections. Red diamond shows the pole from volcaniclastic sites after AMS-tilt correction. Orange and yellow diamonds show the pole positions after the anisotropy corrections with the factors of *f* = 0.8 and *f* = 0.71. The chronology ages are marked along the APW paths. It is clear that the pole from volcaniclastic sites without anisotropy correction highly deviates from the global APW path. Figure from Domeier et al. (2011).

Another example of ambiguous tectonic reconstructions due to the shallow and steep inclinations is the Ediacaran reconstructions. Abrajevitch and Van der Voo (2010) compiled the Ediacaran palaeomagnetic poles from Laurentia (McCausland et al., 2007) and Baltica (Elming et al., 2007; Meert et al., 2007). Palaeomagnetic directions from Laurentia and Baltica show both shallow and steep inclinations in the same intrusion. They addressed that the inclination difference between steep and shallow inclinations from the same intrusion is ~90°. For example, the shallow inclination was observed in the primary rocks in Sept-Îles intrusion in Laurentia (~562 Ma) while the steep inclination was recorded in dykes cutting through the primary intrusion (~561 Ma). The shallow inclination yields the mean palaeomagnetic pole of -20°N/321°E while the steep inclination recorded the mean palaeomagnetic pole of 61°N/295°E. These palaeomagnetic poles suggest that the Laurentia migrated from equator to pole within short time period. Abrajevitch and Van der Voo (2010) noticed that the speed required to migrate the plate from equator to pole with this short time interval would exceed the speed limit for plate tectonics of ~20-30 cm/yr (Meert et al., 1993; Conrad and Hager, 1999). Similar problem also happens to palaeomagnetic data from Baltica. In order to explain this phenomenon, Abrajevitch and Van der Voo (2010) revised the true polar wander (TWP), which is a solid-body rotation of the Earth with respect to its spin axis, causing the geographic locations of the North and South Poles to wander, for Ediacaran. According to the analyses of the TWP based on convection-driven changes in mass anomalies, the TPW should not exceed the speed of 2.5-8° over 10 Myrs (Tsai and Stevenson, 2007; Phillips et al., 2009). Therefore, the TWP would not be a candidate to explain the migrations of the continent from equator to pole in Ediacaran. As the inclination difference between steep and shallow inclinations is ~90°, it would be needed the non-dipole fields exceeding the dipole component to explain this field behaviour. They also noticed that the excursion events always happen within short period of time, e.g., <10 kyr. Therefore, the non-dipole fields and geomagnetic excursions would not well describe this problem. Abrajevitch and Van der Voo (2010) proposed another possibility that would be the unusual equatorial dipole during Ediacaran. The switch between the axial and equatorial dipoles during Ediacaran would describe why the inclination difference from the similar age is ~90° apart.

1.6 Previous tests of the GAD hypothesis over different time-scales

Direct observations of the geomagnetic field since the 16th century have provided data for field modellers to study the evolution of the so-called historical geomagnetic field in time and space. Field modelling involves the use of inversion methods to estimate values for g_l^m and h_l^m. Similar inversion approaches can be applied to palaeomagnetic data over geological timescales. Such models can be instantaneous images of the field, or averages over different timescales. The longer the timescale, the poorer the data coverage, and consequently the greater the errors in the field inversion.

Figure 1.7a shows the 2005 IGRF model of the current day surface intensity. It is clear that the current day field is not a perfect dipole and there is asymmetry between Northern and Southern Hemispheres. Two high-latitude flux patches exist in both the northern and southern hemispheres, and there is also a low field flux patch in the South Atlantic (South Atlantic Anomaly, SAA). Jackson et al. (2000) used the historical data to construct the time-varying field model for the past four centuries, called GUFM1 (AD 1590-1990). Figure 1.7b shows the averaged radial field (B_r) of the Model GUFM1 averaged over 400 years after downward continuation to the CMB, where the source of the geomagnetic field is located (Jackson et al., 2000). The historical model reveals the non-GAD structure and clearly shows that high-latitude flux patches persist over four centuries.

Longer centennial timescale field behaviour is best described by the CALSxk.n model family (Continuous models of Archaeomagnetic and Lake Sediment data for the past x thousand years version n) (e.g., Korte and Constable, 2005; Korte and Constable, 2011; Constable et al., 2016). The CALSxk.n models were constructed to study the field behaviour during the Holocene Epoch. A model for the last 3000 years is the CALS3k.4 (Korte and Constable, 2011). Figure 1.7c shows the average B_r at the CMB for the last 3 ka predicted from this model. The CALS7k model was constructed from archaeomagnetic and palaeomagnetic data spanning from the last 7000 years (Figure 1.7d). The CALS7k model has now been superseded by CALS10k which includes larger dataset and covers the last 10,000 years. The CALS10k family was constructed from sediment, lava and archaeological data (Korte et al., 2011; Constable et al., 2016). The most recent model for 10 ka is CALS10k.2 (Figure 1.7e). The temporal and spatial resolutions of CALS10k.2 are higher than CALS10k.1 because CALS10k.2 includes more data. As can be seen from Figure 1.7c-e, the TAF during 10 ka does not average to a GAD field and both the Northern and Southern Hemisphere field has high-latitude flux patches.

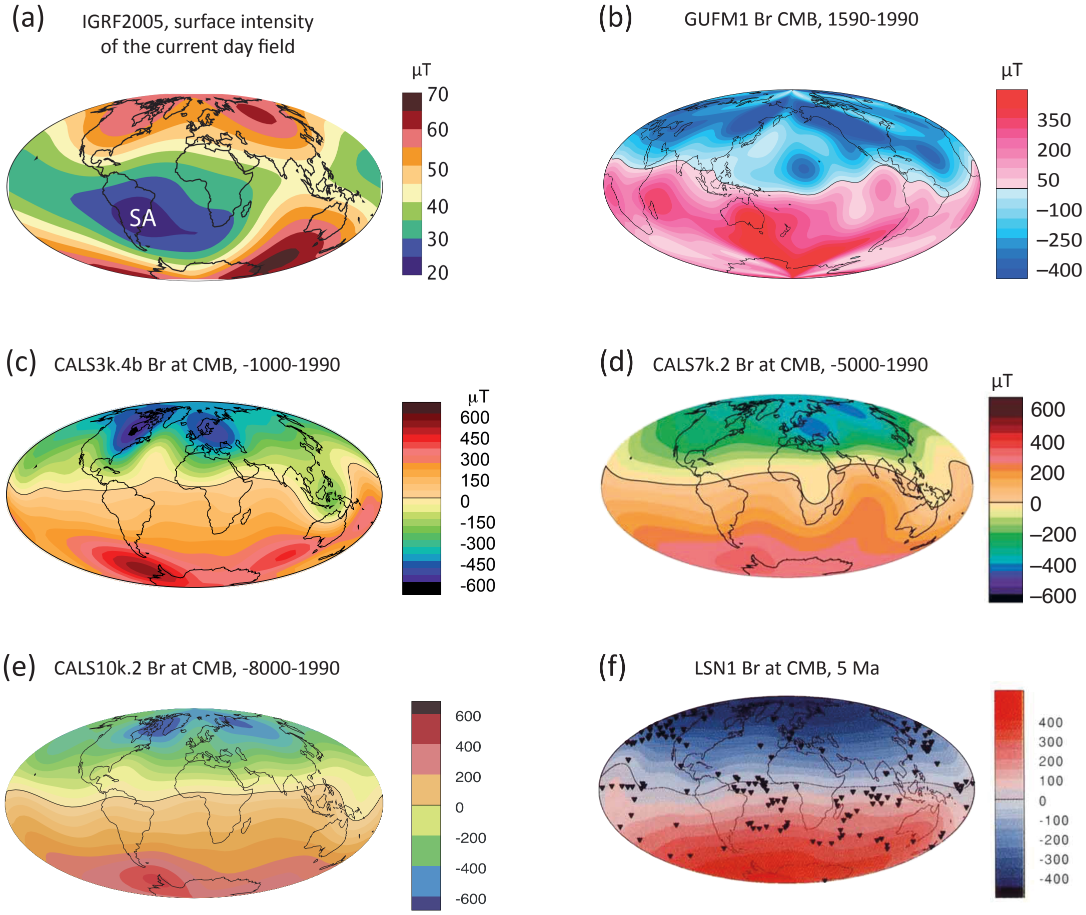

Figure 1.7: (a) Surface intensity of the current day geomagnetic field from IGRF 2005 (figure from Cromwell et al. (2013b)). (b)-(f) time-averaged radial field (B_r) at the core-mantle boundary (CMB). (b) 400 yeas, Model GUFM1 (Jackson et al., 2000) (Figure from Johnson and McFadden (2007)), (c) 0-3 ka, Model CALS3k.4b (Korte and Constable, 2011), (d) 0-7 ka, Model CALS7k.2 (Korte and Constable, 2005) (figure from Constable (2007)), (e) 0-10 ka, Model CALS10k.2 (Constable et al., 2016), and (f) 0-5 Ma, Model LSN1(Johnson and Constable, 1997). Note that the GUFM1 was constructed using historical data, e.g., measurements made on boards and satellite observations. The CALS family models were constructed using archaeomagnetic and lake sediment data while Model LSN1 was constructed from lava flow and sediment data during normal polarity interval.

More recently researchers have focussed on the 5 Ma time window, as this is a long time window, but a recent enough time window that the contribution of plate tectonics can be mostly ignored. Johnson and Constable (1995), here after JC95, compiled 2,187 lava flow data from 104 locations spanning from 0-5 Ma using the inversion method. They found approximately 90% of the field is generated from the axial dipole. Johnson and Constable (1997), here after JC97, improved the database of JC95 and combined the lava flow data with 116 Brunhes and 75 Matuyama data from sediment cores. Their model, here after LSN1 (lava and sediment data during normal polarity interval), shows substantial departure from the GAD field, especially at equatorial and polar regions (Figure 1.7f). Carlut and Courtillot (1998), here after Q94, used the same code as JC95 to compile 3,179 lava flows data spanning the past 5 Ma. Over 50% of the JC95 data was included in Q94. The Model Q94 found an axial quadrupole term of the order of 5% in their dataset. Kelly and Gubbins (1997), here after KG97, improved the palaeomagnetic database from the previous models by combining lava flow, ocean sediment and *intensity* data for the past 5 Ma. Their model reveals high-latitude flux patches at the CMB under Canada and Siberia, similar to those observed in the 400-year historical field model. Unlike previous models, Kono et al. (2000), hereafter K00, compiled the *palaeointensity (only)* model for the last 5 Ma using 279 palaeointensity data spanning latitudes 40°S to 65°N. They found the axial quadrupole of ~6% and the axial octupole of ~5.6% in the TAF. The axial quadrupole is of the opposite sign with the axial dipole. Hatakeyama and Kono (2002), here after H02, compiled the lava flow data of Johnson and Constable (1996). They found the axial quadrupole of ~4.3% and the axial octupole of ~2.1% contributing to the TAF. Cromwell et al. (2018) constructed the new palaeodirection database from lava flow data spanning ca. 10 Ma. Their dataset contains large amount of directional data whose pass the selection criteria of McElhinny and McFadden (1997). However, due to the paucity of ca. 5-10 Ma data, they compiled the model derived from >1,500 lava flow data during normal polarity interval (LN3) spanning ca. 0-5 Ma. They found the persistence of the axial quadrupole of ~3%. The Gauss coefficients from some studies stated above are given in Table 1.1.

Over very long time scale, i.e., 250 Ma, the palaeomagnetic data for constructing the model are sparse. Bloxham (2000) used an alternative approach to test the GAD hypothesis by examining the frequency distribution of the absolute inclination, rather than testing the inclination site-by-site.

Approximately 3,600 data being used in his study clearly shows that 0-250 Ma data conform closely to the GAD hypothesis.

Table 1.1: Gauss coefficients for the TAF models as stated in the text. N and R present normal and reverse polarity intervals.

	Q94 N	Q94 R	JC97 N	JC97 R	KG97	K00	H02 N	H02 R
g_1^0	-30.0	-30.0	-30.0	-30.0	-30.0	-29.5	-30.0	-30.0
g_1^1	0.04	0.11	0.12	0.10	0.46	-1.64	0.40	1.01
h_1^1	0.24	0.46	0.31	0.50	0.26	2.02	0.47	1.35
g_2^0	-1.09	-1.68	-1.08	-1.15	-1.26	1.83	-1.29	-2.41
g_2^1	0.09	-0.19	-0.16	-0.68	-0.20	3.34	-0.61	-1.70
h_2^1	-0.39	-0.61	-0.49	-0.93	-0.51	-3.66	-0.51	-1.48
g_2^2	0.34	0.13	0.32	0.17	0.12	-0.46	0.21	0.80
h_2^2	-0.22	-0.32	-0.28	-0.16	-0.38	1.18	-0.24	-0.61
g_3^0	-0.28	-0.52	-0.28	-0.35	-0.89	-1.62	-0.64	-1.53
g_3^1	0.25	0.23	0.06	0.16	0.32	0.09	0.13	-0.27
h_3^1	-0.44	-0.17	-0.11	0.14	-1.06	0.77	-0.57	0.88
g_3^2	-0.16	0.20	0.09	0.41	0.21	1.50	-0.05	-0.42
h_3^2	0.07	-0.20	0.09	0.09	0.09	-0.45	-0.17	-0.55
g_3^3	0.09	0.41	0.14	0.23	0.23	0.33	0.43	0.43
h_3^3	0.01	-0.37	-0.14	-0.15	-0.34	0.30	-0.39	-0.58

Even if the palaeomagnetic field models for the last five million years show only small contributions of the non-dipole field to the GAD field, the GAD hypothesis does not need to be true, because the models mentioned above were constructed based on global palaeomagnetic data that are limited in spatial coverage. Most palaeomagnetic data are from Northern Hemisphere equatorial to mid-latitudes, because most continental landmasses are in this region. Additionally, access to such regions is relatively straightforward.

1.7 Palaeosecular variations models

Variations of the palaeomagnetic field through time and space is referred to as palaeosecular variation (PSV). The PSV has been a major topic in palaeomagnetic studies for four decades (e.g., Johnson and McFadden, 2007), and is closely linked to study of the GAD hypothesis. Most PSV models are derived from full-vector palaeomagnetic data including palaeodirection and palaeointensity. Distributions of the datasets over the past five million years, which are thought to be insufficient enough to average-out secular variations, are still sufficient to construct palaeomagnetic field models (e.g., Johnson and Constable, 1997; Kelly and Gubbins, 1997; McElhinny and McFadden, 1997; Carlut and Courtillot, 1998; Kono et al., 2000; Hatakeyama and Kono, 2002).

The PSV models are summarised as follows: Model A (Irving and Ward, 1964) considered only non-dipole field variations while Model B (Creer et al., 1959; Creer, 1962) considered only dipole wobbles. Later models (Model C (Cox, 1962), D (Cox, 1970), Model E (Baag and Helsley, 1974), Model M (McElhinny and Merrill, 1975) and Model F (McFadden and McElhinny, 1984)) included both non-dipole fields and dipole wobbles. McFadden et al. (1988) proposed a new model (Model G) which considers dipole and quadrupole families. This model provides a direct link to spherical harmonic terms of degree l and order m, i.e., gauss coefficients g_l^m and h_l^m. Asymmetric terms about the equator ($l - m;\ odd$) such as g_1^0 and h_2^1 are classified as the dipole family while symmetric terms about the equator ($l - m;\ even$) such as g_1^1 and h_3^1 are classified as the quadrupole family. McFadden et al. (1988) calculated the virtual geomagnetic field (VGP) dispersions with latitudes using geomagnetic data from the international geomagnetic reference field 1965 (IGRF65). They found that the VGP dispersions due to dipole family linearly increase from zero at the equator up to 70° while the dispersions due to quadrupole family are constant with latitudes. They applied Model G to predict VGP dispersions derived from 3,719 lava flows spanning 0-5 Ma (McElhinny and McFadden, 1997). The model predicts the VGP dispersions successfully for latitudes below 70° but overestimates high-latitude data (McElhinny and McFadden, 1997).

Giant Gaussian Process (GGP) models for PSV behaviour

A different approach to studying PSV behaviour are forward models, which simulate PSV as Gaussian processes, that is each Gaussian coefficient is allowed to move around a mean value (often zero) via a Gaussian probability distribution. These so-called Giant Gaussian Process (GGP) models were first proposed by Constable and Parker (1988), here after CP88, in the same year that Model G was announced (McFadden et al., 1988). The GGP models do not have time component to them, but if we assume that sufficient time has passed, they represent the statistical process that is GGP. CP88 assumes that the Gauss coefficients has the statistical distribution depending on the degree l for each observation. CP88 described a PSV model following the following properties:

1) All Gauss coefficients are isotropic in their variability, i.e., g_l^m and h_l^m terms do not depend on the orientation of the coordinate system. The statistical distributions for these Gauss coefficients vary only with the degree l.

2) The PSV is described by normal distribution of the Gauss coefficients with their variance derived from the present-day field spectrum. The non-dipole part $(l \geq 2)$ is generated from the white source at the core-mantle boundary which has the variance of $(\sigma_l)^2 = \frac{(c/a)^{2l}\alpha^2}{(l+1)(2l+1)}$, where c/a is the ratio of the Earth's radius over the core radius (~0.547) and α is the fitted parameter to the current day spectrum.
3) All Gauss coefficients have a zero mean, except g_1^0 and g_2^0 terms. The variance of the g_1^0 is treated as special and has a lower value than the variance for $l \geq 2$.

The CP88 model was adjusted to fit the variation in the directional data for the past 5 Ma compiled by Lee (1983). The CP88 parameters are summarised in Table 1.2. The advantage of using the CP88 model is that the declination, inclination and intensity can be predicted anywhere on the Earth's surface. The drawback of the CP88 model is that it fails to predict the variation of the VGP dispersions with latitudes. This model was later modified by Quidelleur and Courtillot (1996), here after QC96. Quidelleur and Courtillot (1996) extensively analysed different parameter for means and variances of the Gauss coefficients. They concluded that increasing the variances for g_2^1 and h_2^1 improves the model to fit the observation data. The parameters of QC96 are also given in Table 1.2. Constable and Johnson (1999), here after CJ98, attempted to fit the lava flow compilations of Johnson and Constable (1996). They found that increasing power to the asymmetric terms $(l - m = odd)$ and decreasing power in the symmetric terms $(l - m = even)$ increases the VGP scatter at high latitudes. Tauxe and Kent (2004), here after TK03, proposed a simple approach to modify CP88 to fit both directional and intensity data. Rather than treating the variances of the asymmetric terms as the special case, they proposed a new parameter (β) which is the ratio of the dipole family over quadrupole family, i.e., $\beta = \frac{\sigma_l^m(l-m=o\quad)}{\sigma_l^m(l-m=even)}$. They also decreased the g_1^0 term to -18 μT following the past 5 Ma VADM of Selkin and Tauxe (2000), and removed the non-zero quadrupole g_2^0 term, setting it to zero. The TK03 successfully describes the dataset compiled by McElhinny and McFadden (1997) but underestimates the high-southern latitude data of Lawrence et al. (2009). Table 1.2 shows the comparison between each PSV model parameter.

Table 1.2: Parameters for the PSV models: CP88 (Constable and Parker, 1988), CJ98 (Constable and Johnson, 1999), QC96 (Quidelleur and Courtillot, 1996), TK03 (Tauxe and Kent, 2004) and this study (Chapter 5).

Parameter	CP88	CJ98	QC96	TK03	This study
g_1^0	-30 μT	-30 μT	-30 μT	-18 μT	-18 μT
g_2^0	-1.8 μT	-1.5 μT	-1.2 μT	0	0
α	27.7 μT	15 μT	27.7 μT	7.5 μT	7.8 μT
β				3.8	4.0
σ_1^0	$0.5\sigma_l = 3\mu\mathrm{T}$	$3.5\sigma_l = 11.72\mu\mathrm{T}$	3.0 μT	$\beta\sigma_l = 6.4\mu T$	$\beta\sigma_l = 12\mu T$
σ_1^1	$0.5\sigma_l = 3\mu\mathrm{T}$	$0.5\sigma_l = 1.67\mu\mathrm{T}$	3.0 μT	$\sigma_l = 1.7\mu T$	$\sigma_l = 3\mu T$
σ_2^0, σ_2^2	$\sigma_l = 2.14\mu\mathrm{T}$	$\sigma_l = 1.16\mu\mathrm{T}$	1.3 μT	$\sigma_l = 0.6\mu T$	$\sigma_l = 0.36\mu T$
σ_2^1	$\sigma_l = 2.14\mu\mathrm{T}$	$3.5\sigma_l = 4.06\mu\mathrm{T}$	4.3 μT	$\beta\sigma_l = 2.2\mu T$	$\beta\sigma_l = 1.4\mu T$
$l - m = odd$	σ_l	σ_l	σ_l	$\beta\sigma_l$	$\beta\sigma_l$
$l - m = even$	σ_l	σ_l	σ_l	σ_l	σ_l

As can be seen from the TAF and PSV models, the global palaeomagnetic database for the past 5 Ma has been continuously updated over the past few decades (e.g., Constable and Parker, 1988; Johnson and Constable, 1995; Johnson and Constable, 1996; McElhinny et al., 1996; Johnson and Constable, 1997; Kelly and Gubbins, 1997; McElhinny and McFadden, 1997; Carlut and Courtillot, 1998; Kono et al., 2000; Hatakeyama and Kono, 2002). New palaeomagnetic data are usually incorporated into the database prior to new model calculations, making direct comparisons of findings from differing model algorithm somewhat meaningless. Approaches of extracting palaeomagnetic information from data has also changed over the years, with stricter criteria now applied (McElhinny and McFadden, 1997). McElhinny and McFadden (1997) proposed that much of the data from older studies contain secondary overprints and were not magnetically cleaned in the laboratory, and that this older data should be reanalysed using the modern analytical techniques. Obtaining unprocessed raw data can be problematic, as this is not traditionally published, and re-analysing the original data is time-consuming. This issue was addressed by the NSF-funded Time-Averaged Field Investigation (TAFI) project, which ran through the late 90s to approximately 2007. This project was a consortium of four universities including Scripps Institution of Oceanography (University of California San Diego), University of Florida, University of Massachusetts and University of Alaska. The TAFI project aimed to improve temporal and spatial coverage of the palaeomagnetic data and upgrade existing data to modern standards. In addition to analysing existing data, this project successfully collected new palaeomagnetic data from many localities such as Nunivak Island in Alaska, British Columbia in Canada, the Snake River Plain, the San Francisco Peaks area of Arizona, the Trans-Mexican Volcanic Belt, Chile, Costa Rica and Patagonia. The new data from this project cover approximately every 10° latitude bands from Arctic to Antarctic. Some individual studies from the TAFI project are summarised in Appendix A according to their geographical locations. It is expected that the availability of the palaeomagnetic data during 0-5 Ma in the future would be sufficient to provide high-resolution TAF and PSV models.

1.8 Core-mantle interactions and non-dipole fields

As illustrated in the palaeomagnetic field models over ca. 5 Ma above, there is the persistence of the non-dipole fields which contribute to the GAD field. This section reviews the possible source of the non-dipole fields at the CMB. Heat flow across the core-mantle boundary (CMB) plays and important role to control cooling rate and solidification of the inner core, and determines the convection in the liquid outer core (Buffett, 2015). The convection in the outer core is controlled by the thermal and chemical buoyancy. Thermal buoyancy is generated by latent heat when the inner core cools down and solidifies (Verhoogen, 1961) and by forming of cold and dense fluid within the outer core near the CMB. Chemical buoyancy is generated when light elements are extracted to the outer core via the inner core solidification (Braginsky, 1963).

According to the present knowledge, two-types of convection occurs within the outer core (Buffett, 2015). The first type of the convection occurs when the CMB heat flows (Q_{CMB}) is higher than the adiabat heat flow on the outer core side (Q_{AD}). The mantle removes the excess heat from the core, while the cold and dense fluid is formed at the top of the core and convects down to the core. Another type of convection occurs when the $Q_{CMB} < Q_{AD}$. In this case the mantle cannot remove excess heat conducted down the adiabat. The excess heat accumulates at the top of the outer core (Gubbins et al., 1982). Naturally, the low viscosity of the outer core maintains the constant temperature that does not exceed 1°C over kilometer-scale within the outer core. The temperature variation in the outer core is very small when compared to the temperature variation in the mantle that could exceed several hundred degrees Celsius (Buffett, 2015). Therefore, the mantle convection is a key to control and limit heat loss from the core, and causes lateral temperature variations at the CMB. The cold slabs in the mantle increase the regional heat flow at the CMB as the temperature difference between the core and mantle increases regional heat flux. Numerical simulations (Zhang and Gubbins, 1993, 1996; Sarson et al., 1997) and experiments (Sumita and Olson, 1999, 2002) show that lateral variations in the CMB heat flow affects the fluid motion in the core. Numerical simulations also show that lateral variations in the heat flow lock the convection pattern in the core to the heat flow pattern at the boundary. Seismic-heterogeneity models reveals that the local heat flows produce the magnetic field with the persistence of the non-dipole fields (Olson and Christensen, 2002), similar to those found in the time-averaged field over ca. 5 Ma (Gubbins and Kelly, 1993; Johnson and Constable, 1997). Figure 1.8 is an example of the lateral variations in the CMB heat flow that controls the magnetic field. Dynamo model that imposes heterogeneous CMB heat flows shows that the lateral variations in the CMB heat flow (Figure 1.8a) correspond to the high-latitude flux lobes observed in the present-day field (Figure 1.8b). Lateral variations in the CMB heat flow may also have the impact on the magnetic reversals. Driscoll and Olson (2011) suggested that high CMB heat flow drives the superchron to the reversal state, while decreasing the heat flow alters frequency of magnetic reversals and drive the dynamo back to the superchron state.

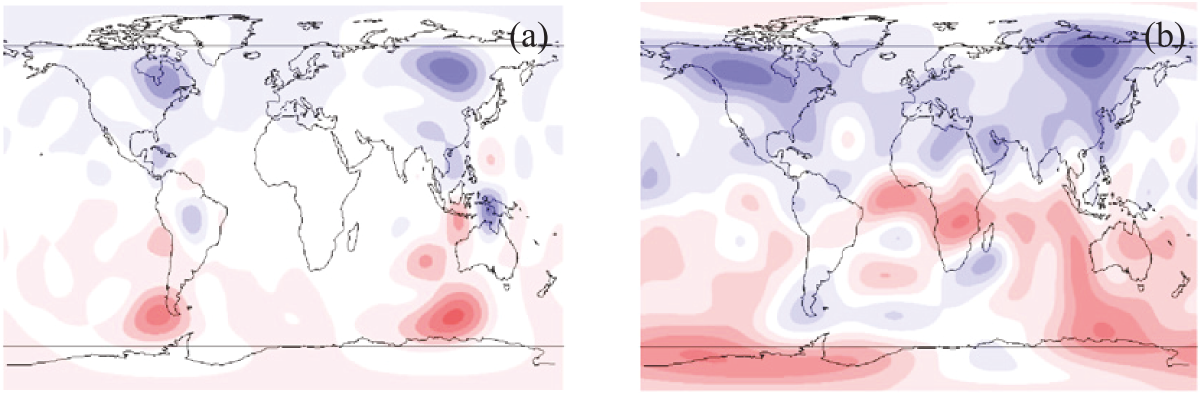

Figure 1.8: (a) simulated radial field at the CMB from the dynamo model that imposes heterogeneous CMB heat flow and (b) radial field at the CMB from the 1990 Earth's magnetic field after downward continuation to the CMB. It is clear that the lateral variations in the CMB heat flow in (a) corresponds to the high-latitude flux lobes in (b). Figures from Gubbins et al. (2007).

1.9 Thesis Objectives

OBJECTIVE 1

It is seen from the palaeomagnetic field models that the time-averaged geomagnetic field shows significant departure from the GAD hypothesis at high-latitudes. As this hypothesis is crucial in most tectonic reconstruction research, if the GAD is invalid in both direction and intensity, it could lead to reconstruction mismatch. Currently, the palaeomagnetic databases have sufficient low- to mid-latitude data, but require more high-latitude data (60°-90°). One aim of this thesis is, therefore, to sample the time-averaged field at high-northern latitudes by measuring palaeodirection using lava flow samples from northern Iceland during 2.5-8.5 Ma. As the current day palaeointensity dataset at high-latitudes are also sparse, this thesis also aims to provide robust palaeointensity data at high-latitudes, improve temporal coverage of the available high-latitude data and finally test the hemispheric asymmetry assumption of the palaeomagnetic field.

OBJECTIVE 2

Accurate isotopic dating is a requirement by the palaeomagnetic community for GAD analysis (e.g., Appendix A). Dated rocks improve temporal resolution of the TAF analysis. This thesis aims to deliver age determinations of the palaeomagnetically sampled lava flows in northern Iceland using the ^{40}Ar/^{39}Ar dating methods in order to improve the temporal resolution of the high-latitude data.

OBJECTIVE 3

Some studies (e.g., Appendix A) found that their mean directions are indistinguishable from the GAD hypothesis; others found significant (~5%) non-dipole contributions to the time-averaged field. This thesis aims to further analyse the time-averaged field at the global level and improve the global palaeomagnetic dataset at high-latitudes by combining the results of this study to the database. I then analyse this new combined database using a GGP PSV model based on the TK03 model.

1.10 Thesis outline

Below is a summary of the material contained within the remaining chapters of this thesis:

Chapter 2: The theory of palaeomagnetism that forms basis of all experiments in this thesis is introduced.

Chapter 3: The geology of Iceland and Icelandic volcanism are introduced. This is followed by a literature review of existing magnetostratigraphy publications of the lava sections in northern Iceland. A brief description of the three fieldwork campaigns are given.

Chapter 4: Within this chapter, I discuss the ^{40}Ar/^{39}Ar age determinations. First, I present the results of the x-ray fluorescent (XRF) analysis prior to the sample selection. Second, the sample preparation process for Ar/Ar dating is given followed by details of the dating method and data interpretation. The radio-isotopic ages are presented.

Chapter 5: In this chapter, I present new palaeomagnetic directional data from northern Iceland. These data were magnetically cleaned using the modern laboratory techniques to remove secondary overprints, and palaeodirectional analysis of the data undertaken. The palaeodirectional results are compared to the GAD hypothesis, which is the primary goal of this thesis. The magnetostratigraphy of the composite section is combined with the ^{40}Ar/^{39}Ar age determinations to construct an age model for the studied section. The results of a rock magnetic study are also presented in this chapter.

Chapter 6: The results from Chapter 4 are added to the global dataset. This global dataset is a new compilation that is constructed by me, using strict selection criteria. I then use PSV models to study to the new global dataset.

Chapter 7: This chapter focuses on the palaeointensity of the geomagnetic field as recorded by the composite section sampled through a lava pile in northern Iceland. I briefly introduce palaeointensity methods, followed by the sample selection methods. Then, the palaeointensity results are presented. Following this, the long-term field strength at high-latitudes is then compared to the GAD hypothesis and other data collected from the palaeointensity database.

Chapter 8: This chapter summarises the main results and conclusions of this thesis.

Chapter 2

Theory of rock magnetism and palaeomagnetism

2.1 Overview

Chapter 2 provides review palaeo- and rock-magnetism theory and methods that form experiments in this thesis.

2.2 Magnetic grain-size and its effect on magnetic behaviour

Rocks in nature consist of assemblages of various magnetic grains. Each grain has a different ability to record the Earth's magnetic field, depending on its size and shape. The smallest magnetic particles are magnetically uniform and are said to single domain (SD) (< 100 nm for magnetite; Nagy et al., (2017); Figure 2.1a). Very small SD particles are magnetically unstable due to thermal energy, and are said to be superparamagnetic (< 30 nm for magnetite at room-temperature over a period of 60 s). SD grains controlled by uniaxial anisotropy obey Néel's (1949). When the grain size increases (>100 μm for magnetite, Figure 2.1d), the magnetisation breaks up into areas of uniform magnetisation separated by magnetic domain walls (Figure 2b). When the magnetic particle comprises many domains, this domain grain is called multidomain (MD) grain (Figure 2.1c). Large MD grains are magnetically unstable and are poor magnetic recorders. Magnetic crystals with only a few domains (e.g., Figure 2.1b) have magnetic behaviour that is similar to that of SD particles; they are commonly termed pseudo-single domain (PSD) grain. The exact magnetic structure found in PSD grains is more complex than that shown in Figure 2.1d (Nagy et al., 2017); current thinking suggests that magnetic materials like magnetite, rather than having simple two-domain structures, have curling vortex structures. In natural igneous rocks, most of grains are thought to be PSD with some SD.

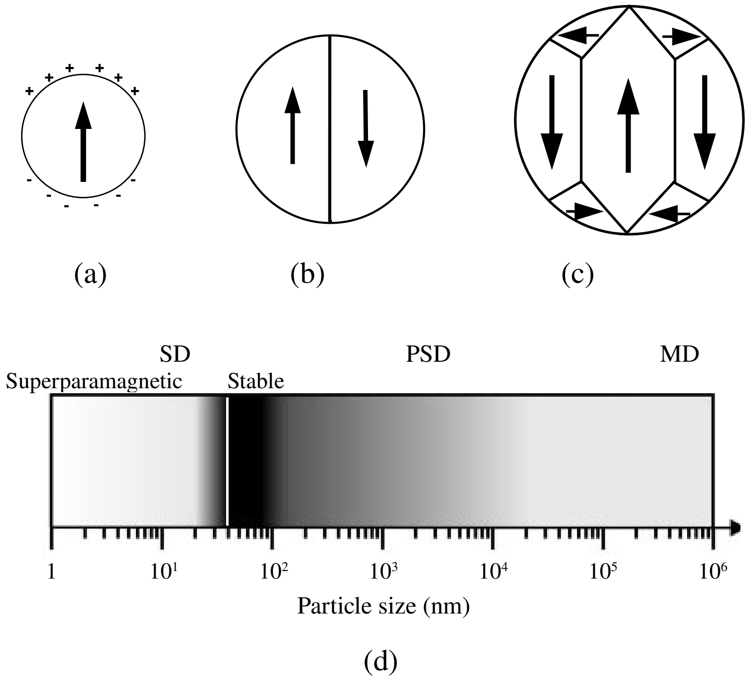

Figure 2.1: “Classical” domain structures of (a) single-domain (SD) grain (b) two-domain grain, (c) multi-domain (MD) grain and (d) domain size of magnetite (redrawn after Butler (1992) and Fabian and Hubert (1999)). For materials like magnetite, the two-domain structure shown are more likely to be curling vortex structures.

2.3 Magnetisation in rocks

Natural remanent magnetisation (NRM) is the magnetisation that has been acquired by natural processes. The NRM is categorised as primary if the NRM has been acquired when the rock forms. There are several ways by which NRM is recorded such as thermoremanent magnetisation (TRM), acquired by cooling of ferromagnetic grains below their Curie temperature under applied weak magnetic fields like that of the Earth, chemical remanent magnetisation (CRM) acquired by precipitation of the magnetic minerals from solution or by alteration of pre-existing minerals, depositional/detrital remanent magnetisation (DRM) recorded by physical alignment of magnetic minerals in liquid which is trapped after sediment lithification, viscous remanent magnetisation (VRM) acquired by exposure to weak magnetic fields such as the Earth's magnetic field over very long time and isothermal remanent magnetisation (IRM) gained by short-time exposure to the strong magnetic field such as the field induced by lightning strike. In this study, I focus on the TRM which is assumed to be the primary remanent magnetisation of all igneous rocks and also Icelandic basalts, although there is some evidence to suggest that thermo-chemical process might also contribute to the magnetisation (Bowles et al., 2012). According to Néel's (1949) theory for SD particles, TRM can be stable over million years, however, thermal excitation causes the TRM acquired in the smallest particles to decay with time at ambient temperatures. The time that the TRM decays to $1/e$ is referred to as relaxation time (τ). Néel (1949) proposed a relation between relaxation time and thermal energy for SD grain as:

$$\tau = \frac{1}{f} \exp\left(\frac{V h_c j_s}{2kT}\right) \tag{2.1}$$

where f is frequency factor ($\sim 10^8$ s^{-1}), V is the activation volume (essentially the grain volume for SD particles), h_c is microscopic coercivity, j_s is saturation magnetisation, k is Boltzmann constant and T is temperature in Kelvin. As can be seen from equation 2.1, the relaxation time of the SD grain relies on grain volume and coercive force (the field that reduces magnetisation to zero).

Magnetic minerals

The most abundant magnetic minerals in igneous rocks are iron-titanium (FeTi) oxides (Tauxe et al., 2010). This section primarily reviews FeTi oxides and oxidation processes that commonly occur to igneous rocks in nature.

2.3.1 Titanomagnetite

Titanomagnetite is commonly found in igneous rocks especially Icelandic basalt (e.g., Stanton et al., 2011; Oliva-Urcia and Kontny, 2012; Døssing et al., 2016). The general chemical formula of titanomagnetite series is $Fe_{3-x}Ti_xO_4$, where x is titanium composition varying from 0 (pure magnetite, Fe_3O_4) to 1 (ulvöspinel, Fe_2TiO_4). It is common to illustrate titanomagnetite series on a ternary diagram (Figure 2.2a). The position from left to right shows the increasing ion from ferrous (Fe^{2+}) to ferric (Fe^{3+}) while the position from bottom to top indicate the increasing titanium content. The crystal structure of magnetite and titanomagnetite is an inverse spinel structure with two sublattices: A and B. The electron spin in the A sublattice is antiparallel to the spin in the B sublattice. In pure magnetite, one Fe^{3+} occupies the A sublattice while other two ions (Fe^{3+} and Fe^{2+}) occupy B sublattice. The net magnetic moment in magnetite is not zero, causing magnetite is ferrimagnetic. With regards to ulvöspinel, a Ti^{4+} which has no magnetic moment occupies a position in B sublattice causing magnetic moments in A and B sublattices to cancel each other out. The zero net magnetic moment results in ulvöspinel being antiferromagnetic.

The Curie temperature of titanomagnetite series vary depending on titanium composition. The Curie temperature of pure magnetite is 580°C (Dunlop and Özdemir, 1997). The Curie temperature decreases when titanium composition increases (Figure 2.2b).

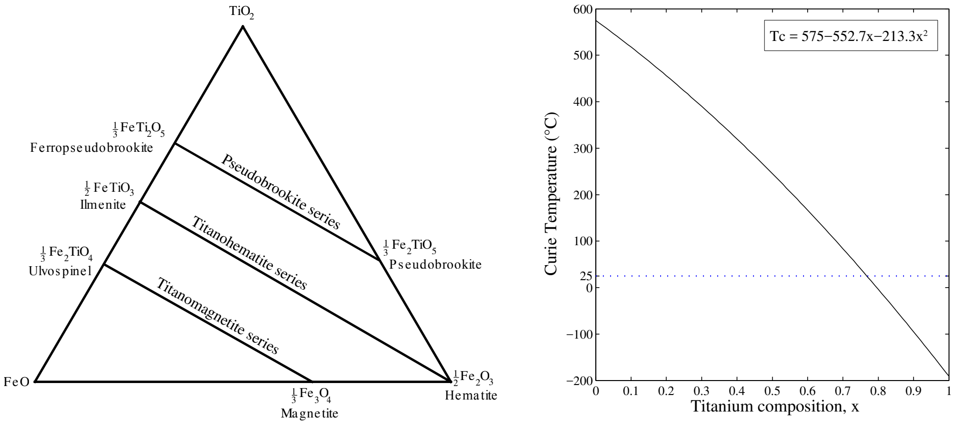

(a) (b)

Figure 2.2: (a) TiO_2-FeO-Fe_2O_3 ternary diagram (modified from Hunt et al. (1995)) and (b) Curie temperature of titanomagnetite series (redrawn after Nagata (1961)).

2.3.2 Titanohematite

Titanohematite is common in silicic rock and red sediment (Dunlop and Özdemir, 1997; Tauxe et al., 2010). The general formula of titanohematite is $Fe_{2-x}Ti_xO_3$, where x is titanium composition. The Curie temperature of titanohematite series varies with the titanium composition (Figure 2.3a). Pure hematite (α-Fe_2O_3) has a Curie temperature of 680°C (Tauxe et al., 2010). Hematite has a small saturation magnetisation at room temperature due to the canted antiferromagnetic moments of Fe^{3+} and Fe^{2+} between adjacent layers (Tauxe et al., 2010). Figure 2.3b shows saturation magnetisation of the titanohematite series measured at room temperature. The titanohematite with low titanium composition ($0<x<0.45$) is antiferromagnetic, while those with high titanium content ($0.45<x<1$) are ferrimagnetic minerals, because the Ti^{4+} replaces Fe^{2+}.

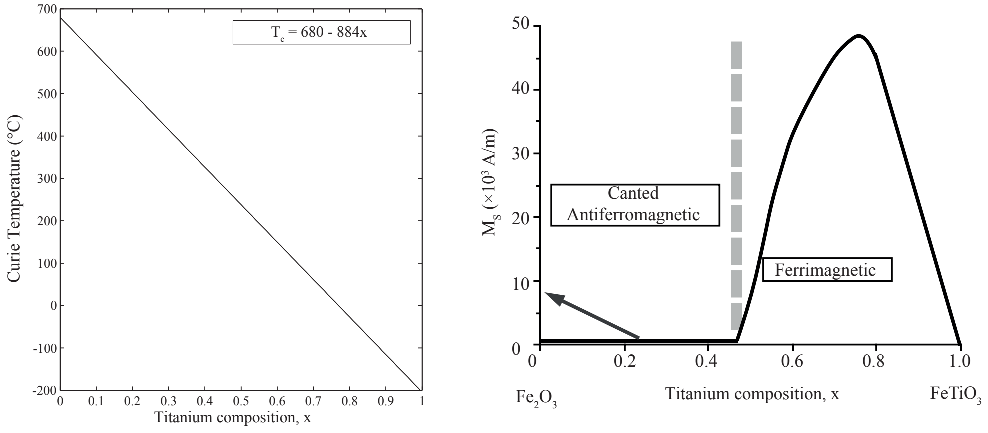

(a) (b)

Figure 2.3: (a) Curie temperature of titanomagnetite series and (b) the saturation magnetisation at room temperature of titanohematite series. Redrawn from Hunt et al. (1995) and Nagata (1961).

2.3.3 Low temperature oxidation

Low-temperature oxidation, known as maghemitisation, is an alteration form of titanomagnetite to titanomaghemite at low temperature (< 350°C) (Özdemir, 1987). The maghemitisation process reduces 1/3 electrons in magnetite and produces vacancies (□) in the spinel structure. This process decreases magnetisation in titanomaghemite because Fe^{2+} in B sublattice is reduced 1/3 cation. Maghemitisation is common in all basalt (Ozima and Ozima, 1971), especially in geothermally active areas such as northeast Iceland (Oliva-Urcia and Kontny, 2012). Walker (1960) also found that the basalt in Eastern Iceland also suffers from regional hydrothermal alteration.

Özdemir and O'Reilly (1982) mimicked the low-temperature oxidation process to synthesise titanomaghemite particles in neutral air in the laboratory. They produced samples with the thermomagnetic curves typical of titanomaghemite (Figure 2.4). The magnetisation drops on warming to 250°C, then, the magnetisation increases after heating above 250°C. They noticed a hump at 400°C as an inversion process from titanomaghemite to an unstable magnetic mineral that has high magnetisation. The final mineral product which is stable is formed during the cooling process. These final products are spinel and ilmenite phases (Özdemir and O'Reilly, 1982; Özdemir, 1987). As the inversion of the mineral occurs when heating titanomaghemite at high temperature, this makes it difficult to determine the true Curie temperature of titanomaghemite (Dunlop and Özdemir, 1997). Determination of titanomaghemite’s Curie temperature might need extrapolation of the data curve prior to the start of inversion (Carvallo et al., 2004). Dunlop and Özdemir (2007) found maghemite's Curie temperature ranged from 590°C to 675°C.

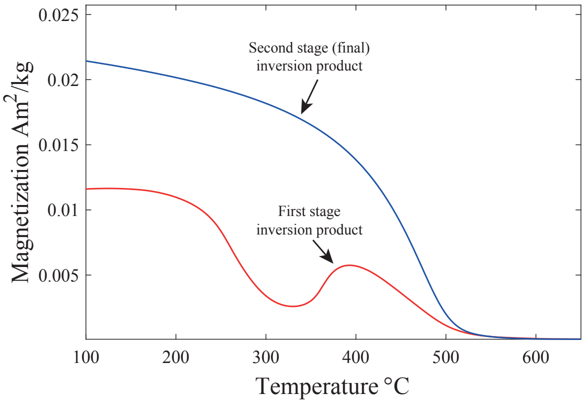

Figure 2.4: Characteristic thermomagnetic curve of titanomaghemite. Red and blue lines show the heating and cooling curves. A hump at 400°C indicate the first in version product. The final product is formed during the cooling process (Özdemir, 1987).

2.4 Methods in palaeo- and rock-magnetism

Magnetic measurements in the laboratory can be roughly split into palaeomagnetic, i.e., study of the natural remanent magnetisation recorded by a rock, and rock magnetic, i.e., using magnetic measurements to investigate the magnetic grain size distribution, magnetic mineralogy and recording fidelity.

2.4.1 Hysteresis loops

Hysteresis loops are measured to understand the magnetic grain-size distribution of a sample, and its recording fidelity. When an external magnetic field (**B**) is applied to ferromagnetic materials, the magnetisation increases with the field (Figure 2.5a). When the field reaches B_{max}, the magnetisation becomes saturated (M_s, saturation magnetisation). When the field is decreased to zero, the magnetisation left is the remanent magnetisation (M_{rs}, b path). With further decreases in the field in opposite direction, the magnetisation decays to zero at B_c (coercivity) and reaches the saturation magnetisation in the opposite direction. When the field is applied in cycle, the magnetisation follows the hysteresis loop. The coercivity of remanence (B_{cr}) is the field that reduces the remanent magnetisation to zero at the origin.

In nature, rock samples are composed by combinations of single domain, pseudo-single domain and multi domain grains. Each type of grains provides different value of hysteresis parameters. In palaeomagnetism, the hysteresis parameters are plotted on the 'Day' plot diagram (Day et al., 1977). The ratio of H_{cr} to H_c is plotted against the ratio of M_{rs} to M_s. High M_{rs}/ M_s ratios are typical for SD grains, and high H_{cr} to H_c ratios are typical for MD grains. The domain states are separated by the boundaries as marked with lines on the graph (Day et al., 1977) (Figure 2.5b).

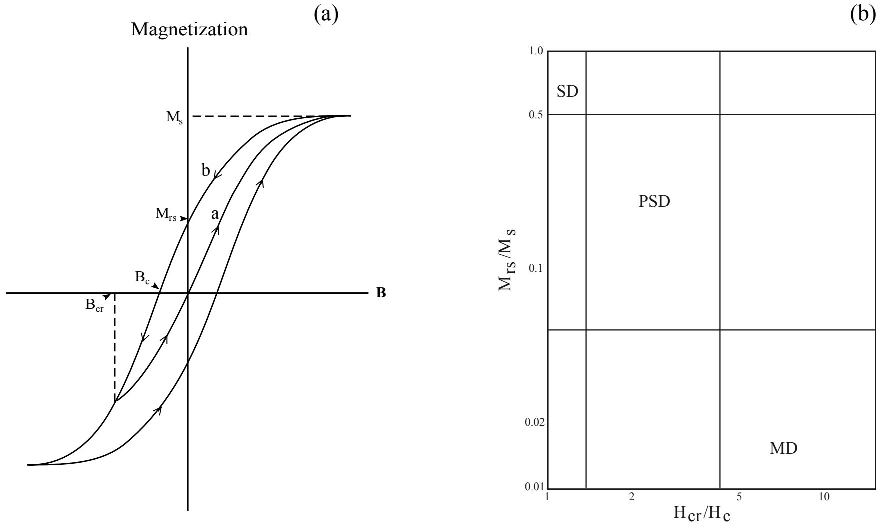

Figure 2.5: (a) A hysteresis loop showing the following parameters: saturation magnetisation (M_s), remanent saturation (M_{rs}), coercivity (H_c), coercivity of remanence (H_{cr}). (b) "Day plot" diagram (Day et al., 1977) where the hysteresis properties are plotted. The SD, PSD and MD boundaries are labelled in (b).

2.4.2 Strong field thermomagnetic curves

The Curie temperature is measured to determine the magnetic mineralogy of sample, and to examine the thermal stability (Dunlop and Özdemir, 1997). It is determined by measuring the strong field thermomagnetic curves. Samples are placed in a saturating or nearly saturating magnetic field (e.g. 100 mT) and the magnetisation is measured while the temperature is increased. Figure 2.6 shows the thermomagnetic curve of pure magnetite and hematite. Determination of the Curie temperature is not as simple as it initially seems. Moskowitz (1981) proposed a method for extrapolating the experimental data to determine the point at which the ferromagnetic contribution drops to zero. A second method is applying the second derivative to the thermomagnetic data (Tauxe, 2003). The maximum peak of the second derivative data is a reasonable estimate of the Curie temperature. This second method is popular; however, this method has a drawback that the second derivative amplifies the noise in the thermomagnetic data. To fix this problem, a running average is commonly used to smooth the data before dating the derivative. In this thesis, I use the second derivative method with a five-point running average to determine the Curie temperature.

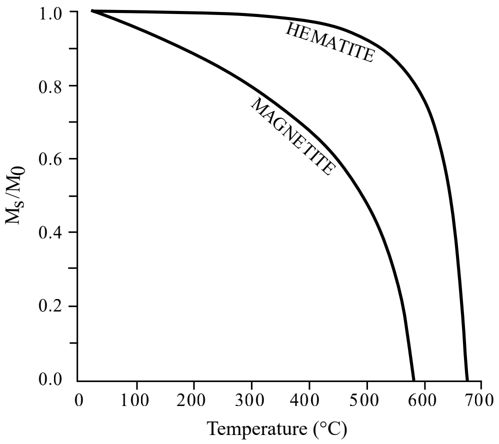

Figure 2.6: Strong field thermomagnetic curves of pure magnetite and hematite. The Curie temperatures are normally determined from the bulk-demagnetisation zone. Figure from Pullaiah et al. (1975).

2.4.3 Thermal demagnetisation

Thermal demagnetisation is undertaken to determine the direction of the recorded NRM. By heating samples to temperature T_{emag} in a zero-magnetic field environment; magnetic grains that have unblocking temperature $T_{ub} \leq T_{emag}$unblock. The T_{ub} is the temperature at which the magnetisation becomes unblocked if the magnetic grains are heated above this temperature. Natural rocks contain a range of different grains with different T_{ub}. The variations of T_{ub} in different grains allow us to perform step-wise thermal demagnetisation instead of one single heating step. The NRM remaining is measured after each demagnetisation step and plotted on the orthogonal projection plot diagram, known as Zijderveld diagram (Zijderveld, 1967). The directions of the primary NRM were determined by principal component analysis (PCA) technique (Kirschvink, 1980).

2.4.4 Alternating field demagnetisation

Alternating-field (AF) demagnetisation is similar to thermal demagnetisation, in that it aims to step-wise demagnetise samples to isolate the primary magnetisation. Instead of heating the sample, an alternating field is applied (Figure 2.7). AF demagnetisation is quicker than thermal demagnetisation, and is particularly useful for samples containing organic material, e.g., sediments (Tauxe, 2010). The amplitude of the alternating magnetic field linearly decays with time (Figure 2.7a). For example, when the peak field is set to 100 mT, the magnetic grains that have the coercive force ≤ 100 mT are flipped up along the applied field (point 1, Figure 2.7b). When the peak field is switched to the opposite direction (-99 mT), the grains whose magnetic moments have coercivities ≤ 99 mT are flipped down and their magnetisation becomes locked in the down direction when the field is decreased (point 2, Figure 2.7b). The process runs to the point 3 (Figure 2.7b). When the field is decreased below 98 mT, the grains whose have coercive force ≤ 98 mT are locked in the upward direction. This process continues until the field decays to zero. In principle, half of the grains are fixed along one direction while remaining grains become stuck along the opposite direction. The net magnetisation becomes zero (Tauxe et al., 2010). This process is repeated in three directions (static), or is completed only once whilst tumbling the sample around two rotation axes.

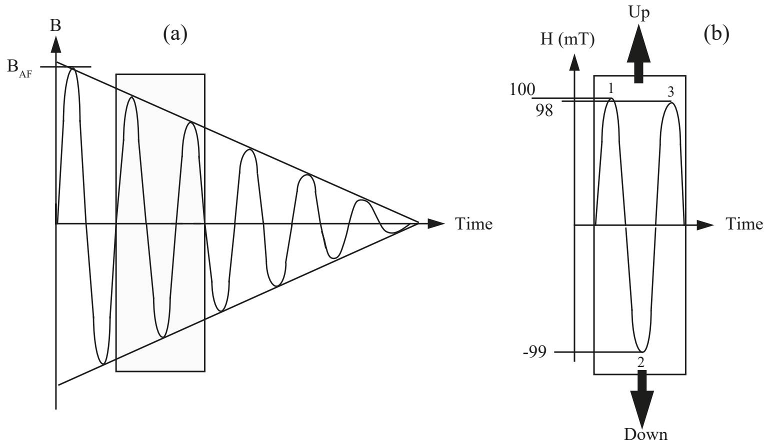

Figure 2.7: (a) schematic of the altermatic-field wave form decaying to zero with time and (b) an example case of the AF demagnetisation in the block of (a) when the peak field is set to 100 mT. The field decays with time to 98 mT, locking magnetic moments in the upward and downward directions. Figure from Butler (1992).

2.4.5 Principle of absolute palaeointensity determination

Palaeointensity estimates can provide valuable information of the ancient geomagnetic field (B_{anc}), and its formation within the Earth's core. Palaeointensity determination follows the assumption that the acquired remanence (M_{NRM}) is linearly proportional to field for small fields < 200 µT, i.e., $M_{NRM} = \mu_{anc} B_{anc}$ under the Earth's field and $M_{lab} = \mu_{lab} B_{lab}$ under the known laboratory field, where μ_{anc} and μ_{lab} are constants (Tauxe and Yamazaki, 2007). As μ_{anc} and μ_{lab} are assumed to be identical, the ancient magnetic field strength (B_{anc}) can be determined by comparing the measured M_{NRM} to a laboratory induced magnetisation M_{lab} (laboratory field is B_{lab}), that is, (Tauxe and Yamazaki, 2007; Tauxe et al., 2010):

$$B_{anc} = \frac{M_{NRM}}{M_{lab}} B_{lab} \tag{2.2}$$

In theory, palaeointensity determination appears to be simple, as we only need to apply the laboratory field and measure induced remanence. However, in practice, many factors can lead to palaeointensity failure. For example, multi-domain and pseudo-single domain grains give erroneous palaeointensity determination as their blocking (T_b) and unblocking (T_{ub}) temperatures are not identical. Also, magnetic minerals can alter during the experiment, changing the capacity of samples to acquire remanence. Additionally, the assumption that induced magnetisation is linearly proportional can also fail for some samples, if the laboratory field direction not parallel to the ancient field direction can also lead to problems, and the specimens that are anisotropic can also yield incorrect palaeointensity estimates (Tauxe and Yamazaki, 2007; Tauxe et al., 2010).

Thellier and Thellier (1959) proposed a step-wise heating method to determine ancient geomagnetic field intensity. The Thellier-Thellier method is based on the Néel's theory for single domain grains (Néel, 1949). The basic process is to heat specimens up and cool specimens down under the laboratory field (B_{lab}). The NRM is replaced by partial thermal remanent magnetisation (pTRM). Therefore, the total remanent magnetisation is:

$$M_1 = M_{NRM} + M_{pTRM} \tag{2.3}$$

where M_1 is the total remanence. M_{NRM} and M_{pTRM} are the NRM remaining and pTRM-gained (M_{lab} in Equation 2.2). Then, the specimens are heated up and cooled down again under the opposite polarity laboratory field $(-B_{lab})$. The new total remanence is determined by Equation 2.4:

$$M_2 = M_{NRM} - M_{pTRM} \tag{2.4}$$

From Equation 2.3 and 2.4, M_{NRM} and M_{pTRM} can be determined, if we know the laboratory field, B_{anc} can be obtained from Equation 2.2. The Thellier-Thellier method is based on law of independence, additivity and reciprocity (Thellier, 1938; Thellier and Thellier, 1959).

The law of independence states that the pTRM acquired by cooling between T_2 and T_1 is completely independent from other two temperature steps. In SD theory, the TRM can be broken into portions of pTRM. For example, the TRM acquired between 600°C and 500°C is referred to as pTRM(600, 500). The pTRM in one window is in theory independent of those in other windows. The net TRM of a sample is the summation of pTRM from different windows. This principle is referred to as “law of additivity” (Butler, 1992; Tauxe and Yamazaki, 2007). The law of reciprocity state that the pTRM acquired by cooling from T_2 and T_1 can be removed completely after reheating specimens to T_2 in a zero field, i.e., blocking temperature and unblocking temperature are identical $(T_b = T_{ub})$ (Tauxe et al., 2010).

Coe (1967) proposed the modified Thellier-Thellier method by first heating samples in a zero magnetic field. This method allows the direct measure of the NRM remaining after each demagnetisation step. Then, samples are re-magnetised in an applied laboratory field. The pTRM gained can be determined after zero field/infield steps. In this research, I plan to use the IZZI protocol (Tauxe and Staudigel, 2004), which is the combination of zero field/infield (ZI) (Coe, 1967) and infield/zero field (IZ) (Aitken et al., 1988) measurement steps in the palaeointensity experiment. During the experiment, samples can lose capacity to acquire remanence due to mineralogical changes. This is usually identified using a so-called pTRM check step (Coe et al., 1978), that is alternated in the IZZI protocol between Z and I steps in order to check mineralogical changes. The pTRM-tail check (Riisager and Riisager, 2001) is the zero-field step which is alternated between ZI and IZ steps in order to check non-SD behaviour.

Palaeointensity data are usually illustrated in an Arai plot (Nagata et al., 1963), which is a plot of the NRM remaining against the pTRM-gained (Figure 2.8). The slope of the graph is the ratio of the NRM and pTRM gained. The ancient geomagnetic field can be determined following this relation:

$$B_{anc} = -slope \times B_{lab} \tag{2.5}$$

It is simple to estimate palaeointensity if the data displays straight-line behaviour on the Arai plot. The difficulty of data interpretation arises when the sample is not that of an ideal SD grain assemblage. Levi (1977) showed that that the PSD and MD grains of magnetite exhibit a concave-up curve on the Arai plot. Xu and Dunlop (2004) performed Thellier-Thellier-type experiment on synthetic sized magnetite samples (mean sizes 0.6, 1, 6, 20 and 135 μm). The samples were induced with a TRM with an applied laboratory field of 100 μT. Similar to the findings of Levi (1977) their results show that the degree of curvature of the concave-up curve increases when the particle size increases. Shcherbakov and Shcherbakova (2001) reported that fitting low temperature segment on the concave-up curve results in overestimates of palaeointensity of approximately 60%. McClelland and Briden (1996) suggested that if there is no alteration found in the data, determining the slope of the line connecting two-end points would provide the best estimate of palaeointensity. Biggin and Thomas (2003) performed the Thellier-Thellier experiment on intrusive igneous rocks thought to have large magnetic grains. Their results show curvature on the Arai plot. Biggin and Thomas (2003) found a similar deviation from their results. Biggin and Thomas (2003) shows that there is not much difference between fitting two-end points and fitting as large segment as possible.

Shaar et al. (2011) performed a palaeointensity experiment on slag samples to quantify the laboratory conditions which potentially affect the Arai plot curvature. Firstly, they magnetised samples in the known laboratory field (B_{anc}). Then, they performed the palaeointensity experiment using the IZZI protocol under the varying applied laboratory field (B_{lab}) which is proportional to the B_{anc}. They also varied the angle between the B_{lab} and B_{anc} (θ). They found that the straight-line Arai plot occurs when the $B_{lab} = B_{anc}$ and $\theta = 0°$. This is clearly a circular argument. The convex curves occur when the laboratory field in the oven is stronger than the ancient field. Additionally, zigzagging behaviour, which is unique for the IZZI protocol (Tauxe and Staudigel, 2004; Yu and Tauxe, 2005; Shaar et al., 2011) was found by Shaar et al. (2011) for all of their non-SD slag samples. They found that the degree of zigzagging yields the maximum when the laboratory field is antiparallel to the ancient field $(\theta = 180°)$.

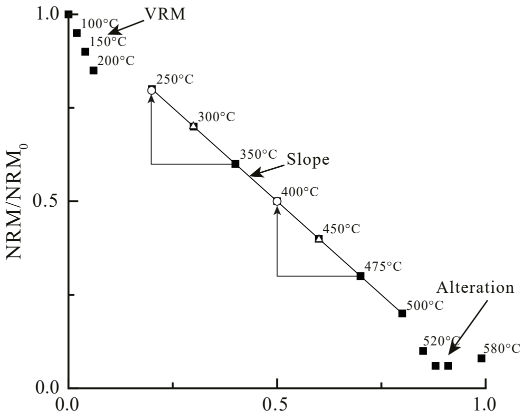

Figure 2.8: Schematic diagram of the Arai plot (Nagata et al., 1963). The black squares show the relation between NRM remaining and pTRM gained at each temperature step. Circles and triangles represent pTRM checks and pTRM-tail checks. It is clear that scatter points at low temperature steps are a result of viscous remanent magnetisation (VRM) while the scatter points at high temperature steps are due to thermal alteration. The linear segment (black line) is used to determine palaeointensity as it show the best fit line.

Chemical alteration during heating is a serious drawback of palaeointensity experiments, that can lead to very low success rates. For example, Tanaka et al. (2009) performed the Thellier's experiments on lava basalts from Okataina volcanic centre, New Zealand. Approximately 43% of samples passed the selection criteria. Mochizuki et al. (2006) measured palaeointensity on basalt from lava flows in New Zealand, all of their samples failed the palaeointensity experiment due to thermal alteration. Døssing et al. (2016) performed the palaeointensity experiment on 205 specimens from Eastern Iceland. Of these, 44 specimens (~21%) yielded successful results. There are many other potential examples from the literature. The major causes of alteration in nature are low temperature oxidation as mentioned in section 2.3.3. The low-temperature oxidation reduces 1/3 of cation in B sublattice and decreases the ancient field intensity in samples. Chemical alteration can also happen in the laboratory during step-wise heating protocols (Carvallo et al., 2006), primarily oxidation during laboratory heating causes an inversion of titanomaghemite to another mineral (Özdemir, 1987). Another serious drawback of palaeointensity experiments is that it is very time consuming.

Oxidation and reduction during the heating process can lead to thermal alteration in the samples during palaeointensity experiments. Several studies have proposed methods that minimize thermal alteration. Carlut and Quidelleur (2000), Carlut et al. (1999) and Valet et al. (1998) show that palaeointensity experiments performed in inert atmospheres can improve the quality of data. They separated samples into two groups. Group 1 was performed in neutral atmosphere both during heating and cooling processes, while group 2 was conducted in argon atmosphere during the heating process but in nitrogen atmosphere during cooling process. In Valet et al. (1998) study, their results show that 77% of samples run in argon atmosphere yielded successful results while only 53% of the samples run in neutral air passed the selection criteria. With regards to Carlut and Quidelleur (2000) and Carlut et al. (1999) studies, approximately 42% and 44% of their samples run in neutral air required the pTRM correction to restore linearity of the data while only 16% and 35% of the samples run in controlled atmosphere required this correction. In this thesis, I performed palaeointensity experiments under controlled helium atmosphere in order to try to prevent alterations.

2.4.6 Q_{PI} criteria

A new set of quality criteria to assess reliability of published palaeointensity data (Q_{PI}) was proposed by Biggin and Paterson in 2014. The Q_{PI} criteria were developed following the idea of quality (Q) criteria for palaeomagnetic poles (Van der Voo, 1990). Since the Q criteria has been proposed, palaeomagnetists began to assess the quality of their palaeomagnetic poles by grading the Q score from 0 to 7. While Q criteria was aimed to be applied at the palaeomagnetic poles that are averaged from many site-mean directions, the Q_{PI} criteria were designed to be applied at the level of the individual cooling unit or sampling site. Eight Q_{PI} criteria are now used to assess reliability of palaeointensity estimates in the community as defined below:

AGE: this criterion was designed to assess the radiometric or stratigraphic ages for tracing palaeomagnetic dipole moment (PDM) variations.

STAT: as the site-mean palaeointensity is averaged from specimens from the same cooling unit, this criterion was set to prevent outliers. The STAT criterion requires at least 5 specimens per cooling unit to average site-mean intensity. The per cent standard deviation must be $\leq 25\%$.

TRM: this criterion required microscopic analysis to rule out sources of non-TRM such as low temperature oxidation. This criterion can be met by assessing a representative cooling unit which extended to the formation level.

ALT: alterations during heating can happen in palaeointensity experiments even though the experiments are performed in the controlled atmosphere as stated in the previous section. This criterion require alteration checks to be performed during palaeointensity runs. For example, the pTRM check (Coe et al., 1978) is required in the IZZI protocol to meet the ALT criterion.

MD: non-ideal SD grain can cause Arai plot curvature or failure in palaeointensity estimates. In Thellier-type experiments, this criterion can be met by obtaining pTRM tail check for checking MD grains (Riisager and Riisager, 2001).

ACN: This criterion requires evidence to prove that the palaeointensity estimates are not biased due to 1) anisotropy of TRM, 2) cooling rate effects and 3) non-linear TRM effects. To meet this criterion, all three issues must be checked. The first of these issues rarely affect igneous rocks. A simple check is to measure the angle (γ) between the pTRM acquired at the last step used for palaeointensity estimates and the lab field direction. The second issue can affect the large intrusions that cool over hundreds of kyr. This bias can be corrected by performing cooling rate correction to meet this criterion. The last issue causes the bias on palaeointensity data when the laboratory field and ancient field strengths are not identical. Typically, this effect is minimal in the lava flow samples if the two fields are within a multiple of ~1.5 times of each other. A simple approach to test the non-TRM effects is to run palaeointensity experiments on specimens from the same core under different laboratory field strength. This issue is met if two palaeointensity estimates are nearly identical.

TECH: this criterion considers that palaeointensity estimates from one experiment are not sufficient to confirm if the results are reliable, i.e., only results from Thellier-Thellier experiment do not meet this criterion. All Thellier-type experiments are considered as the same technique. To meet this criterion, as least two palaeointensity techniques are required to be performed, e.g., Thellier-Thellier modified by Coe along with Shaw family method.

LITH: to meet this criterion, the mean palaeointensities are averaged from more than one lithology or samples from the same lithology that have different unblocking temperature.

Biggin and Paterson (2014) revised 25 studies on the PINT15 database and found that 99% of these studies meet AGE and ALT criteria. This result shows that the palaeointensity community is now aware of the alterations that always occur during the experiments, as can be seen in many studies that perform the pTRM checks (e.g., Cromwell et al., 2013b; Di Chiara et al., 2014). The hardest criteria to be met are ACN and LITH. Only 1% and 2% of these studies pass these criteria.

Chapter 3

Fieldworks in Iceland

3.1 Brief introduction to northern Iceland

This section reviews existing studies in northern Iceland. Most geological research in Eyjafjordur and Skagafjördur was conducted before 1980 (Kristjansson et al., 2004). A Dutch drilling project in the 1960s included stratigraphic mapping and palaeomagnetic dating of the east of Eyjafjordur (Hebeda et al., 1974) (Figure 3.1). This project revealed a thick zone of normal polarity in the stratigraphic section, dating back to chron C5n. Johannesson (1991) and Johannesson and Saemundsson (1998) reported that the thick normal-polarity zone extends to 10 km south of Akureyri. On the western flank of Eyjafjordur, Aronson and Saemundsson (1975) carried out K/Ar dating and reported the ages of the west flank are around 7.2-9.5 Ma. Saemundsson et al. (1980) performed K/Ar dating and palaeomagnetic dating in the Tröllaskagi peninsular, which is located between the western flank of Eyjafjordur and Skagafjördur. Their results reveal that the oldest rocks are approximately 12 Ma at the north coast of the peninsula. They also found a thick normal polarity zone in their stratigraphic section which corresponds to the Dutch expedition section (Figure 3.1) (Hebeda et al., 1974). The youngest rocks of their section were dated back to 9 Ma. Kristjansson et al. (2004) carried out a palaeomagnetic study in Eyjafjordur south of Akureyri. Their composite section is comprised of more than 300 lava flows covering 2.8 km thick (Figure 3.1) with the youngest profiles located in Eyjafjardardalur. They reported the age of their youngest units as approximately 5 Ma (Hardarson et al., 1999). The ages of the exposed terrane at the edge of the Icelandic Highlands (~50 km south of Akureyri) is c. 3-3.5 Ma (Johannesson and

Saemundsson, 1998). Johannesson (1991) reported the general picture of the Tröllaskagi peninsular. The lava pile on the peninsula forms a north-south trending anticlinal structure with the axis tilted toward the south of Saemundsson et al. (1980) study areas and Eyjafjardardalur (Johannesson, 1991). East of the anticline the strata is tilted toward southeast, while west of the anticline the strata is tilted to the southwest.

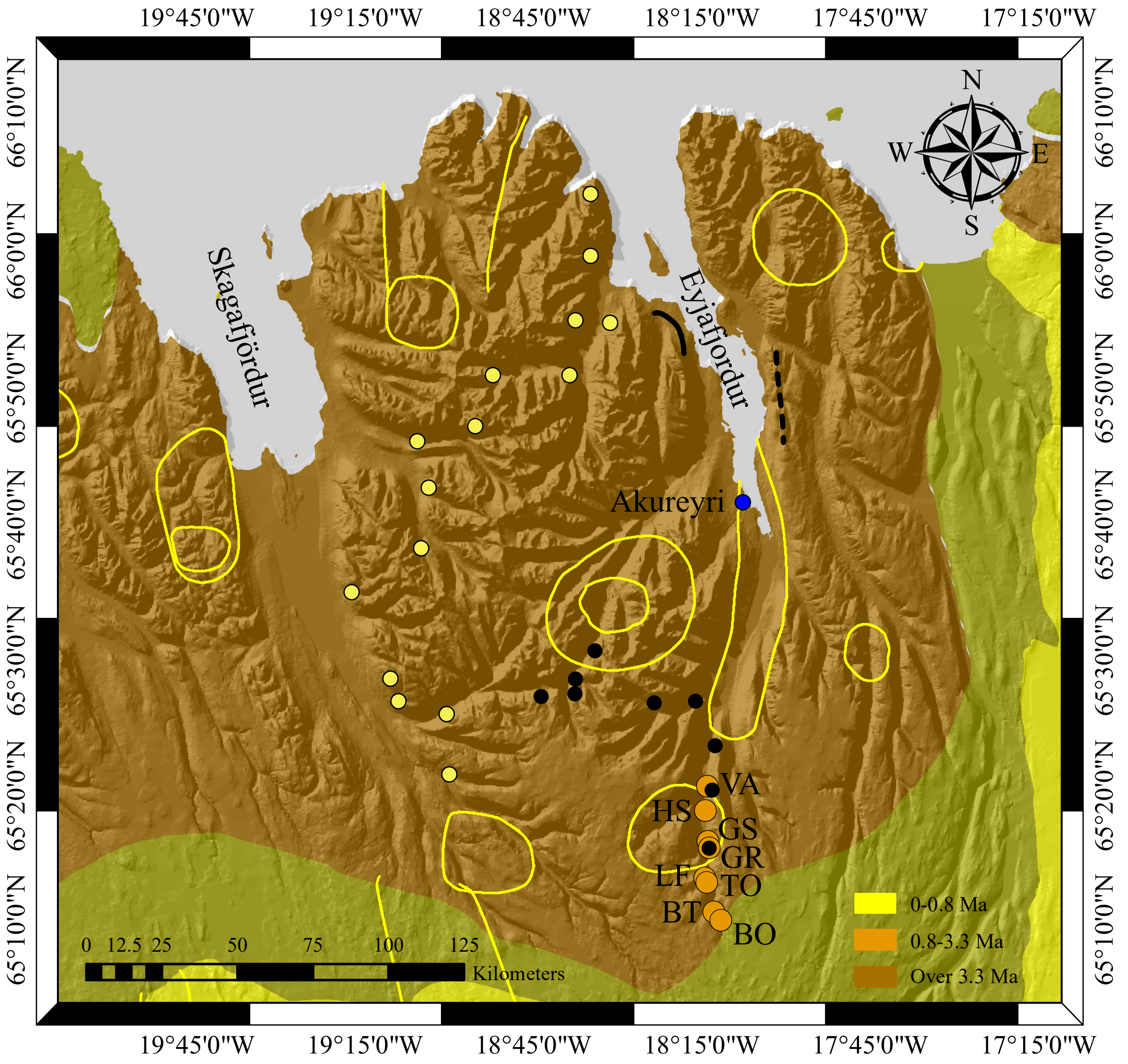

Figure 3.1: Map of Skagafjördur, Eyjafjordur and Tröllaskagi peninsular. The blue circle is the centre of Akureyri city. The dash line on the east coast of Eyjafjordur represents the location of the Dutch expedition in the 1960s (Hebeda et al., 1974) and the black line on the west coast of Eyjafjordur shows the K-Ar dated areas reported in Aronson and Saemundsson (1975). Yellow circles and black circles show the study location of Saemundsson et al. (1980) and Kristjansson et al. (2004). Orange circles represent the location of lava piles of this study. Yellow lines show the location of extinct tertiary central volcanoes. Geological data from Johannesson and Saemundsson (1998) and Hjartarson and Sæmundsson (2014).

3.2 Eyjafjordur and Eyjafjardardalur valley

The study area of this research is located in Eyjafjardardalur valley, south of Akureyri (Figure 3.1 and 3.2). The study locations are located in vicinity of a Neogene central volcano (Torfufell Central Volcano) (yellow line in Figure 3.1). Dr. Morten S. Riishuus mapped stratigraphic sections in the valley prior to fieldwork campaigns in 2014. There are eight lava sections in the study area ordering from north to south: Vatnsendi (VA), Halldorsstadir (HS), a short profile north of Granastadir (GS), Granastadir (GR), Laekjafjall (LF), Torfnahnjukur (TO), a short gully north of Botn (BT), and Botn (BO) (Figure 3.2). The stratigraphic sections of lower Eyjafjardardalur include VA, HS, GS and GR (Figure 3.3) while those of upper Eyjafjardardalur include LF, TO, BT and BO (Figure 3.4). The source of lava sections from VA toward lower GR is the Torfufell Central Volcano (Johannesson and Sæmundsson, 2009). After the volcanism waned, the Torfufell system was buried by basalt lavas originated from other volcanic systems, i.e., the source of lava sections from middle GR towards BO is nearby central volcano. According to Hjartarson (2003), Torfufell Central Volcano has not been mapped or investigated with any accuracy. The lava piles in the study areas provide approximately 150 lava flows covering a time span ~8.5-2.5 Ma (from VA to BO). Each single lava flow is determined by observations of internal architecture of the flows, direct contacts and from occurrences of palaeosol interbeds (red beds); the time gap between eruptions was usually long enough for palaeosol to deposit. These palaeosol layers have been formed by weathering process of tephras in the warm and humid climate during Neogene period (Óskarsson et al., 2012). The lava piles in the valley mostly consists of tholeiite (aphyric), porphyritic and olivine basalt, with small contribution of mild alkaline basalts (Saemundsson et al., 1980; Kristjansson et al., 2004). Rhyolite flows were found only on top of VA and HS and the bottom of GS; rhyolite flow at GS relates to the flank of Torfufell central volcano. Kristjansson et al. (2004) measured regional tectonic tilts of the lower Eyjafjardardalur of ~5-8° southeast at low altitudes and the tilts decrease to ~1-3° southeast on top of the mountains. The tectonic tilts decrease to 1° southeast in the upper Eyjafjardardalur area (BT and BO sections). The tectonic tilts reported by Kristjansson et al. (2004) were used for tilt corrections for palaeomagnetic directions in Chapter 5. During the stratigraphic mapping, Dr Morten recorded two major hiatuses which are located between GS1 and GSA2, and above TO15. These two hiatuses could lead to long missing time intervals in the stratigraphic sections. Note that the major hiatuses include poor exposures and palaeosols that affect unambiguous stratigraphic correlations between two sections. Note also that the minor hiatuses are the poor exposures palaeosols within the stratigraphic column which do not involve the stratigraphic correlations.

Section VA is the oldest profile with the age of approximately ca. 8.0 Ma at the bottom of the section. Section VA is located between HO and VE of Kristjansson et al. (2004) (Figure 3.1). Lava flows at low altitudes of section VA (VA1-VA7) mostly consist of porphyritic basalt with two layers of aphyric (tholeiite) basalt (Figure 3.3). Lava shield above 300 m to 470 m (VA8-VA29) consists mostly of aphyric basalt with two flows of olivine basalt. Lava shields are the principal delegate of low-discharge flood basalt typically ≤300 m^3/s (Thordarson and Larsen, 2007). This lava shield is corelated to HS6 and HS7 according to their lithology (Figure 3.3). The section from VA21 to VA30 is complicated by the presence of an olivine basalt dyke. This dyke could be the feeder for the olivine basalt group higher up, e.g., VA30. Lava flows above GR33 mostly are olivine basalt and aphyric basalt with a rhyolite flow on top of GR37.

Section HS is located between VA and GS of this study, and VE and GR of Kristjansson et al. (2004) (Figure 3.1). This section was not drilled by Kristjansson et al. (2004). At low altitudes of section HS, the lava units consist mainly of aphyric and olivine basalt, while flows in the middle of HS are mainly porphyritic basalt with olivine basalt (Figure 3.3). On top of section HS, we recorded aphyric basalt flows from HS19 to HS23. We observed a large dyke cutting through flow HS21 and a rhyolite dyke cutting through flow HS24. The lava flows above HS24 shows a thick rhyolite flow of approximately 200 m.

Section GS is the shortest section among eight lava sections. A rhyolite flow (GS1) at the bottom of GS was expected to be related to the rhyolite flows on top of VA and HS (Figure 3.3). The rhyolite flow usually relates to the flank zone of the central volcanoes (Jakobsson et al., 2008) (Torfufell central volcano in this study). We found a silicic tuff layer with obsidian spine deposited between GS1 and GSA2. This layer is recorded as a major hiatus. We added HS and GS sections between VE and GR in order to improve the stratigraphic correlation between VE and GR as Kristjansson et al. (2004) missed many flows between these two sections.

Section GR is the youngest profile in Kristjansson et al. (2004). Lava flows between GR1 and GR20 are mostly porphyritic and aphyric basalt with some flows of olivine basalt (Figure 3.3). There are two thick sedimentary horizons between GR5 and GR6, and GR6 and GR7 at the lower GR. Flows between GR22 and GR34 consist mainly of olivine and porphyritic basalt. Poor exposures between GR25 and GR26, and above GR33 are recorded as minor hiatuses. A thick red bed of 4 m was found between GR28 and GR29. The top of GR was thought to be correlated to the bottom of section LF according to lithology of flows. The lava flows on top of section GR have been tilted ~4° toward the southeast (recorded by Kristjansson et al. (2004)).

Section LF consists mainly of porphyritic and olivine basalt flows (Figure 3.4). Aphyric basalt was found only in LF1. A fault was observed around LF6 and LF7. There was a flow of tillite and palagonite tuff deposited between LF7 and LF8. This palagonite tuff layer is likely related to a palagonite tuff layer deposited below TOM3 (Figure 3.4).

Lava flows at low altitudes of TO (TOM3-TO2) consist mainly of porphyritic basalt, with olivine basalt in TOM3 and TOM2. Aphyric and porphyritic basalt was found between TO3 and TO7. A thick aphyric basalt flow (~40 m) was found in TO12. The lava flows on the upper TO consist of porphyritic basalt flows and should be correlated to lower BT (BT3 and BT4) according to their lithology (Figure 3.4). The hiatus above TO15 is recorded as a major hiatus.

Section BT1 and BT2 consist of olivine basalt while the upper flows are porphyritic basalt flows (Figure 3.4). We found two palagonite tuff layers deposited between BT2 and BT3, and between BT4 and BT5. These tuff layers are recorded as minor hiatuses. BT5 and BT6 should be correlated to BO5 according to the altitudes of the flows and regional tectonic tilt of the upper Eyjafjardardalur (~1°). However, a northeast trending fault between BT and BO was observed. BT5 and BT6 are likely related to the bottom of BO according to their lithology (Figure 3.4).

Section BO is the youngest profile in the study area. The age of this section is approximately c. 3.0 Ma (Johannesson and Saemundsson, 1998). Lava flows in this section consists of porphyritic and aphyric basalt (Figure 3.4). Three palagonite tuff layers between BO6 and BO7, BO9 and BO10, and BO10 and BO11 were recorded as minor hiatuses.

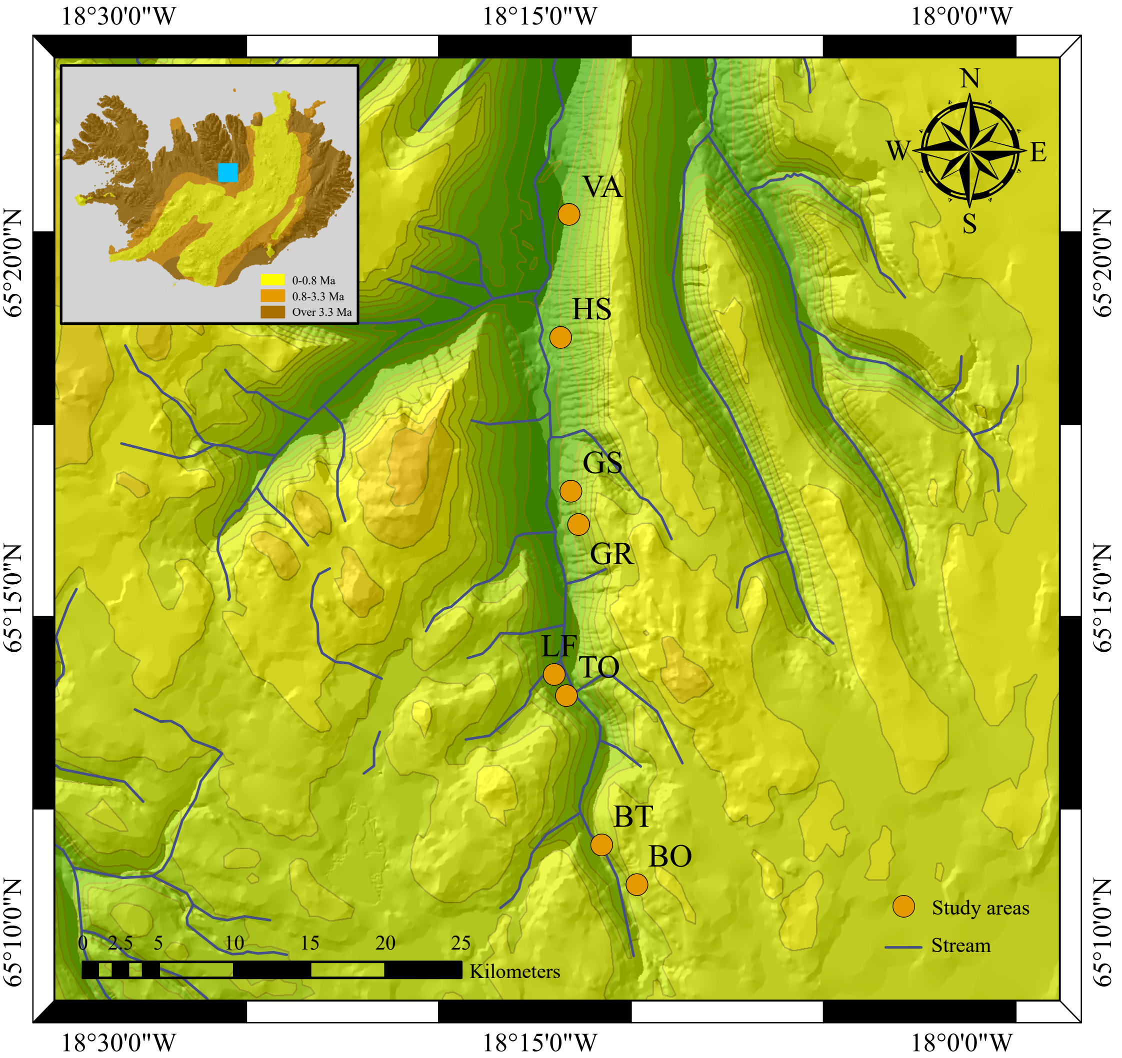

Figure 3.2: The expansion map of Eyjafjardardalur valley. Orange circles show locations of eight rock units and blue lines represent the main stream. Geological data from Johannesson and Saemundsson (1998) and Hjartarson and Sæmundsson (2014).

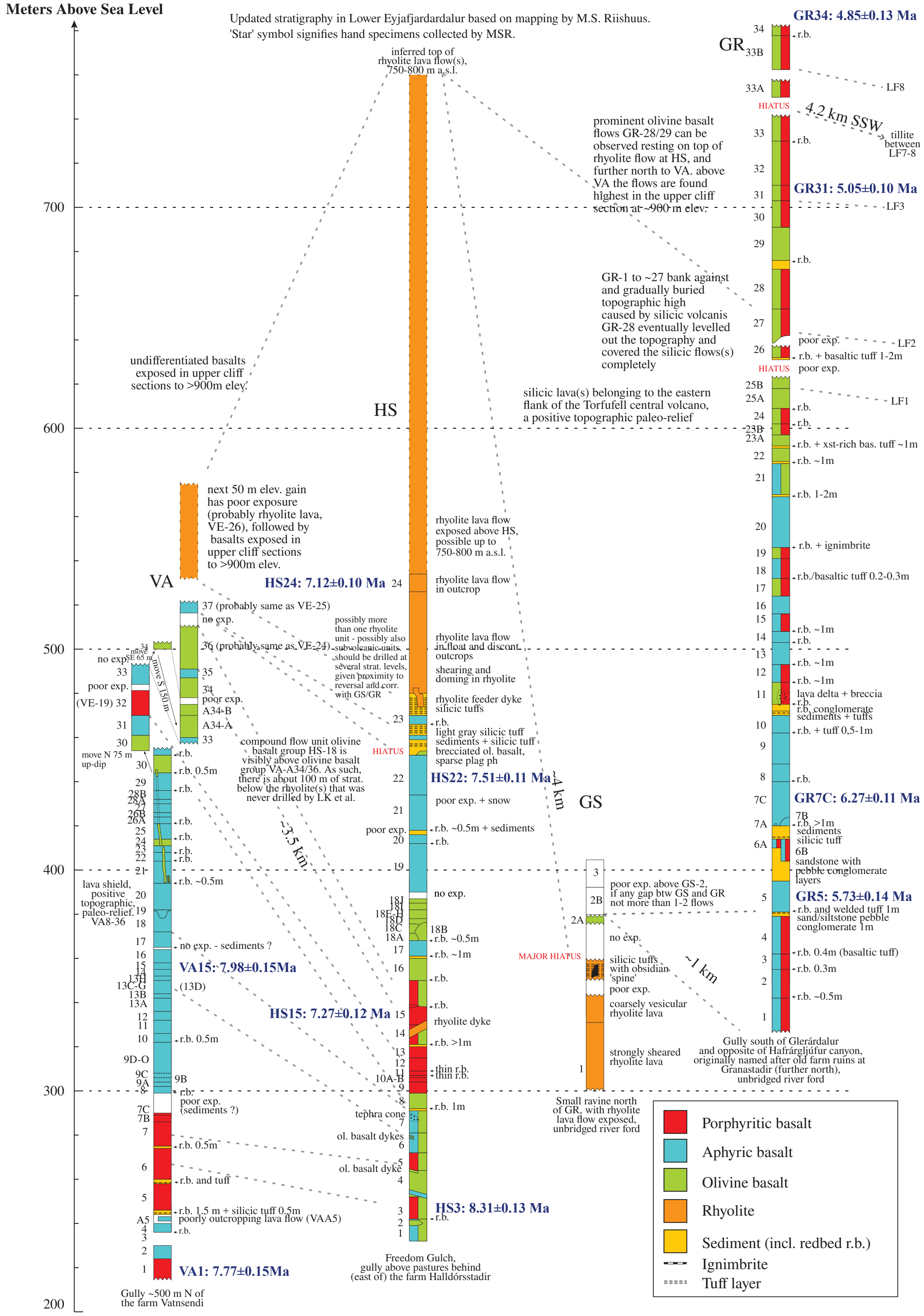

Figure 3.3: Stratigraphic map of lower Eyjafjardardalur valley showing section VA, HS, GS and GR. Grey dash line presents possible correlations recorded by Dr Morten according to regional dip, altitudes and lithology. A major hiatus is recorded between GS1 and GSA2 and two possible hiatuses are recorded near the top of GR.

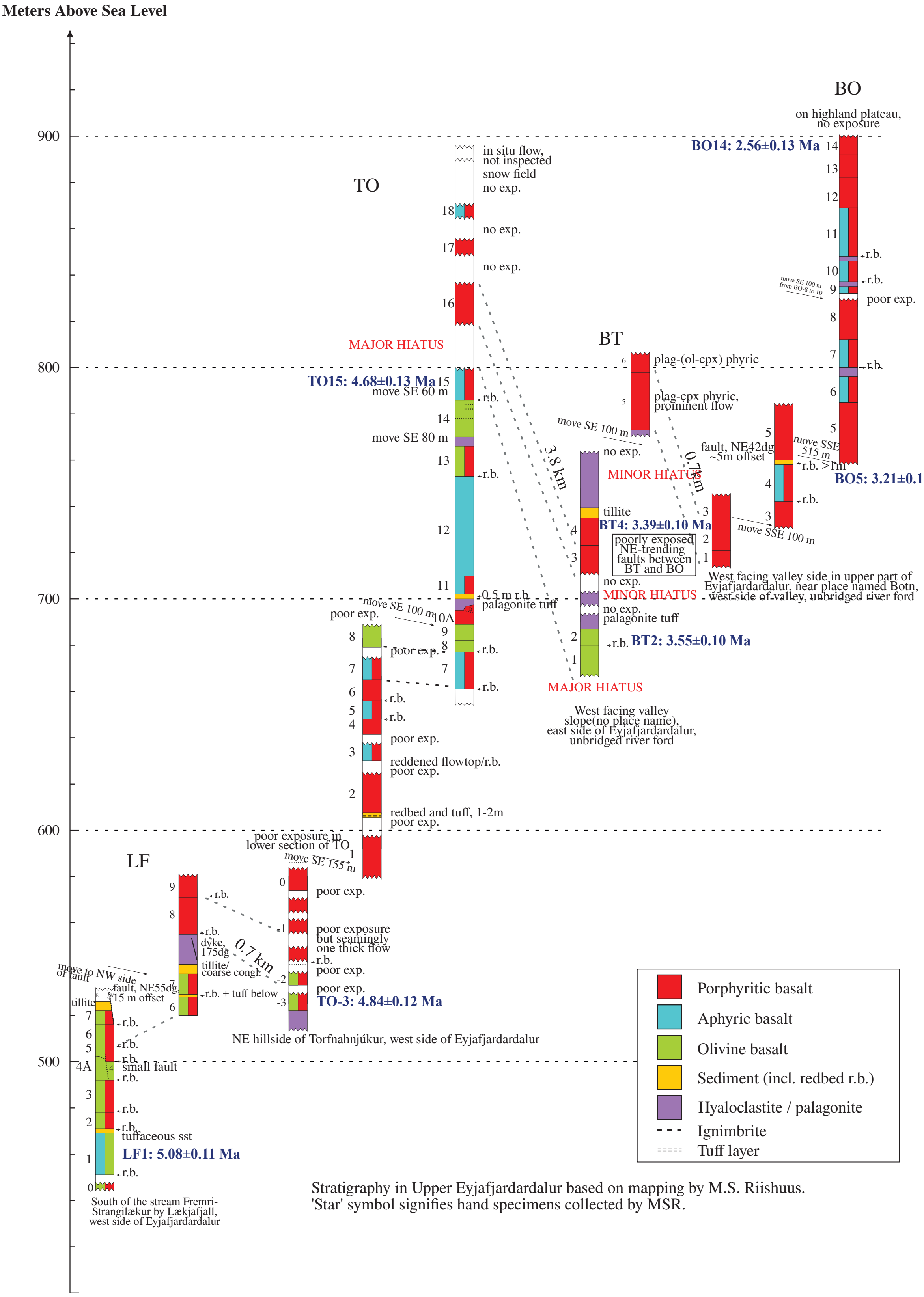

Figure 3.4: Stratigraphic map of upper Eyjafjardardalur valley showing LF, TO, BT and BO sections. Grey dash line presents possible correlations recorded by Dr Morten according to regional dip, altitudes and lithology. A major hiatus is recorded between TO15 and BT1.

3.3 Fieldworks

The samples for this project were collected over three field campaigns in the summers of 2014, 2015 and 2016, working our way up the valley from the oldest to the youngest sections. A standard palaeomagnetic petrol-drill with a diamond drill bit, cooled with water, was used to collect samples (Figure 3.5a). Most of the sections, were small gullies cut by streams, with exposures all the way up stream. Sampling such outcrops, led us to identify *in situ* outcrops. Many lava flows are separated by red palaeosol or tuff beds; however, some lava flows appear separate but are from the same eruption. We name these flows as VAAX and VABX (e.g., VAB9 and VAO9), where X is the flow number. Approximately 7-14 cores were taken from each lava flow. To make sure that the samples are not collected from rotated outcrops and to avoid the possibility of lightning strikes (albeit not a big problem in Iceland), we traversed along the base of individual lava units to sample cores from the same flow over ranges up to 50-100 m. We avoided to sample cores from the top of the flow as it is re-magnetised by an overlying flow. The cores were orientated (azimuth and hade) using a Pomeroy orienter fitted with a Brunton compass (Figure 3.5b and 3.5c). We also collected the Sun compass using a Sun needle when it was possible (Figure 3.5b). The Sun compass is preferred in this study, because magnetic compass readings can be deflected by local magnetic anomalies in the underlying terrain (e.g., Cromwell et al., 2013b). When unable to obtain the Sun compass readings during the day of core collection due to overcast conditions or shadows, we made careful notes of drill hole location and number (Figure 3.5e), and returned to the sites on a sunny day to collect the Sun compass at specific times. Some Sun compass readings were made on subsequent field trips a year later, e.g., profile GR was sampled in 2015, but the Sun compass readings were made in 2016.

In 2014, we started drilling into outcrops of the section VA (Figure 3.2). Only for VA8 we did not obtain enough cores following the criteria stated above due to the poor exposure of the outcrop. We split sampling locations above VA29 by moving north 75 m (left of the stream) to collect VA30-VA33. Then, we moved southward along the dip of the flows to collect VA34 to VA36. On top of VA, most of the sites displayed poor outcrops especially VA37. The rocks show slate-like fractures, which may have led to poor orientation of the azimuths. Thick rhyolite flow was observed above VA37.

Section HS is located ~3.5 km south of the section VA (Figure 3.2). We again collected from the hillside of HS and moved upstream to the top of the mountain. We primary collected 7-12 cores from section HS, except flow HS24. HS24 is rhyolite, which is very hard to drill and blunted the drill bits. We had no dressing stone with us, so did not collect a full set of samples for HS24. A picture of the section VA and HS is shown in Figure 3.6a.

Figure 3.5: (a) a petrol-drilling machine with a diamond drill bit. (b) A Pomeroy with a Brunton compass and a sun needle. (c) a team member was measuring an orientation of a core. (d) an example outcrop that was cut by a stream (on the right but not in the picture). (e) orientated cores with drilled holes. The drill holes were marked in alphabets. The holes with alphabets were sketched in the fieldnote for re-orientating the Sun compass next day or next year if the weather conditions were poor. Dr Morten also painted the flow number for each unit (prior to the fieldwork trip) for our tracking (when he was absence), re-visiting and future research.

Section GS is located 1 km north of section GR (Figure 3.2). We obtained more than eight cores per flow and one melon-size obsidian sample from this section. The first fieldwork season stopped at GS due to the time limit in the field.

The second fieldwork campaign was held in 2015 for two weeks. We successfully collected palaeomagnetic cores from section GR, LF, TO and BT in 2015. We started drilling section GR which is the steepest profile amongst the eight drilled profiles (Figure 3.6b). There are several flows above GR34, which were previously drilled by Kristjansson et al. (2004). Paint marks left by Kristjansson et al. (2004) were found and helped us to know exactly which units we were sampling with respect to the earlier study, e.g., GR34. However, the team stopped drilling at GR34, because sites above GR34 appear to mostly consist of large loose, frost-wedged boulders. It was difficult to identify *in situ* outcrops. For future reference and location of sampling sites, we painted the corresponding flow number on many lava flows in yellow paint. The profile ID lettering was painted at the base of the individual profile (e.g., Figure 3.5d).

Section LF is located ~4 km south-southwest of section GR on the western hillside of the valley (Figure 3.2). This section was cut by a main stream (Figure 3.6c). We started drilling on the south side of the stream. This meant that most of the outcrops were in shadow all day; we even went at 05:00 in the morning to confirm this. Consequently, we did not obtain many Sun compass readings from this section. We split sampling locations for LF6 and LF7 into two locations: south of the fault and north of the fault.

Section TO is located ~0.7 km south of the section LF (Figure 3.2). The lower TO units (TOM3-TO0), were poorly exposed due to vegetation cover on lower slope (Figure 3.4). Outcrops between TO1-TO5 were better exposed, but nearly all of the cores broke. There is also poor exposure of the outcrops above TO8. Therefore, we moved ~155 m to the south to find promising outcrops to extend TO profile further up. We named the new outcrops as TO site 2. At TO site 2, TO7 and TO8 were drilled again in order to confirm that palaeomagnetic directions from site 1 and site 2 are from the same lava flow. Then, we started drilling up the hill toward TO14. Again there was very poor exposure on upper TO (and elsewhere on upper valley shoulders Eyjafjardardalur). Dr. Riishuus mapped the section TO toward TO18 (in 2016) in order to confirm lava lithology and for correlation with profile BT. The distance between TO and BT and poor exposure between the two profiles (and locally poor exposure high on TO) raised concerns in terms of securing overlap. However, we did not collect cores from lava flows above TO14, because of the rock hardness, limited availability of *in situ* units and time constraints in the field.

Section BT is the second shortest profile among the eight profiles located approximately 3.8 km south of the section TO and on the eastern hillside of the valley (Figure 3.2). We got minimum 10 cores per flow from this profile.

Section BO was mapped in 2014 (Figure 3.4). However, this unit was left until 2016 to sample when the final fieldwork campaign was held. This section is located approximately 0.7 km south of BT. We started drilling from BO1 to BO14. Due to the poor exposure of the outcrops above BO3, we moved southward to drill BT3 again and proceed toward BT5. Then, we moved southward again for better exposure of flows above BO5. We continued drilling from BO5 to BO14. The area of section BO is presented in Figure 3.6d.

Overall, we spent a total of 5 weeks in northern Iceland during three fieldwork seasons, collecting ~1800 cores. Approximately 86% of the cores taken had Sun compass. This is high for Iceland, for example Døssing et al. (2016) managed 71% of Sun readings in their study while the SCRIPPS team got no Sun readings during their fieldwork due to the poor weather conditions (general talk to the local researchers in the University of Iceland). The magnetic compass readings was adjusted azimuths using international geomagnetic reference field (IGRF) model 2012, while Sun shadow data were converted to sample azimuths using PmagPy software (Tauxe et al., 2016).

Figure 3.6: Photograph showing lava sections in Eyjafjardardalur valley: (a) VA and HS, (b) GR, (c) LF and (d) BO. It is clear seen from (a) that the general trend of the lava flows has been tilted toward the south (dash line).

The Sun compass is wide spread used in the palaeomagnetic community as the uncertainties derived from the orientation errors in the field are ~3°. These uncertainties are due to improper insertion of the Pomeroy into the drill hole, measurements of time and location, deviations of Pomeroy from the horizonal plane (Tauxe et al., 2010). To assess the azimuthal difference between the magnetic compass and Sun compass readings, the cumulative distribution function (CDF) of the azimuthal difference was plotted on Figure 3.7. Note that 1,589 data whose have both magnetic compass and Sun compass azimuths were used to calculate the CDF. The cores whose have only magnetic azimuths (e.g., many sites in LF) are not considered here as there is no Sun compass as a reference. The median of the azimuthal deviations is -1.06° with the median absolute deviation (MAD) of 5.09°. The 95% confidence limit covers the lower and upper bounds of -17.4° and 19.1°. Therefore, using the specimens without the Sun compass readings in this thesis can yield the magnetic compass error with the maximum of ~19° caused by the strong magnetisation in the underlying terrain.

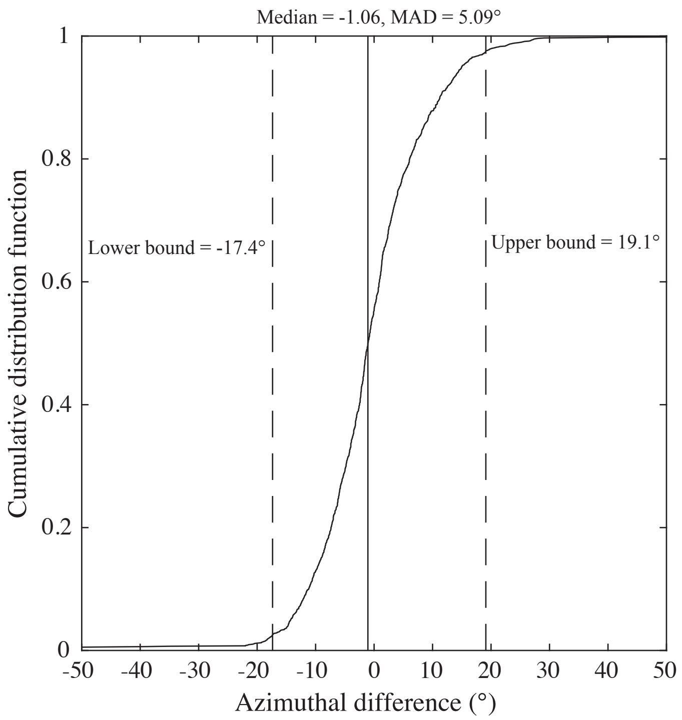

Figure 3.7: Cumulative distribution function of the azimuthal difference between the Sun compass and magnetic compass readings. The vertical black line shows the median while the vertical dash lines represent the 95% confidence bound.

Chapter 4

^{40}Ar/^{39}Ar Geochronology

4.1 Overview

Absolute radiometric age determinations of the composite stratigraphy in Eyjafjardardalur are crucial for the modern time-averaged field study presented in this thesis. This chapter provides a brief overview of methods, results and interpretations of ^{40}Ar/^{39}Ar age determinations from Eyjafjardardalur. Firstly, selection of reliable samples for ^{40}Ar/^{39}Ar dating is given. Following this, the groundmass preparation and dating method are presented. Then, data interpretation is discussed.

4.2 Motivation behind this work

According to previous paleomagnetic research in northern Iceland (Saemundsson et al., 1980; Kristjansson et al., 2004), little information is available on the geology of Tröllaskagi peninsula and Eyjafjardardalur. Important aspects of the local geologic record is given in lithostratigraphic sections in Saemundsson et al. (1980) and Kristjansson et al. (2004), and the broader geology and tectonic structures are mapped by Johannesson and Saemundsson (1998). Most studies (Hebeda et al., 1974; Aronson and Saemundsson, 1975; Kristjansson et al., 2004) focus on the geology around Akureyri but no radio-isotopic dating has been reported from Eyjafjardardalur valley, south of Akureyri. Unpublished results by Hardarson et al. (1999) indicates an age of c. 5 Ma for the top of GR. There are no further dating results of the upper Eyjafjardardalur, approximately 50 km south of Akureyri. Johannesson and Saemundsson (1998) provides the general geology of the upper Eyjafjardardalur, giving the boundary between Miocene and Plio-Pleistocene strata (younger than c. 3-3.5 Ma) based on the occurrence of deposits relating to glacial processes. This work aims to provide high-precision absolute radiometric age determinations of the Eyjafjardardalur composite section (~1.6 km) in order to understand the time-averaged geomagnetic field recorded in northern Iceland. The ^{40}Ar/^{39}Ar age determinations in conjunction with litho- and magnetostratigraphy from this study will serve useful to studies of Neogene tectono-magmatic processes in Iceland, for regional correlations across Iceland as well as to further the understanding of the local geology of northern Iceland.

4.3 Principle of ^{40}Ar/^{39}Ar dating

The ^{40}Ar/^{39}Ar dating works on the basis of decaying of potassium (parent element) to argon (daughter element). Potassium has three isotopes in nature including ${}^{39}_{19}\mathrm{K}$ (~93.2581%), ${}^{40}_{19}\mathrm{K}$ (~0.01167) and ${}^{41}_{19}\mathrm{K}$ (~6.7302) (Steiger and Jäger, 1977). Of these, only ${}^{40}_{19}\mathrm{K}$ is the radioactive decay parent element. Argon also has three natural occurring isotopes including ${}^{36}_{18}\mathrm{Ar}$ (~0.337%)), ${}^{38}_{18}\mathrm{Ar}$ (~0.063%) and ${}^{40}_{18}\mathrm{Ar}$ (~99.6%) (Nier, 1950; Steiger and Jäger, 1977). These isotopes are stable and only ${}^{40}_{18}\mathrm{Ar}$, denoted as ${}^{40}_{18}\mathrm{Ar}^*$ (radiogenic argon, for atmospheric ${}^{40}_{18}\mathrm{Ar}$ and excess ${}^{40}_{18}\mathrm{Ar}$ are denoted as ${}^{40}_{18}\mathrm{Ar}_a$ and ${}^{40}_{18}\mathrm{Ar}_E$.), is a daughter element from the decay of ${}^{40}_{19}\mathrm{K}$. From the natural occurring abundances above, the atmospheric ratio of ^{40}Ar/^{36}Ar, denoted as (^{40}Ar/^{36}Ar)$_a$, is always 295.5 (Nier, 1950). This ratio is needed in the data correction.

The ${}^{40}_{19}\mathrm{K}$ has four modes of decay. The dominant decay mode is the decay from potassium to calcium (at ground state) following the reaction below:

$${}^{40}_{19}\mathrm{K} \rightarrow {}^{40}_{20}\mathrm{Ca} + {}^{0}_{-1}e$$

This decay mode often yields 89.52% in nature (McDougall and Harrison, 1999). Other three modes are the decay from potassium to argon. The most common decay mode is the decay from ${}^{40}_{19}\mathrm{K}$ to ${}^{40}_{18}\mathrm{Ar}$ (excited state) via electron capture. Then, the ${}^{40}_{18}\mathrm{Ar}$ at the excited state releases energy (gamma ray) and drops to the ground state. This decay mode yields 10.32% of the time (McDougall and Harrison, 1999). Other two decay modes are the direct decay from ${}^{40}_{19}\mathrm{K}$ at the excited state to ${}^{40}_{18}\mathrm{Ar}$ at the ground state via electron capture, and β^+ and gamma decays following the reactions below:

$$ {}^{40}_{19}\mathrm{K} + {}^{0}_{-1}e \rightarrow {}^{40}_{18}\mathrm{Ar} $$

$$ {}^{40}_{19}\mathrm{K} \rightarrow {}^{40}_{18}\mathrm{Ar} + {}^{0}_{+1}e + \gamma $$

However, these two reactions are quite rare and considered as insignificant mode. The direct decay to the ground state via electron capture likely happens at around 0.16% of the time while positron together with gamma decays occurs at approximately 0.001% of the time (McDougall and Harrison, 1999). The decay constant for the total decay (all modes) (λ) is approximately 5.543×10^{-10} a^{-1} (Steiger and Jäger, 1977). Therefore, the half-life of ${}^{40}_{19}\mathrm{K}$ is approximately 1.25 Ga.

In the ${}^{39}\mathrm{Ar}/{}^{40}\mathrm{Ar}$ dating, firstly, samples are irradiated by fast neutron with an energy of >0.1 MeV in a nuclear reactor (Dickin, 2018). This process produces a manmade argon (${}^{39}_{18}\mathrm{Ar}$) following the reaction below (Dickin, 2018):

$$ {}^{39}_{19}\mathrm{K} + {}^{1}_{0}n \rightarrow {}^{39}_{18}\mathrm{Ar} + {}^{1}_{1}p + energy $$

Here the ${}^{39}_{18}\mathrm{Ar}$ is denoted as ${}^{39}_{18}\mathrm{Ar}_K$ because this product is a result from the neutron irradiation of potassium. As the ${}^{39}_{18}\mathrm{Ar}_K$ is not the natural occurring isotope of argon, therefore, it serves as an effective proxy for ${}^{40}_{18}\mathrm{Ar}^*$. If the ratio of ${}^{40}_{18}\mathrm{Ar}^*/{}^{39}_{18}\mathrm{Ar}_K$ of unknown age samples ($({}^{40}_{18}\mathrm{Ar}^*/{}^{39}_{18}\mathrm{Ar}_K)_u$) is known, the ages can be calculated from (Dickin, 2018):

$$ {}_u = \frac{1}{\lambda}\ln\left\{ \left(\frac{{}^{40}_{18}\mathrm{Ar}^*}{{}^{39}_{18}\mathrm{Ar}_K}\right)_u + 1 \right\} \tag{4.1} $$

where ${}_u$ is the age of unknown age sample, λ is the total decay constant, J is the irradiation parameter of known age samples where J is (Dickin, 2018):

$$ = \frac{\left(e^{\ \ {}_s} - 1\right)}{({}^{40}_{18}\mathrm{Ar}^*/{}^{39}_{18}\mathrm{Ar}_K)_s} + 1 \tag{4.2} $$

where $({}^{40}_{18}\mathrm{Ar}^*/{}^{39}_{18}\mathrm{Ar}_K)_s$ is the ratio of radiogenic argon over manmade argon of known age standard and ${}_s$ is the age of the standard. In order to determine J in Equation 4.2, the known age standard must be irradiated with an unknown sample at the same time.

Data correction

In order to calculate the accurate ages of the samples, data correction must be performed in order to obtain the precise ages. The first correction would be ${}^{40}_{18}\mathrm{Ar}_{a}$ correction. The atmospheric argon can be adsorbed onto the surface of the grains or analytical equipment (Lee, 2013). It can also be diffused into the grains during mineral crystallisation when the rocks form. In order to subtract the atmospheric argon from the radiogenic argon, the ${}^{36}_{18}\mathrm{Ar}$ must be measured in the mass spectrometer. As the $({}^{40}\mathrm{Ar}/{}^{36}\mathrm{Ar})_{a}$ is always 295.5, the ${}^{40}_{18}\mathrm{Ar}_{a}$ can be calculated following this relation.

Another interference in the argon-argon dating is from the isotope argons such as ${}^{36}_{18}\mathrm{Ar}$, ${}^{37}_{18}\mathrm{Ar}$, ${}^{38}_{18}\mathrm{Ar}$, ${}^{39}_{18}\mathrm{Ar}$ and ${}^{40}_{18}\mathrm{Ar}$ which are induced by neutron bombardment of calcium, chlorine and potassium (Lee, 2013; Dickin, 2018). These isotopes can affect argon ratio which results in wrong age determination. However, it appears that several works tended to ignore these interferences (Dickin, 2018). Mitchell (1968) claimed that precise ages could be determined without interference correction on minerals over 1 Ma in age. However, the most important reactions that their interferences should be corrected are (Lee, 2013; Dickin, 2018):

$$ {}^{40}_{19}\mathrm{K} + {}^{1}_{0}n \rightarrow {}^{40}_{18}\mathrm{Ar} + {}^{1}_{1}p $$

$$ {}^{40}_{20}\mathrm{Ca} + {}^{1}_{0}n \rightarrow {}^{36}_{18}\mathrm{Ar} + {}^{4}_{2}\ \mathrm{e}^{2+} + {}^{1}_{0}n $$

$$ {}^{40}_{20}\mathrm{Ca} + {}^{1}_{0}n \rightarrow {}^{37}_{18}\mathrm{Ar} + {}^{4}_{2}\ \mathrm{e}^{2+} $$

$$ {}^{42}_{20}\mathrm{Ca} + {}^{1}_{0}n \rightarrow {}^{39}_{18}\mathrm{Ar} + {}^{4}_{2}\ \mathrm{e}^{2+} $$

These induced argon isotopes can interfere the argon ratios in the system. Of the four reactions above, ${}^{37}_{18}\mathrm{Ar}$ is also radioactive decay with a half-life of 35.1 days (Stoenner et al., 1965). The amount of ${}^{37}_{18}\mathrm{Ar}$ produced by the second last reaction is large when calcium is present in the sample (McDougall and Roksandic, 1974). Therefore, further corrections for the time interval between the neutron irradiation and the analysis in the laboratory should also be performed. The ratio of ${}^{40}\mathrm{Ar}^{*}/{}^{39}\mathrm{Ar}$ can be corrected following Equation 4.3 (McDougall and Roksandic, 1974):

$$\frac{{}^{40}_{18}\mathrm{Ar}^{*}}{{}^{39}_{18}\mathrm{Ar}}=\frac{\left(\frac{{}^{40}_{18}\mathrm{Ar}}{{}^{39}_{18}\mathrm{Ar}}\right)_m-2\ 5.5\times\left(\frac{{}^{36}_{18}\mathrm{Ar}}{{}^{39}_{18}\mathrm{Ar}}\right)_m+2\ 5.5\times\left(\frac{{}^{37}_{18}\mathrm{Ar}}{{}^{39}_{18}\mathrm{Ar}}\right)_m\left(\frac{{}^{36}_{18}\mathrm{Ar}}{{}^{37}_{18}\mathrm{Ar}}\right)-\left(\frac{{}^{40}_{18}\mathrm{Ar}}{{}^{39}_{18}\mathrm{Ar}}\right)}{1-\left(\frac{{}^{37}_{18}\mathrm{Ar}}{{}^{39}_{18}\mathrm{Ar}}\right)_m\left(\frac{{}^{39}_{18}\mathrm{Ar}}{{}^{37}_{18}\mathrm{Ar}}\right)} \tag{4.3}$$

where subscript m denotes the ratios measured in the mass spectrometer (with ${}^{37}_{18}\mathrm{Ar}$ correction during the time interval between the irradiation in nuclear reactor and the analysis in the laboratory). 295.5 is the $({}^{40}\mathrm{Ar}/{}^{36}\mathrm{Ar})_a$ ratio. The ratios of $({}^{36}_{18}\mathrm{Ar}/{}^{37}_{18}\mathrm{Ar})$, $({}^{39}_{18}\mathrm{Ar}/{}^{37}_{18}\mathrm{Ar})$ and $({}^{40}_{18}\mathrm{Ar}/{}^{39}_{18}\mathrm{Ar})$ are determined by irradiating pure salts of Ca and K in the reactor. These ratios vary depending on the reactor, typically range of 0.006-0.031, 2.1-2.7 and 6.3-3.0 (Dalrymple et al., 1988).

4.3.1 Total fusion

The total fusion is a conventional method which produces a single age. After irradiation and a period of cooling, samples must be completely dissolved and fused in order to extract ${}^{40}_{18}\mathrm{Ar}$, ${}^{39}_{18}\mathrm{Ar}$, ${}^{37}_{18}\mathrm{Ar}$ and ${}^{36}_{18}\mathrm{Ar}$ (McDougall and Roksandic, 1974). The early generation of mass spectrometer required several milligrams of purified mineral separates in order to extract sufficient amount of argon isotopes to calculate an age. Nowadays, the sensitivity of mass spectrometer is improved. Therefore, single crystals can be fused with a furnace or a laser in order to the determine the argon age (Lee, 2013).

4.3.2 Step heating

In the step heating method, samples did not have to be completely dissolved and fused in one shot in order to extract argon from the whole grain but can be step-wise heated to gradually release argon from the system. Argon released from each heating step can be used to construct an age spectrum or a isochron diagram, and a plateau age or isochron age can be determined (Merrihue and Turner, 1966). An advantage of the step heating over total fusion is that this method can detect anomalous subsystems within the samples and these anomalous subsystems can be omitted from age determination. The fundamental principle of the step heating is based on solid-state diffusion theory as shown in Figure 4.1a. Consider a spherical mineral grain with well distribution of ${}^{39}_{19}\mathrm{K}$ within the grain. The neutron bombardment produces ${}^{39}_{18}\mathrm{Ar}$ which is also uniformly distributed throughout the grain. When the grain is heated to a temperature "T1" at a time interval "t", the argon in the shell "S1" diffuses out of the system and returns an apparent age "A1". Then, the grain is heated at a slightly higher temperature "T2" at the same time interval with "t". The argon in the shell "S2" diffuses out of the grain and yield an age "A2". The most inside shell "S9" will require heating at the highest temperature "T9" in order to release argon which returns an apparent age "A9". The apparent ages from each heating step are used to construct the age spectrums against cumulative $^{39}_{18}$Ar release (or fraction of $^{39}_{18}$Ar release). If the system is closed and the $^{40}_{18}$Ar is also uniformly distributed inside the grain, then the ratio of $^{40}_{18}$Ar over $^{39}_{18}$Ar is identical for every heating steps and the age spectrum yields an ideal plateau age as shown in Figure 4.1b.

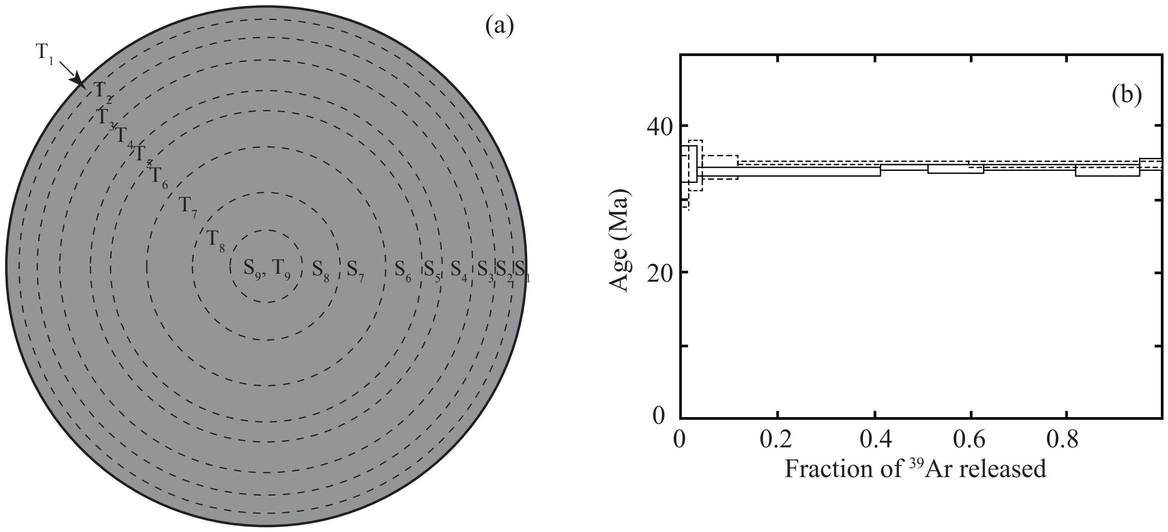

Figure 4.1: (a) a spherical grain showing layers S_1 at the rim to S_9 at the core. The incremental heating steps from T1 to T9 are required to release argon from each shell in order to determine apparent ages. The apparent ages are used to plot the age spectra and determined the plateau age (b) ideal age spectra which show no disturbance in the system. Figures from Lee (2013) and York (1984).

4.3.2.1. Plateau age

There is no conventional method to determine a plateau age in geochronological community. Workers usually determine a plateau from at least three or more contiguous steps comprising more than 50% of the $^{39}_{18}$Ar released which overlap at the 2σ (e.g., Fleck et al., 1977). In practice, the age spectra might not be ideal as samples could suffer from argon loss, excess argon or argon recoil.

Argon loss

Some age spectrum diagrams show the down step at low temperature which is a result of argon loss after the rocks formed (Figure 4.2). There are three possible scenarios which cause argon loss from the outer shell of the grain. The first scenario is from the reheating. In this case samples tend to experience a moderate to high temperature during geological events such as igneous intrusion, contact metamorphism and hot fluid flow (e.g., Turner, 1968). For example, if rocks are in contact with a heat source within a short period of time, samples could suffer from partial argon loss. Argon is lost only from the region nearest the grain boundary while the original argon is remained at the grain core. The second scenario is due to slow regional cooling (Lee, 2013). For example, if samples are subject to slow cooling due to regional metamorphism, partial argon loss can occur in the samples. The last scenario is due to impurities in the grains which cause degassing the low temperature heating step (Lee, 2013).

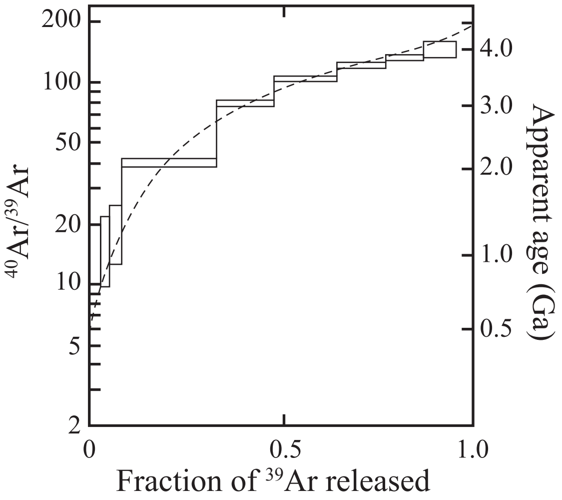

Figure 4.2: An age spectrum diagram showing argon loss from the grains. It is clear that the up steps at the low temperature show partial argon loss near the surface of the grains. The dash line represents the best fit curve. Figure from Turner (1968).

Excess argon

Due to thermal activation, the excess argon ($^{40}_{18}\mathrm{Ar}_E$) from the external environment can diffuse into mineral grains if the argon partial pressure outside the mineral grains is higher than that inside the grains (Lee, 2013). The possible source of the excess argon would be radiogenic argon itself. When the potassium bearing minerals are reheated, the radiogenic argon in the system diffuses through the surrounding areas and is now considered as excess argon (Lee, 2013). Another possible source is from external sources such as groundwater, fluid inclusions and magma intrusions from the lower crust

(Kelley, 2002). Most of these sources contain $^{40}_{18}\mathrm{Ar}$. The diffusion of argon from the external source usually affects the low temperature steps resulted in anomalously old apparent age at low temperature steps (Figure 4.3a). Another case of excess argon is represented in Figure 4.3b. This saddled-shape of age spectrum shows anomalously old apparent ages both at low and high temperature steps (Lanphere and Dalrymple, 1976; McDougall and Harrison, 1999). The saddle shape commonly occurs in low potassium rocks and minerals such as plagioclase, amphibole and clinopyroxene (Kelley, 2002). Melt or fluid inclusions release argon at low temperature while melt, fluid or solid inclusions release argon at high temperature when minerals decompose at high temperature (Esser et al., 1997; Boven et al., 2001).

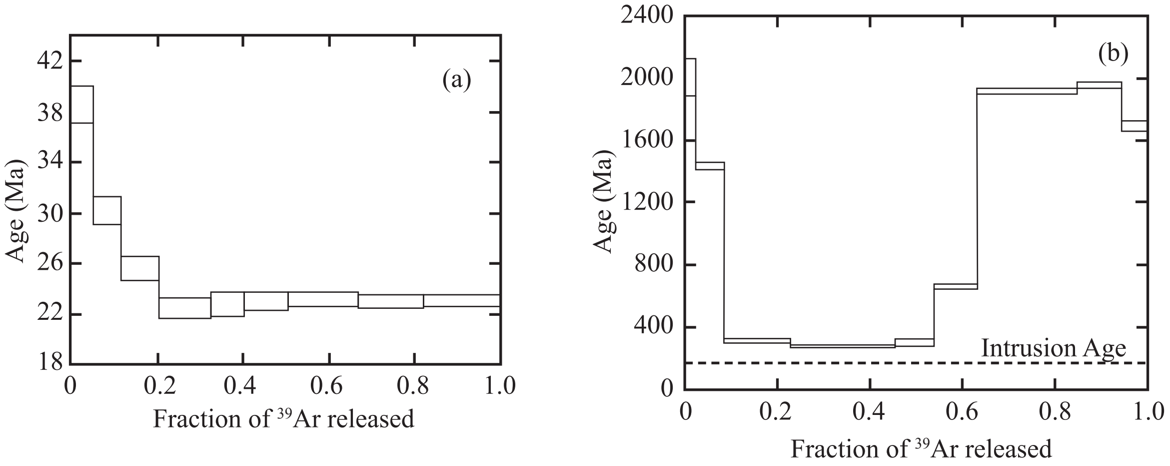

Figure 4.3: The age spectrum diagrams showing two cases of excess argon. (a) step heating release excess argon at low temperature steps yielding old apparent age at low temperature. The true age of the sample can be determined at high temperature steps. (b) saddled-shape age spectrum showing argon released at low temperature steps due to melt and fluid inclusions. Melt, fluid and solid inclusions decompose and release argon at high temperature steps. The dash line shows the intrusion age of the sample. Figures from Lee (2013) and Lanphere and Dalrymple (1976).

Argon recoil

During the irradiation, when fast neutrons interact with $^{39}_{19}\mathrm{K}$ to produce $^{39}_{18}\mathrm{Ar}$, there is recoil energy associated with this process. Turner and Cadogan (1974) calculated that this effect could move an $^{39}_{18}\mathrm{Ar}$ atom approximately 0.08 μm from its original place. In order to test the recoil process, they crushed a sample into a grain size of 1-10 μm. The recoil energy would move $^{39}_{18}\mathrm{Ar}$ atoms from potassium bearing minerals to low-potassium minerals such as plagioclase, pyroxene and ilmenite (Figure 4.4a) (Lee, 2013). This results in old apparent age at low temperature steps and young apparent age at high temperature (Figure 4.4b). The true apparent age can be determined from the intermediate temperature steps (when compared with the normal sample in Figure 4.4b). Turner and Cadogan (1974) also suggested that part of argon also recoil out of the samples. For this reason, dating of fine-grained samples must be interpreted with care. This recoil problem of dating fine-grained minerals leads to the development of encapsulation techniques. Smith et al. (1993) show that the recoil problem could be resolved by placing samples in a vacuum-sealed capsule prior to irradiation. The ${}^{39}_{18}\text{Ar}$ which recoils out of the samples can be measured in a mass spectrometer when breaking a capsule.

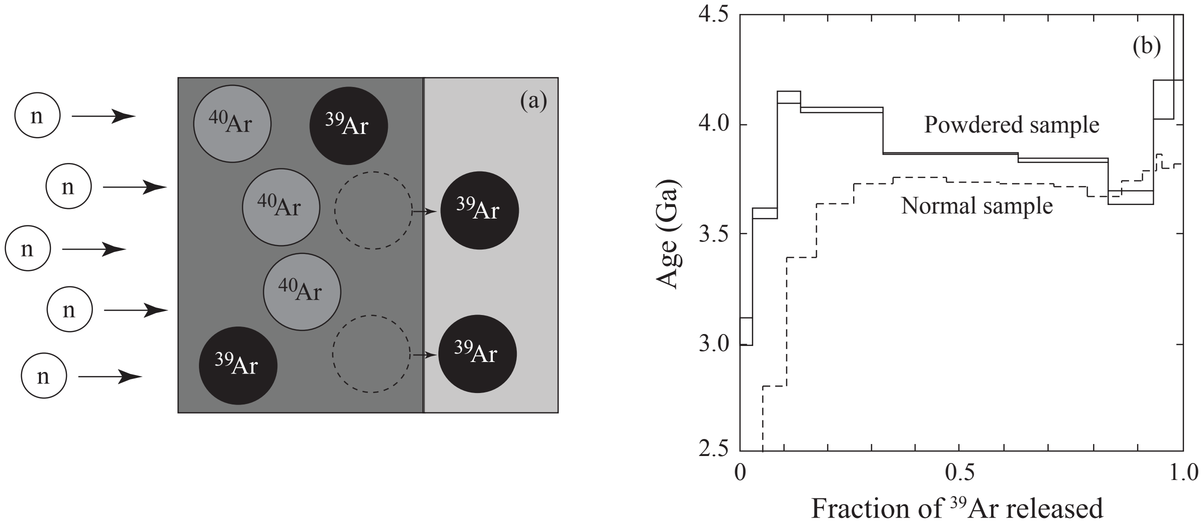

Figure 4.4: (a) A diagram showing neutron bombardment of ${}^{39}_{19}\text{K}$ to produce ${}^{39}_{18}\text{Ar}$ during irradiation process. The recoil energy releases ${}^{39}_{18}\text{Ar}$ from rich-K bearing (dark shade) to low-K bearing (light shade) phases. (b) argon recoil in powdered samples. The dash line shows the age spectrum of normal-size sample. It is clear that the recoil process yields old apparent ages at low-temperature steps and young apparent ages at high-temperature steps. Figures from Lee (2013) and Turner and Turner and Cadogan (1974).

4.3.2.2. Isochron age

In both K-Ar and Ar-Ar dating, the total amount of argon ${}^{40}_{18}\text{Ar}_{o\ al}$ which is a combination of radiogenic argon (${}^{40}_{18}\text{Ar}^*$) and initial atmospheric argon (${}^{40}_{18}\text{Ar}_i$) is measured in a mass spectrometer. Therefore,

$$ {}^{40}_{18}\text{Ar}_{o\ al} = {}^{40}_{18}\text{Ar}_i + {}^{40}_{18}\text{Ar}^* \tag{4.4} $$

Substituting Equation 4.1 into Equation 4.4 yields:

$$ {}^{40}_{18}\text{Ar}_{o\ al} = {}^{40}_{18}\text{Ar}_i + {}^{39}_{18}\text{Ar} \cdot \frac{(e \quad -1)}{\quad} \tag{4.6} $$

As ${}^{40}_{18}\mathrm{Ar}_i$ is an unknown amount in the samples, therefore, a stable isotope of ${}^{36}_{18}\mathrm{Ar}$ is used as a reference. Dividing Equation 4.6 by ${}^{36}_{18}\mathrm{Ar}$ yields:

$$\left(\frac{{}^{40}_{18}\mathrm{Ar}}{{}^{36}_{18}\mathrm{Ar}}\right)_{o\ al} = \left(\frac{{}^{40}_{18}\mathrm{Ar}}{{}^{36}_{18}\mathrm{Ar}}\right)_i + \left(\frac{{}^{39}_{18}\mathrm{Ar}}{{}^{36}_{18}\mathrm{Ar}}\right)\cdot\frac{(e \quad -1)}{\quad} \tag{4.8}$$

Equation 4.8 has the straight-line relation: $y = m \quad + c$. The isochron age of the unknown-age samples can be determined from the slope $(e \quad -1)/$ while the *y*-intercept intercept indicates the atmospheric ratio of ${}^{40}_{18}\mathrm{Ar}/{}^{36}_{18}\mathrm{Ar}$ which is often 295.5. Figure 4.5a shows an example of isochron diagram. The ${}^{40}_{18}\mathrm{Ar}/{}^{36}_{18}\mathrm{Ar}$ is plotted against ${}^{39}_{18}\mathrm{Ar}/{}^{36}_{18}\mathrm{Ar}$, illustrated as error ellipses which always lie nearly parallel to the best-fit line (dash line). The drawback of the isochron diagram is that a slightly change in ${}^{36}_{18}\mathrm{Ar}$ can cause huge errors in the argon ratios.

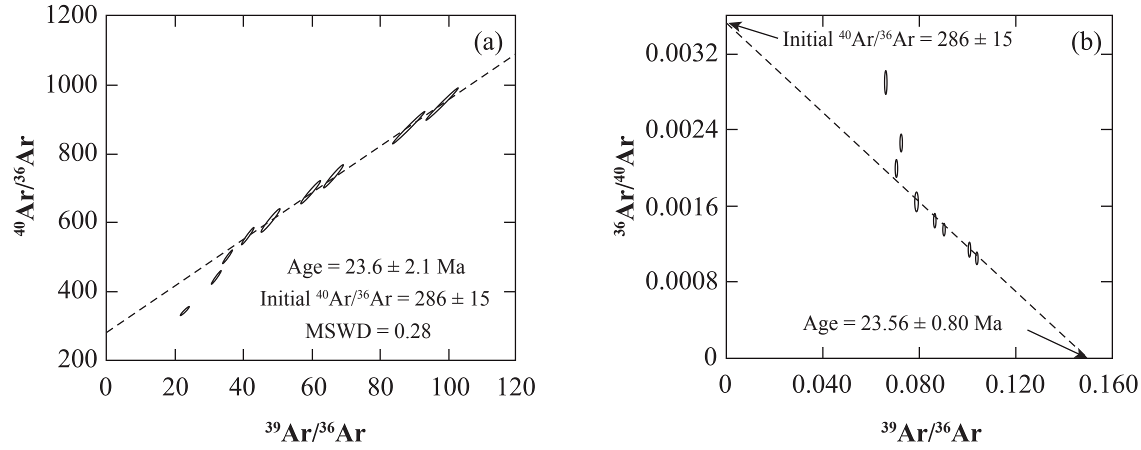

Figure 4.5: (a) isochron and (b) inverse isochron diagrams. The dash lines represent the best-fit lines which correspond to the steps used to define the plateau age. The first three error ellipses in both (a) and (b) do not lie along the best fit lines. The slope of the best-fit line in (a) is used to determine the isochron age while the *x*-intercept of the best fit line in (b) is used to calculate the inverse isochron age. The *y*-intercept in (b) corresponds to the inverse ratio of the ${}^{40}_{18}\mathrm{Ar}/{}^{36}_{18}\mathrm{Ar}$, which normally yields 1/295.5 or ~3.384 × 10^{-3}. Figure from Lee (2013).

4.3.2.3. Inverse isochron age

In order to reduce the large correlation error above, inverse isochron is used. Dividing Equation 4.6 by ${}^{40}_{18}\mathrm{Ar}$ to get:

$$1 = \frac{{}^{40}_{18}\mathrm{Ar}_i}{{}^{40}_{18}\mathrm{Ar}_{\ o\ al}} + \left(\frac{{}^{39}_{18}\mathrm{Ar}}{{}^{40}_{18}\mathrm{Ar}}\right)_{o\ al} \cdot \frac{(e \quad -1)}{\quad} \tag{4. }$$

If ${}^{40}_{18}\mathrm{Ar}_i = {}^{36}_{18}\mathrm{Ar}_i \cdot v$, where v is the initial argon ratio $({}^{40}_{18}\mathrm{Ar}/{}^{36}_{18}\mathrm{Ar})_i$, therefore

$$1 = \frac{{}^{36}_{18}\mathrm{Ar}_i \cdot v}{{}^{40}_{18}\mathrm{Ar}_{total}} + \left(\frac{{}^{39}_{18}\mathrm{Ar}}{{}^{40}_{18}\mathrm{Ar}}\right)_{total} \cdot \frac{\left(e \quad - 1\right)}{\;} \tag{4.10}$$

Then, dividing Equation 4.10 by v and rearranging the equation to get

$$\left(\frac{{}^{36}_{18}\mathrm{Ar}}{{}^{40}_{18}\mathrm{Ar}}\right)_{total} = \frac{1}{v} - \left(\frac{{}^{39}_{18}\mathrm{Ar}}{{}^{40}_{18}\mathrm{Ar}}\right)_{total} \cdot \frac{\left(e \quad - 1\right)}{v} \tag{4.11}$$

It is seen that Equation 4.11 also has a straight-line relation, where $\left(e \quad - 1\right)/$ is the slope. Figure 4.5b shows an example of the inverse isochron diagram. The age of the unknown samples can be determined from the *x*-intercept, where the *x*-intercept = $/\left(e \quad - 1\right)$. The *y*-intercept indicates the inverse ratio of ${}^{40}_{18}\mathrm{Ar}/{}^{36}_{18}\mathrm{Ar}$, which often yields 1/295.5 or ~3.384 × 10^{-3}.

4.4 Methods

4.4.1 X-ray fluorescent (XRF) analysis

Prior to the isotopic dating, whole-rock XRF analysis was performed on a set of hand samples from select stratigraphic levels. Melon-size (~2kg) samples were taken from cores of lava flows during the field seasons in order to avoid glass. Firstly, basalt samples were crushed to powder size in an agate mortar using a Tema Mill. Then, the powder samples were packed in grip seal bags and shipped to the School of Geography, Geology and the Environment, the University of Leicester for the XRF analysis. The samples were analysed for major elements and loss of ignition (LOI) using the PANalytical Axios-Advanced XRF spectrometer. The major element and LOI data are given in Table 4.1 with accepted samples for the ^{40}Ar/^{39}Ar dating. The sub-set of samples selected for ^{40}Ar/^{39}Ar dating were chosen based on preferential high concentrations of K_2O (more radiogenic argon), low LOI (less secondary alteration, less likely to have undergone argon loss) and stratigraphic positions (top and bottom of individual profiles, near obvious hiatuses). The initial selection was made in the field with preference of sampling fresh (bluish-hued), massive material (more crystalline, less glass) from the core of lava flows that were less vesicular and lower modal proportions of secondary mineral assemblages. Note: the hand samples were assessed and collected in the field by Dr Morten during the field survey, the sample preparation for XRF was performed by myself.

Table 4.1: XRF major element concentrations (wt%) for samples collected for $^{40}Ar/^{39}Ar$ dating. The last column indicates whether they were selected for dating or not.

Sample	**SiO_2**	**TiO_2**	**Al_2O_3**	**Fe_2O_3**	**MnO**	**MgO**	**CaO**	**Na_2O**	**K_2O**	**P_2O_5**	**SO_3**	**LOI**	**Total**	**Select?**
VA1	47.50	3.24	13.10	15.63	0.194	5.92	10.44	2.52	0.401	0.367	<0.003	0.18	99.46	**Yes**
VA2	48.08	2.95	13.28	14.71	0.184	6.12	10.89	2.45	0.190	0.336	<0.003	0.49	99.65	No
VA15	48.98	3.37	12.82	15.91	0.226	5.39	9.77	2.71	0.505	0.370	<0.003	-0.31	99.71	**Yes**
VA20	48.50	2.52	13.75	14.18	0.186	6.52	11.28	2.57	0.198	0.220	<0.003	-0.09	99.79	No
HS1	47.98	3.26	12.98	15.97	0.216	5.98	10.44	2.48	0.208	0.322	<0.003	-0.11	99.70	No
HS3	48.60	2.64	13.59	14.14	0.184	6.42	11.16	2.42	0.345	0.237	<0.003	0.06	99.76	**Yes**
HS15	47.91	2.56	15.64	13.97	0.185	5.23	11.47	2.61	0.208	0.229	<0.003	-0.18	99.79	**Yes**
HS17	48.18	2.65	13.25	15.30	0.208	6.37	10.93	2.49	0.164	0.277	<0.003	-0.04	99.75	No
HS22	58.50	1.37	13.56	12.81	0.267	1.60	5.42	3.76	1.494	0.566	<0.003	0.22	99.53	**Yes**
MSR14-002	73.39	0.16	12.60	2.29	0.095	0.36	0.98	3.99	2.643	0.010	<0.003	2.55	99.04	No
HS24	75.51	0.16	12.25	2.43	0.045	0.05	0.52	4.75	3.362	0.014	<0.003	0.39	99.46	**Yes**
GR4	47.39	3.71	12.92	16.58	0.225	5.36	10.08	2.77	0.338	0.386	<0.003	-0.04	99.69	No
GR5	48.47	2.70	13.81	14.57	0.208	5.81	10.67	2.85	0.436	0.240	<0.003	-0.04	99.69	**Yes**
GR7c	48.74	3.56	12.68	16.39	0.217	4.75	9.50	2.85	0.677	0.451	<0.003	-0.15	99.63	**Yes**
GR31	48.42	2.43	14.40	13.77	0.189	6.46	11.78	2.51	0.313	0.239	<0.003	-0.56	99.92	**Yes**
GR32	48.52	2.50	13.89	14.31	0.197	6.55	11.68	2.58	0.289	0.221	<0.003	-0.75	99.95	No
GR34	48.45	1.70	14.12	12.83	0.183	7.81	12.72	2.20	0.179	0.144	<0.003	-0.49	99.80	**Yes**
LF1	48.75	2.98	13.12	16.25	0.232	5.32	10.03	2.85	0.412	0.314	<0.003	-0.46	99.76	**Yes**
LF8	48.46	2.49	13.74	14.19	0.196	6.44	11.50	2.53	0.317	0.224	<0.003	-0.63	99.42	No
LF9	47.94	1.57	14.58	12.29	0.173	8.03	12.70	2.07	0.181	0.124	<0.003	-0.14	99.48	No
TOM3	48.32	2.67	14.14	15.01	0.213	6.05	11.13	2.51	0.340	0.244	<0.003	-0.65	99.96	**Yes**
TO1	48.47	1.64	14.92	12.42	0.178	7.56	12.66	2.16	0.197	0.144	<0.003	-0.07	100.25	No
TO15	48.80	1.91	14.49	14.04	0.199	6.99	11.57	2.39	0.242	0.176	<0.003	-0.62	100.16	**Yes**
BT2	48.14	2.85	13.26	15.23	0.214	6.53	11.36	2.51	0.257	0.251	<0.003	-0.66	99.91	**Yes**
BT4	48.53	2.42	14.29	13.53	0.188	6.65	11.96	2.48	0.262	0.204	<0.003	-0.58	99.91	**Yes**
BO2	48.33	2.24	14.39	13.42	0.185	6.99	11.97	2.38	0.224	0.191	<0.003	-0.41	99.90	No
BO5	48.55	2.32	13.71	14.13	0.197	7.00	11.93	2.37	0.231	0.193	<0.003	-0.51	100.08	**Yes**
BO14	48.92	1.64	14.20	12.19	0.173	8.03	13.09	2.05	0.133	0.134	<0.003	-0.54	100.01	**Yes**

4.4.2 ^{40}Ar/^{39}Ar dating

The ^{40}Ar/^{39}Ar geochronology was performed at the Scottish University Environment Research Centre (SUERC), University of Glasgow under a NERC Isotope Geosciences Facilities grant to my supervisor Dr. Muxworthy. Prior to the sample preparation processes, two weeks were spent in the SUERC during October 2016 in order to learn sample preparation methods. Firstly, the samples were crushed into coarse grain sizes and sieved to produce ~250-500 μm fraction. Then, the groundmass concentrate, and plagioclase were sorted using a Frantz magnetic separator. Non-magnetic fraction such as olivine and pyroxene in the groundmass was eliminated during this process leaving highly potassic groundmass. Acid leaching was performed with ~5% nitric acid to remove carbonate from the groundmass. The samples were then cleaned with de-ionised water until the water ran clear. Finally, the concentrated-plagioclase groundmass was hand-picked (positive picking) under the binocular microscope. Approximately 0.6-1 g of the groundmass per sample was hand-picked and a total of 17 groundmass samples were sent to the SUERC for the ^{40}Ar/^{39}Ar dating. The irradiation and the ^{40}Ar/^{39}Ar dating were handled and performed by Dr Dan Barford, the research collaborator at SUERC. Note, additional five samples: VA2, VA20, HS1, HS17 and GR4 were sent for the argon-argon dating in *January 2018* in order to better constrain timing of few critical stratigraphic levels as the first batch of samples were inconclusive. These additional age data may not arrive timely for submission of the thesis.

Samples and neutron flux monitors were packaged in copper foil and stacked in quartz tubes with the relative positions of packets precisely measured for later reconstruction of neutron flux gradients. The sample package was irradiated in the Oregon State University reactor, Cd-shielded facility. Alder Creek sanidine (1.1891±0.0008 (1σ) Ma, Niespolo et al. (2017)) was used to monitor ^{39}Ar production and establish neutron flux values (J) for the samples. Gas was extracted from samples via step-heating using a mid-infrared (10.6 μm) CO_2 laser with a non-Gaussian, uniform energy profile and a 3.5 mm beam diameter rastered over a sample well. The samples were housed in a doubly-pumped ZnS-window laser cell and loaded into a copper planchette containing nine 1 cm^2 square wells. Liberated argon was purified of active gases, e.g., CO_2, H_2O, H_2, N_2, CH_4, using three Zr-Al getters; one at 16°C and two at 400°C. Data were collected on a GVi instruments ARGUS V multi-collector mass spectrometer using a variable sensitivity faraday collector array in static collection (non-peak hopping) mode (Mark et al., 2009; Sparks et al., 2011). Time-intensity data are regressed to inlet time with second-order polynomial fits to the data. The average total system blank for laser extractions, measured between each sample run, was 1.5 ± 0.1×10^{-15} mol ^{40}Ar, 1.1 ± 0.3×10^{-17} mol ^{39}Ar, 6.2 ± 2.5×10^{-18} mol ^{36}Ar. Mass discrimination was monitored on a daily basis, between and within sample runs by analysis of an air standard aliquot delivered by an automated pipette system (see raw data for D values applied to individual steps). All blank, interference and mass discrimination calculations were performed with the MassSpec software package (MassSpec, version 8.058, authored by Al Deino, Berkeley Geochronology Center). Inverse-variance-weighted plateau ages, or composite plateau ages for replicated samples, were chosen as the best estimates of the emplacement ages.

Plateau ages were defined and calculated following these criteria:

- Steps overlap in age within 2σ uncertainty.
- Minimum ^{39}Ar content for a step is ≥ 0.1% of total ^{39}Ar release.
- Minimum of three contiguous steps.
- Minimum of 50% of ^{39}Ar in the chosen steps.
- The inverse isochron formed by the plateau steps yields an age indistinguishable from the plateau age at 2σ uncertainty.
- The trapped component composition, derived from this inverse isochron, is indistinguishable from the composition of air at the 2σ uncertainty level.
- Age and uncertainty were calculated using the mean weighted by the inverse variance of each step.
- "Composite" ages are calculated by combining all accepted plateau steps from each sample run and weighting these by the inverse of variance.

Note: the total fusion, plateau and isochron ages were determined by Dr Dan Barfod. The figures of the age spectrum and inverse isochron diagrams presented in this Thesis were provided by Dr Dan Barfod and later modified by myself.

4.5 Results

A summary of the plateau spectrum ages, isochron ages and total fusion age data are presented in Table 4.2 while raw data, isochron and plateau diagrams are given in Appendix B. All errors herein are given at the 2σ level. Sample VA1 has a plateau age of 7.77 ± 0.15 Ma (Figure 4.6a). The plateau age agrees fairly well with the isochron age (Figure 4.6b) and total fusion age (integrated age) of 7.79 ± 0.17 Ma and 7.74 ± 0.30. Sample VA15 provides the age spectrum of 7.98 ± 0.15 Ma (Figure 4.6c), in agreement with the isochron age (Figure 4.6d) and total fusion age of 7.88 ± 0.22 Ma and 7.93 ± 0.38 Ma within 2σ. The ages of VA1 and VA15 are problematic as VA1 lies at the bottom of VA section, indicating the oldest age of the VA. However, both samples yielded fairly flat age spectrum. Therefore, both samples are included in the linear regression age model (Chapter 5).

HS3 yielded very concordant data with a plateau age of 8.31 ± 0.13 Ma, in agreement with the isochron and integrated ages of 8.32 ± 0.13 Ma and 8.31 ± 0.11 Ma. Samples HS15 shows a fairly flat age spectrum of 7.27 ± 0.12 (Figure 4.6e and 4.7a), in agreement with isochron (Figure 4.6f and 4.7b) and total fusion ages of 7.32 ± 0.16 Ma and 7.27 ± 0.10 Ma. With regards to HS22, the plateau age (Figure 4.7c and 4.7e) is consistent with isochron (Figure 4.7d and 4.7f) and total fusion ages at 2σ. However, the age spectrums show a down-step spectrum at high temperature, indicating ^{39}Ar recoil. Recoil likely returns anomalously old apparent ages. Therefore, HS22 is not included in the age model. Samples HS24 shows flat age spectrum with a plateau age of 7.12 ± 0.10 Ma (Figure 4.8a). The plateau age agrees well with the isochron age (Figure 4.8b) and total fusion age of 7.10 ± 0.07 Ma and 7.10 ± 0.17 Ma.

Sample GR5 yielded concordant data with a plateau age of 5.73 ± 0.14 Ma, in agreement with isochron and integrated ages of 5.74 ± 0.11 Ma and 5.73 ± 0.13 Ma. GRC7 provides a plateau age of 6.27 ± 0.11 Ma (Figure 4.8c), which is older than GR5. The plateau is in agreement with an isochron age of 6.36 ± 0.15 Ma (Figure 4.8d). A total fusion age (6.11 ± 0.65 Ma) is slightly lower than the plateau and isochron ages, but in agreement with these ages at 2σ. The isochron diagram shows a *y*-intercept at 0.0036, which is equal to the ^{40}Ar/^{36}Ar ratio of 277.8 (Figure 4.8d). Compared to the (^{40}Ar/^{36}Ar)$_a$ ratio of 295.5, it is clear that the ^{36}Ar excess in the system. Excess argon can cause the numerical age to be older than the true age of the dated samples. Therefore, the ambiguous age of GRC7 is not included in the regression age model. GR31 yielded slightly disturbed age spectrum with a plateau age of 5.05 ± 0.10 Ma (Figure 4.8e), in agreement with isochron (Figure 4.8f) and total fusion ages of 4.97 ± 0.33 Ma and 5.00 ± 0.35 Ma. Sample GR34 provides a plateau age of 4.85 + 0.13 Ma. The plateau age agrees with isochron and integrated age of 4.89 ± 0.13 Ma and 4.85 ± 0.12 Ma. The numerical ages of GR31 and GR34 support an unpublished age of approximately 5 Ma on top of GR in Hardarson et al. (1999) study.

Sample LF1 provides a plateau age of 5.08 ± 0.11 Ma, in agreement with a total fusion age of 5.08 ± 0.09 Ma. An isochron age of 5.34 ± 0.25 Ma is slightly older than the plateau and integrated ages but coincides with these ages at 2σ.

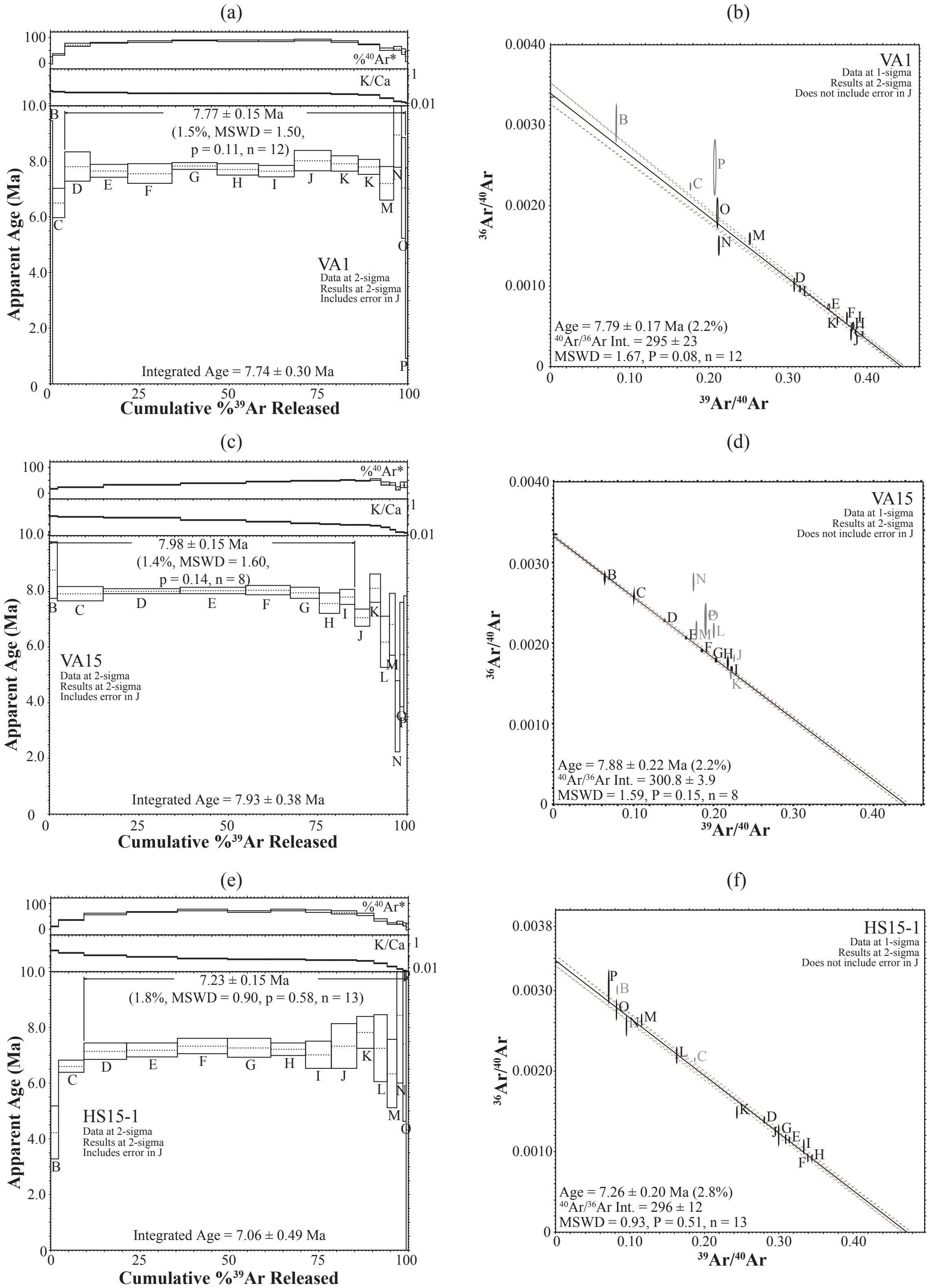

Figure 4.6: Left columns shows the age spectrum diagrams of (a) VA1, (c) VA15 and (e) HS15 (first run) and right column shows inverse isochron diagram of (b) VA1, (d) VA15 and (f) HS15 (first run) from step-up heating. Integrated age (total fusion age) is also marked in the age spectrum diagrams. The light grey ellipses in the inverse isochron diagram indicate data from step heating that are excluded from the plateau age calculation.

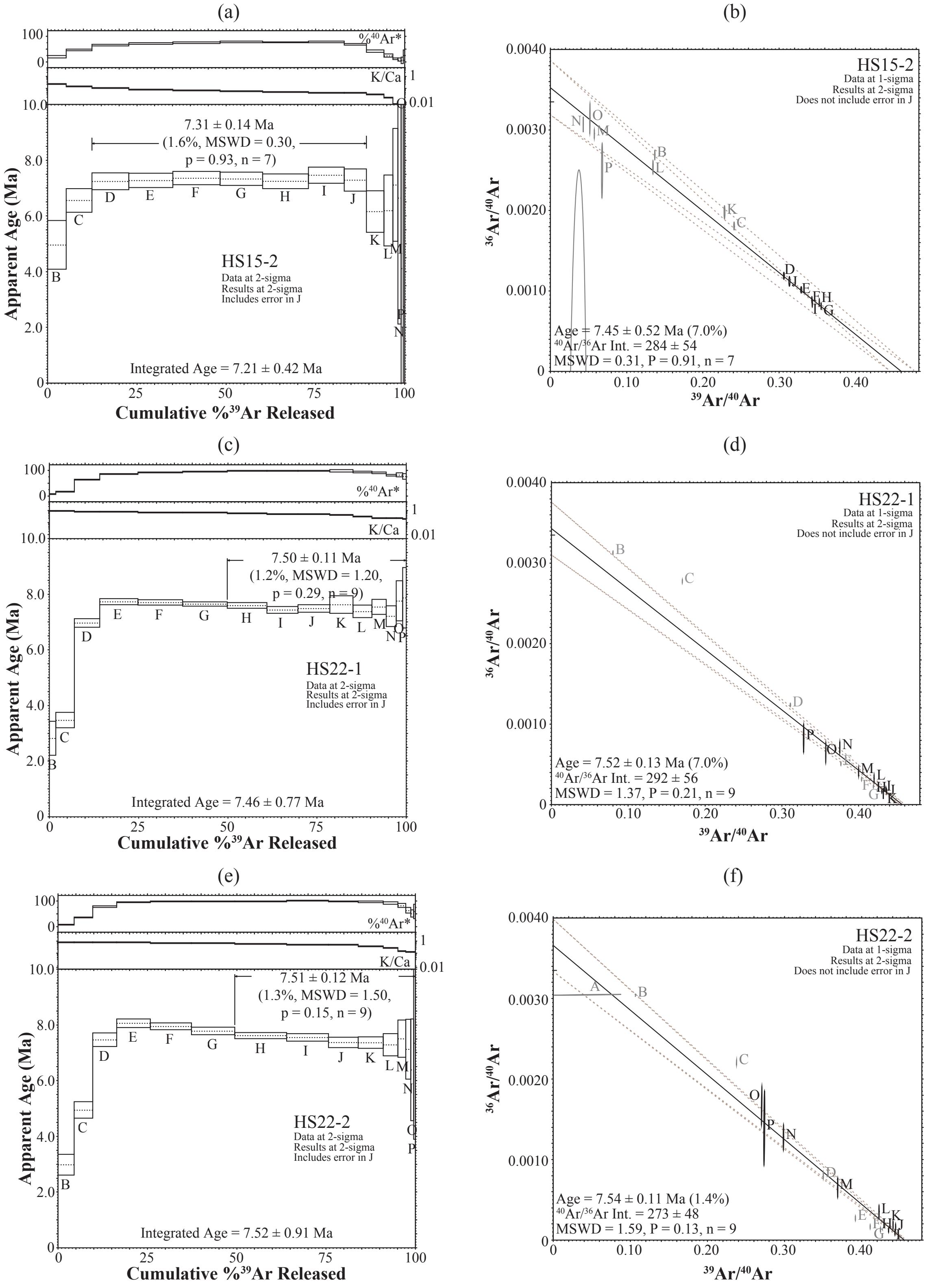

Figure 4.7: Left columns shows the age spectrum diagrams of (a) HS15 (replicated), (c) HS22 and (e) HS22 (replicated) and right column shows inverse isochron diagram of (b) HS15 (replicated), (d) HS22 and (f) HS22 (replicated) from step-up heating. Integrated age (total fusion age) is also marked in the age spectrum diagrams. The light grey ellipses in the inverse isochron diagram indicate data from step heating that are excluded from the plateau age calculation. It is clear that plateau diagrams of HS22 show a down step which indicates argon recoil.

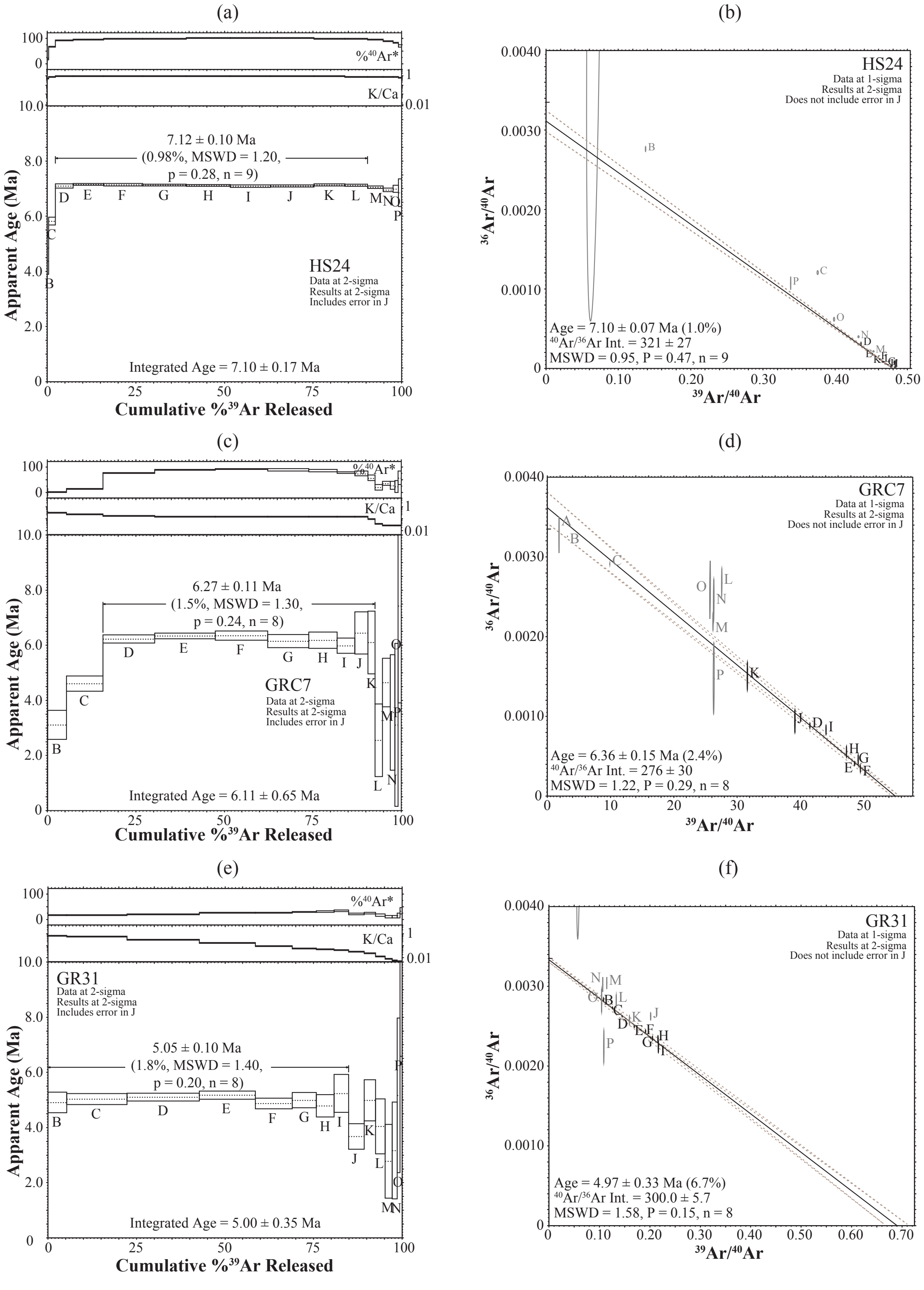

Figure 4.8: Left columns shows the age spectrum diagrams of (a) HS24, (c) GRC7 and (e) GR31 and right column shows inverse isochron diagram of (b) HS24, (d) GRC7 and (f) GR31 from step-up heating. Integrated age (total fusion age) is also marked in the age spectrum diagrams. The light grey ellipses in the inverse isochron diagram indicate data from step heating that are excluded from the plateau age calculation.

TOM3 yielded fairly concordant data with a plateau age of 4.84 ± 0.12 Ma, in agreement with the isochron and total fusion age of 4.92 ± 0.27 Ma and 4.75 ± 0.49 Ma. The $^{40}Ar/^{36}Ar$ value is 297.4. The numerical ages of TOM3 seem to agree with the numerical ages of GR34 at 2σ. Both samples are formed during the Sidufjall subchron. Sample TO15 yielded a concordant data with a plateau age of 4.68 ± 0.13 Ma, in agreement with the isochron and total fusion ages of 4.58 ± 0.18 Ma and 4.62 ± 0.50 Ma.

Sample BT2 gave a plateau age of 3.55 ± 0.10 Ma, with 100% of ^{39}Ar release. The plateau age is consistent with an integrated age of 3.55 ± 0.10 Ma but slightly lower than an isochron age (3.78 ± 0.27 Ma). Sample BT4 yielded a concordant data with a plateau age of 3.39 ± 0.10 Ma with 100% of ^{39}Ar, in agreement with an isochron age (3.32 ± 0.20 Ma) and total fusion age (3.39 ± 0.09 Ma).

Sample BO5 shows a slight scatter of ages: a plateau age (3.21 ± 0.12 Ma), isochron age (3.37 ± 0.21 Ma) and total fusion age (3.08 ± 0.58). However, the ages agree with each other at 2σ. BO14 shows the youngest plateau age of 2.56 ± 0.13 Ma, in agreement with isochron and integrated ages of 2.60 ± 0.39 Ma and 2.56 ± 0.12 Ma.

Overall, the $^{40}Ar/^{39}Ar$ dating results show a total of 15 high-precision ages, except HS22 and GRC7 due to the argon recoil and excess argon. The mean sum weighted deviates (MSWD) for all data are <2.5 (general accepted MSWD limit (e.g., Brooks et al., 1972)). The agreement between plateau, isochron and total fusion ages indicates that the primary argon reservoirs are not affected by alteration and the isotope system has remained closed after the rocks have formed. The plateau ages from 15 samples are used for the linear regression age model in Chapter 5. Note, the age models in this thesis will be updated for publications when five new argon ages are issued. The Alder Creek sanidine (ACs, 1.1891±0.0008 (1σ) Ma, Niespolo et al. (2017)) monitor age (optimization calibration) used here differs (significantly) by only 0.36% from the weighted mean astronomical calibration age of 1.1848 Ma for ACs. The astronomical calibration age of ACs is consistent with the 28.201 Ma of Fish Canyon sanidine (FCs, Kuiper et al., 2008) used in the geomagnetic polarity timescale 2012 (GPTS2012, Ogg (2012)). Recalibration of the reported ages to an age for ACs of 1.1848 Ma would lower the ages by 1-3 kyr. This calibration issue is negligible for correlating the reported ages and magnetostratigraphy to the GPTS2012 and the ages as given in Table 4.2 are used throughout the thesis without recalibration.

Table 4.2: Summary of plateau, isochron and total fusion ages from the Eyjafjardardalur. MSWD is mean sum weighted deviates (general accepted MSWD limit is < 2.5). N is incremental heating steps used in plateau age calculations and N-total is the total incremental heating steps. Rejected samples for linear regression age models are marked as italic.

sample	Age spectrum						Isochron			Integrated Age
	Age±2σ (Ma)	Ca/K	MSWD	N	N-total	^{39}Ar (%)	Age±2σ (Ma)	MSWD	^{40}Ar/^{36}Ar intercept	Age±2σ (Ma)
VA1	7.77±0.15	28	1.50	12	15	95	7.79±0.17	1.67	295	7.74±0.30
VA15	7.98±0.15	10.3	1.60	8	15	86	7.88±0.22	1.59	300.8	7.93±0.38
HS3	8.31±0.13	12.0	1.00	17	17	100	8.32±0.13	1.07	297.8	8.31±0.11
HS15	7.27±0.12	32	0.70	20	20	100	7.32±0.16	0.71	295	7.27±0.10
HS22	*7.51±0.11*	*4.0*	*1.30*	*18*	*18*	*100*	*7.53±0.10*	*1.31*	*282*	*7.51±0.08*
HS24	7.12±0.10	0.114	1.20	9	15	88	7.10±0.07	0.95	321	7.10±0.17
GR5	5.73±0.14	16.0	1.80	15	15	100	5.74±0.11	1.96	297.4	5.73±0.13
GR7C	*6.27±0.11*	*6.9*	*1.30*	*8*	*16*	*77*	*6.36±0.15*	*1.22*	*276*	*6.11±0.65*
GR31	5.05±0.10	17	1.40	8	15	85	4.97±0.33	1.58	300.0	5.00±0.35
GR34	4.85±0.13	56	0.90	22	22	100	4.89±0.13	0.88	295.1	4.85±0.12
LF1	5.08±0.11	16.8	1.20	18	18	100	5.34±0.25	0.94	296.0	5.08±0.09
TOM3	4.84±0.12	15.3	1.40	8	15	80	4.92±0.27	1.56	297.4	4.75±0.49
TO15	4.68±0.13	40	1.10	13	15	96	4.58±0.18	0.99	308	4.62±0.50
BT2	3.55±0.10	22.8	1.20	14	14	100	3.78±0.27	1.01	294.7	3.55±0.10
BT4	3.39±0.10	24.9	1.30	14	14	100	3.32±0.20	1.40	300.2	3.39±0.09
BO5	3.21±0.12	93	1.00	13	15	89	3.37±0.21	0.79	296.5	3.08±0.58
BO14	2.56±0.13	59	1.00	22	22	100	2.60±0.39	1.07	298.0	2.56±0.12

Chapter 5

Palaeomagnetic directions

5.1 Palaeomagnetic methods

A total of 1,809 cores were cut into standard 25.4 mm specimen size which yielded 1,809 specimens and 814 sister specimens. Top specimens were subjected to progressive demagnetisations, because orientation lines were marked on the topmost core segments during sample collection; the use of sister specimens (deeper along the core) for palaeodirection analysis can leads to orientation errors if the cores were bent during drilling in the field. Therefore, pristine sister specimens from lower in the core were subjected to palaeointensity experiments only. The palaeodirection measurements were performed in a dynamic Helmholtz cage at Imperial College London. Approximately 6-7 unbroken cores per lava flow with Sun azimuths were submitted to progressive tumbling alternating field (AF) demagnetisation using a Molspin AF demagnetiser. For LF section that our team could not collect the Sun readings, 6-7 unbroken cores per flow with compass readings were submitted to demagnetisation experiments. Firstly, the specimens' natural remanent magnetisation (NRM) were measured with an AGICO JR5A spinner or a Molspin Minispin until the NRM dropped below 5%. Samples for which the NRM could not be removed under 100 mT were statically AF demagnetised up to 200 mT in a DTECH 2000. The thermal demagnetisation was performed with one sample per lava flow to test thermal stability of the samples. A step-wise heating protocol from 100°C to 650°C was used in a ASC dual-chamber palaeomagnetic oven. The heating was conducted in air.

The characteristic components of NRM were determined by principal component analysis (PCA) (Kirschvink, 1980) on orthogonal projection (“Zijderveld”) diagrams (Zijderveld, 1967). Five points or more were used to determine the palaeodirections. For studies of the time-averaged geomagnetic field it is at present recommended to average site mean directions from at least five samples per site ($n \geq 5$) (Johnson et al., 2008). Using $n < 5$ causes less reliable estimates of the precision parameter k (e.g., Tauxe et al., 2003); therefore, approximately 5-8 specimens per site were used to determine site-mean directions in this study. Compared to studies in Iceland prior to 2005, researchers usually collected around 2-4 samples per site (e.g., McDougall et al., 1976; Watkins et al., 1977; Eiríksson et al., 1990; Helgason and Duncan, 2001; Kristjansson et al., 2004). Only a few research campaigns in Iceland have collected greater than five samples per site (e.g., Udagawa et al., 1999; Døssing et al., 2016; Tanaka and Yamamoto, 2016). The site-mean direction was calculated using the Fisher statistics (Fisher, 1953) on PuffinPlot v.1.03 (Lurcock and Wilson, 2012). Samples whose maximum angular deviation (MAD) on the PCA exceeds 5° were rejected from site-mean direction calculation.

5.2 Results

5.2.1 Palaeodirection

Palaeomagnetic directions were successfully measured on 156 lava flows of the lava pile exposed in the upper (southern) half of Eyjafjardardalur. Icelandic basalts are characterised by strong magnetisation. Figure 5.1 and 5.2 show representative orthogonal projection diagrams, NRM intensity decay plots and equal-area projections from AF demagnetisation and thermal demagnetisation experiments. The AF demagnetisation data commonly showed straight-line trends toward the origin of the Zijderveld diagram (Zijderveld, 1967) (Figure 5.1a, d and g), overprinted by a viscous remanent magnetisation (VRM). This secondary component was removed by alternating peak fields of 5-10 mT. Figure 5.1b, e and h illustrate the NRM decay after step-wise AF demagnetisation. The NRM in most samples drops by 75% after the 50 mT AF field is applied. The equal area projections (Figure 5.1c, f and i) show tightly grouped points.

With regards to thermal demagnetisation (Figure 5.2), not all samples provided reliable data as thermal alteration occurs during step-wise heating in some specimens. Overall, several samples in the study area yield successful results, e.g., TO3M1 (Figure 5.2a-c) and BO12K1 (Figure 5.2d-f). The

Zijderveld diagrams exhibit straight line toward the origin (Figure 5.2a and d). The NRM decay plots show that these samples are titanomagnetite with titanium composition $x \approx 0$ (Figure 5.2b and e) while the NRM directions are tightly grouped on the equal area projections (Figure 5.2c and f). Such sample material is preferred for palaeointensity experiments as it exhibits good thermal resistance with no sign of alteration found. Figure 5.2g-i show an example of overprint in flow HS20. Of all the lava flows in the valley only HS20 was found to be affected by re-magnetisation (Figure 5.2g). The field notebook recorded during the field trips indicates that flow HS20 was cut by an intrusive dyke. This overprint was removed when the specimen was heated above 450 °C. Finally, the primary NRM was determined at the bulk demagnetisation steps. The characteristic curve of titanomaghemite was also found as the NRM intensity shows a hump at 400 °C (Figure 5.2h). It is clearly seen that the directions due to the overprint are scatter on the stereo plot (Figure 5.2i). Significant alterations were also found when the samples were heated at 630 °C and 650 °C (Figure 5.2i). Figure 5.2j-l represents a specimen (LF9F1) that undergoes alteration during a thermal demagnetisation experiment. The data scatter on all plots and principal component analysis cannot be made from such samples. This type of data is rejected from site-mean direction determination and palaeointensity experiment (Chapter 7).

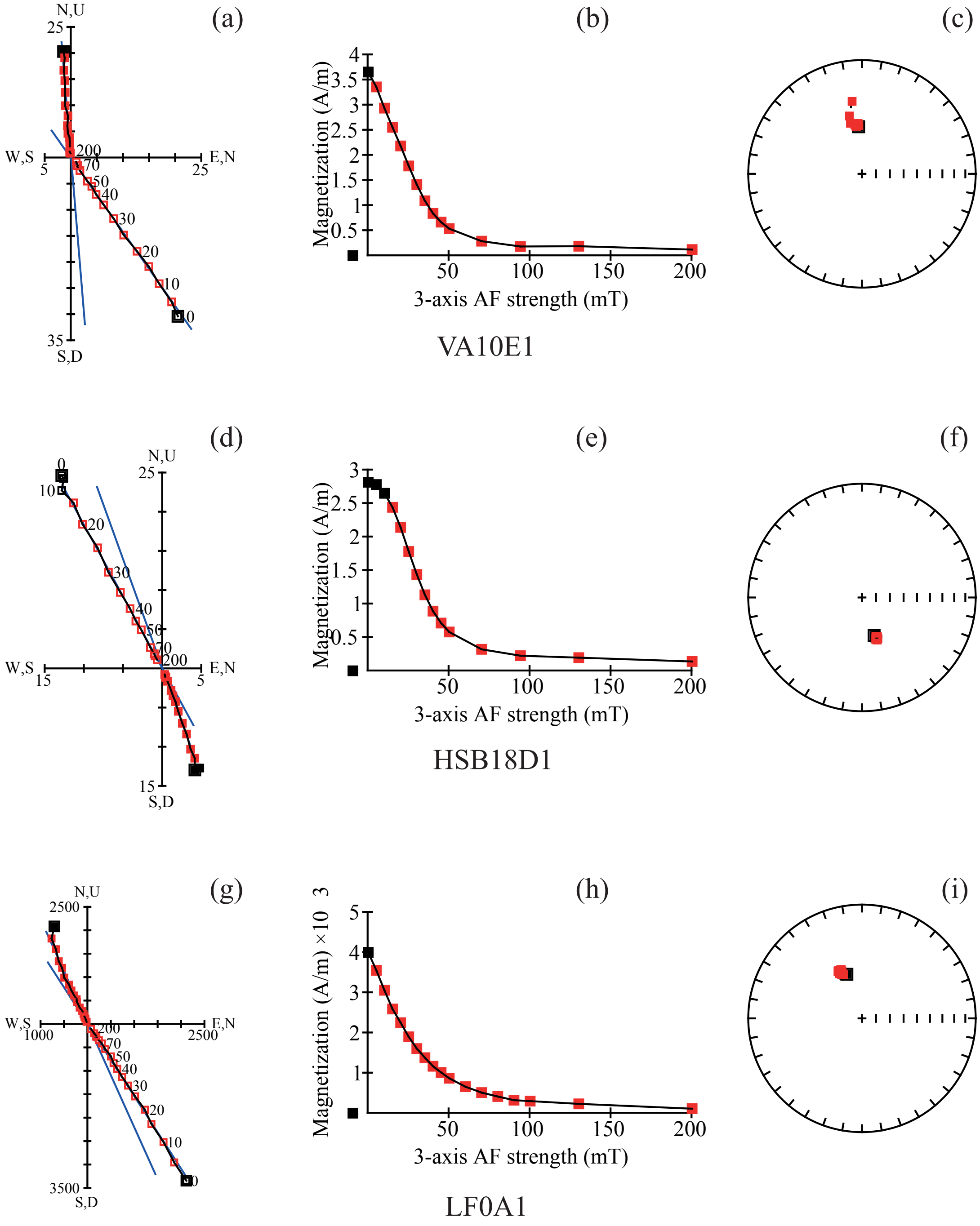

Figure 5.1: Representative samples yielding successful AF demagnetisation experiment. (a), (d) and (g) Zijderveld diagrams (Zijderveld, 1967) showing vertical component (open squares) and horizontal component (filled squares) of the field recorded during the step-wise demagnetisation. (b), (e) and (h) NRM decay plots. (c), (f) and (i) equal area projections showing the directions recorded during the step-wise demagnetisation, with north oriented toward the top of the figure. Red squares represent points used in principal component analysis (PCA) (Kirschvink, 1980) for direction determination. It is clear that these samples record reliable directions and the NRM decay nearly zero. The data are tightly grouped on the stereo plots.

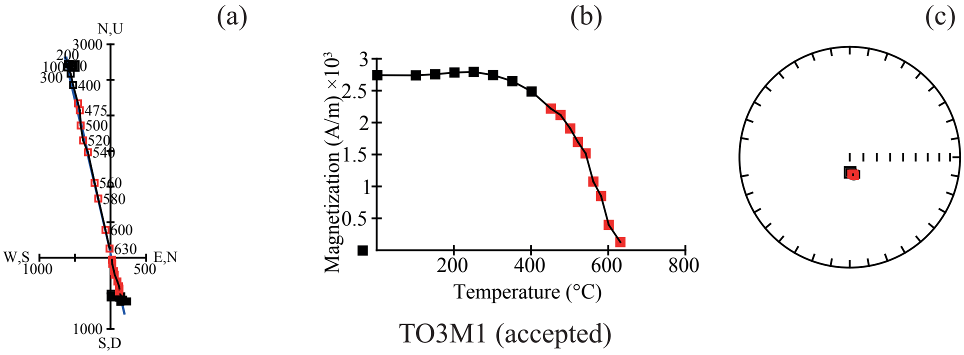

TO3M1 (accepted)

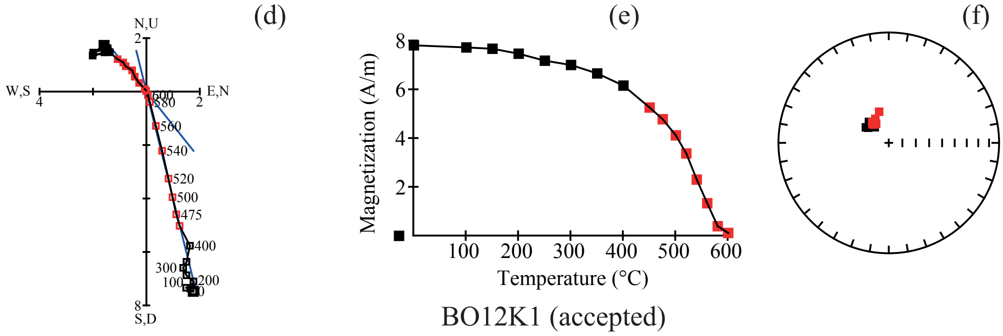

BO12K1 (accepted)

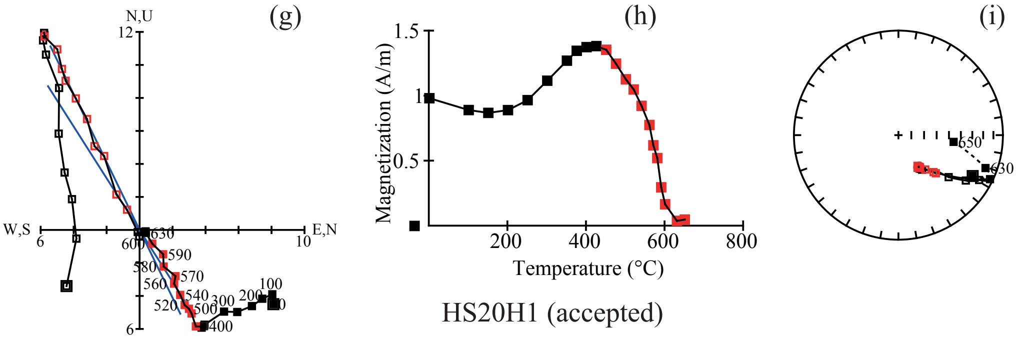

HS20H1 (accepted)

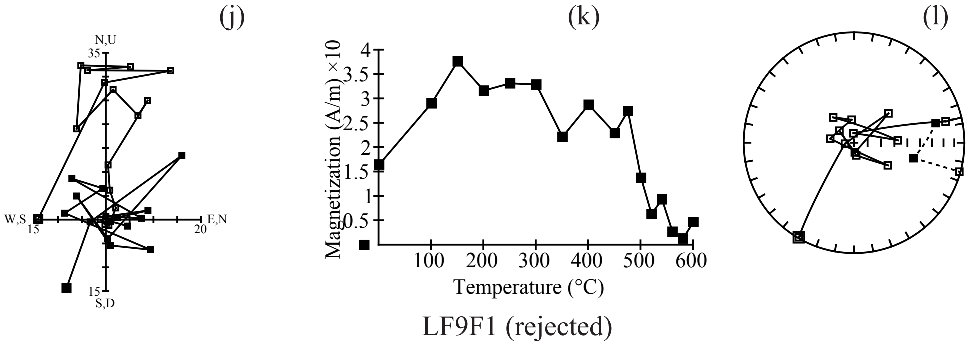

LF9F1 (rejected)

Figure 5.2: Representative samples from step-wise thermal demagnetisation experiment. (a), (d), (g) and (i) Zijderveld diagrams (Zijderveld, 1967) showing vertical component (open squares) and horizontal component (filled squares) of the field recorded during the step-wise demagnetisation. (b), (e), (h) and (k) NRM decay plots. (c), (f), (i) and (l) equal area projections showing the directions recorded during the step-wise demagnetisation, with north oriented toward the top of the figure. Red squares represent points used in principal component analysis (PCA) (Kirschvink, 1980). Accepted samples (marked accepted) show reliable directional results and the NRM decays nearly zero at the bulk demagnetisation steps. The data are well grouped on the stereo plots. Rejected sample (marked rejected) shows scatter data on all plots.

The site mean directions were calculated for 156 lava flows. Of these, 83 lava flows record normal polarity magnetisation, while 73 flows record reverse polarity magnetisation. For data from lava flows that were drilled at two sampling sites, and these sites are ~100 m apart, Watson's V_w test (Tauxe et al., 2010) was applied in order to confirm if the two data sets have a common mean direction. These flows are TO7 site1 and TO7 site2; TO8 site1 and TO8 site2; BO3 site1 and BO3 site2; BO5 site1 and BO5 site2. All separated flows pass the statistic V_w. Then specimen level data from the two sites were combined and site mean directions were calculated. Then, 156 site mean directions were applied the tilt correction using the recorded tilts and dips given by Kristjansson et al. (2004). All the site mean directions were adjusted the dip direction of 135° with different dip angles. VA and HS were adjusted the dip angles of 6° and 5° while GS toward GR17 were corrected the dip angle of 4°. GR18 toward TOD14 were adjusted the dip angle of 3°. The upper Eyjafjardardalur (BT and BO) has very small incline and was corrected the tectonic tilt with the dip angle of 1°. The details of site mean directions including uncorrected and corrected tilts along with related data are given in Table 5.1.

In order to test whether the lava flows accuired the NRM prior to or after the tectonic tilt, a field test of palaeomagnetic stability (fold test) was applied to the dataset. If the NRM was acquired prior to the folding, the NRM directions scatter after the folding. When the structural correction is made and the adjusted NRM directions converge, the NRM directions are said to pass the fold test. However, if the NRM was acquired after the folding, the NRM directions should converge prior to the structural correction. When the structural correction is applied, the NRM directions scatter. The NRM directions are said to fail the fold test. This study I applied the bootstrap method of Tauxe and Watson (1994) to perform the fold test in order to test the stability of 156 site mean directions. This method works by using eigenvalues (τ) of the rotation matrix of the dataset. When the data become more tightly grouped during the unfolding process, the variance along the principal axis increases (Tauxe et al., 2010). Therefore, the τ_1 is used to examine the per cent unfolding in Tauxe and Watson (1994). The NRM directions of the input dataset are illustrated in Figure 5.3a. The tectonic tilts and dips mentioned above were used to unfold the NRM directions as shown in Figure 5.3b. A cumulative distribution function (black line) of maxima in τ_1 during tilt adjustment of representative 1,000 pseudo-samples drawn from the dataset in Figure 5.3a is presented in Figure 5.3c. It seen that 95% confidence bounds (vertical dash lines) include 100% unfolding which indicate a pre-tilt magnetisation. A total of 156 directional data passes the bootstrap fold test at 95% confidence level. Therefore, the lava flows in the study area acquired the NRM prior to the tectonic tilt. On the other hand, if the confidence bound exclude 100% untilting but include 0% untiling, the post-tilt magnetisation is presence.

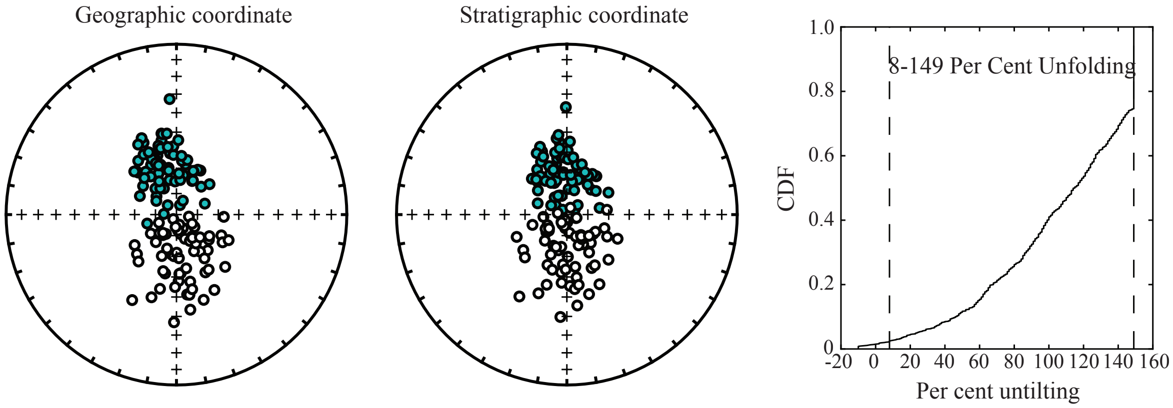

(a) (b) (c)

Figure 5.3: (a) and (b) equal area projections of the input dataset (geographic coordinate) and unfolded dataset (stratigraphic coordinate). Blue and open circles represent normal and reverse polarity magnetisations. (c) a cumulative distribution function of the per cent unfolding. Vertical dash lines show the boostrap 95% confidence bounds. It is clearly seen that 95% confidence bounds include 100% untilting which indicate a pre-tilt magnetisation. This dataset pass the bootstrap fold test at 95% confidence limit.

Figure 5.4 illustrates a bin-count chart of the number of samples per site in Eyjafjardardalur used to calculate site mean directions. The bulk of site mean directions in this study are derived from c. 7-8 specimens per site with maximum 16 specimens. As I selected seven specimens for AF demagnetisation and one specimens for thermal demagnetisation, site mean directions calculated from <8 specimens per site was because some specimens failed the thermal demagnetisation experiment, or directional data were scattered, e.g., TO1 (Table 5.1). For a few sites our team could not collect enough samples ($n = 8$ cores per site for this study) due to limited outcrops, e.g., VA8 ($n = 5$) or difficult and/or dangerous to access to outcrops, e.g., HS24 ($n = 3$) (Table 5.1).

Two lava flows that have been erupted in a short time interval and display indistinguishable directions may not record secular variation (Mankinen et al., 1985). They are not considered distinct and have to be combined to be considered for the GAD analysis. A group of lava flows that have identical directions is referred to as a directional group (DG) (Chenet et al., 2008). I applied the DG test to all data in order to detect rapid recurrent eruption events. I found a total of 18 DGs across eight units (3 in VA, 3 in HS, 5 in GR, 4 in TO and 3 in BO). Directional data from the same DG were combined and mean DG directions were calculated. The 95% confidence limit cannot be obtained in case mean

DG directions were derived from only two adjacent flows $(n = 2)$. The statistic $\sigma = \sqrt{\sum((\alpha_{95}(1))^2 + (\alpha_{95}(2))^2)}$ and angular distance δ were used for this case. The selection criteria of σ ≤ 15° was used to select reliable DGs.

After combining the DGs, 135 site mean directions were identified with selection criteria of $n \geq 5$, $k \geq 50$ (Johnson et al., 2008) and $\alpha_{95} \leq 10°$ (Opdyke et al., 2010) to exclude poor-quality data. Johnson et al. (2008) tested the relation between k cut-off and virtual geomagnetic pole (VGP) dispersion (S_F) (the scatter of the VGP about the Earth's spin axis). They found that using low k cut-off results in poor-quality data and overestimates VGP dispersion, while using very high k cut-off (e.g. 250) leads to noisy estimates of S_F due to low data numbers. Using $\alpha_{95} \leq 10°$ is still ambiguous; Opdyke et al. (2010) found that using $\alpha_{95} \leq 10°$ with $n \geq 5$ slightly increases S_F. However, I combined these criteria to exclude low-quality data in this study. The reason for choosing $\alpha_{95} \leq 10°$ stems from the number of samples per site in pre-2005 studies from Iceland is lower than five $(n \approx 3 \text{ to } 4)$. Site mean directions derived from $n < 5$ (e.g., $n = 2$) can provides $k > 100$ but $\alpha_{95} \approx 20°$ (e.g., TO1) (Table 5.1). To compare my data with pre-2005 Iceland studies (Chapter 6), I applied strict criteria to exclude all low-quality data in both my study and other Iceland studies.

As a result of the criteria, 10 lava flows fail our site level criteria and were omitted from further steps. Figure 5.5a-c represent an example of rejected sites from the time-averaged field calculation. The data scatter significantly on the stereo plots, yielding very high 95% confidence cone. The causes of data scatter are normally from poor orientation of the cores due to poor weather in Iceland, hardness of some flows and blunt drill bits. Figure 5.5d-f show an example of accepted sites for the time-average field study. The data are tightly grouped on the equal area projections with small 95% confidence error.

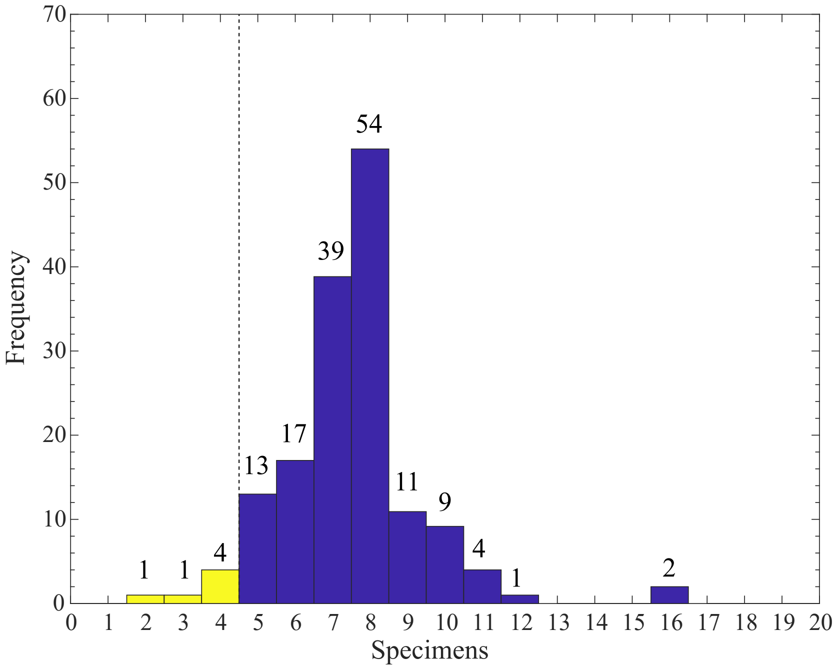

Figure 5.4: A histogram represents the frequency of the number of specimens used to derive site mean directions. It is seen that palaeodirections are generally derived from 7 to 8 specimens per site. The vertical dash line illustrates the n cut-off. Yellow bars present rejected sites. A total of 151 sites meets the minimum number of samples per site ($n \geq 5$) recommended by Johnson et al. (2008).

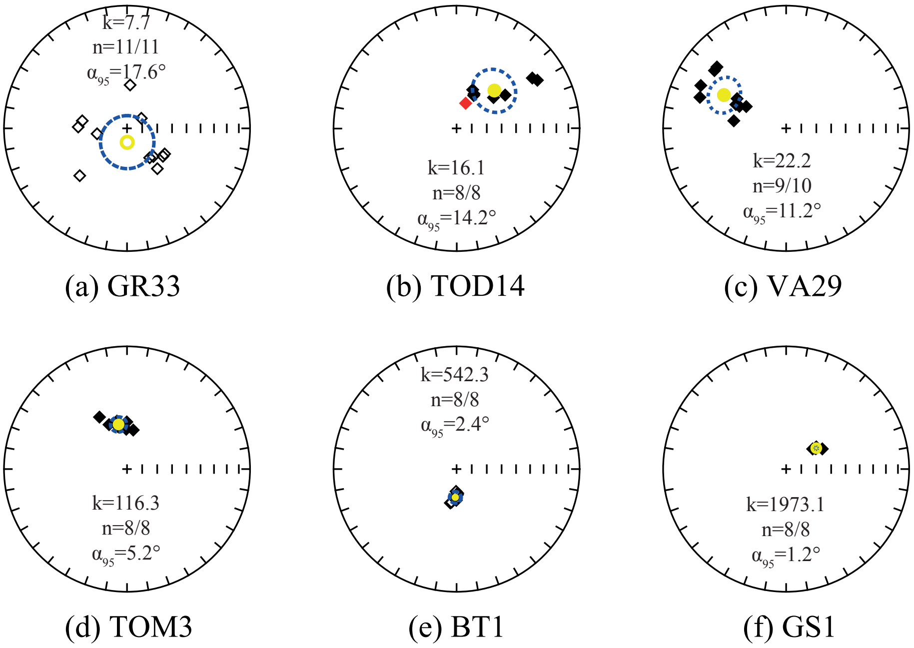

(a) GR33 (b) TOD14 (c) VA29

(d) TOM3 (e) BT1 (f) GS1

Figure 5.5: Equal-area projections show the directions recorded during the site-mean direction determination, with north oriented toward the top of the figure. (a)-(c) rejected sites from time-averaged field (TAF) analysis and (d)-(f) accepted sites for TAF study. Yellow circles indicate normal (closed) and reverse (opened) polarity sites. Dash blue circle represents 95% confidence limit. The directional data are scatter on (a)-(c) with very wide 95% confidence error (>10°) and well group on (d)-(c) with almost unseen 95% error cone (≤10°).

Table 5.1: Palaeomagnetic data of Eyjafjardardalur valley. Notations as follows: λ and φ are site latitudes and longitudes; Dec_u and Inc_u are Declination and Inclination prior to tilt correction; Dec and Inc are Declination and Inclination after structural correction; α_{95} and k are 95% confidence limits and precision parameters following Fisher (1953); n/N, where n is the number of samples used in site mean direction determination and N is the total number of samples fully demagnetised; R is the length of resultant vector; λ_p and φ_p are virtual geomagnetic pole (VGP) latitudes and longitudes with 95% confidence ellipse along the major (d_m) and minor (d_p) axes; λ', φ' and λ_p', φ_p' denote palaeolatitudes and palaeolongitudes of the site locations (λ, φ), and VGP latitudes and longitudes after the plate corrections using no-net-rotation MORVEL (Argus et al., 2011). Light grey cells represent sites identified in the same directional groups (DGs) following Chenet et al. (2008). Dark grey cells represent combined DG sites; the α_{95} cannot be calculated when DGs are derived from two sites, $\sigma = \sqrt{\sum((\alpha_{95}(1))^2 + (\alpha_{95}(2))^2)}$ was given with angular distance (δ) between two mean directions.

Site	λ (°N)	φ (°E)	Dec_u (°)	Inc_u (°)	Dec (°)	Inc (°)	α_{95} (°)	k	n/N	R	λ_p (°)	φ_p (°)	d_m (°)	d_p (°)	λ' (°N)	φ' (°E)	λ_p' (°)	φ_p' (°)
VA1	65.34533	-18.2331	342.2	60.1	348.0	65.3	3.3	425.5	6/8	6.0	71.0	187.3	5.3	4.3	65.00852	-15.1533	71.2	190.8
VA2	65.34522	-18.2328	356.1	59.0	3.8	63.3	2.4	536.2	8/8	8.0	69.4	154.1	3.8	3.0	65.00891	-15.1573	69.7	157.1
VA3	65.34514	-18.2325	348.5	73.2	3.7	77.7	3.4	273.1	8/8	8.0	88.1	32.7	6.3	5.9	65.00936	-15.1612	87.9	29.9
VA4	65.34518	-18.2324	25.0	72.3	44.2	73.4	2.8	449.8	7/8	7.0	69.0	67.9	5.1	4.6	65.00973	-15.164	69.0	70.0
VA5	65.34520	-18.2318	312.4	77.1	310.2	83.1	2.8	335.8	9/9	9.0	71.2	-52.1	5.5	5.4	65.0113	-15.176	70.9	-48.5
VA6	65.34525	-18.2317	344.6	57.5	350.2	62.6	2.1	586.8	9/11	9.0	67.9	180.7	3.3	2.6	65.01271	-15.1873	68.3	184.1
VA7	65.34508	-18.2313	317.7	62.7	318.4	68.7	2.4	350.9	11/11	11.0	65.2	239.4	4.1	3.5	65.01357	-15.1954	65.4	243.2
VA8	65.34501	-18.2304	335.4	51.7	338.6	57.3	9.2	70.7	5/5	4.9	59.9	196.8	13.4	9.8	65.01267	-15.2073	60.1	200.1
VAB9	65.34494	-18.2300	260.4	60.5	250.7	63.6	2.8	459.5	7/8	7.0	33.2	-70.9	4.5	3.5	65.01294	-15.2098	33.0	-67.7
VAO9	65.34492	-18.2295	348.6	53.4	353.9	58.3	4.5	153.5	8/8	8.0	63.4	172.4	6.6	4.9	65.01429	-15.2206	63.7	175.5
VA10	65.34498	-18.2293	349.5	50.0	354.2	54.8	1.6	1206.8	8/8	8.0	59.7	171.2	2.3	1.6	65.0147	-15.2232	60.1	174.3
VAO9-VA10					354.0	56.5	σ=4.8	δ=3.5	2/2		61.5	171.8	3.3	2.4			61.8	175.0
VA11	65.34487	-18.2292	348.1	57.2	354.2	62.1	5.7	81.2	9/9	8.9	67.8	173.0	8.9	6.9	65.0151	-15.2274	68.1	176.1
VA12	65.34489	-18.2289	335.5	49.2	337.4	55.7	4.2	207.5	7/8	6.9	57.3	195.7	5.9	4.2	65.01547	-15.2299	57.6	199.0
VAD13	65.34484	-18.2285	330.3	74.6	339.5	80.2	3.1	323.5	8/8	8.0	80.6	-62.3	5.9	5.7	65.01662	-15.2394	80.4	-58.4

…continue from previous page…

Site	λ (°N)	φ (°E)	Dec_u (°)	Inc_u (°)	Dec (°)	Inc (°)	α_{95} (°)	k	n/N	R	λ_p (°)	φ_p (°)	d_m (°)	d_p (°)	λ' (°N)	φ' (°E)	λ_p' (°)	φ_p' (°)
VA14	65.34488	-18.2282	58.4	54.4	66.1	52.6	3.2	359.0	7/7	7.0	39.7	77.7	4.4	3.0	65.01709	-15.2426	39.7	80.4
VA15	65.34486	-18.2279	64.3	63.9	74.9	61.4	4.2	332.0	5/6	5.0	44.0	63.2	6.5	5.0	65.01733	-15.2445	43.9	65.9
VA16	65.34485	-18.2277	67.7	62.8	77.4	60.0	4.6	212.2	6/7	6.0	41.5	62.3	7.0	5.3	65.01783	-15.2485	41.5	65.0
VA15-VA16					76.3	60.6	σ=6.2	δ=1.9	2/2		42.6	62.7	4.3	3.3			42.6	65.4
VA17	65.3447	-18.2276	253.0	75.4	229.3	77.1	3.2	364.5	7/8	7.0	45.4	-45.0	5.9	5.5	65.01837	-15.2541	45.2	-41.9
VA18	65.3446	-18.2271	172.4	-50.9	177.5	-55.6	3.5	474.0	5/8	5.0	-60.7	-14.1	5.0	3.6	65.01913	-15.2607	-61.1	-11.1
VA19	65.34479	-18.227	175.8	-61.8	184.5	-66.0	4.5	150.2	8/8	8.0	-72.8	-28.4	7.4	6.1	65.01931	-15.2606	-73.1	-25.6
VA20	65.34476	-18.2269	178.1	-58.0	185.7	-62.1	3.8	248.4	7/8	7.0	-67.8	-29.3	6.0	4.6	65.02031	-15.269	-68.1	-26.4
VA19-VA20					185.1	-64.2	σ=5.9	δ=3.9	2/2		-70.4	-28.9	4.6	3.7			-70.7	-26.1
VA21	65.34449	-18.2265	124.5	-79.6	110.9	-85.4	2.5	562.4	7/8	7.0	-67.1	139.3	5.0	5.0	65.0209	-15.2756	-66.8	142.6
VA22	65.34447	-18.2262	233.6	-74.8	253.3	-72.8	2.8	395.7	8/8	8.0	-56.7	228.4	5.0	4.4	65.02122	-15.2782	-56.6	231.0
VA23	65.34478	-18.2259	208.6	-79.5	241.4	-79.5	6.6	70.9	8/8	7.9	-67.1	213.6	12.6	12.0	65.02178	-15.28	-67.0	215.9
VA24	65.34449	-18.2259	190.9	-61.2	201.0	-64.1	2.5	479.1	8/8	8.0	-67.4	-58.8	4.0	3.2	65.02176	-15.2822	-67.7	-56.3
VA25	65.34446	-18.2257	186.9	-70.8	203.3	-73.8	2.5	487.0	8/8	8.0	-78.1	-92.0	4.5	4.1	65.02233	-15.2869	-78.1	-90.3
VA27	65.34441	-18.2251	233.9	-65.2	246.0	-63.6	3.0	350.1	8/8	8.0	-49.9	248.6	4.7	3.7	65.02304	-15.2927	-49.8	251.2
VA28	65.34436	-18.2249	331.3	51.3	333.8	57.0	8.3	53.8	7/7	6.9	58.4	203.5	12.1	8.8	65.02351	-15.2967	58.6	206.8
VA29	65.34436	-18.2248	304.9	36.9	304.0	42.8	11.2	22.2	9/10	8.6	36.4	230.9	13.8	8.6	65.02419	-15.3023	36.5	234.1
VA30	65.34506	-18.2242	356.6	32.6	359.4	37.0	3.2	301.3	8/8	8.0	45.3	162.6	3.7	2.2	65.02557	-15.3073	45.6	165.5
VA31	65.3454	-18.2237	332.9	63.2	337.6	68.8	3.5	258.3	8/8	8.0	72.7	213.5	5.9	5.0	65.02668	-15.3131	72.8	217.0
VA32	65.3448	-18.2238	321.1	74.0	324.6	80.0	2.7	515.5	7/8	7.0	76.0	-71.2	5.1	4.9	65.02702	-15.3211	75.8	-67.0

…continue from previous page…

Site	λ (°N)	φ (°E)	Dec_u (°)	Inc_u (°)	Dec (°)	Inc (°)	α_{95} (°)	k	n/N	R	λ_p (°)	φ_p (°)	d_m (°)	d_p (°)	λ' (°N)	φ' (°E)	λ_p' (°)	φ_p' (°)
VA33	65.3451	-18.223	47.4	68.5	62.1	67.5	5.6	142.7	6/7	6.0	55.5	66.8	9.4	7.8	65.02869	-15.3316	55.5	69.1
VA34	65.34449	-18.2222	357.6	74.2	16.8	77.9	3.5	377.7	6/9	6.0	83.1	51.7	6.5	6.1	65.03038	-15.35	82.9	52.7
VA35	65.34318	-18.2225	356.0	58.0	3.4	62.3	3.3	282.6	8/8	8.0	68.2	155.2	5.1	4.0	65.02941	-15.3532	68.5	157.9
VA36	65.34273	-18.2227	324.6	58.2	326.7	64.1	2.8	380.6	8/8	8.0	63.5	220.9	4.5	3.6	65.03041	-15.3656	63.7	224.2
VA37	65.34277	-18.2209	99.1	-84.0	26.5	-86.3	8.2	87.5	5/6	5.0	-58.6	155.5	16.3	16.3	65.03844	-15.4304	-58.3	158.3
HS1	65.31492	-18.24	296.9	70.4	291.1	75.1	2.8	557.6	6/8	6.0	60.8	-82.2	5.2	4.7	64.98089	-15.1863	60.6	-78.5
HS3	65.31458	-18.2394	339.2	61.9	343.8	66.4	2.4	520.1	8/8	8.0	71.4	197.1	4.0	3.3	64.98243	-15.2013	71.7	200.6
HS4	65.31474	-18.2377	272.8	84.0	217.4	85.9	3.8	309.7	6/8	6.0	58.5	-27.7	7.6	7.5	64.98327	-15.2052	58.1	-24.6
HS5	65.31494	-18.2377	317.2	61.5	317.7	66.5	5.6	99.0	8/8	7.9	62.6	235.8	9.2	7.6	64.98894	-15.2505	62.8	239.5
HS6	65.31484	-18.2371	334.4	76.2	344.5	80.7	4.0	132.7	11/11	10.9	81.4	-51.7	7.7	7.4	64.99071	-15.2654	81.1	-47.9
HS7	65.31488	-18.2367	328.4	75.3	335.0	80.1	4.3	195.3	7/8	7.0	79.3	-67.3	8.3	7.9	64.99705	-15.3174	79.1	-62.7
HS6-HS7					340.7	80.5	σ=5.9	δ=1.7	2/2		80.7	-58.5	5.4	5.2			80.4	-54.4
HS8	65.31494	-18.2362	336.1	60.7	339.9	65.4	2.0	793.8	8/10	8.0	69.2	202.5	3.2	2.6	64.99753	-15.3204	69.5	206.1
HS9	65.31484	-18.2357	331.3	57.0	333.9	61.8	1.7	1004.0	8/9	8.0	63.4	207.6	2.7	2.1	64.99769	-15.322	63.6	211.0
HS10	65.3149	-18.2352	315.6	61.0	315.7	66.0	2.9	378.2	8/8	8.0	61.3	237.2	4.7	3.8	64.99792	-15.323	61.4	240.7
HS11	65.31491	-18.2351	333.1	69.1	338.3	73.8	1.9	849.6	8/8	8.0	78.7	232.9	3.4	3.1	64.99844	-15.3271	78.8	237.4
HS12	65.31493	-18.2349	338.1	63.4	342.9	67.9	2.2	655.4	8/8	8.0	73.1	201.5	3.6	3.0	64.9993	-15.334	73.4	205.0
HS13	65.31483	-18.2344	336.7	68.5	342.7	73.1	2.8	347.2	9/9	9.0	79.6	220.5	4.9	4.4	65.00394	-15.3731	79.8	224.9
HS14	65.31483	-18.2344	345.3	55.6	349.5	59.9	3.4	266.3	8/8	8.0	64.7	180.6	5.1	3.9	65.00462	-15.3788	65.0	183.7
HS15	65.31483	-18.2344	342.2	64.8	348.1	69.1	2.2	634.8	8/8	8.0	76.0	192.7	3.7	3.2	64.96015	-15.0111	76.3	196.8
HSB15	65.31484	-18.2331	342.8	65.4	349.0	69.7	2.3	496.4	9/9	9.0	77.0	192.0	4.0	3.4	65.00565	-15.386	77.2	195.5
HS15-HSB15					348.6	69.4	σ=3.2	δ=0.7	2/2		76.5	192.3	2.6	2.2			76.7	195.8

…continue from previous page…

Site	λ (°N)	φ (°E)	Dec$_u$ (°)	Inc$_u$ (°)	Dec (°)	Inc (°)	α_{95} (°)	k	n/N	R	λ_p (°)	φ_p (°)	d$_m$ (°)	d$_p$ (°)	λ' (°N)	φ' (°E)	$\lambda_p{}'$ (°)	$\varphi_p{}'$ (°)
HS16	65.31484	-18.2331	138.7	-67.3	139.7	-72.3	4.3	200.8	7/7	7.0	-69.6	68.3	7.6	6.7	65.00649	-15.3931	-69.6	72.0
HS17	65.31483	-18.2321	132.2	-60.5	125.6	-65.1	12.9	51.8	4/8	3.9	-59.1	60.7	10.6	8.6	65.00716	-15.3978	-59.2	64.1
HSB18	65.31487	-18.2311	147.5	-69.0	151.2	-73.8	4.0	143.5	10/10	9.9	-75.8	62.9	7.3	6.6	65.00881	-15.4103	-75.9	66.7
HSJ18	65.31486	-18.2318	153.6	-64.6	157.7	-69.3	8.8	28.1	11/11	10.6	-73.3	34.5	14.9	12.7			-73.5	38.2
HS19	65.3149	-18.2306	137.0	-55.5	137.3	-60.5	3.8	181.0	9/9	9.0	-56.2	48.0	5.8	4.4	65.01095	-15.4274	-56.4	51.2
HS20	65.31481	-18.2293	135.9	-57.6	136.0	-62.6	8.2	47.0	8/8	7.9	-57.9	51.9	12.8	10.0	65.01119	-15.429	-58.0	55.2
HS19-HS20					136.7	-61.5	σ=9.0	δ=2.2	2/2		-57.0	49.8	6.2	4.8			-57.2	53.0
HS21	65.31481	-18.2293	92.7	-67.3	83.1	-70.7	5.0	177.9	6/8	6.0	-45.7	107.2	8.7	7.6	65.01271	-15.4417	-45.5	110.2
HS22	65.31492	-18.2278	114.8	-66.3	109.8	-70.3	5.2	137.5	7/8	6.9	-55.9	89.2	8.0	6.9	65.01434	-15.453	-55.9	92.5
HS23	65.31498	-18.2265	74.7	-69.0	62.0	-71.0	8.7	111.4	4/8	4.0	-39.6	121.2	15.2	13.3	65.01642	-15.4687	-39.4	124.2
HS24	65.31525	-18.2231	339.5	80.4	1.7	84.5	8.3	220.4	3/3	3.0	76.1	-16.9	16.4	16.2	65.02207	-15.5106	75.9	-14.2
GS1	65.27658	-18.2331	28.6	66.0	37.6	66.9	1.2	1973.1	8/8	8.0	64.9	92.5	2.1	1.7	65.04531	-16.0557	65.1	94.1
GSA2	65.27658	-18.2331	27.3	66.1	36.3	67.0	5.1	139.5	7/8	7.0	65.6	93.8	8.5	7.0	65.04768	-16.0764	65.7	95.5
GSB2	65.27651	-18.2314	154.8	-82.9	176.8	-86.4	3.0	353.4	8/8	8.0	-72.5	160.4	5.9	5.8	65.04761	-16.0747	-72.2	162.6
GS3	65.27651	-18.2314	215.5	-87.4	279.5	-85.6	3.5	303.5	7/8	7.0	-62.5	180.7	6.9	6.8	65.04761	-16.0747	-62.3	182.8
GR1	65.26729	-18.2301	153.3	-49.0	154.9	-52.8	3.6	185.7	10/10	10.0	-54.7	19.6	4.9	3.4	65.03944	-16.0834	-54.9	21.9
GR2	65.26769	-18.2296	147.8	-30.7	148.4	-34.6	8.3	54.1	7/7	6.9	-39.3	21.5	9.5	5.5	65.04069	-16.0903	-39.4	23.8
GR3	65.26798	-18.2295	181.3	-36.9	183.6	-39.6	4.7	163.3	7/8	7.0	-47.1	-23.1	5.7	3.4	65.04145	-16.0942	-47.4	-21.0
GR4	65.26822	-18.2291	170.8	-50.6	173.9	-53.8	1.9	962.1	7/7	7.0	-58.8	-8.5	2.7	1.9	65.04281	-16.1035	-59.1	-6.3
GR5	65.26856	-18.2292	183.6	-70.1	193.1	-72.5	3.2	364.4	7/7	7.0	-80.2	-63.7	5.6	5.0	65.0442	-16.1128	-80.4	-62.8

…continue from previous page…

Site	λ (°N)	φ (°E)	Dec$_u$ (°)	Inc$_u$ (°)	Dec (°)	Inc (°)	α_{95} (°)	k	n/N	R	λ_p (°)	φ_p (°)	d$_m$ (°)	d$_p$ (°)	λ' (°N)	φ' (°E)	λ_p' (°)	φ_p' (°)
GR6	65.26831	-18.2278	174.8	-82.5	202.1	-83.8	6.2	94.8	7/8	6.9	-73.9	177.2	11.3	11.1	65.04519	-16.1224	-73.7	179.1
GR7A	65.26851	-18.2282	176.6	-73.7	187.6	-76.4	8.1	131.0	4/4	4.0	-86.6	-94.0	14.9	13.8			-86.6	-95.1
GRB7	65.26774	-18.2278	167.9	-80.5	187.3	-83.5	6.2	152.2	5/5	5.0	-77.9	169.4	12.2	12.0	65.00275	-15.7593	-77.6	171.8
GR6-GRB7					191.0	-81.7	3.0	294.5	3/3		-79.0	179.0	6.8	6.7			-80.5	183.1
GRC7	65.26774	-18.2278	154.4	-70.6	159.1	-74.4	3.6	276.1	7/7	7.0	-79.6	55.9	6.6	6.0	65.04633	-16.1374	-79.7	59.5
GR8	65.26774	-18.2278	179.7	-71.8	189.8	-74.4	5.4	125.1	7/7	7.0	-83.7	-67.4	9.8	8.9	65.04685	-16.142	-83.9	-67.1
GR9	65.26827	-18.2271	155.8	-66.2	159.6	-69.9	9.1	44.7	7/7	6.9	-74.7	33.0	15.7	13.5	65.04829	-16.1493	-74.8	35.7
GR8-GR9					172.9	-72.7	σ=10.6	δ=10.2	2/2		-82.1	10.1	9.6	8.5			-82.3	12.9
GR10	65.26827	-18.2271	120.1	-81.4	107.9	-85.2	3.6	348.2	6/7	6.0	-66.5	138.4	7.1	7.0	65.04882	-16.1539	-66.3	140.8
GR11	65.26824	-18.2268	121.0	-64.2	118.7	-68.1	3.2	349.3	7/7	7.0	-56.4	77.2	5.4	4.6	65.04977	-16.1622	-56.5	79.6
GR12	65.26822	-18.2265	162.3	-46.4	164.4	-49.9	3.9	240.3	7/7	7.0	-54.1	5.0	5.2	3.5	65.05028	-16.1665	-54.3	7.2
GR13	65.26832	-18.2263	127.8	-70.4	126.0	-74.3	3.5	303.7	7/7	7.0	-65.8	86.4	6.3	5.7	65.05103	-16.1721	-65.8	88.9
GR14	65.26835	-18.2263	160.8	-77.8	172.2	-81.3	4.3	201.8	7/7	7.0	-81.9	145.3	8.2	8.0	65.05138	-16.175	-81.6	148.0
GR15	65.26852	-18.2264	212.3	-66.2	221.4	-66.8	9.5	41.0	7/7	6.9	-63.4	-92.0	15.8	13.0	65.05208	-16.1797	-63.4	-90.3
GR16	65.26852	-18.2264	245.1	-80.8	264.5	-78.8	3.3	338.9	7/7	7.0	-59.2	207.6	6.2	5.9	65.0526	-16.1843	-59.1	209.3
GR17	65.26852	-18.2259	147.4	-65.1	149.7	-68.9	3.0	401.2	7/7	7.0	-70.0	46.3	5.1	4.4	65.05312	-16.1884	-70.1	48.7
GR18	65.26823	-18.2254	213.6	-78.3	228.2	-78.5	3.5	246.1	8/8	8.0	-71.2	222.0	6.7	6.3	65.05342	-16.1931	-71.0	223.7
GR19	65.26844	-18.2252	177.2	-61.5	181.2	-63.7	6.0	161.1	5/5	5.0	-70.0	-20.7	9.6	7.6	65.05395	-16.1958	-70.3	-18.7
GR20	65.26855	-18.2249	324.3	64.7	325.5	67.7	5.0	123.1	8/8	7.9	67.0	228.9	8.4	7.0	65.05556	-16.2087	67.1	231.4
GR21	65.26848	-18.2245	25.8	71.9	34.9	72.7	3.9	127.5	12/12	11.9	72.2	79.2	6.9	6.1	65.05647	-16.217	72.3	80.4
GR22	65.26832	-18.224	25.4	66.2	32.1	67.0	1.5	1909.8	6/8	6.0	67.2	99.3	2.5	2.1	65.05677	-16.2205	67.3	100.8

…continue from previous page…

Site	λ (°N)	φ (°E)	Dec$_u$ (°)	Inc$_u$ (°)	Dec (°)	Inc (°)	α_{95} (°)	k	n/N	R	λ_p (°)	φ_p (°)	d$_m$ (°)	d$_p$ (°)	λ' (°N)	φ' (°E)	λ_p' (°)	φ_p' (°)
GRA23	65.26832	-18.224	5.2	71.1	12.6	72.8	5.8	173.8	5/5	5.0	80.9	115.5	10.4	9.2	65.05716	-16.2239	81.0	116.8
GRB23	65.26857	-18.2237	10.3	65.6	16.2	67.2	1.9	1569.8	5/5	5.0	72.5	125.1	3.2	2.7	65.05773	-16.2265	72.7	126.7
GR24	65.26857	-18.2237	5.9	64.1	11.1	65.9	1.9	705.7	9/9	9.0	71.9	137.5	3.2	2.6	65.05819	-16.2305	72.1	139.1
GRA23 -GR24					13.3	68.6	3.0	455.4	3/3		74.5	130.5	3.4	2.8			75.2	130.0
GRA25	65.26869	-18.2235	354.0	60.4	357.6	62.7	4.1	353.0	5/5	5.0	68.7	166.5	6.4	5.0	65.0589	-16.2355	69.0	168.6
GRB25	65.26864	-18.2231	350.4	67.3	355.1	69.6	2.5	575.0	7/8	7.0	77.9	175.9	4.3	3.7	65.05924	-16.2386	78.0	178.0
GR26	65.26867	-18.2227	316.9	83.9	318.6	86.9	4.9	128.9	8/10	7.9	69.6	-30.1	9.7	9.7	65.06017	-16.2463	69.3	-27.9
GR27	65.26866	-18.2224	11.3	63.3	16.5	64.8	3.2	297.6	8/9	8.0	69.5	128.0	5.2	4.2	65.06121	-16.2551	69.6	129.8
GR28	65.26898	-18.2223	21.6	67.8	28.7	68.8	5.9	77.3	9/9	8.9	70.5	99.9	10.0	8.5	65.06269	-16.2654	70.6	101.4
GR27-GR28					22.4	67.0	σ=6.7	δ=6.2	2/2		70.5	114.1	5.8	4.8			70.7	115.6
GR29	65.26879	-18.2214	20.2	85.2	57.6	85.5	3.0	515.6	6/7	6.0	68.7	2.8	5.9	5.8	65.06374	-16.2755	68.6	4.8
GR30	65.26868	-18.2211	24.7	82.7	48.8	83.1	4.4	185.2	7/8	7.0	71.4	15.1	8.7	8.5	65.06441	-16.2821	71.2	17.0
GR29-GR30					52.0	84.3	σ=5.3	δ=2.5	2/2		70.2	8.9	5.1	5.1			70.1	10.6
GR31	65.26875	-18.2208	68.8	75.5	78.5	74.1	4.3	324.3	5/9	5.0	56.1	42.4	7.7	6.9	65.06494	-16.2858	56.0	44.0
GR32	65.2688	-18.2206	171.7	-43.0	173.4	-45.4	5.2	86.9	10/10	9.9	-51.4	-8.8	6.6	4.2	65.06823	-16.3144	-51.6	-6.8
GR33	65.26892	-18.2202	179.2	-80.8	195.5	-82.6	17.6	7.7	11/11	9.7	-78.6	181.6	34.4	33.6	65.06913	-16.3209	-78.5	183.3
GRA33	65.26877	-18.219	207.4	-42.9	207.1	-43.3	5.0	105.7	9/11	8.92	-45.9	-58.8	5.6	3.5	65.07053	-16.3336	-46.1	-57.1
GRB33	65.26893	-18.2185	192.5	-53.2	196.1	-54.8	6.8	79.0	7/8	6.9	-58.5	-43.9	9.7	6.8	65.07198	-16.3446	-58.7	-42.2
GR34	65.26891	-18.2182	168.4	-57.0	171.2	-59.5	4.0	196.3	8/9	8.0	-64.5	-2.4	6.0	4.5	65.07235	-16.3478	-64.7	-0.5

…continue from previous page…

Site	λ (°N)	φ (°E)	Dec$_u$ (°)	Inc$_u$ (°)	Dec (°)	Inc (°)	α_{95} (°)	k	n/N	R	λ_p (°)	φ_p (°)	d$_m$ (°)	d$_p$ (°)	λ' (°N)	φ' (°E)	λ_p' (°)	φ_p' (°)
LF0	65.23139	-18.2402	336.0	57.1	337.9	59.9	3.0	398.2	7/8	7.0	62.5	199.9	4.6	3.5	65.02057	-16.2458	62.7	202.1
LF1	65.23111	-18.2409	340.1	64.9	343.1	67.6	2.1	680.5	8/8	8.0	72.8	200.5	3.5	3.0	65.02173	-16.2592	73.0	203.0
LF2	65.23097	-18.2413	10.1	70.9	17.9	72.5	3.9	291.1	6/8	6.0	78.7	105.0	7.0	6.2	65.02355	-16.2768	78.8	105.9
LF3	65.23092	-18.2413	41.5	72.2	50.8	72.2	4.8	136.6	8/8	7.9	65.1	66.0	8.4	7.4	65.02713	-16.3091	65.1	67.5
LF4	65.23068	-18.2414	357.1	61.3	1.1	63.4	4.7	138.8	8/8	7.9	69.7	159.5	7.5	5.9	65.02741	-16.3138	69.9	161.4
LF5	65.23051	-18.2417	310.5	69.0	309.8	72.0	4.2	212.0	7/8	7.0	65.1	-103.5	7.3	6.5	65.0277	-16.3182	65.1	-101.2
LF6	65.23044	-18.2421	304.2	78.4	300.6	81.3	4.2	205.7	7/8	7.0	68.5	-61.5	8.2	7.9	65.02821	-16.3237	68.4	-59.5
LF7	65.23037	-18.2422	350.0	68.6	355.0	70.9	2.7	617.1	6/8	6.0	79.8	178.1	4.7	4.1	65.02852	-16.3273	80.0	180.2
LF8	65.23017	-18.2436	181.1	-55.0	184.4	-57.0	6.3	78.6	8/8	7.9	-62.3	-25.8	9.2	6.7	65.03324	-16.3725	-62.4	-23.9
LF9	65.22996	-18.2439	222.3	-78.0	236.3	-77.8	3.5	364.6	6/8	6.0	-67.8	222.7	6.6	6.2	65.03368	-16.3785	-67.7	224.0
TOM3	65.22588	-18.2337	346.6	57.1	349.3	59.6	5.2	116.3	8/8	7.9	64.5	180.9	7.8	5.8	65.02715	-16.3467	64.7	182.9
TOM2	65.22567	-18.2341	168.1	-53.1	170.4	-55.6	7.5	65.7	7/8	6.9	-60.4	-2.5	10.7	7.7	65.02875	-16.3632	-60.5	-0.5
TOM1	65.22549	-18.2343	216.4	-79.2	232.2	-79.3	3.5	195.3	10/10	10.0	-70.0	217.0	6.6	6.3	65.02921	-16.3692	-70.0	218.2
TO0	65.22509	-18.2349	196.8	-48.0	199.9	-49.4	9.4	51.8	6/8	5.9	-52.9	-47.4	12.5	8.3	65.03024	-16.3824	-53.1	-45.7
TO1	65.22408	-18.2327	173.3	-51.5	175.8	-53.8	19.2	171.1	2/10	2.0	-59.0	-11.6	26.9	18.8	65.03065	-16.393	-59.2	-9.6
TO2	65.22408	-18.2327	123.2	-71.2	121.1	-74.1	4.7	208.3	6/8	6.0	-63.7	89.1	8.4	7.6	65.03233	-16.408	-63.6	91.3
TO3	65.22355	-18.234	153.1	-75.9	157.7	-78.7	2.9	678.8	5/8	5.0	-80.7	101.0	5.6	5.3	65.0327	-16.4174	-80.7	103.4
TO4	65.22355	-18.234	146.1	-73.4	148.5	-76.4	4.4	162.4	8/8	8.0	-76.6	81.6	8.1	7.5	65.03334	-16.4231	-76.6	84.3
TO3-TO4					151.7	-77.3	σ=5.3	δ=3.1	2/2		-78.3	87.1	5.2	4.9			-78.3	89.8
TO5	65.22344	-18.2341	164.1	-85.0	195.9	-87.2	5.7	182.8	5/8	5.0	-70.5	166.3	11.3	11.3	65.03374	-16.4278	-70.4	168.1
TO6	65.22337	-18.2342	173.5	-82.4	193.2	-84.5	3.3	341.2	7/8	7.0	-75.7	171.9	6.5	6.4	65.03419	-16.4326	-75.4	173.5
TO7	65.22322	-18.2343	184.1	-84.1	213.9	-85.4	2.4	399.4	10/10	10.0	-72.1	178.3	4.8	4.8	65.03533	-16.4442	-71.9	180.2
TO5-TO7					201.1	-85.8	3.0	2479.0	3/3		-72.9	173.5	3.6	3.5			-72.6	173.6

…continue from previous page…

Site	λ (°N)	φ (°E)	Dec$_u$ (°)	Inc$_u$ (°)	Dec (°)	Inc (°)	α_{95} (°)	k	n/N	R	λ_p (°)	φ_p (°)	d_m (°)	d_p (°)	λ' (°N)	φ' (°E)	λ_p' (°)	φ_p' (°)
TO8	65.22242	-18.2327	153.4	-58.9	155.1	-61.7	5.0	93.4	10/10	9.9	-63.7	25.9	7.8	6.0	65.03478	-16.445	-63.8	27.9
TO9	65.22237	-18.2328	149.7	-59.3	151.1	-62.2	3.7	175.4	10/10	9.9	-63.0	32.3	5.7	4.4	65.03525	-16.4497	-63.1	34.4
TO8-TO9					153.1	-62.0	σ=6.2	δ=1.9	2/2		-63.4	29.2	4.5	3.5			-63.5	31.3
TOA10	65.22224	-18.2329	225.0	-63.2	230.9	-63.0	5.1	221.7	5/8	5.0	-55.6	-96.5	8.1	6.4	65.03551	-16.4533	-55.6	-95.0
TOB10	65.22224	-18.2329	219.0	-61.0	224.4	-61.2	5.6	145.2	6/9	6.0	-56.3	-87.3	8.6	6.6	65.03564	-16.4544	-56.4	-85.8
TOA10-TOB10					227.3	-62.1	σ=7.6	δ=3.6	2/2		-56.1	-91.6	5.4	4.2			-56.2	-90.1
TO11	65.22201	-18.2328	357.4	57.0	0.7	59.2	5.9	68.6	10/10	9.9	64.7	160.5	8.8	6.6	65.03618	-16.4612	64.9	162.3
TO12	65.22202	-18.233	350.1	50.4	352.4	52.8	3.2	230.9	10/10	10.0	57.9	173.8	4.4	3.0	65.03895	-16.4862	58.0	175.5
TO13	65.22146	-18.2332	326.0	68.0	327.6	70.9	4.6	127.8	9/9	8.9	71.4	235.0	8.0	6.9	65.03922	-16.494	71.5	237.3
TOA14	65.22072	-18.2319	305.0	74.6	302.6	77.5	6.2	221.6	4/4	4.0	67.2	-79.8	11.6	10.9	65.03976	-16.5042	67.1	-77.7
TOD14	65.22072	-18.2322	40.8	54.0	45.0	54.1	14.2	16.1	8/8	7.6	49.5	98.3	20.0	14.0	65.04066	-16.5126	49.5	99.8
BT1	65.18774	-18.2111	176.8	-69.1	178.6	-69.8	2.4	542.3	8/8	8.0	-78.5	-14.0	4.1	3.5	65.04752	-16.8559	-78.6	-12.7
BT2	65.18843	-18.2129	169.7	-63.8	170.9	-64.6	2.0	790.7	8/8	8.0	-70.6	1.0	3.2	2.5	65.04911	-16.8659	-70.8	2.5
BT3	65.18838	-18.212	116.1	-62.1	115.4	-63.1	4.0	196.1	8/8	8.0	-49.9	73.3	6.2	4.9	65.05463	-16.9165	-49.9	74.8
BT4	65.18855	-18.2117	216.8	-73.6	220.2	-73.7	2.7	413.2	8/8	8.0	-71.0	249.6	4.9	4.4	65.05646	-16.9315	-71.0	250.5
BT5	65.18836	-18.2101	144.6	-77.2	145.4	-78.1	6.6	71.2	8/8	7.9	-76.1	95.7	12.5	11.7	65.06466	-17.0078	-76.0	97.1
BT6	65.18806	-18.2093	4.9	61.7	6.3	62.3	3.8	214.9	8/8	8.0	68.1	149.5	5.9	4.6	65.06794	-17.0404	68.2	150.6
BO1	65.1834	-18.2034	145.7	-76.6	146.5	-77.6	2.3	592.6	8/8	8.0	-76.4	91.4	4.3	4.0	65.0597	-17.0014	-76.3	93.2
BO2	65.1834	-18.2034	134.0	-74.4	133.9	-75.4	2.6	454.1	8/8	8.0	-70.0	85.7	4.8	4.4	65.06179	-17.0209	-69.9	87.0
BO3	65.18364	-18.2033	20.9	67.6	23.2	68.0	2.2	284.8	16/16	16.0	71.5	110.4	3.7	3.1	65.06352	-17.0347	71.6	111.3
BO4	65.18272	-18.2017	16.6	70.3	19.1	70.7	9.7	33.3	8/8	7.8	76.2	110.1	16.9	14.7	65.06499	-17.0554	76.2	110.9
BO3-BO4					21.9	68.9	σ=10.0	δ=3.1	2/2		73.0	110.4	5.4	4.6			73.1	111.3

…continue from previous page…

Site	λ (°N)	φ (°E)	Dec$_u$ (°)	Inc$_u$ (°)	Dec (°)	Inc (°)	α_{95} (°)	k	n/N	R	λ_p (°)	φ_p (°)	d$_m$ (°)	d$_p$ (°)	λ' (°N)	φ' (°E)	λ_p' (°)	φ_p' (°)
BO5	65.18277	-18.2014	353.2	50.4	354.0	51.2	3.1	142.8	16/16	15.9	56.5	171.1	4.2	2.8	65.06921	-17.094	56.6	172.2
BO6	65.17866	-18.1962	318.7	66.7	318.9	67.7	4.4	162.5	8/8	8.0	64.5	237.1	7.3	6.1	65.06673	-17.1043	64.5	238.4
BO7	65.17866	-18.1962	199.5	-69.0	201.9	-69.4	2.0	780.9	8/8	8.0	-73.6	-71.1	3.4	2.9	65.0691	-17.1266	-73.7	-70.2
BO8	65.17894	-18.1952	193.2	-62.1	194.2	-63.5	3.7	263.5	7/8	7.0	-67.3	-46.6	5.7	4.5	65.0719	-17.1493	-67.3	-45.7
BO9	65.17872	-18.1943	195.5	-73.2	198.5	-73.7	2.8	380.8	8/8	8.0	-79.9	-83.9	5.1	4.6	65.07257	-17.1568	-79.9	-83.5
BO10	65.17848	-18.1939	6.2	73.4	8.9	74.0	1.7	1017.4	8/8	8.0	83.5	118.9	3.1	2.8	65.07395	-17.1717	83.6	119.0
BO11	65.1784	-18.1935	3.4	70.3	3.0	71.6	2.1	828.5	7/8	7.0	79.8	143.7	4.7	4.1	65.07727	-17.2033	80.0	144.2
BO10-BO11					7.1	72.5	σ=3.2	δ=3.2	2/2		81.9	134.1	2.8	2.5			81.9	134.7
BO12	65.17854	-18.1928	332.5	72.1	333.5	73.1	3.0	350.1	8/8	8.0	76.1	236.4	5.3	4.7	65.07933	-17.2208	76.1	237.9
BO13	65.17837	-18.1925	1.4	54.0	2.4	54.7	2.9	359.6	8/8	8.0	60.0	157.9	4.1	2.9	65.08062	-17.2345	60.1	158.8
BO14	65.17851	-18.1924	352.7	57.1	353.7	57.9	5.3	160.2	6/6	6.0	63.1	172.8	7.8	5.7	65.08209	-17.2469	63.2	173.7
BO13-BO14					358.8	56.1	σ=6.1	δ=5.8	2/2		61.5	163.8	4.2	3.0			61.6	164.8

5.3 Magnetostratigraphy

Using palaeomagnetic data in Table 5.1, I made site-to-site correlations between adjacent profiles. The Watson's V test (Watson, 1983) was chosen to test if two directional data have the same common mean with 95% confidence level. This test works under the null hypothesis that two mean directions have the same common mean. First, directional data from each lava flow between two adjacent rock units were compared. If two site-mean directions are nearly identical, the directional data at specimen level from two sites were used to calculate the Watson's V value and the critical V value. If the Watson's V value exceeds critical V, the null hypothesis is rejected. Nine correlations were found throughout the valley and are given in Table 5.2 along with Watson's V values and critical V values. These correlations were also considered with lithostratigraphy given in Chapter 3 in order to confirm if two sites have the same types of rocks.

Table 5.2: Site-to-site correlations, Watson's V and V critical values from Watson's V test (Watson, 1983). If the Watson's V exceeds V critical, the null hypothesis that two mean directions have the same common mean with 95% confidence will be rejected.

Site correlation	Watson's V	V critical
VA7-HS5	1.0	7.1
VAD13-HS7	0.2	6.5
VA31-HS8	6.2	6.7
GRA23-LF2	3.1	7.4
GRA25-LF4	4.2	6.8
GRB33-LF8	3.2	6.8
LF8-TOM2	2.7	7.0
LF9-TOM1	0.9	6.4
BT5-BO1	0.1	6.9

Next, the correlations in Table 5.2 and palaeomagnetic direction data in Table 5.1 were used to construct new composite sections and magnetic polarity columns in Figure 5.6-5.8. The altitude of the bottom of VA1 was normalised to zero and the cumulative heights were calculated for the lava sections. Here I grouped rock units into three groups: VA-GS, GR-TO and BT-BO according to the major hiatuses between these groups (Chapter 3). Figure 5.6 shows magnetic polarity columns along with sections of VA-GS. Here, I correlated three pairs of sites: VA7-HS5, VAD13-HS7 and VA31-HS8 between VA and HS units. These correlations introduce two major hiatuses on the magnetic polarity column in HS section: a hiatus between HS5 and HS6, and a hiatus between HS7 and HS8. These hiatuses are successfully recorded in aphyric basalt in the VA section (VA8-VA12 and VA14-VA30).

This suggests that the eruption rate at VA is higher than the eruption rate at HS because of the rapid build-up of a local lava shield between VA8 and VA30. This lava shield (and local topographic high) was later gradually buried by porphyritic basalt, olivine basalt and aphyric basalt. Finally, the top of VA and HS was buried by massive rhyolite flows originating in the Torfufell central volcano. This rhyolite flow also buried toward the bottom of GS which is nearer the Torfufell central volcano (Hardarson et al., 2008). A thickness of the rhyolite flows above HS section is approximately 300 m, yielding 760 m altitude above sea level (see the stratigraphic log in Chapter 3). Taking a tectonic tilt ~6° in to account, the top of HS should be correlated to GS1 at an altitude of 320 m above sea level. However, the fieldwork team did not collect palaeomagnetic cores on top of HS to confirm this correlation because the site locations above HS are hard to sample. Only three cores were collected from HS24 at altitude of about 526 m above sea level. Therefore, sites above HS24 are classified as a hiatus and the top HS24 is correlated to the bottom of GS1 (Figure 5.6 and 5.10). The GS location is on the flank of a complex central volcano system that produces a lava dome with a rhyolite core surrounded by obsidian. The stratigraphic log for GSB2 and GS3 has not been made in the field because of very poor exposure on this grassy slope. Normal polarity magnetisations are recorded in GS1 and GSA2 while reverse polarity magnetisations are recorded in GSA2 and GS3.

Figure 5.7 depicts magnetic polarity columns along with sections from GR to TO. The reverse polarity magnetisations are recorded in lower section of GR. Therefore, I correlate top of GSA2 to bottom of GR1. The time gap of ~1.3 Myr between HS24 (7.12 ± 0.10 Ma) and GR5 (5.73 ± 0.14 Ma) (Chapter 4) suggests that the volcanism waned after the silicic volcanism in the Torfufell system had ended. The central volcano was onlapped and later buried by three lava groups: GR1-GR5, GR7-GR20 and GR21-TO. The sediment between GR5 and GR7 is possibly from erosion products from remnants of the Torfufell central volcano. The site-to-site correlation between GR and LF was made for three pairs of flows: GRA23-LF2, GRA25-LF4 and GRB33-LF8 while two correlations between LF and TO: LF8-TOM2 and LF9-TOM1 were made. The palaeomagnetic measurements were not made for TO15 and TO16 as we did not successfully drill these sites due to the hardness of flows and the time constrain in the field. The numerical ages of TOM3 (4.84 ± 0.12 Ma) and TO15 (4.68 ± 0.13 Ma) suggests that there were rapid eruptions throughout 0.16 Myr.

Figure 5.8 shows magnetic polarity columns and the sections of BT and BO. Because there are no palaeodirection data from TO15 and TO16, the correlation between top of TO and bottom of BT was made based on lithostratigraphy, altitudes of the site above sea level and an assumed tectonic tilt of ~1° on top of the valley. Tectonic tilt and distance between TO and BT do not allow for the existence of any significant succession of (unmapped) strata in between top-TO and base-BT. Porphyritic basalt found in TO16 was correlated to porphyritic basalt found in BT3 and BT4. BT1, BT2 and a major hiatus between BT2 and BT3 was correlated to a hiatus between TO15 and TO16. The numerical ages of TO15 and BT2 (3.55 ± 0.10 Ma) indicate a long-time gap of c. 1.1 Myr between TO15 and base of BT. Site-to-site correlation between BT and BO was made for BT5-BO1 (Figure 5.8).

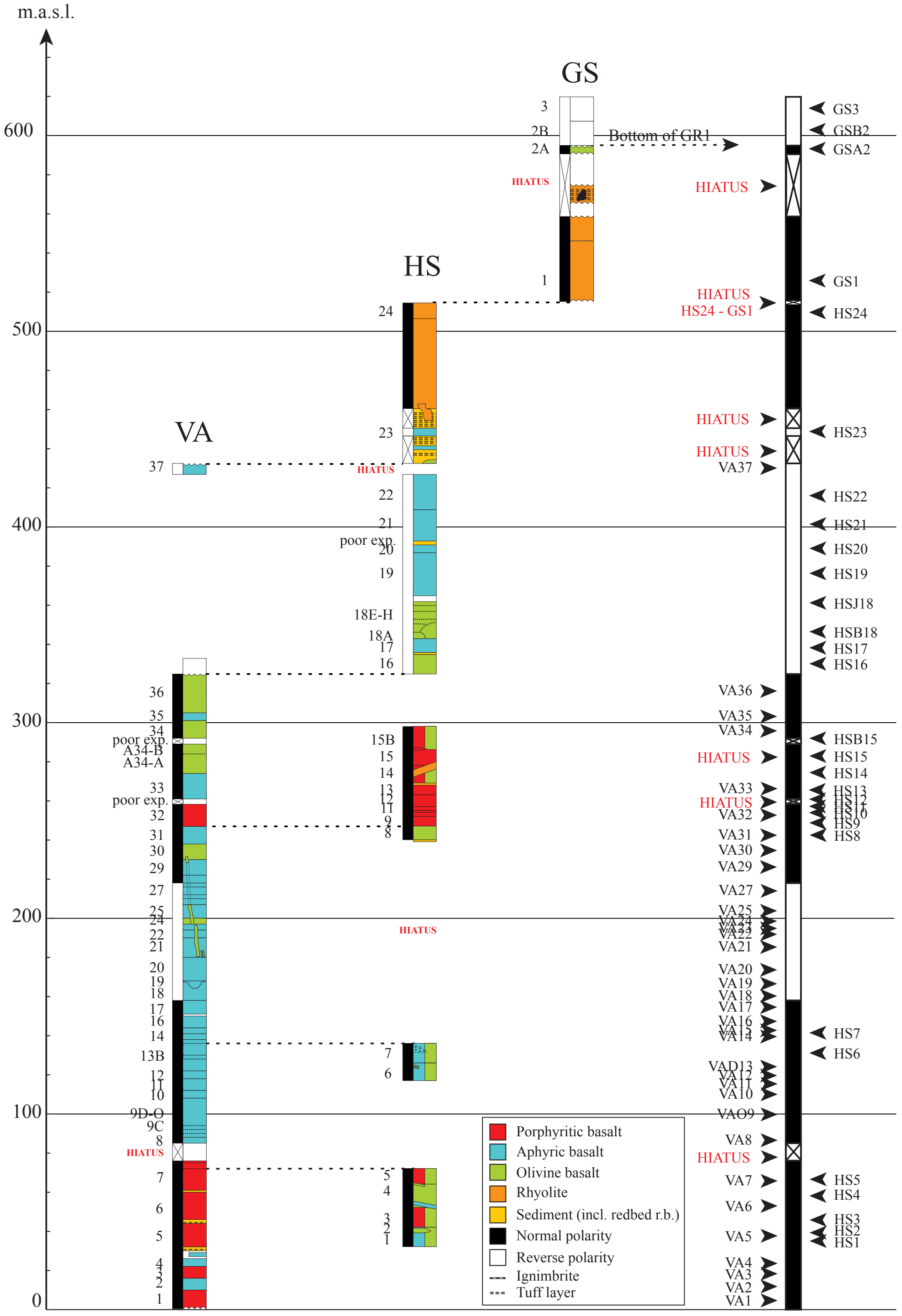

Figure 5.6: The composite height of VA, HS and GS sections. Site-to-site correlations are given as dash lines with labels on. Colours on the sections represent types of rocks recorded during stratigraphic mapping in the field by Dr Morten Riishuus. The polarity columns are given along with the sections with black and white representing normal and reverse polarity magnetisations.

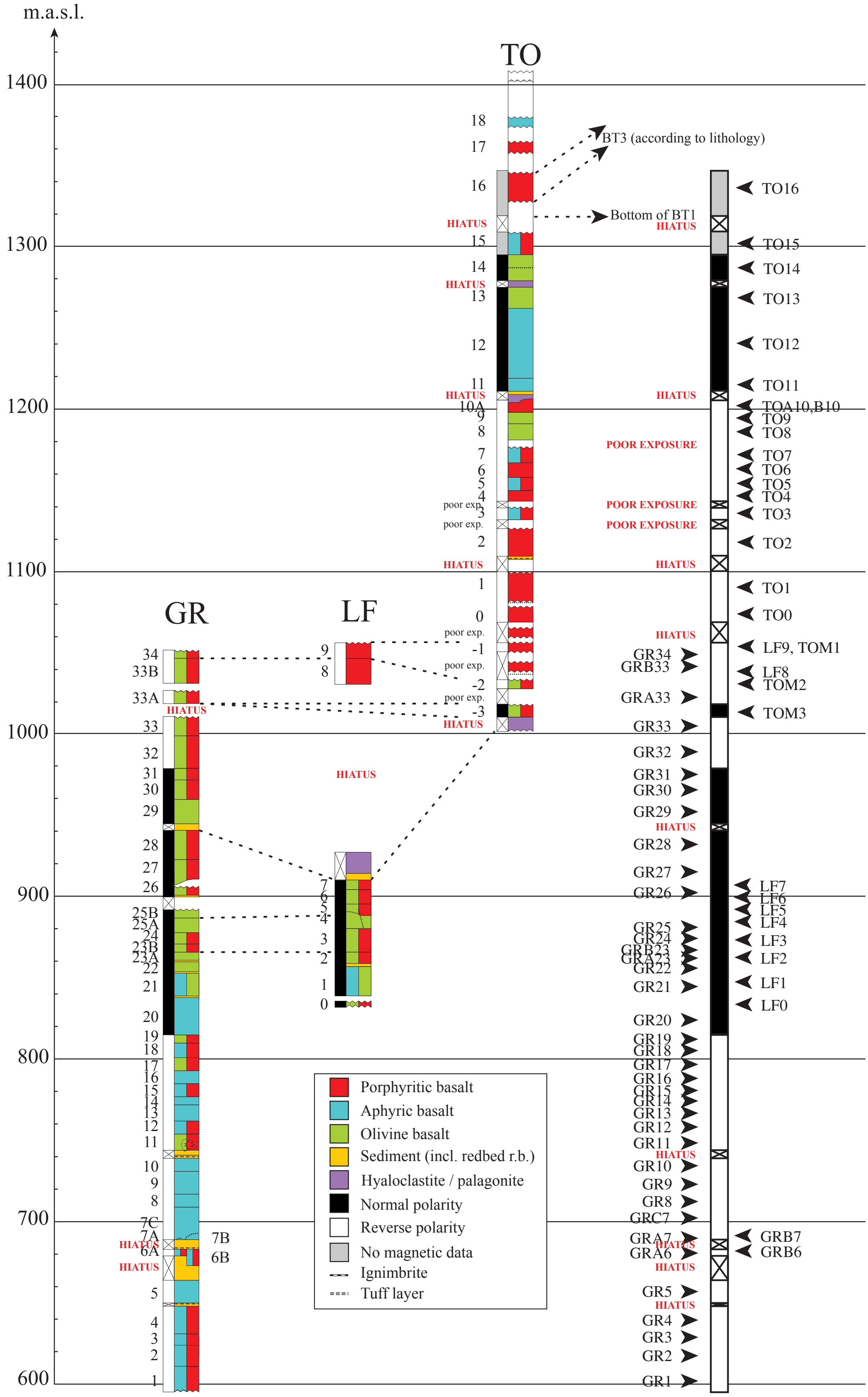

Figure 5.7: The composite height of GR, LF and TO sections. Site-to-site correlations are given as dash lines with labels on. Colours on the sections represent types of rocks recorded during stratigraphic mapping in the field by Dr Morten Riishuus. The polarity columns are given along with the sections with black and white representing normal and reverse polarity magnetisations. Grey colour on the polarity column represents a site without palaeodirection data.

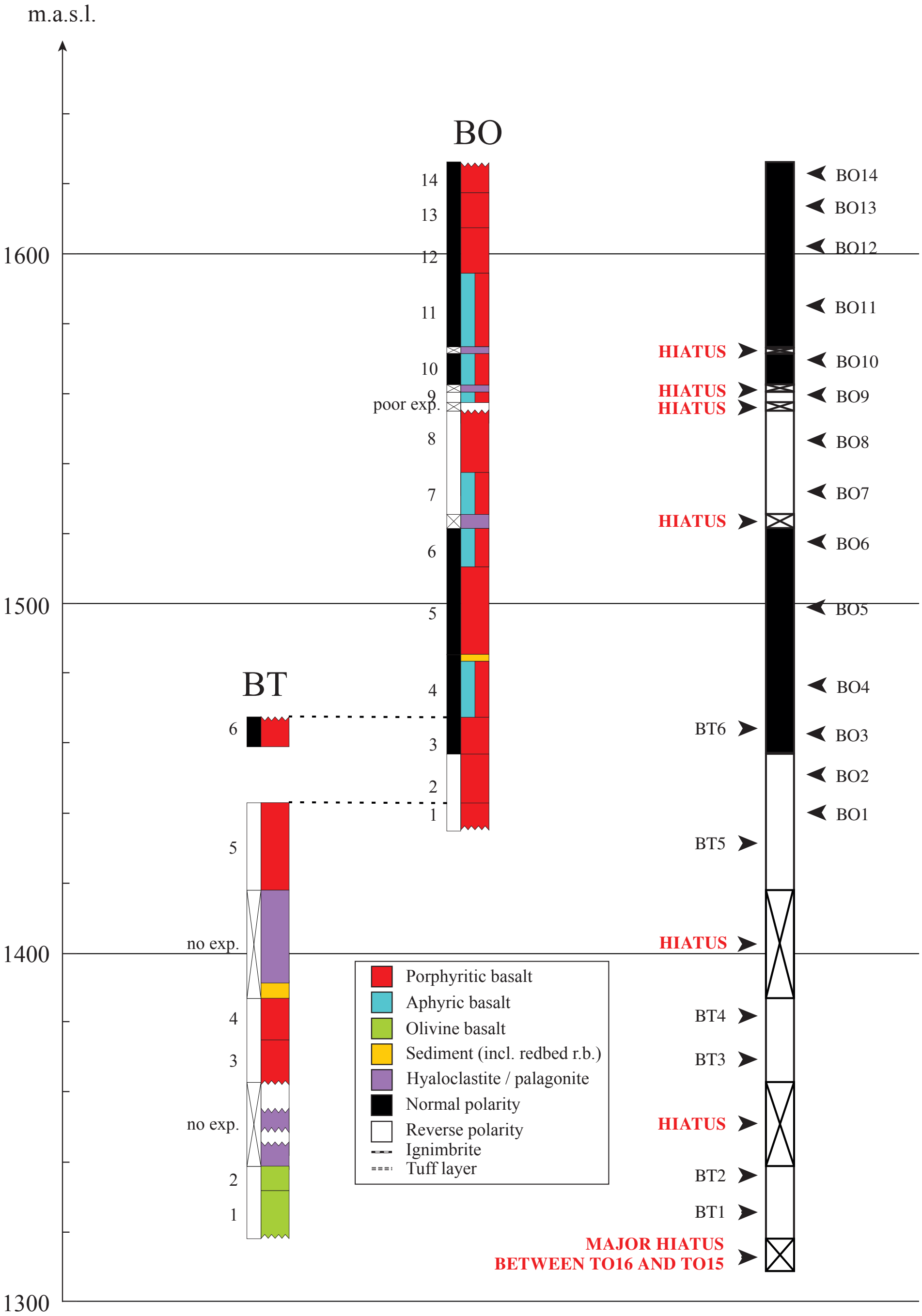

Figure 5.8: The composite height of BT and BO sections. Site-to-site correlations are given as dash lines with labels on. Colours on the sections represent types of rocks recorded during stratigraphic mapping in the field by Dr Morten Riishuus. The polarity columns are given along with the sections with black and white representing normal and reverse polarity magnetisations.

A composite magnetostratigraphic column (Figure 5.10) was made by combining eight individual polarity columns in Figure 5.6-5.8. This column depicts a successive 1,600 m lava pile spanning from ~2.6-8.5 Ma in Eyjafjardardalur valley. There are two major hiatuses and four minor hiatuses recorded in the composite column. The small hiatuses were also marked as “Hiatus” along the composite column. The hiatuses typically coincide with sedimentary horizons, lack of exposure and/or marked jumps toward younger absolute radiometric ages. Here I divide the composite column into lower, middle and upper sections according to two major hiatuses. The lower section covers from 0 to 560 m in elevation, whilst the middle column covers from approximately 590 to 1310 m in height. Heights above 1320 m are classified as the upper section. In an attempt to correlate the composite column with the geomagnetic polarity time scale (GPTS) (Ogg, 2012), the linear regression age model was constructed under the assumption that the volcanic build-up rate and sediment accumulation rate are fairly constant within each section (lower/middle/upper) (Figure 5.9) (McDougall et al., 1976; McDougall et al., 1977; Watkins and Walker, 1977; Døssing et al., 2016). Prior to the regression age model, 15 numerical ages (Chapter 4) were plotted against the cumulative height (Figure 5.9a). Then, the linear interpolation lines were calculated for three sections (Figure 5.9b). After that, the cumulative height of each lava flow boundary was used to calculate the interpolated ages using the regression model (Figure 5.9c).

The interpolated ages of the composite column agree well with the GPTS (Figure 5.10). Lower section consists of four normal polarity intervals, three reverse polarity intervals, two minor hiatuses and one major hiatus. These intervals cover chron C4 and C3B spanning 8.06 to 7.15 Ma. There is one missing subchron: C3Br.1n which is thought to have occurred during Minor Hiatus 1. The boundary between C3Br.1r and C3Bn occurred during Minor Hiatus 2. The major hiatus that marks the top of lower section represents a significant time interval covering almost the entire chron C3A, spanning from 7.15 to 6.05 Ma.

With regards to middle section, the time of this section starts from ca. 6.05 Ma toward 4.5 Ma, recording a 1.55 Myr time interval (Figure 5.10). This section includes three normal and three reverse polarity intervals. These intervals are C3An.1n, C3r, C3n.4n (Thvera), C3n.3r, C3n.3n (Sidufjall), C3n.2r and C3n.2n (Nunivak). The earliest occurrence of palagonite tuff, hyaloclastite and tillite in Eyjafjardardalur between LF7 and LF8 must reflect a local/ephemeral glaciation and thereby marks the onset of global climate cooling in the early Pliocene. The major hiatus on top of the middle section shows the time interval from 4.5 Ma until nearly the end of Gilbert (~3.60 Ma).

The beginning of the upper section starts at around 3.66 Ma which is nearly the end of chron C2Ar (Figure 5.10). This section covers the whole Gauss interval. The palaeomagnetic direction records only two normal and two reverse polarity intervals while the Gauss interval includes three normal and two reverse polarity subchrons. The missing interval is C2An.3n, which coincides with predicted ages of Minor Hiatus 3. The C2An.2r (Mammoth) interval is considered as missing and would be recorded in sediment of Minor Hiatus 4. The palagonite tuff and tillite deposits associated with Minor Hiatus 3 and Minor Hiatus 4 at c. 3.5-3.3 Ma correlate well with the climate cooling period that preceded the Mid Pliocene warm period at c. 3.2 Ma. The interpolated age of Hiatus 11 coincides well with boundary between C2An.1r (Kaena) and C2An.1n. Both numerical age (2.56 ± 0.13 Ma) and interpolated age (2.61 ± 0.13 Ma) show that the time of the upper section ends at the boundary between Pliocene and Pleistocene. The three palagonite tuff deposits (hiatuses 10-12) between 3.1-2.6 Ma reflect the global cooling toward the Pliocene-Pleistocene boundary and onset of the northern hemisphere glaciation. The upper section covers the time interval of approximately one million years.

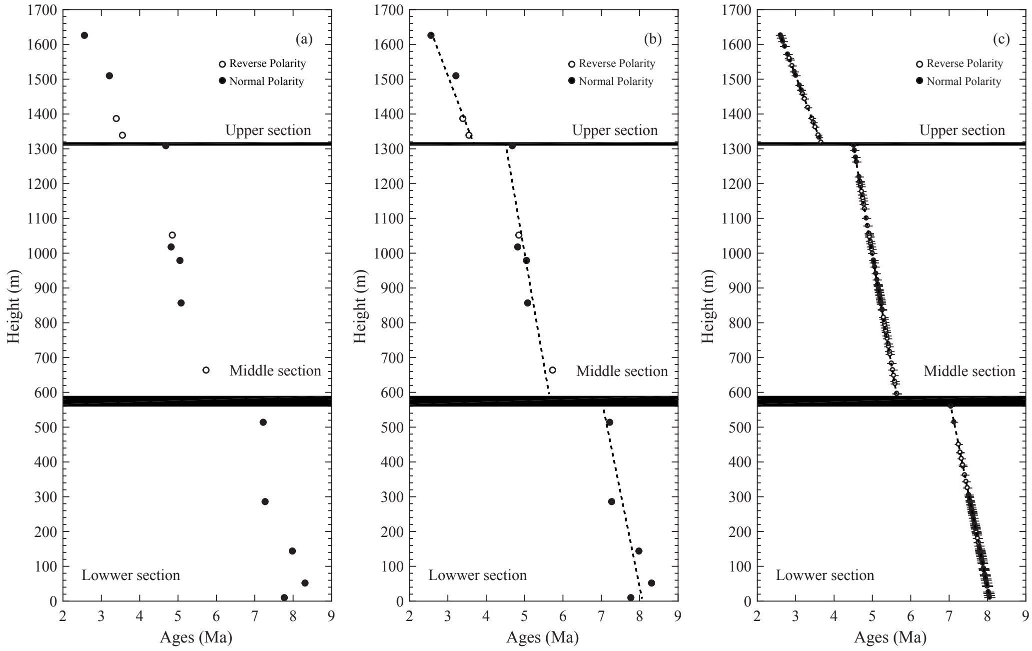

Figure 5.9: (a) numerical ages plotted against cumulative height of lava sections. The lower, middle and upper sections are separated by two major hiatuses (marked black areas). (b) linear regression lines (dash lines) for each lava section. (c) interpolated ages for individual lava flow with the error bar calculated using regression model in (b). Black and open circles represent sites recoded normal and reverse polarity magnetisations.

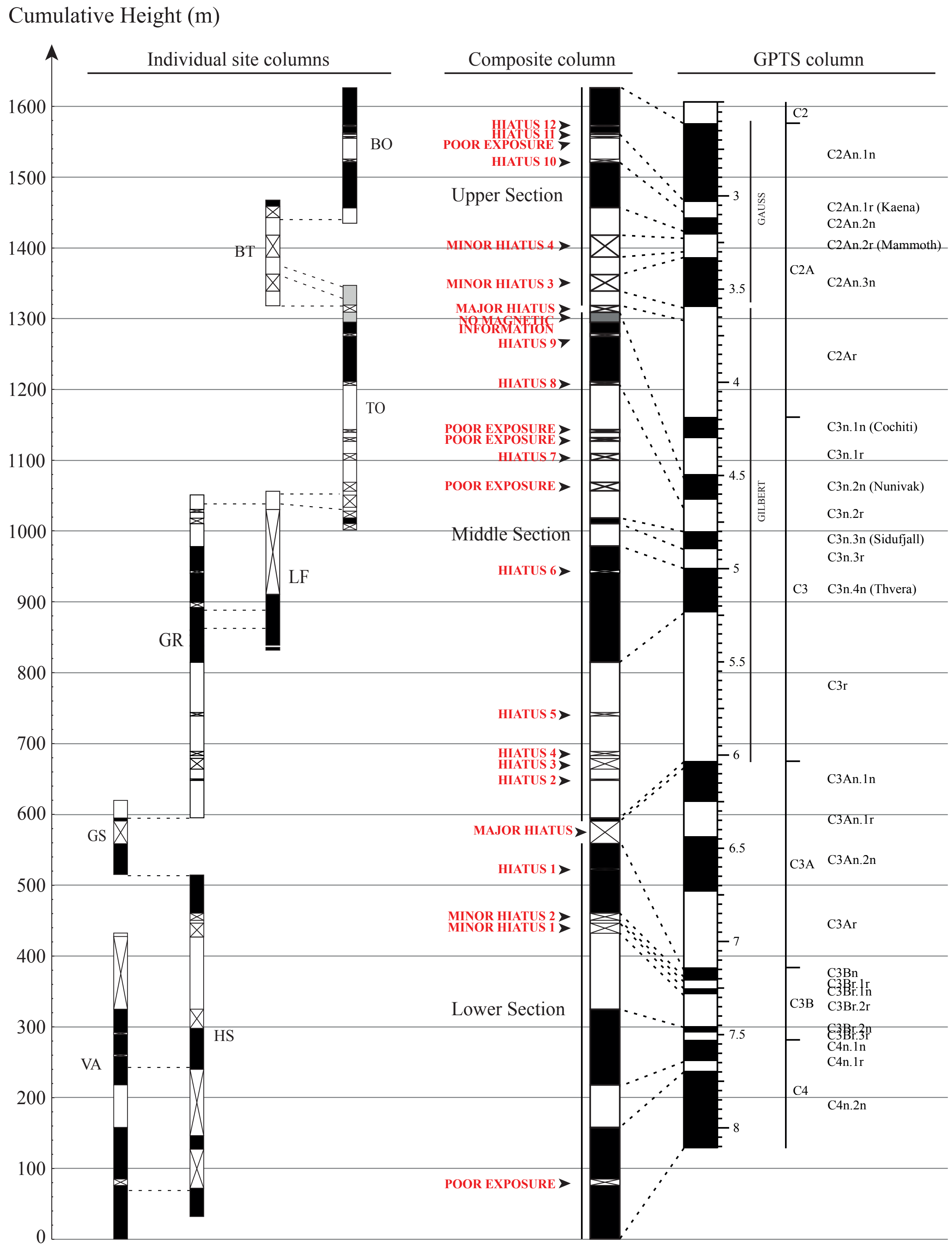

Figure 5.10: A new composite magnetostratigraphy for the Eyjafjardardalur valley. The locations of individual sections (VA to BO) are given on the left of the figure. A composite column was made by combining individual site columns together. Hiatuses and poor exposures are recorded along with the column. Minor hiatuses possibly record short missing time intervals (<0.5 Ma) while major hiatuses indicate long missing time interval (>0.5 Ma). The small hiatuses are also marked as "Hiatus". The geomagnetic polarity time scale (GPTS) column were redrawn from the geologic time scale 2012 (Ogg, 2012). Polarity chrons and subchrons are given along the right side of the GPTS column. The correlations between northern Iceland time scale with the GPTS are represented as dash lines.

5.4 Deviation from the GAD hypothesis

Prior to the time-averaged field study, the plate motions of the local study areas are also taken into account because if the plates move north-south directions with high movement rates (e.g., Pacific and Indian plates), the distances that the plate move would cause error in the GAD. I used the no-net-rotation model (NNR-MORVEL) of Argus et al. (2011) to calculate palaeolocations of the study areas. The reason for choosing the NNR-MORVEL model over other models such as hotspot model (HS3-NUVEL-1A) because HS3-NUVEL-1A was constructed but constrains the relative plate angular velocities to consistency with NUVEL-1A (DeMets et al., 1994). NNR-MORVEL was improved upon NUVEL-1A and the angular velocity for the North America plate from NNR-MORVEL differs from NUVEL-1A by 0.021° M/a (Argus et al., 2011) which do not much affect plate reconstructions for ca. 2.6-8.5 Ma rocks in Iceland (<20 km). The plate velocity of 18.4 mm/yr and azimuth of 283.2° were retrieved from the NNR-MORVEL model by indicating fixed Eurasian plate and moving North America plate (my study area is located on the North American plate, west of the rift). With predicted ages of each lava flow from the linear regression age model (previous section), I have made estimates of the plate motion for each lava flow since their formation. With these information and the individual site locations, the directional cosine can be used to determine palaeolatitudes and palaeolongitudes of each individual site (Tauxe et al., 2010). Details of palaeolocations are given in Table 5.1.

The departure of the time-averaged field from the GAD hypothesis can be determined from $\Delta I = I_{obs} - I_{GAD}$ and $\Delta D = D_{obs} - D_{GAD} = 0$, where I_{obs}, D_{obs} are the inclination and declination observed at local study sites and I_{GAD}, D_{GAD} are the inclination and declination predicted by the GAD hypothesis (Equation 1.5). Prior to the site-mean direction calculation, a total of 125 directional data were used to calculate virtual geomagnetic pole (VGP) (Table 5.1). The site locations and palaeolocations were used to calculate the VGP for the individual site. Four lava flows record low latitude VGP (< 45°) and were excluded from the time-averaged field study as they might record the unstable field during transition. The mean directions were calculated for three different time intervals including 7.0-8.5 Ma, 4.5-6.0 Ma, and 2.6-3.6 Ma (Table 5.3). It is clear that the mean directions during these time intervals show significant deviation from the GAD hypothesis (Inc = 77.0° for northern Iceland), except the reverse polarity data during 7.0-8.5 Ma that show an agreement with the GAD inclination within 95% confidence limit. The equal area projections for individual time intervals are presented in Figure 5.11a, 5.11c and 5.11e. Mean declination and inclination for normal (65 sites) and reverse (56 sites) polarity data during 2.6-8.5 Ma are 352.1°/70.3° and 176.8°/-72.5° with 95% confidence limits of 3.0° and 4.0° (Table 5.3). Figure 5.11g shows an equal area projection of the site mean directions during 2.6-8.5 Ma. Both normal and reverse polarity dataset pass the reversal test at class A level (McFadden and McElhinny, 1990) with 95% confidence. Then, the reverse polarity magnetisations were flipped to normal polarity magnetisations and a combined mean direction (Dec = 354.1°, Inc = 71.4° and α_{95} = 2.4°) was calculated for all 121 lava flows. The inclination from this study deviates approximately 6.0° from the GAD inclination (77°) at 65°N. Figure 5.11h shows a stereo plot of VGPs for 125 sites (included four low latitude VGPs in the plot). These VGPs were calculated using the palaeolocations after the plate motion correction as stated above. (The stereo plots for individual time intervals are also presented in Figure 5.11b, 5.11d and 5.11f). A combined mean VGP location of 80.6°N/184.6°E with d_m/d_p = 4.2°/3.7° shows the departure from the geographic north by approximately 10° on the opposite side of the sampling location indicating far-sided effect.

I recalculated 129 site-mean directions from the Kristjansson et al. (2004) study for the time window 5-8 Ma. All of the Kristjansson et al. (2004) data pass the site selection criteria of $\alpha_{95} \leq 10°$ and $k \geq 50$, but the criteria of $n \geq 5$ cannot be applied to the study and other studies in Iceland before 2005 because the focus of traditional paleomagnetic studies in Iceland required many flows in stratigraphic succession rather than many samples from individual sites/flows (Kristjansson, 2013). My study emphasises both high-resolution stratigraphic coverage as well as high sample density per site. The mean directions of 353.7° and 71.0° with α_{95} of 3.0° from Kristjansson et al. (2004) study agree with our 2.6-8.5 Ma data. I combined this study data with 0-3 Ma data (38 sites) from Jökuldalur, eastern Iceland in order to improve temporal coverage of the dataset toward 0-8.5 Ma (Døssing et al., 2016). Combining data together, results in declination of 354.5° and inclination of 72.2° with an α_{95} of 2.0°. I obtained the mean VGP of 81.8°N and 184.5°E (D_m/D_p = 3.5°/3.1°) (Figure 5.11j). The evidence from the palaeodirection and the mean VGP location shows that the palaeomagnetic field during 0-8.5 Ma in Iceland departs from the GAD field. The VGP error ellipse does not coincide with the Earth's spin axis.

Table 5.3: The mean directions for different time intervals. This study data were combined with Døssing et al. (2016) data to improve temporal coverage for the time span 0-8.5 Ma. Dec and Inc are mean declination and inclination. N and R are the number of sites used to calculate mean direction and resultant vector. k and α_{95} are the precision parameter and 95% confidence interval. Plat and Plon are mean VGP latitude and longitude with the 95% error ellipse with the major and minor axes of d_m and d_p. The Plat and Plon of this study are the mean VGP after the plate motion correction. For Døssing et al. (2016) data, the plate motion correction was not made for the VGP calculation as their study location is consider to be young and would not be much affected by the plate motion.

Age (Ma)	Polarity	Dec (˚)	Inc (˚)	N	R	k	α_{95} (˚)	Plat (˚)	Plon (˚)	d_m (˚)	d_p (˚)
2.6-3.6	All	353.5	70.4	17	16.64	43.9	5.4	79.0	183.1	9.3	8.1
	N	355.1	65.7	7	6.87	47.4	8.9				
	R	171.8	-73.7	10	9.80	45.4	7.2				
4.5-6.0	All	359.8	70.6	55	52.98	26.8	3.8	79.8	164.4	6.6	5.7
	N	1.5	71.5	23	22.45	40.1	4.8				
	R	178.7	-70.0	32	30.54	21.2	5.7				
7.0-8.5	All	347.3	72.3	49	47.31	28.5	3.9	80.3	208.5	6.9	6.1
	N	345.5	70.2	35	34.00	33.7	4.2				
	R	174.5	-77.5	14	13.41	22.0	8.7				
2.6-8.5	All	354.1	71.4	121	116.86	29.0	2.4	80.6	184.6	4.2	3.7
	N	352.1	70.3	65	63.23	36.2	3.0				
	R	176.8	-72.5	56	53.66	23.5	4.0				
0-8.5	All	354.7	72.2	159	153.98	31.4	2.0	81.8	184.7	3.5	3.1
	N	351.3	71.0	74	72.03	37.1	2.7				
	R	178.0	-73.2	85	82.00	28.0	3.0				

7-8.5 Ma

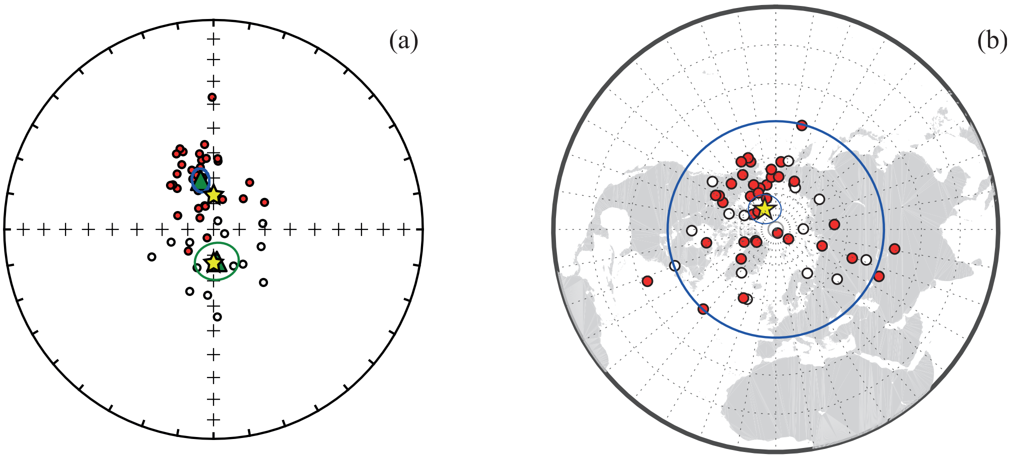

4.5-6 Ma

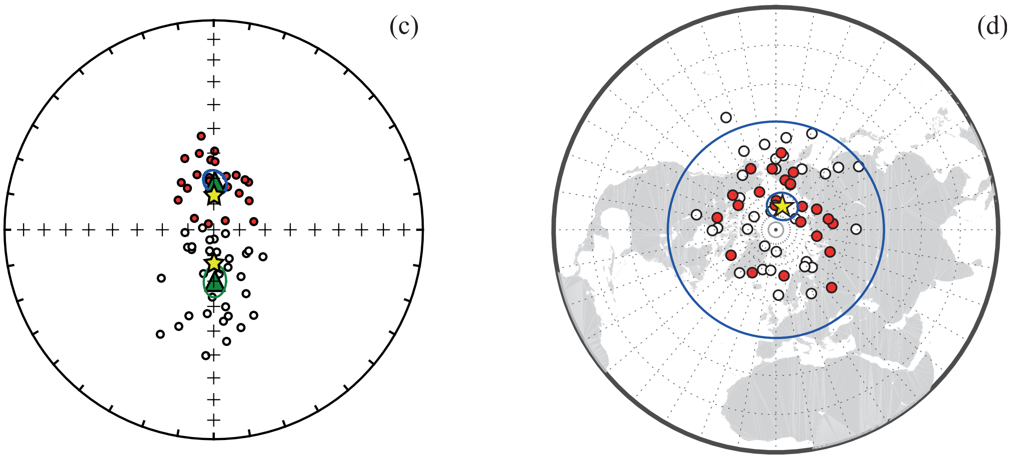

2.6-3.6 Ma

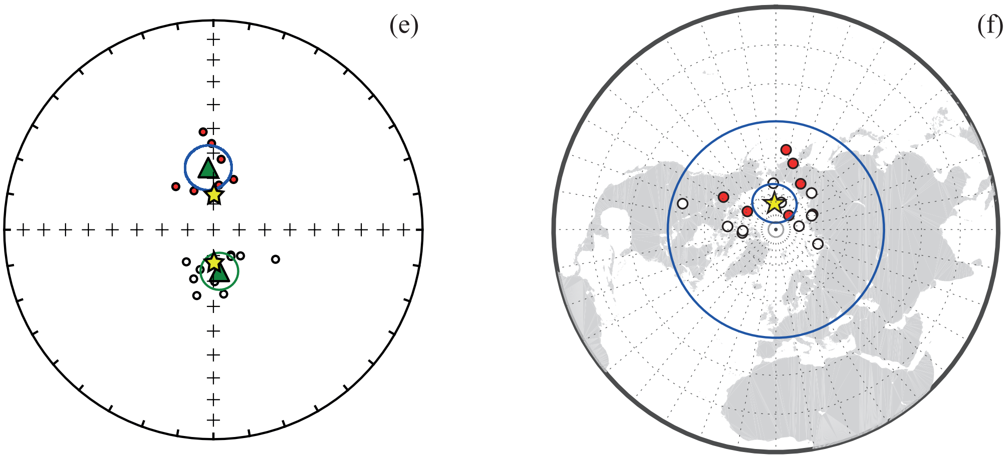

2.6-8.5 Ma

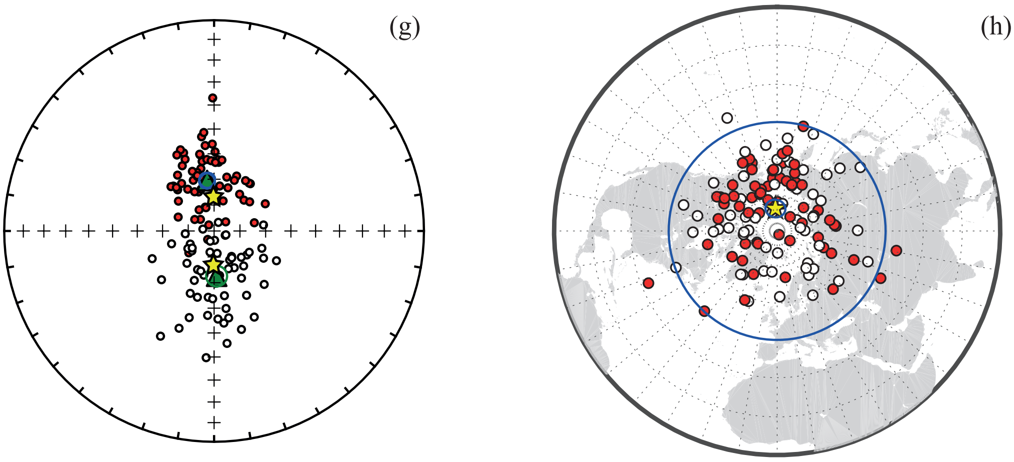

0-8.5 Ma

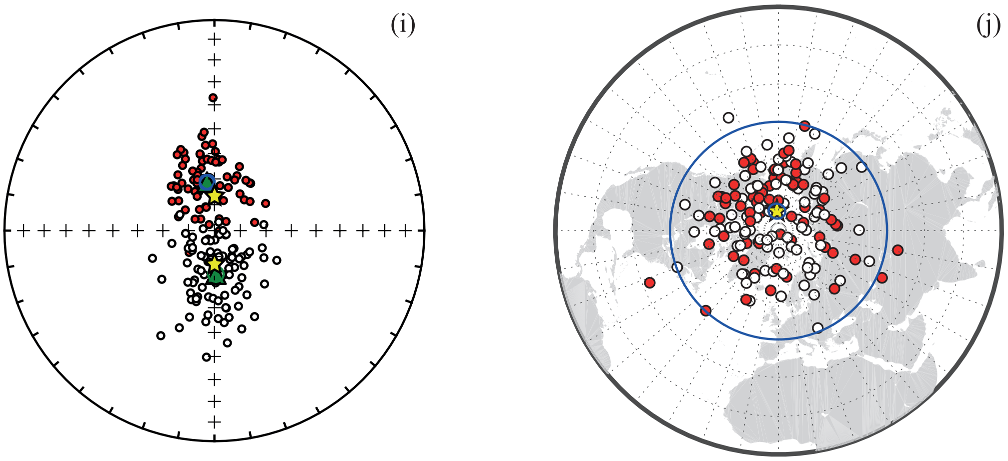

Figure 5.11: (a), (c), (e), (g) and (i) Equal area projection of site mean directions for 7-8.5 Ma, 4.5-6 Ma, 2.6-3.6 Ma, 2.6-8.5 Ma and 0-8.5 Ma. Red (open) circles represent normal and reverse polarity data. Yellow stars show normal and reverse GAD inclinations for Iceland. Green triangles represent calculated mean normal and reverse directions with 95% confidence circles. (b), (d), (f), (h) and (j) Stereo plot of virtual geomagnetic pole (VGP) for 7-8.5 Ma, 4.5-6 Ma, 2.6-3.6 Ma, 2.6-8.5 Ma and 0-8.5 Ma. Red (open) circles represent normal and reverse polarity data. Reverse polarity data are antipode VGP and were plotted in the northern hemisphere. A yellow star shows mean VGP position with 95% confidence limit. Blue circle indicates VGP cut-off at 45°N and 45°S.

An important objective of the time-averaged field studies is to determine the dispersion of the VGP through time and space. Cox (1969) generally used the angular variance of the VGPs about the Earth's spin axis, known as scatter statistic (S), to study palaeosecular variation of the geomagnetic field. Here I use the modified S statistic (S_F) which is corrected for within-site scatter (McElhinny and McFadden, 1997).

$$S_F = \sqrt{(N-1)^{-1}\sum_{i=1}^{N}\left((\Delta_i)^2 - \frac{S_w^2}{\overline{n}}\right)} \tag{5.1}$$

where N is the total sites, Δ_i is the angle between the ith VGP and the Earth's spin axis, S_w is within-site scatter (defined as $81°/\sqrt{k_w}$, is the site-level precision parameter) and $\overline{n}$ is the average number of samples per site. S_F with error bounds was calculated using the bootstrap method of Tauxe et al. (2010). Firstly, the VGPs were used to calculate the S_F using Equation 5.1. To calculate the 95% error bound, a set of 1,000 VGP data was randomly drawn from the original VGP data. After that, this pseudo-sample of data was used to calculated S_F following Equation 5.1. The second and third processes were repeated for 1,000 times. A total of 1,000 S_F was sorted from the lowest to the highest. Finally, a 95% confidence interval was determined from the S_F lying between the 25th and 975th S_F.

It has been common practice that lava flows that record low-latitude VGPs are excluded from studies of palaeosecular variation as the lava flows likely record transitional field behaviours (e.g., Lawrence et al., 2009; Cromwell et al., 2013b). Vandamme (1994) proposed the "Vandamme" criterion to derive VGP latitude cut-off as based on S_F, that is

$$\lambda_V = 90° - (1.5S_F + 5)° \tag{5.2}$$

Firstly, all VGP data are used to compute S_F and then the λ_V is derived. The VGP dispersion is calculated again after low-latitude VGPs are omitted by λ_V. The benefit of this method is that all data are included. Another method is to use a constant VGP latitude cut-off, e.g., $|\lambda| = 45°$ (e.g., Johnson et al., 2008). VGPs between 45°N and 45°S were classified as transition and were excluded from S_F determination. In order to assess which methods are suitable for this study, I calculate the S_V using the Vandamme cut-off of 38.9°, yielding $S_V = 25.6_{23.7}^{27.5}$ for 124 sites. Only VAB9 was classified as transition. While using 45° co-latitude cut-off ($\lambda_{45°}$), results in $S_{F(45°)} = 24.5_{23.1}^{26.4}$ (121 sites). Four sites are determined as transition if the constant cut-off is applied. A drawback of the Vandamme criterion is that if the data contain several low-latitude VGPs, the Vandamme algorithm will converge and not remove these sites (Johnson et al., 2008). Low-latitude VGPs are common in my data; therefore, Vandamme cut-off is not suitable for this study. Here, I also focus on studying stable polarity field behaviour; therefore, I chose a constant VGP latitude cut-off of 45° to omit transitional data rather than Vandamme cut-off which may include transitional data.

A question arises of the effect of the application of the DGs to the VGP dispersion. I calculated the $S_{F(45°)}$ for 137 lava flows (denoted as $S_{Fo(45°)}$) whose pass the modern TAF criteria prior to the DG combination, yielding $S_{Fo(45°)} = 24.1_{22.6}^{25.7}$. It is seen that $S_{Fo(45°)}$ is slightly lower (but not significant) than $S_{F(45°)}$. The slightly lower $S_{Fo(45°)}$ would be a result of the pulsed eruptions which could not record the secular variations. The overlying flows tend to record nearly the same field directions as recorded in the underlying flows. This effect returns the low VGP scatter as the fields recorded in the underlying and overlying flows are not significantly different. Given the important to the pulsed eruptions which could affect the capture of real secular variations, the $S_{F(45°)}$ derived from the dataset with DGs was used to compare with other Iceland studies.

To compare my result with another study in Eyjafjardardalur, I recalculated VGP dispersion for 5-8 Ma data from Kristjansson et al. (2004) study. Typically Kristjansson et al. (2004) collected approximately 2-4 cores per site. Their S_F derived from 116 lava flows is $25.1_{23.2}^{27.0}$. I also compared our mean dispersion with published data from Jökuldalur, eastern Iceland (0-3 Ma) (Døssing et al., 2016). Døssing et al. (2016) improved the number of samples to approximately 10 specimens per site. The S_F from younger rocks ($20.4_{17.7}^{23.2}, N = 38$) is significantly lower than 2.5-8.5 Ma rocks. Another evidence showing low S_F in younger basalts is from Tanaka and Yamamoto (2016) study in Storutjarnir, north central Iceland. The number of samples from the study in Storutjarnir is around 5 specimens per site. I re-calculated the VGP dispersion using 131 data spanning from 2.5-3.5 Ma from their study, yielding $S_F = 19.5_{18.0}^{21.1}$. Their S_F overlaps with Jökuldalur data. In order to study the field behaviour during 0-8.5 Ma, I combined my data with Jökuldalur data in order to improve temporal coverage of the dataset. Combining data together results in $S_F = 23.7_{22.1}^{25.1}$ for 159 sites.

Figure 5.12 illustrates the VGP dispersions from (1) Jökuldalur, eastern Iceland (~0.6-3.1 Ma) (Døssing et al., 2016), (2) combined this study with Jökuldalur (0-8.5 Ma), (3) this study (2.6-8.5 Ma), (4) Eyjafjordur, northern Iceland (5-8 Ma) (Kristjansson et al., 2004) and (5) Storutjarnir, north central Iceland (2.5-3.5 Ma) (Tanaka and Yamamoto, 2016) versus site latitudes. Here I compared the VGP dispersion data with palaeosecular variation models: Model G (black line) (McFadden et al., 1988) and TK03 (blue line) (Tauxe and Kent, 2004). Both Model G and TK03 were designed to fit the VGP dispersions from 3,719 lava flows in McElhinny and McFadden (1997). It is clear that the VGP dispersions from (3) and (4) significantly higher than both Model G and TK03 with no overlap of 95% confidence limit. With regards to (1) and (5), both studies agree well with PSV models. Averaging the field over 0-8.5 Ma in (2) decreases VGP dispersion. However, it is still hard to compare data in (2) with data in (5) because a 1 Myr interval in (5) might not be long enough to record secular variation.

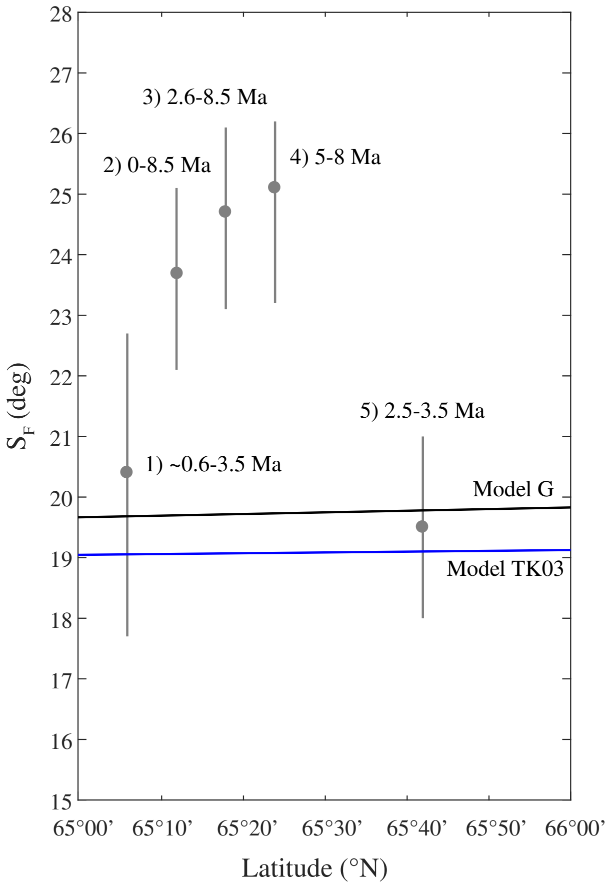

Figure 5.12: VGP dispersions (S_F) with 95% bootstrap upper and lower bounds from (1) Jökuldalur, eastern Iceland (Døssing et al., 2016), (2) combined this study with Jökuldalur, (3) this study, (4) Eyjafjordur, northern Iceland (Kristjansson et al., 2004) and (5) Storutjarnir, north central Iceland (Tanaka and Yamamoto, 2016). Black and blue lines represent PSV model G (McFadden et al., 1988) and the statistical GGP PSV model TK03 (Tauxe and Kent, 2004).

5.5 Discussion

5.5.1 Palaeomagnetic studies

A mean declination and inclination of 354.1° and 71.4° with 95% confidence limit of 2.4° were found in this study and are significantly lower than the GAD field predicted for the study area (Dec = 0°, Inc = 77°), with no overlap of error cone. The shallow inclination of 71° was also recorded in 8-5 Ma sections of Kristjansson et al. (2004) in Eyjafjordur while the whole lava sections in their study covering timespan 8-5 Ma recorded the shallow inclination of 73.3°. This shallow inclination was not observed only in northern Iceland during tertiary period but also found in other regions of Iceland. For example, the shallow inclination of 72° was found in Tertiary bed rock during 15 Ma in northwest Iceland (Kristjansson et al., 2003) and 2-7 Ma rocks in Borgarfjordur, western Iceland (Watkins et al., 1977). However, the shallow inclination has not been found in young lava flows, e.g., 0-3 Ma (Udagawa et al., 1999; Døssing et al., 2016; Tanaka and Yamamoto, 2016).

A question arises of the possible sources of shallow inclination observed in northern Iceland. There are several possible causes that can scatter palaeodirection (e.g., Urrutia-Fucugauchi et al., 2004; Speranza et al., 2008): 1) local magnetic anomalies generated by strong magnetisation in underlying lava flows (Baag et al., 1995; Valet and Soler, 1999; Speranza et al., 2006); 2) shape anisotropy and magnetic refraction; 3) block movements when lava flows formed; 4) local tectonic movements and tectonic complications; 5) insufficiently averaged secular variation; 6) bias from overprint; 7) averaging of unit vectors (Creer, 1983); 8) permanent non-dipole field. The first scenario was tested by Baag et al. (1995) in both models and fieldwork data. Baag et al. (1995) suggests that high magnetic susceptibility terrain especially north and south slopes can cause the shallow inclination of approximately 10°. The degree of the inclination anomalies has the direct variation with the degree of the terrain slope. This local magnetic anomaly causes the shallow inclination in the overlying lava flow if the lava flows into terrain slopes, valleys or ponds (Baag et al., 1995). Baag et al. (1995) also noticed that no geomagnetic deflections occur on or above flat-flows. This also applies to the flood basalts in northern Iceland which has high magnetisation and tends to form horizonal flows. Therefore, the shallow inclinations observed in this study is likely not a result of local magnetic anomaly. However, this local magnetic anomaly should not be avoided as the topography of the terrain during the lava flows formed is not known. This raise a question for future study. The major concern of this study is that our team drilled the cores along the eastern and western flanks of the valley. The local magnetic anomaly in the terrain could deflect the compass needle during core orientation (Baag et al., 1995). As I obtained an 86% Sun orientation success rate during three field seasons, the possibility that the deflection is due to inaccuracies in magnetic compass readings can be neglected. With regards to factor 2), Coe (1979) analysed the effect of shape anisotropy on the acquisition of NRM. He concluded that the effect of shape anisotropy is small for lava flows with the NRM intensities <200 mA/m. Castro and Brown (1987) suggested that the effect of shape anisotropy could be enhanced in the thick lava flows. The magnetic refraction effect should not shallow the inclination more than 2° with respect to the local geomagnetic field during the time of remanent acquisition (Tanguy, 1970). Therefore, the shallow inclination in this study could be the effect of shape anisotropy because the NRM intensities in the specimens usually >200 mA/m. Moreover, the thickness of the lava flows ranges from ~2 to 40 m. Note: previous research of our group carried out by Døssing et al. (2016) did not notice shallow inclination as Arne and I measured the Icelandic basalt from Jökuldalur which has the same nature of basalt samples from Eyjafjardardalur such as NRM intensities >200mA/m. The magnetic refraction is neglected in this study as the refraction effect could not shallow the inclination down more than 2° (Tanguy, 1990). Sampling through block movement is also resolved because our team typically spread drilling locations along 50-100 m distance along individual lava flows to collect 8-12 cores. The regional tectonic tilt was corrected prior to mean direction calculation. The plate motion correction was also performed and there was very small plate movement toward the north direction (~0.1°-0.3°) according to the NNR-MORVEL. As the GAD inclination depends on geographic latitudes according to Equation 1.5, slow northward movement means that palaeolatitude of the study area is slightly different from the current day latitude. Therefore, the GAD inclination during the time of remanent acquisition is not much different from the current day GAD inclination. However, the local tectonic complication that our team could not observe in the field should not be avoided but is hard to resolve in this study. The concentration of the data which covers time span ~2.6-8.5 Ma could resolve the problem of insufficient data points for averaging secular variation out. Regarding Tanaka and Yamamoto (2016) and Døssing et al. (2016) studies, the secular variations were averaged out during ~1.5 Myr time interval. The bias from the overprint as pointed out by McElhinny and McFadden (1997) was also resolved as the specimens were demagnetised until the NRM drops <5% of the original NRM intensities. Another bias arises from use of unit vectors. Creer (1983) suggested that the use of unit vectors could shallow the inclination few degrees from the GAD inclination. However, this problem was not detected in previous research of our group as Døssing et al. (2016) also used the same technique to average mean inclination. The last factor which causes the shallow inclination is the persistence of permanent non-dipole fields. Both axial quadrupole and octupole causes in negative and positive inclination anomalies in northern and southern hemispheres (Merrill, 1996). Though, some factors could be the causes of shallow inclination in this study such as shape anisotropy and tectonic complication, I believe that the main factor should be the persistence of the non-dipole fields which contribute to the GAD field during different time interval from other studies such as Døssing et al. (2016) and Tanaka and Yamamoto (2016) which support the GAD theory.

The VGP dispersion recorded in ~2.6-8 Ma lava flows is significant high while 0-3 Ma basalt show the presence of low VGP dispersion. The behaviour of high VGP dispersion was also confirmed by Kristjansson et al. (2004). Model G of McFadden et al. (1988), which assumes the high VGP dispersion at high latitudes resulting from a dipole family, underestimates both data from this study and Kristjansson et al. (2004). The palaeosecular variation model of Tauxe and Kent (2004) (TK03), assumes the palaeomagnetic field is a Giant Gaussian Process (GGP), also underestimates VGP dispersion for the Tertiary rocks. With regards to 0-3 Ma rocks, both Model G and TK03 agree fairly well with 0-3 Ma VGP dispersion (Figure 5.12). The higher dispersion might be the effect of quadrupole and octupole fields which dominated ~2.6-8 Ma. The effect of non-dipole fields which contribute to the time-averaged field during 0-8.5 Ma on the Iceland data and the global palaeomagnetic dataset will be examined later in Chapter 6.

5.5.2 Lava succession across Eyjafjordur

A pioneer palaeomagnetic study in northern Iceland was performed by Saemundsson et al. (1980) on 450 lava flows, with a composite stratigraphic section of 5,000 m in the Trollaskagi peninsula (between Eyjafjordur and Skagafjordur). K-Ar dating was also performed in their section, yielding 12 Ma at the lower most section. They found a rapid build-up of lava piles on top of their section (9 Ma). Kristjansson et al. (2004) extended the sections from 9 Ma flows toward 5 Ma units, with a stratigraphic column of 3,000 m in Eyjafjardardalur. Kristjansson et al. (2004) correlated their lower most section to the upper most section of Saemundsson et al. (1980). The present study extends the composite stratigraphic sections by adding profiles in the upper Eyjafjardardalur from 8 Ma toward 2.5 Ma (Figure 3.1, Chapter 3). Here, the correlation of the lower most sections of Eyjafjardardalur between this study and Kristjansson et al. (2004) was made according to an agreement of palaeomagnetic directions between two individual sites. The lithology of lava flows was also taken into account. The VA section in this study is located between HO and VE sections of Kristjansson et al. (2004) (Figure 3.1, Chapter 3). Only one correlation was made between HO and VA. The site-mean direction of HO52 shows an agreement with the site-mean direction of VA7 (Figure 5.13).

With regards to the correlation between VA and VE, four possible correlations were made between these sections (Figure 5.13). VA19 was correlated to VE4, while VA25 was correlated to VE8. VA27 was correlated to VE9. Another correlation is between VA36 and VE24. However, VE24 altitude is slightly higher than the altitude of VA36. According to the stratigraphic log (Figure 5.13), the aphyric basalt shield in VE is thicker than the aphyric basalt shield in VA. This suggests the accumulation rate of the lava shield in VE is slightly higher than the accumulation rate of the lava shield in VA.

The section HS of this study is located between VE and GR (Figure 3.1, Chapter 3). Only one correlation (VE21-HSB15) was made (Figure 5.13). Overall, the correlation between this study and Kristjansson et al. (2004) study shows that at least 200 m section was missing between VE and GR in Kristjansson et al. (2004) study as they correlated the rhyolite flows on the top of VE26 to the rhyolite flows on the bottom GR1. Using the correlation as stated above, a composite lava pile of ~9,600 m in northern Iceland covers time span 2.5-12 Ma.

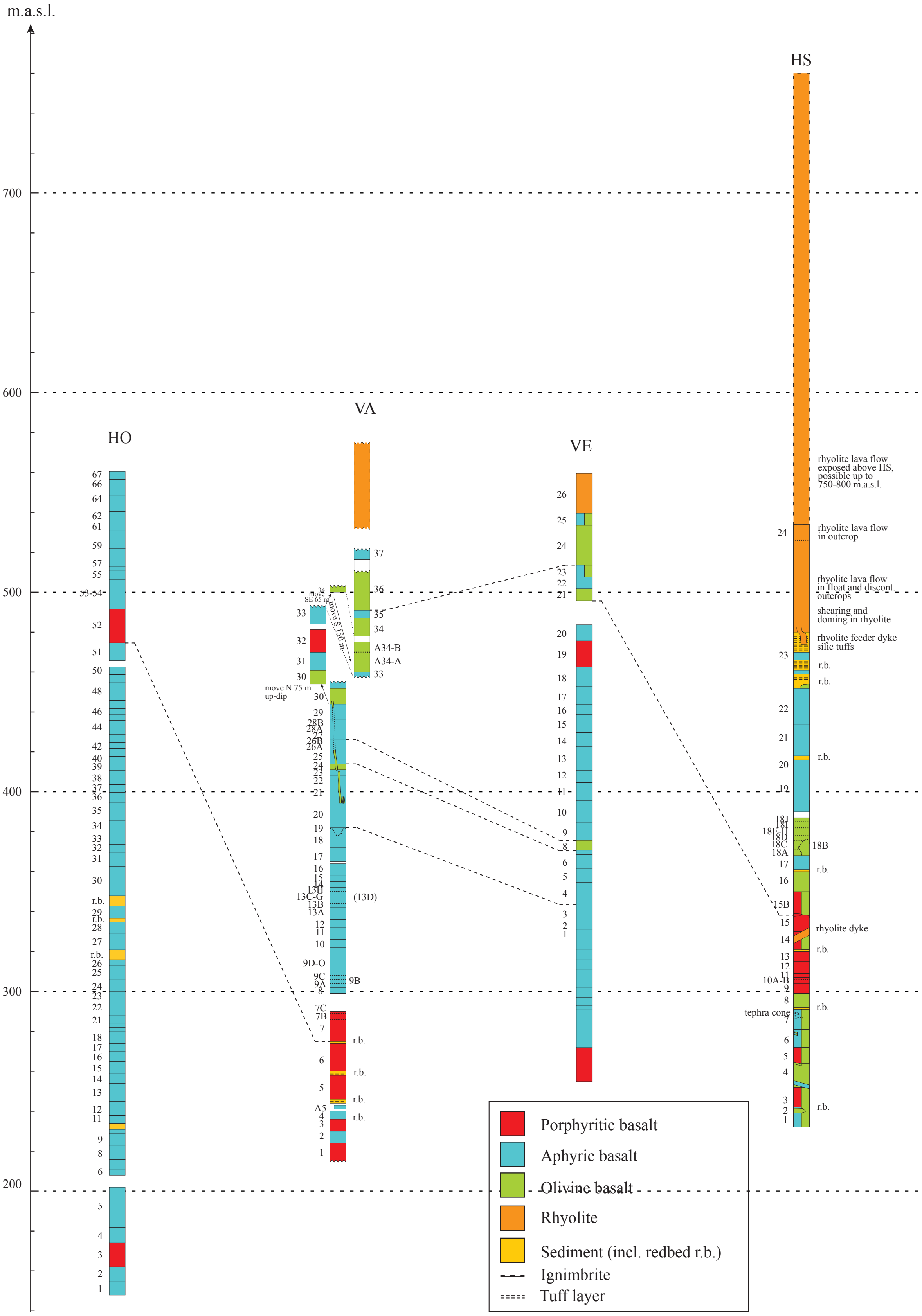

Figure 5.13: Stratigraphic map of lower Eyjafjardardalur valley showing HO, VA, VE and HS sections. Dash line presents possible correlations according to palaeomagnetic direction and lithology. HO and VE sections were modified from Kristjansson et al. (2004).

Two adjacent flows that have been erupted in a short time interval may not record the secular variation of the Earth's magnetic field (Mankinen et al., 1985). An approach to detect pulsed eruption is to apply the DG test which has been used with a series of continuous sections in large igneous provinces such as the Greenland traps (e.g., Riisager et al., 2002), the Central Atlantic magmatic province (e.g., Knight et al., 2004), the Deccan traps (e.g.,Chenet et al., 2008), the Etendeka traps (e.g., Dodd et al., 2015) and the North Atlantic Igneous Province (Suttie et al., 2014). The analysis of the DG in this study found a total of 18 DGs (Table 5.1) indicating pulsed eruption occurred in Eyjafjardardalur, especially a series of four continuous DGs recorded in the TO section. These lava flows might not have sufficient time interval to record secular variation of the Earth's field.

Accumulation rates of lava flow for each section were also considered. Using Figure 5.10, the accumulation rates across the Eyjafjardardalur and across the time of formation were calculated (Figure 5.14). The crustal accretion rate of the lower section is significantly high, with a rate of ~545 m/Myr. This accumulation rate continued for nearly one million years. The accumulation rate of the middle section is relatively slower than that of the lower section, with a rate of ~445 m/Myr lasting for nearly 1.5 Ma. The crustal accretion rate for the upper section is significantly lower than the below sections, with a rate of 296 m/Myr which is maintained from around 3.6 to 2.6 Ma.

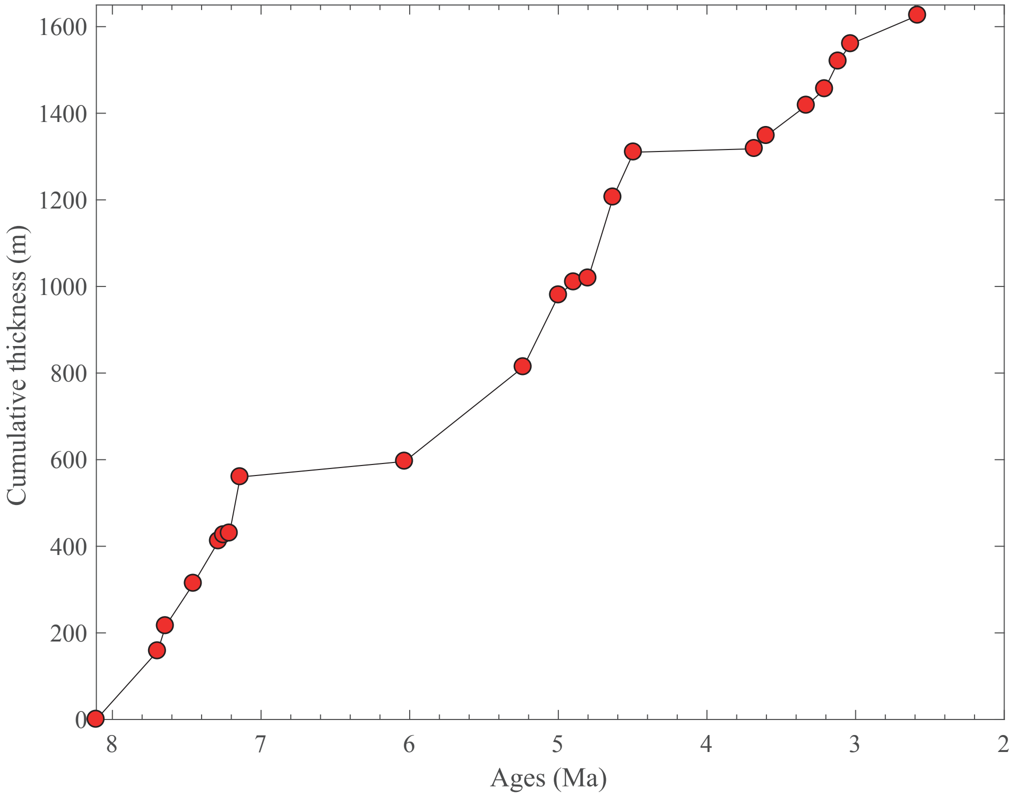

Figure 5.14: A plot cumulative thickness of the lava pile with respect to time. The time span was derived from the GPTS in Figure 5.13.

Chapter 6

Modified statistical model for palaeosecular variation

6.1 Overview

The aim of this chapter is to study the possible causes of the departure of the time-averaged palaeomagnetic field from the geocentric axial dipole (GAD) hypothesis during the last 8.5 Ma. As shallow inclinations are commonly observed in northern Iceland data, even in data from young samples, it is likely that tectonic movements are not the cause of these observed shallow inclinations even after the plate movement correction. This chapter mainly focuses on the investigation of the non-dipole components that contribute to the Iceland data and global palaeomagnetic dataset. Initially, the motivation behind this work is discussed, followed by an analysis of the global palaeomagnetic data collection. I then consider an assessment of Icelandic data quality. To explain these differences, I modify existing palaeosecular variation (PSV) models to fit the current palaeomagnetic dataset. Finally, the determination of the non-dipole fields using the modified PSV model is discussed.

6.2 Motivation behind this work

The first order approximation of the time-average field (TAF) is the geocentric axial dipole (GAD) field (Merrill et al., 1996). However, the deviations of the palaeomagnetic field from the GAD field during 0-5 Ma have been observed in both observational data (e.g., Opdyke et al., 2006) and models constructed from global palaeomagnetic datasets (e.g., Johnson and Constable, 1995; Carlut and Courtillot, 1998). The motivation of this work is to answer why the inclinations observed in Iceland do not follow the GAD trend. I also extend my interest toward the global-level data as better resolution of the Earth's field can be provided when temporal and spatial coverage of the observed locations is improved.

Palaeomagnetic modellers have used both forward and inverse approaches to determining the non-dipole field contributions. Generally, they have found ~4-5% permanent contribution of the non-dipole field to the TAF (e.g., Constable and Johnson, 1999; Kono et al., 2000; Hatakeyama and Kono, 2002). For example, Lawrence et al. (2006) used a forward method to determine paleomagnetic field properties for data from the last 0-5 Ma. They estimated axial quadrupole (g_2^0) and axial octupole (g_3^0) components of 4% and 6%. Johnson et al. (2008) also considered a 0-5 Ma lava dataset. They also used the forward method to capture the field and found the $g_2^0 = 0.03g_1^0$ and $g_3^0 = 0.03g_1^0$ in the global dataset. However, there is still poor temporal and spatial coverage at 60-80°N and 60-65°S in the dataset used by Johnson et al. (2008). This study aims to improve temporal and spatial coverage at high-latitudes and capture the non-dipole components in the TAF during 0-8.5 Ma.

6.3 Palaeosecular variation (PSV) model compilation

Here, I consider PSV behaviour determined from lavas only from the past 8.5 Myr. I do not consider sedimentary data, as there are added problems in analysing global datasets of sedimentary data and lavas are thought to be more reliable recorders (Johnson and Constable, 1995). Prior to the PSV model, the palaeomagnetic data are collated and poor-quality data rejected from the PSV compilation. Previous PSV studies have their own criteria to omit poor quality data, but most of the studies (e.g., Quidelleur et al., 1994; Johnson and Constable, 1996; McElhinny and McFadden, 1997; Johnson et al., 2008) generally suggest the following criteria:

1. Palaeomagnetic data should be from lava flows or thin dykes and the drilled cores should be taken from outcrops determined to be *in situ*. There should be no tectonic effects after the remanent acquisition, i.e., the rocks should be relatively young. If there is evidence of tectonic effects found in the study, data should be subjected to tectonic correction (e.g., Johnson et al.,

2008). Sites without tectonic correction are likely to have high scatter in palaeomagnetic directions (Lawrence et al., 2006).

2. Each study set the minimum number of specimens per site in order to assess within-site orientation error in the form of 95% confidence limit (α_{95}) or the Fisher precision parameter (k) (Fisher, 1953).
3. Transitional data are omitted using the virtual geomagnetic pole (VGP) cut-off. Generally the constant VGP cut-off of 45° or the Vandamme cut-off (Vandamme, 1994) are used. If the VGP data fall below these cut-offs, the data are rejected from further study.
4. Modern laboratory methods are used to determine the characteristic remanent magnetisation (ChRM) with no overprints left in the data. The overprints would result in high-data scatter (e.g., McElhinny and McFadden, 1997; Johnson et al., 2008). The modern study (e.g., Johnson et al., 2008) requires minimum DMAG 4 of McElhinny and McFadden (1997) to select high-quality data. DMAG 4 indicates that the principal component analysis (PCA) (Kirschvink, 1980) is employed to the data on the Zijderveld diagrams (Zijderveld, 1967).

The most referred PSV lava flow (PSVL) database is from McElhinny and McFadden (1997) (here after MM97) consisting of 3719 data points. Of these, a total of only 440 data meet the modern laboratory cleaning of DMAG 4. Johnson et al. (2008), here after J08, later compiled the MM97 database and found only 394 pass the DMAG 4 criteria. It is clear that using the DMAG 4 criteria to omit low-quality data during earlier studies was insufficient for data analysis. The purpose of MM97 database study was to fit the “Model G” of McFadden et al. (1988). This database was used later by Tauxe and Kent (2004) to fit the statistical PSV Model TK03. Johnson et al. (2008) updated the recent PSVL database which includes 394 data from McElhinny and McFadden (1997), new palaeomagnetic data from Time-Averaged Field Investigations (TAFI) project and palaeomagnetic data from Japan and New Zealand in their PSV model compilation. The J08 dataset, provides approximately over 2000 high-quality data.

Data collection

In order to construct a PSV model for lava data, I have collated a new palaeomagnetic dataset from the MagIC database (https://www.earthref.org/MagIC). Data that have not been uploaded to the

MagIC database were collated from literature search engines. Over 4000 data entries were obtained from the literature. These data span latitudes from 80°S to 80°N and meet the DMAG = 4 and 5 criteria. DMAG 5 indicates that magnetic vectors are isolated using two or more demagnetization methods with the principle component analysis. A total of 95 study areas are used in the PSV compilation and their locations are presented in Figure 6.1. This database also contain some studies used in J08 such as Australia (Opdyke and Musgrave, 2004), Patagonia (Mejia et al., 2004) and New Zealand (Tanaka et al., 1996). Previous compilation of the global dataset by Johnson et al. (2008) suggests that the selection criteria of $n \geq 5$ and $k \geq 50$ were appropriate for omitting poor quality data from the global dataset. The criteria of $\alpha_{95} > 10°$ (Opdyke et al., 2010) was also applied to the dataset to omit outlier data with $\alpha_{95} > 10°$ but $k \geq 50$. These outliers occur when the number of samples per site is fairly low, i.e., $n \leq 4$, as in some studies such as James Ross Island (Kristjansson et al., 2005) and Iceland (e.g., Kristjansson et al., 2004). The constant VGP latitude cut-off of 45° (λ_{45}) was used to omit transitional data (Johnson et al., 2008). The iterative Vandamme criterion (Vandamme, 1994) was not used here because if several low-VGP-latitude sites are present in the dataset, the Vandamme cut-off would include transitional data into the dataset (Johnson et al., 2008).

All selected studies in the Table 6.1 meet the criteria as stated above. The exception to this is the dataset from James Ross Island and Iceland for which only four cores or smaller were available for the PSV compilation. However, the James Ross Island data were included in the analysis, because only two studies at high-southern latitudes between 60°S and 70°S (Deception Island and James Ross Island) are available for this timespan (Table 6.1). Therefore, the James Ross Island data are valuable for capturing high-southern latitude field behaviour. In this case, $n \geq 4$, $\alpha_{95} \leq 10°$ and $k \geq 50$ were used to select reliable data. With regards to Icelandic data, much of the published data from Iceland were collected with the objective to sample many flows rather than collect many samples per flow to improve within site error (Kristjansson, 2013). Fieldwork campaigns held between 1964-2011 mostly collected around 2-4 cores per site. However, the previous studies in Iceland are still compared with the modern studies in Iceland. Therefore, these data were classified into two groups: (1) studies performed prior to 2005 (1428 data) and (2) studies performed since 2005. The study of Udagawa et al. (1999) (314 data) was included in the post-2011 classification as the data were of high quality. Appropriate assessment of Icelandic data quality was not done in J08. I reassess quality of the data from Iceland in the next section.

Table 6.1: Lists of accepted studies for the PSVL compilation. Study areas are grouped into 10° latitude bins, e.g., S80-71 is the bin between -80˚ and -71˚. Lat. and Lon. are site latitudes and longitudes. R and N are the number of sites that records normal and reverse polarity magnetisation.

Bin	Site	Site No.	Lat. (˚)	Lon. (˚)	R	N	Total	Ages (Ma)	Bin total	Reference
S80-71	1. McMurdo	1	-77.9	165.1	43	64	107	0.026-7.94	107	Lawrence et al. (2009)
S70-61	2. James Ross Island	3	-64.0	302.0	8	5	13	3.95-6.16	26	Baraldo et al. (2003)
	3. Deception Island	2	-63.0	299.5	0	13	13	0.15		Kristjansson et al. (2005)
S60-51	4. Patagonia	4	-51.1	289.4	11	26	37	0.165-4.08	37	Mejia et al. (2004)
S50-41	5. Patagonia	6	-47.0	288.9	11	15	26	0.067-7.86	72	Brown et al. (2004)
	6. Possession Island	5	-46.4	51.8	18	17	35	0.5-4		Camps et al. (2001)
	7. Chile (site 1)	7	-41.2	287.5	0	11	11	1835-1454 AD		Roperch et al. (2015)
S40-31	8. Chile (site 2)	12	-38.7	288.3	0	41	41	8000-1408 AD	235	Roperch et al. (2015)
	9. New Zealand	8	-38.5	176.0	26	42	68	1.18		Tanaka et al. (1996)
	10. New Zealand	8	-38.5	176.0	0	24	24	0.032-0.23		Tanaka et al. (1997)
	11. New Zealand	8	-38.5	176.0	0	14	14	0.1-21 ka		Tanaka et al. (2009)
	12. Victoria - Australia	9	-37.7	144.3	21	14	35	0-5		Opdyke and Musgrave (2004)
	13. Tristan da Cunha island - South Atlantic	73	-37.1	347.7	0	31	31	80 ka		Shah et al. (2016)
	14. Northern Patagonia	10	-36.1	290.9	4	18	22	0-1.9		Quidelleur et al. (2009)
S30-21	15. Easter Island	13	-27.1	251.0	0	17	17	0.35	76	Miki et al. (1998)
	16. Reunion	15	-21.3	55.7	0	22	22	0.012-0.098		Chauvin et al. (1991)
	17. Reunion	14	-21.1	55.5	0	37	37	0.07-0.13		Raïs et al. (1996)
S20-11	18. Society Island	16	-16.9	208.0	41	68	109	0.9-110	109	Yamamoto et al. (2002)
S10-0	19. Java, Indonesia	17	-7.4	112.0	0	24	24	0-6.7	157	Elmaleh et al. (2004)
	20. Fernando de Noronha, Brazil	19	-3.9	327.6	12	14	26	1.8-3.3		Leonhardt et al. (2003)
	21. Galapagos Island	20	-0.9	270.0	25	36	61	3		Kent et al. (2010)
	22. Ecuador	18	-0.4	281.7	29	17	46	0.018-2.71		Opdyke et al. (2006)

…continue from previous page…

Bin	Site	Site NO.	Lat. (°)	Lon. (°)	R	N	Total	Ages (Ma)	Bin total	Reference
N0-10	23. Mount Kenya	21	0.1	37.6	9	51	60	0.3-5.36	208	Opdyke et al. (2010)
	24. Sao Tome	26	0.3	6.6	18	20	38	0-8		Opdyke et al. (2015)
	25. Loiyangalani	22	3.8	36.7	16	15	31	3.5-4.84		Opdyke et al. (2010)
	26. Ruiz-Tolima volcanic chain, Colombia	23	4.9	284.6	4	42	46	0.089-1.2		Sánchez-Duque et al. (2016)
	27. Cameroon Volcanic Line, West Africa	24	6.5	13.3	0	6	6	0.9-2.6		Ubangoh et al. (1998)
	28. Costa Rica	25	10.0	275.6	3	24	27	0.057-2.11		Cromwell et al. (2013a)
N11-20	29. Afar, Ethiopia	27	11.8	41.5	51	53	104	0.59-3.27	336	Kidane et al. (2003)
	30. Martinique Island	43	14.7	298.7	5	9	14	0-2.27		Tanty et al. (2015)
	31. Guadalupe Island	28	16.0	61.7	0	26	26	0-1		Carlut et al. (2000)
	32. Santo Antão, Cape Verde	33	17.0	334.7	2	25	27	0.41-0.54		Brown et al. (2009)
	33. Los Tuxtlas volcanic field, Mexico	34	18.4	264.8	5	4	9	0.8-2.6		Alva-Valdivia et al. (2001)
	34. Central Mexico	37	18.5	259.7	0	10	10	0-0.02		Gonzalez et al. (1997)
	35. Isla Socorro - Mexico	35	18.7	249.0	0	9	9	0.55		Sbarbori et al. (2009)
	36. Chichinautzin volcanic field, central Mexico	36	19.1	260.8	0	7	7	0.002-0.039		Morales et al. (2001)
	37. Tacambaro area, Central Mexico	44	19.1	258.5	7	21	28	0-4.18		Peña et al. (2014)
	38. Xitle Volcano, Central Mexico	38	19.3	260.8	0	10	10	1965 BP		Alva-Valdivia (2005)
	39. West of Mexico City	29	19.4	261.9	10	1	11	1.28-4.14		Mejia et al. (2005)
	40. Mauna Loa volcano, Hawaii	39	19.5	204.8	0	8	8	0-0.028		Valet et al. (1998)
	41. Michoacan-Guanajuato volcanic field, Central Mexico	40	19.7	258.2	6	14	20	0-2.1		Conte-Fasano et al. (2006)
	42. Central and western Mexico	41	19.8	258.4	2	9	11	0.56-2.78		Peña et al. (2011)
	43. Eastern Alkaline Province, Mexico	42	19.8	262.8	6	4	10	1.53-7.33		Goguitchaichvili et al. (2007)
	44. Trans-Mexican volcanic belt, Mexico	30	20.0	259.0	3	29	32	0-3.5		Michalk et al. (2013)

…continue from previous page…

Bin	Site	Site NO.	Lat. (°)	Lon. (°)	R	N	Total	Ages (Ma)	Bin total	Reference
N21-30	45. Kohala Mountain, Hawaii	49	20.1	204.2	0	9	9	0.06-0.4	245	Brassart et al. (1997)
	46. Trans-Mexican volcanic belt	32	20.2	257.8	15	13	28	0-7.81		Ruiz-Martínez et al. (2010)
	47. Maui, Hawaii	45	20.6	203.7	0	10	10	0-0.7		Herrero-Bervera and Valet (2007)
	47. Pleistocene Tequila Volcanic Field, Western Mexico	50	20.8	256.2	2	11	13	0.1-0.9		Ceja et al. (2006)
	49. Tepic-Zacoalco rift region	31	21.0	255.6	3	4	7	0.3-4		Calvo-Rathert et al. (2013b)
	50. Ceboruco-San Pedro volcanic field	48	21.1	252.1	1	9	10	0-0.6		Petronille et al. (2005)
	51. Oahu, Hawaii	45	21.3	202.2	10	0	10	1.8-2.6		Herrero-Bervera and Valet (2003)
	52. Oahu, Hawaii	45	21.3	202.2	0	14	14	0.03-0.68		Herrero-Bervera and Valet (2002)
	53. Oahu, Hawaii	45	21.6	201.7	0	80	80	3-3.2		Laj et al. (1999)
	54. Canary Island	51	28.2	344.0	0	38	38	0-0.013		Kissel et al. (2015)
	55. Teno volcano, Tenerife	47	28.3	343.1	2	8	10	5.7		Leonhardt and Soffel (2006)
	56. La Palma Island	46	28.8	17.9	11	5	16	0.39-1.86		Tauxe et al. (2000)
N31-40	57. Southwestern USA	52	35.3	248.1	10	13	23	0-4.03	145	Tauxe et al. (2003)
	58. Ontake Volcano, Japan	54	35.9	137.5	0	24	24	0.4-0.7		Tanaka et al. (2007)
	59. Ontake Volcano, Japan	55	35.9	137.5	0	33	33	0.02-0.08		Tanaka and Kobayashi (2003)
	60. South-eastern Spain	56	37.7	358.4	3	6	9	2.61-8.2		Calvo-Rathert et al. (2009)
	61. Sao Miguel, Azores	53	37.8	334.7	13	14	27	0-2.5		Johnson et al. (1998)
	62. Zao Volcano Group, Japan	59	38.1	140.5	0	6	6	0.21-0.36		Otake et al. (1993)
	63. Aeolian Islands, Sicily	57	38.4	15.0	0	14	14	0.1-0.13		Laj et al. (1997)
	64. Datong monogenetic volcanoes, China	58	40.0	113.8	0	9	9	0.52		Yamamoto et al. (2007)

…continue from previous page…

Bin	Site	Site NO.	Lat. (°)	Lon. (°)	R	N	Total	Ages (Ma)	Bin total	Reference
N41-50	65. Djavakheti Highland, Southern Georgia	64	41.4	43.9	0	16	16	2-2.75	335	Calvo-Rathert et al. (2011)
	66. Lesser Caucasus, Georgia	65	41.4	43.3	6	4	10	3.57		Calvo-Rathert et al. (2013a)
	67. Southern Caucasus, Georgia	67	41.7	44.0	7	8	15	1.55		Goguitchaichvili et al. (2000)
	68. Snake River Plain, US	60	43.0	246.4	9	13	22	0.1-5.75		Tauxe et al. (2004)
	69. Boring Volcanic Field, US	62	45.5	237.7	69	52	121	0.06-3.2		Hagstrum et al. (2017)
	70. Indian Heaven Volcanic Field, Washington	61	46.0	121.8	0	56	56	0-3.75		Mitchell et al. (1989)
	71. Perşani Mountains, East Carpathians	63	46.0	25.4	12	21	33	0.4-0.9		Panaiotu et al. (2013)
	72. East Carpathians	66	46.2	25.8	24	38	62	0.4-4.42		Panaiotu et al. (2012)
N51-60	73. British Columbia	68	51.5	237.6	0	49	49	0-0.76	170	Mejia et al. (2002)
	74. Aleution Islands, Alaska	69	53.2	190.0	9	62	71	0-2		Stone and Layer (2006)
	75. Nunivak	70	60.0	193.5	14	36	50	0.97		Coe et al. (2000), cited from Johnson et al. (2008)
N61-70	76. Helgason (0-5Ma)	71	64.0	343.0	130	23	153	0-5	1428	Helgason and Duncan (2001)
	77. Mosfellssveit area, SW-Iceland	71	64.2	338.3	132	33	165	1.6-2.2		Kristjansson et al. (1991)
	78. Þjórsárdalur valley, Iceland	71	64.2	340.5	23	14	37	0.8-1		Kristjánsson et al. (1998)
	79. Southwest and South Iceland	71	64.2	339.1	70	32	102	0-3		Kristjánsson (2010)
	80. Esja, Eyrarfjall and Akrafjall mountains, SW- Iceland	71	64.3	338.0	147	82	229	1.8-4.5		Kristjansson et al. (1980)
	81. Southwestern Iceland	71	64.3	338.6	18	8	26	2-3		Kristjansson and Sigurgeirsson (1993)
	82. Skarðsheiði, South-Western Iceland	71	64.5	338.3	62	35	97	3.58		Kristjánsson and Guðmundsson (2001)
	83. Borgarfjördur, Western Iceland	71	64.5	338.0	139	119	258	2-7		Watkins et al. (1977)
	84. Iceland	71	64.6	340.5	19	44	63	0.78		Kristjánsson et al. (1988)
	85. Central Western Iceland	71	65.0	337.2	44	17	61	5-7		Kristjánsson and Jóhannesson (1999)
	86. Fljótsdalur, Eastern Iceland	71	65.1	345.0	36	25	61	3.8-6.5		Leó Kristjánsson and Ágúst Guðmundsson (2005)
	87. Bessastadaa, Eastern Iceland	71	65.1	345.0	20	12	32	4.8-6.5		McDougall et al. (1976)

…continue from previous page…

Bin	Site	Site NO.	Lat. (°)	Lon. (°)	R	N	Total	Ages (Ma)	Bin total	Reference
N61-70	88. Eyjafjördur, Northern Iceland	71	65.3	341.8	40	74	114	5-8		Kristjansson et al. (2004)
	89. Tjörnes and Flatey, North Iceland	71	66.0	343.0	18	12	30	0-2.5		Eiríksson et al. (1990)
N61-70	90. Jokuldalur, Eastern Iceland	71	65.1	344.5	24	13	37	0.48-3.43	314	Udagawa et al. (1999)
	91. Storutjarnir, Northern Iceland	71	65.7	342.3	63	66	129	2.58-4.187		Tanaka and Yamamoto (2016)
	92. Jokuldalur, Eastern Iceland		65.2	344.6	29	9	38	0-3 Ma		Døssing et al. (2016)
	93. Eyjafjardardalur, northern Iceland		65.3	341.8	49	61	110	2.5-8.5		This study
N71-80	94. Janmayen-Splitbergen	72	70.9	351.3	0	23	23	0-0.46	29	Cromwell et al. (2013b)
	95. Splitbergen	72	79.0	12.5	3	3	6	8.32		Cromwell et al. (2013b)
								Total	4029	

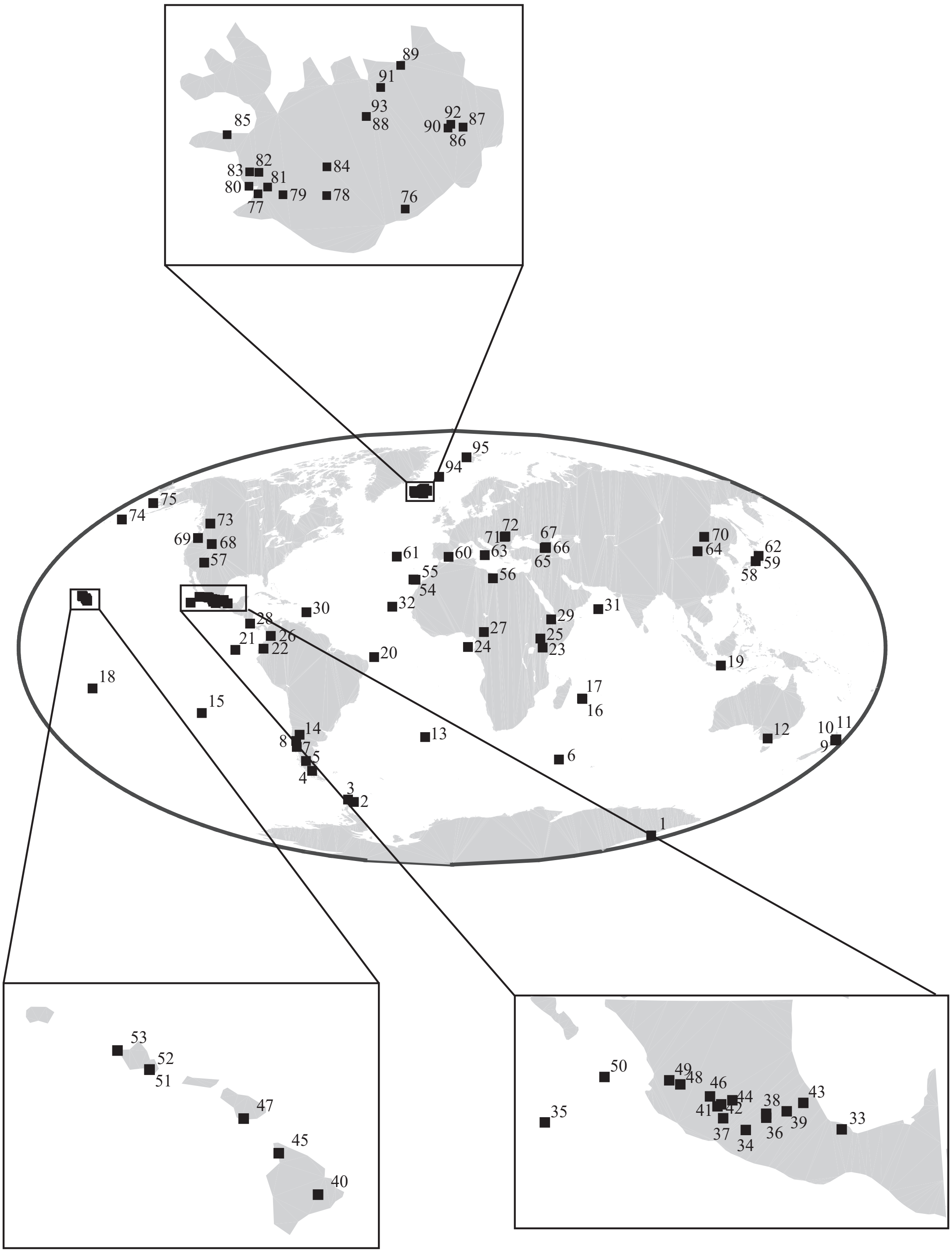

Figure 6.1: The locations of the accepted studies for PSVL compilation. The number marked on the map corresponds to the location number in Table 6.1.

6.3.1 Assessment of quality of data from Iceland

The assessment of the data quality is crucial to accurately quantify PSV (e.g., Johnson and Constable, 1996; McElhinny and McFadden, 1997). Typically, site mean directions with an associated k less than (or α_{95} greater than) a cut-off value are omitted from the analysis, as discussed above. Here I followed the same approach as reported by Johnson et al. (2008). I determine the cut-off value for k that is appropriate for the Icelandic data by examining the VGP dispersion (S_F) following Equation 5.1 (Chapter 5) along with 95% bootstrap confidence error (Tauxe et al., 2010). The Icelandic data provide a total of 2071 data points that pass the λ_{45° cut-off. To assess the appropriate k cut-off (k_{cut}) for the dataset, firstly the S_F was calculated for the whole dataset. Then, the k_{cut} of 10 was applied to the dataset, i.e., the data whose have $k < 10$ were omitted from the dataset and the S_F was calculated for the remaining data. This process is repeated until the $k_{cut} = 200$ was applied. Using $k_{cut} = 200$ results in the remaining data = 1281 (Figure 6.2). As the pre-2005 studies in Iceland are included in the analysis; therefore, the minimum number of specimens per site used in this assessment is three $(n = 3)$. Using n lower than this results in less reliable estimate of k (Tauxe et al., 2003). The S_F data were plotted against k_{cut} as illustrated in Figure 6.2. It is clearly seen that S_F has a gradual increase from 21.8° to 22.1° when $k_{cut} = 20$ is applied. Applying k_{cut} between 20 and 60 increases S_F slightly and the S_F yields the maximum peaks when k_{cut} of 50 and 60 are applied. There is a gradual drop of the S_F between k_{cut} = 60 and 80. After that the S_F fluctuates between 21.8° and 21.9° when $k_{cut} \geq 80$. Here, I chose $k_{cut} = 80$ to reject poor quality data from the Iceland dataset because choosing $k_{cut} = 100$ would results in a high rate of sample rejection, while the S_F for $k_{cut} = 100$ is slightly different from the S_F for $k_{cut} = 80$. Using $k_{cut} = 80$ results in the remaining data = 1773. Then, the criteria of $\alpha_{95} \leq 10°$ was applied to omit outlier data. This gave 1742 data entries for Iceland.

With the inclusion of 1742 data entries from Iceland to the global database, 4029 data points were obtained from 95 study areas (including the present study) for the age range 0–8.5 Ma. Of the 4029 data points, 2347 recorded normal polarity magnetisation while 1682 recorded reverse polarity magnetisation. Figure 6.3 shows age distributions of the new global dataset. Most of the numerical ages of the data are obtained from the reference. In some cases, if the geological epoch was reported, the middle point of the epoch time span was used. It is clearly seen that the bulk of the dataset (~85%) falls within 0-4 Ma while only 620 data points are from sites whose ages are above 4 Ma.

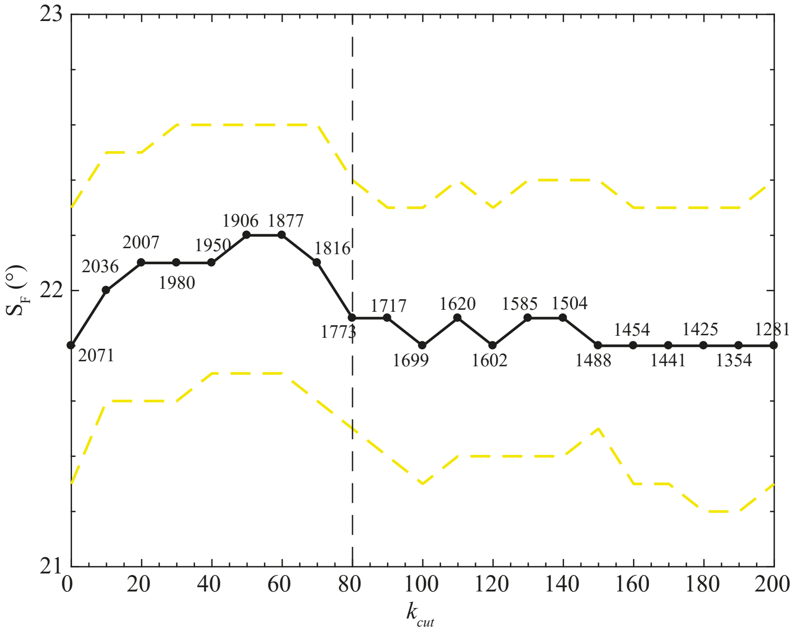

Figure 6.2: VGP dispersion (S_F) versus cut-off value of the Fisher precision parameter (k_{cut}) (Fisher, 1953) for the Iceland dataset. The reverse polarity data were flipped to the northern hemisphere and combined with normal polarity data prior to S_F calculation. Only sites whose $n \geq 3$ were included in the assessment, yielding a total of 2071 site before applying k_{cut}. Black circles show the S_F of the dataset after the poor-quality data are omitted by k_{cut}. The number of sites after omitting poor quality data is also represented along with the S_F data points. Upper and lower yellow dash lines illustrates the 95% bootstrap error bounds (Tauxe et al., 2010) while the vertical dash line indicates the appropriate $k_{cut} = 80$ for the dataset from Iceland.

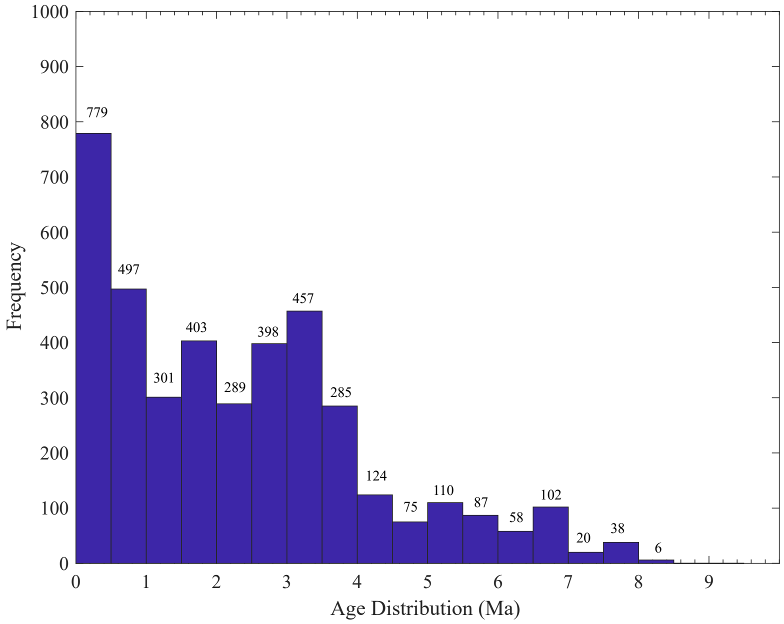

Figure 6.3: A histogram showing the age distribution of accepted global dataset between 0-8.5 Ma. It is clear that majority of site falls within 0-4 Ma (3409 data).

6.4 Modified statistical model for PSV

The virtual geomagnetic pole dispersion (S_F) was used to characterise the PSV in this study (Merrill et al., 1996). In this section I compare the global dataset with Model G (McFadden et al., 1988) and the statistical PSV model of Tauxe and Kent (2004), here after TK03. McFadden et al. (1988) separated the dipole family $(l - m = odd)$ and quadrupole family $(l - m = even)$ of the IGRF65 and determined S_F. They found that S_F at the equator are the result of the quadrupole features while latitudinal dispersions are the results of the dipole features. The relation between the VGP dispersions and latitudes was computed using (McFadden et al., 1988):

$$S = \sqrt{A^2\lambda^2 + B^2} \tag{6.1}$$

where A and B are constants determined by least square fitting while λ is the geographical latitude in degree.

The statistical model for PSV was first proposed by Constable and Parker (1988), here after CP88. This model assumes that PSV is a Giant Gaussian Process (GGP). The gauss coefficients (g_l^m, h_l^m) in the Model CP88 have zero mean with standard deviations that are a function of degree l; the exceptions to this are the axial dipole (g_1^0) and axial quadrupole (g_2^0) terms. The standard deviations of the Gauss coefficients are given by:

$$\sigma_l^2 = \frac{\left(\frac{c}{a}\right)^2 l\alpha^2}{(l+1)(l+2)} \tag{6.2}$$

where $\frac{c}{a}$ is the is the ratio of the core radius to the Earth's radius (~0.547) and α is a fitted parameter. The CP88 model successfully predicts the inclination variation with latitudes, but fails to describe the S_F. Constable and Johnson (1999) improved the CP88 to fit both directional and intensity data by increasing the g_2^1 and h_2^1. They successfully described the variations of the S_F of their dataset. Tauxe and Kent (2004) modified the parameters of the CP88, but preserved part of the original model (the spatial power spectrum of the non-dipole field is consistent with the white source near the core-mantle boundary). Rather than treating the g_2^1 and h_2^1 specially, the modeller assigns the power to the antisymmetric term $(l - m = odd)$ with the ratio:

$$\beta = \frac{\sigma_l^m(l - m = odd)}{\sigma_l^m(l - m = even)} \tag{6.3}$$

where $\beta = 3.8$. The parameter β allows for more variation in the higher order parameters that effect S_F. Tauxe and Kent (2004) also decreased g_1^0 from -30 μT (original CP88) to -18 μT and set $g_2^0 = 0$. This reflects the idea of the low axial dipole of 46 ZAm^2 for 0.3-300 Myr field (Selkin and Tauxe, 2000). The parameters for each model are summarised in Table 1.2 (Chapter 1). The benefit of using statistical GGP model is that the distributions of directions as a result of axial quadrupole and axial octupole can be easily generated and compared with the global palaeomagnetic dataset. Therefore, I selected this zonal model (Model TK03) to describe the global palaeomagnetic dataset and avoided complications.

In order to simulate the PSVL for 0-8.5 Ma, data were group into 10° latitude bins. All accepted data (Table 6.1) were used to calculate S_F with 95% bootstrap confidence errors using Equation 5.1 (Chapter 5). S_F was calculated separately for normal polarity and reverse polarity data, as well as a combined dataset (Figure 6.5). The antipode directions of the reverse polarity data were calculated before the S_F was determined.

To modify the Model TK03 I varied α and β from the original model to fit the PSVL data. The α term can be adjusted by changing the "$afact$" in the TK03, where $\alpha = g_1^0/afact$. The $afact$ was varied from 2.2 to 2.5 μT with 0.01 μT interval while β was varied from 3.8 to 4.2 with 0.1-grid interval. The g_1^0 was not modified as this condition satisfied the low dipole term over geological time. A total of 1000 data points were generated for each latitude using the GGP model. These were combined into 10° latitude bins and S_F was calculated. Model transitional fields were also omitted using λ_{45}. In each model simulation, ~250 (~2.5%) to 350 (3.5%) of 10,000 data points in each latitude bin were omitted by λ_{45}. The root mean square (RMS) misfit was calculated to determine how much the model deviates from the PSVL dataset following Equation 6.4:

$$RMS = \sqrt{\frac{1}{N}\sum_{i=1}^{N}\left(S_{sim(i)} - S_{obs(i)}\right)^2} \tag{6.4}$$

where N is the number of the data used in the RMS calculation. S_{sim} and S_{obs} are S_F from the simulated data and the PSVL dataset. I found the appropriate RMS misfit when the α was increased to 7.8 (7.5 from TK03) and the β was slightly increased to 4.0 (3.8 from the TK03) (Figure 6.4). This condition returns the RMS misfit of 2.17°. I also simulated the S_F from the original TK03 and found the RMS misfit of 2.37°. The simulated S_F data from the modified version of the TK03 is used for comparison with the global dataset for normal polarity, reverse polarity and combined datasets as shown in Figure 6.5. Both Model G and TK03 are also presented in Figure 6.5.

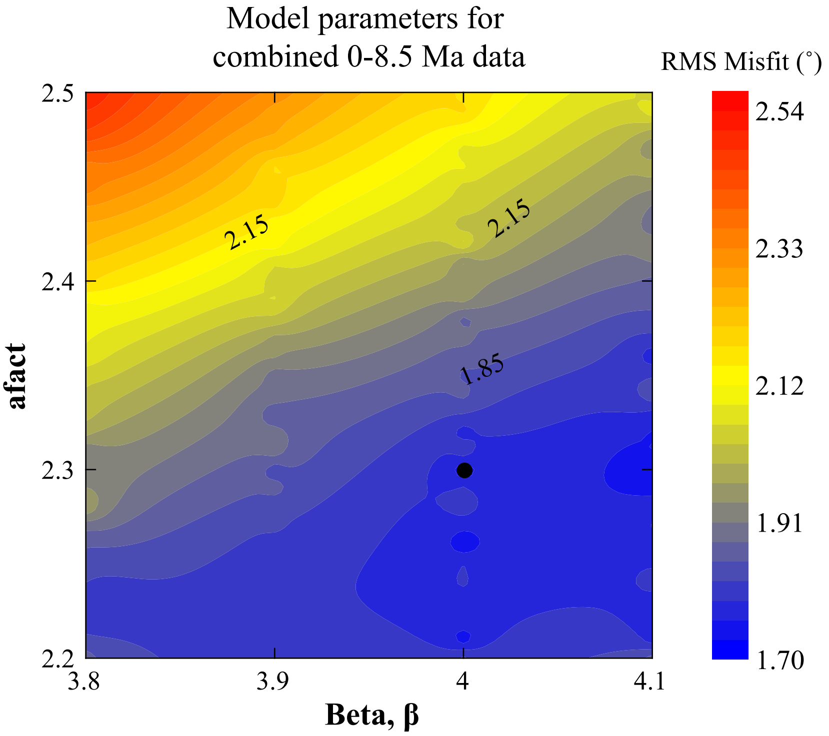

Figure 6.4: A contour plot of RMS misfits between observed VGP dispersions and simulated VGP dispersions for 0-8.5 Ma dataset. The simulated VGP dispersions are obtained from the modified TK03.GAD. The observed VGP dispersions are obtained from the global PSVL dataset. It is clear that β=4.0 and *afact*=2.3 μT, where *afact*=18μT /α, returns the low west RMS misfit for 0-8.5 Ma dataset.

The normal polarity dataset shows little variation in S_F from low- to mid-latitudes in both the northern and southern hemispheres (Figure 6.5a). At high southern latitudes S_F determined from James Ross Island (Kristjansson et al., 2005) and Deception Island (Baraldo et al., 2003) is fairly low while S_F from McMurdo (Lawrence et al., 2009) is higher. With regards to Iceland data, the S_F for pre-2005 studies (530 data) is significant higher than the S_F for post-2005 studies (149 data). Both Model G and TK03 fit the low-latitude data fairly well but underestimate mid- to high-latitude data. The modified TK03 shows better improvement to fit low- to mid-latitude data but still fails to estimate high-southern latitudes data.

The reverse polarity data show higher S_F than the normal polarity data (Figure 6.5c). The pre-2005 studies in Iceland also show significant higher S_F than the post-2005 dataset. The existing models: Model G, TK03 and modified TK03 fit some data points at low- to mid-latitudes but still fail to predict high-latitude data especially Iceland and McMurdo.

The combined dataset shows less latitudinal variation than the reverse polarity dataset (Figure 6.5e). Model G fits the low-latitude data fairly well but underestimates some mid-northern latitude data. Model TK03 shows the best fit to mid-southern latitude data but underestimates equatorial data to mid-northern latitudes data. The modified TK03 significantly improves the S_F estimates for low-latitudes to mid-southern latitudes. This model still fails to describe S_F from 40°N to 70°N. In order to fit the mid- to high-latitude S_F in both Northern and Southern Hemispheres, a non-zero mean g_2^0 term is required. Overall, the modified TK03 in this study significantly improves from the original TK03.

The effect of λ_{45} was also considered in this study. Figure 6.5b, 6.5d and 6.5f show the VGP dispersions during normal polarity, reverse polarity, and combined normal and reverse polarity datasets when the transitional sites ($45°S < \lambda_p < 45°N$) were included in the S_F calculations. The λ_{45} cut-off omitted ~2% to 5% of the transitional fields during normal polarity period. Only McMurdo (75°S) and Iceland (65°N) the datasets contain ~15% of the transitional fields (Figure 6.5a-b). With regard to reverse polarity interval, the proportions of the transition data vary from ~2% to 20% (Figure 6.5d). These proportions were omitted by the λ_{45} cut-off prior to the S_F calculations (Figure 6.5c). The combined normal and reverse polarity datasets mainly contain ~0.5% to 7.7% of the transitional fields. There are four latitude bins including 75°S (McMurdo), 45°S, 65°N (Iceland) and 75°N (Jan Mayen and Spit Bergen) that record the proportions of transitional fields >10%. As ~2.5% to 3.5% of the unstable fields were simulated by the modified TK03, the proportions of the transitional sites contained in all observational datasets are different from the simulated PSV data.

In the case of the VGP dispersions, though the transitional fields were omitted by the criteria of $n \geq 3$, $\alpha_{95} \leq 10°$ and $k \geq 50$ or not recorded in some latitudes bins such as 65°S, 55°S, 25°S, 5°S, 5°N and 75°N in the normal polarity dataset, 65°S in the reverse polarity dataset, and 65°S, 25°S and 75°N in the combined normal and reverse polarity dataset (Figure 6.5b, 6.5d and 6.5f), it is clear that the S_F calculated from the datasets with the transitional fields show significantly high dispersions when compared to the S_F derived from the datasets without <45°-latitude VGPs (Figure 6.5a, 6.5c and 6.5e). Besides this, the low-latitude VGPs also increase the 95% confidence limits in the datasets. It is seen from Figure 6.5b that when 12 low-latitude VGPs were included in McMurdo data (75°S) during normal polarity interval, the S_F shows significant departure from all existing PSV models. This departure also occurs in the datasets obtained from 35°S, 45°N and 65° (Iceland). With regard to reverse polarity data, overall, the VGP dispersions observed in the datasets with the inclusion of the unstable fields (Figure 6.5d) are higher scatter than those without the transitional fields (Figure 6.5c). The VGP dispersions at 75°S, 45°S and 65°S show significant departure from all existing PSV models. This departure also happens to Iceland datasets obtained from both pre-2005 and post-2005 studies. The departure of the S_F from the PSV models also happens to the combined normal and reverse polarity data (Figure 6.5f). Overall, the inclusions of the transitional sites in the S_F calculations yield the high VGP scatters with large 95% confidence bounds.

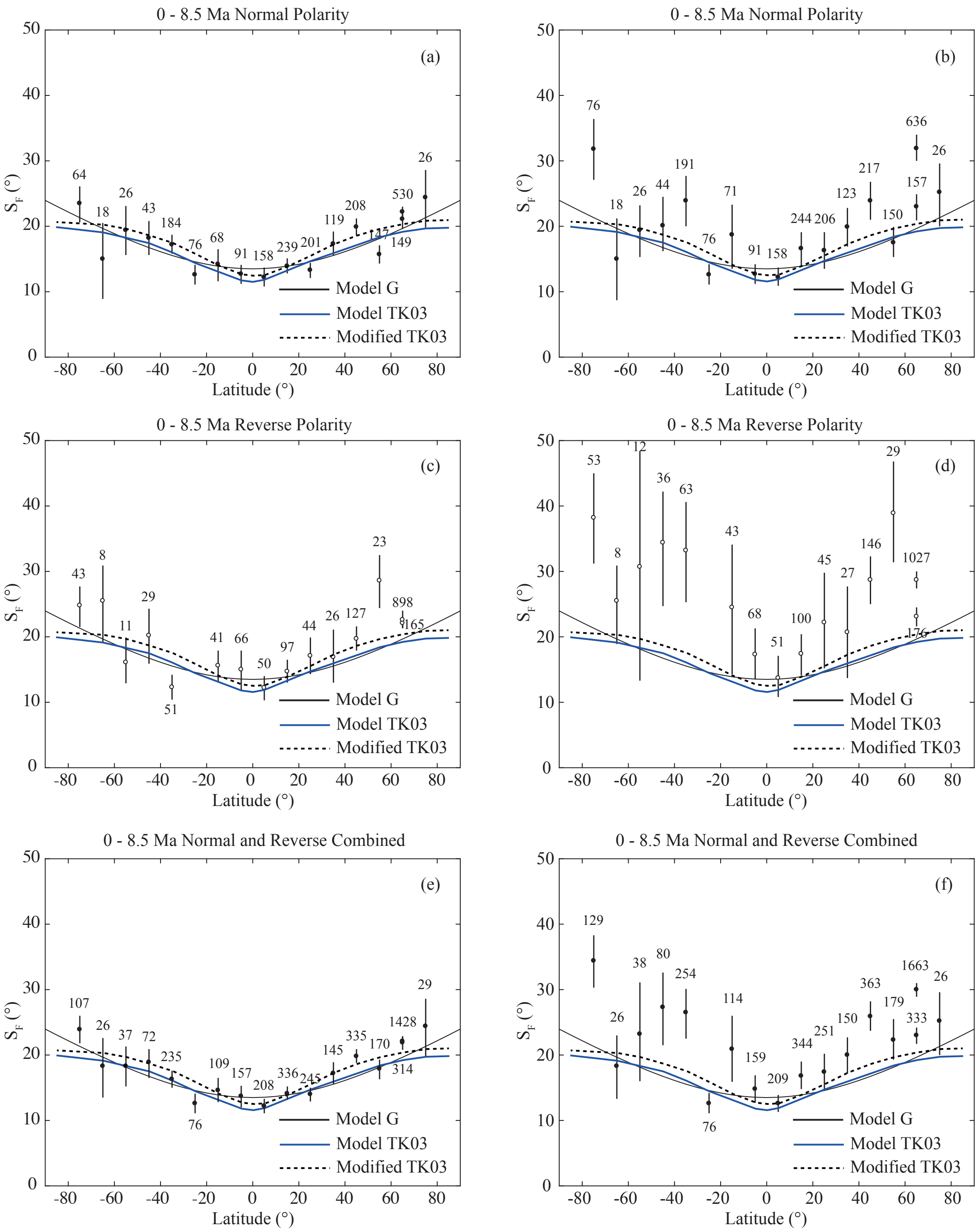

Figure 6.5: The VGP dispersion versus latitudes during (a)-(b) normal polarity interval (c)-(d) reverse polarity interval and (e)-(f) combined normal and reverse polarity. Left column shows the VGP scatters after the low latitude VGPs are omitted, while right column illustrates the VGP scatters when the low latitude VGPs (<45°) are included in the S_F calculations. The number of sites used in S_F calculation is given above or below the data points. Black and blue lines represent Model G (McFadden et al., 1988) and TK03 (Tauxe and Kent, 2004) while dash line shows the modified version of Model TK03 (this study).

6.5 Time-averaged palaeomagnetic field

In this section I aim to determine the deviation of the time-averaged field (TAF) from the GAD hypothesis. The GAD inclination versus latitude can be computed using Equation 1.5 (Chapter 1) while the deviation of the observed inclinations from the GAD can be determined following Equation 1.6 (Chapter 1). In order to calculate the observed mean inclinations, the site mean direction data from the PSVL dataset are grouped into 10° latitudinal bins. Transitional data were excluded from the PSVL dataset using the latitude cut-off of 45° as described above, before the mean directions for each bin were calculated. The TAF during normal polarity and reverse polarity were calculated separately. For the combined dataset the reverse polarity data were flipped into the northern hemisphere data and combined with the normal polarity data.

In order to determine the effect of the non-dipole field that contributes to the PSVL dataset, the modified TK03 in the previous section was used. A grid search approach was performed to find the best-fitting g_2^0 and g_3^0 to the PSVL inclinations. The g_2^0 term was varied from 0% to 9% of g_1^0 while the g_3^0 term was varied from -5% to 5% of g_1^0. A total of 1000 directional data was generated for each latitude. The simulated data were group into 10° latitude bins and mean inclination was calculated after omitting all transitional data using the same cut-off as stated above. The RMS misfit between the simulated data and the observed data was calculated for each non-dipole contribution following Equation 6.5.

$$RMS = \sqrt{\frac{1}{N}\sum_{i=1}^{N}\left(I_{sim(i)} - I_{obs(i)}\right)^2} \qquad (6.5)$$

where N is the number of the data used in the RMS calculation. I_{sim} and I_{obs} are the inclinations from the simulated data and the PSVL dataset. The RMS for each model condition is presented as contour plots in Figure 6.6. The normal polarity dataset is best fit by $g_2^0 = 0.04g_1^0$ and $g_3^0 = 0.01g_1^0$. The reverse polarity dataset has higher non-dipole component than the normal polarity data, with $g_2^0 = 0.06g_1^0$ and $g_3^0 = 0.02g_1^0$. The combined normal and reverse datasets are best fit by $g_2^0 = 0.04g_1^0$ and $g_3^0 = 0.01g_1^0$.

The axial quadrupole component found in this study is higher than the corresponding component found in the time-averaged field investigation (TAFI) data of Johnson et al. (2008) for both normal $(g_2^0 = 0.02g_1^0)$ and reverse $(g_2^0 = 0.04g_1^0)$ polarity datasets. Possible reasons for this difference, are, firstly, that this study has a far greater number of data points (2347) than Johnson et al. (2008) (1012), particularly at high latitude. Most of high-northern latitude data in their study are from 50°N to 55°N including Aleutians (Stone and Layer, 2006), Nunivak (Coe et al., 2000) and British Columbia (Mejia et al., 2002). There are also no data between 60°S and 65°S. The PSVL data in this study includes a total of 1742 data from Iceland and 29 data from Jan Mayen and Spitsbergen (Cromwell et al., 2013b) to improve spatial coverage at high-northern latitudes between 60°N and 80°N. The high-southern latitudes data (60°S-65°S) from Brandy Bay (Kristjansson et al., 2005) and Deception Island (Baraldo et al., 2003) were also included in the PSVL dataset. The model of Johnson et al. (2008) did not include these data. Secondly, the time span of the PSVL dataset (0-8.5 Ma) is longer than the TAFI dataset (0-5 Ma). The results would reflect the different non-dipole components during different time span. The lower non-dipole fields during normal polarity are consistent with a stronger virtual axial dipole moment (VADM) during normal polarity period as suggested previously (Tauxe and Yamazaki, 2007).

The axial quadrupole contribution in the combined dataset is also smaller than that found in the TAFI dataset for reason stated above but agree with the dataset of Lawrence et al. (2006). However, the axial octupole of $g_3^0 = 0.01g_1^0$ is significantly lower than that found in Lawrence et al. (2006) $(g_3^0 = 0.06g_1^0)$, but agrees with the g_3^0 derived from combined continental igneous and oceanic sediment data (McElhinny et al., 1996). The non-dipole components found in each study are summarised in Table 6.2.

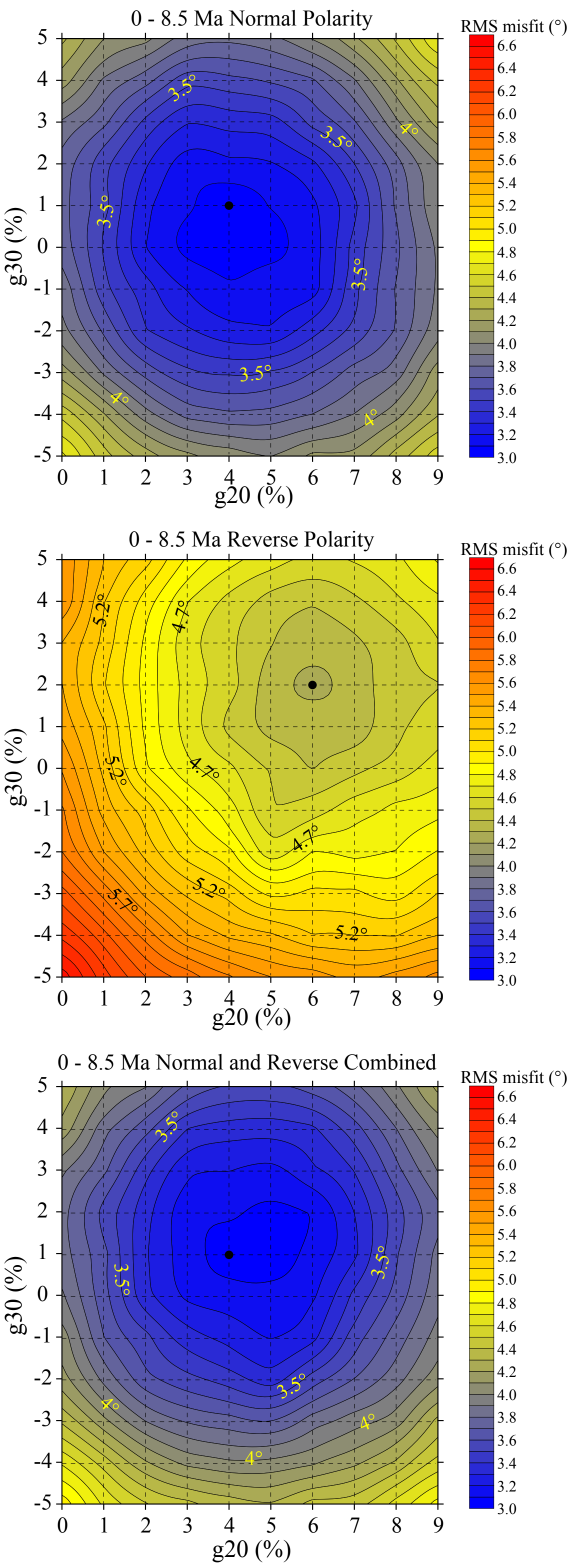

Figure 6.6: Contour plots of RMS misfits between observed inclinations and simulated inclinations for (a) normal polarity interval (b) reverse polarity interval and (c) normal and reverse combine. The simulated inclinations are obtained from modified TK03 with g_2^0 and g_3^0 contributions in the data. The observed inclinations are obtained from the global PSVL dataset. It is clear that $g_2^0 = 0.04g_1^0$ and $g_3^0 = 0.01g_1^0$ returns the low west RMS misfit for normal polarity and combined dataset while $g_2^0 = 0.06g_1^0$ and $g_3^0 = 0.02g_1^0$ provides the lowest misfit for reverse polarity interval.

The best-fitting g_2^0 and g_3^0 for normal polarity, reverse polarity and combined datasets were used to simulate the inclinations versus latitudes. The inclination anomalies were calculated following Equation 1.6 and are presented in Figure 6.7. It is clear that the GAD plus $g_2^0 = 0.04g_1^0$ and $g_3^0 = 0.01g_1^0$ anomaly line is best fit normal polarity data in the southern hemisphere but describes only some data points in the northern hemisphere including Iceland data. With regards to the reverse polarity data, the GAD field combined with $g_2^0 = 0.06g_1^0$ and $g_3^0 = 0.02g_1^0$ terms fit almost all of the data points in the northern hemisphere, but still fails to fit low-latitude data in the southern hemisphere. The combined dataset shows the deviation from the GAD field especially at high-northern latitude while the GAD plus $g_2^0 = 0.04g_1^0$ and $g_3^0 = 0.01g_1^0$ terms is a better fit for the southern hemisphere data. It is clear that Iceland data deviates from the GAD field as stated in Chapter 5. The shallow inclinations of 74.2° derived from 1,428 data points in pre-2005 studies and 74.5° derived from 314 data points in post-2005 studies in Iceland are a result of the non-dipole fields ($g_2^0 = 0.04g_1^0$ and $g_3^0 = 0.01g_1^0$) which contribute to the GAD field.

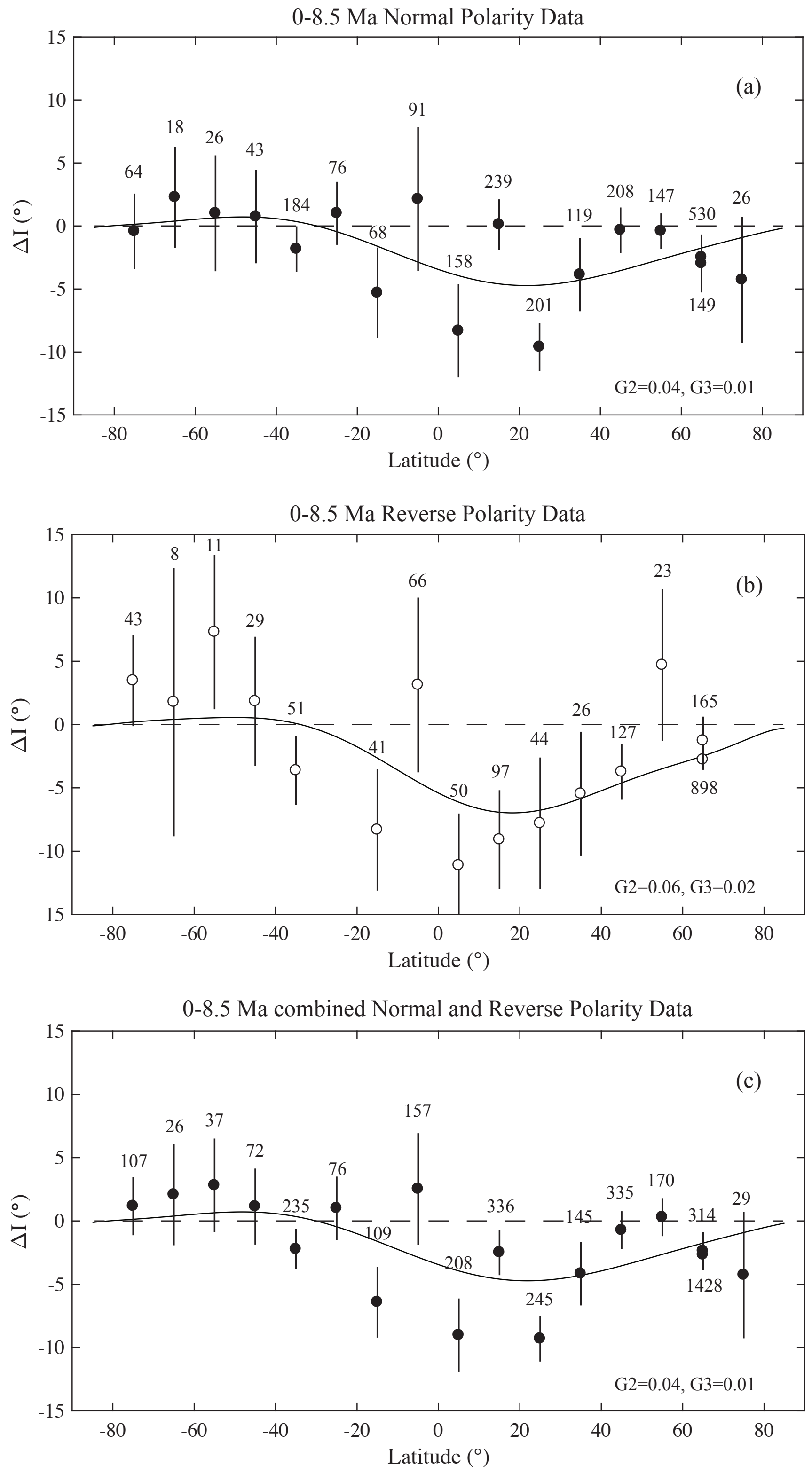

Figure 6.7: The observed inclination anomalies from PSVL dataset versus latitudes during (a) normal polarity interval, (b) reverse polarity interval and (c) combined normal and reverse polarity. The GAD inclination is presented as the dash line ($y = 0$). The inclination anomalies with $g_2^0 = 4\%$ and $g_3^0 = 1\%$ are presented as the black lines in (a) and (c), and the inclination anomaly with $g_2^0 = 6\%$ and $g_3^0 = 2\%$ is presented as the black line in (b). The numbers on the figures next to the data points, detail the number of data points used to calculate each data point.

6.6 Discussions

The simple modifications to Model TK03 (β = 3.8 and α = 7.9 μT) shows significant improvements to fit the global palaeodirection dataset during ca. 8.5 Ma. As the earlier GGP model, Model CP88 (Constable and Parker, 1988), chose β = 1.0, this model fails to describe latitudinal variations of the VGP. Tauxe and Kent (2004) modified β = 3.8 to satisfy the VGP dispersions for ca. 0-5 Ma dataset of MM97 (McElhinny and McFadden, 1997). However, their model underestimates the datasets of this study. One reason would be because the time spans between two datasets are 3.5 Myr difference. This could reflect the field behaviour during different time intervals which required different statistical parameters to describe the field. Another reason would be the presence of the high-quality data in the MM97 database. The MM97 database contains 3,719 data points. Of these, 440 data meet the DMAG 4 criteria. Compared to this study dataset, almost all of the data (~2,588) meet DMAG 4 and 5 criteria, except for the data from Iceland before 2005 and James Ross Island. The overprints in the MM97 data could lead to the different statistical parameters from this study. From these reasons, Model TK03 is not considered here to be appropriate to describe this study dataset and must be improved to fit the current dataset.

The difference in S_F between normal and reverse data was observed previously (McElhinny et al., 1996), but the origins are not clearly understood. One possible hypothesis is that there is an overprint in the reverse polarity data (McElhinny and McFadden, 1997). However, this problem should have been avoided during data selection as DMAG was set to 4 and 5. A second possible reason is that the non-dipole field, which contributes to the GAD field during reverse polarity interval, is higher than the non-dipole field during the normal polarity interval. The second hypothesis is clearly answered by the TAF models in Section 6.5 that the axial quadrupole and octupole during reverse polarity interval are 2% and 1% higher than those during normal polarity interval. The axial quadrupole component found in this study is higher than the corresponding component found in the time-averaged field investigation (TAFI) data of Johnson et al. (2008) for both normal $(g_2^0 = 0.02g_1^0)$ and reverse $(g_2^0 = 0.04g_1^0)$ polarity datasets. Possible reasons for this difference are, firstly, that this study has a far greater number of data points (2347) than Johnson et al. (2008) (1012), particularly at high latitude. Most of high-northern latitude data in their study are from 50°N to 55°N including Aleutians (Stone and Layer, 2006), Nunivak (Coe et al., 2000) and British Columbia (Mejia et al., 2002). There are also no data between

60°S and 65°S. The PSVL data in this study includes a total of 1742 data from Iceland and 29 data from Jan Mayen and Spitsbergen (Cromwell et al., 2013b) to improve spatial coverage at high-northern latitudes between 60°N and 80°N. The high-southern latitudes data (60°S-65°S) from James Ross Island (Kristjansson et al., 2005) and Deception Island (Baraldo et al., 2003) were also included in the PSVL dataset. The model of Johnson et al. (2008) did not include these data. Secondly, the time span of the PSVL dataset (0-8.5 Ma) is longer than the TAFI dataset (0-5 Ma). The results would reflect the different non-dipole components during different time span. The lower non-dipole fields during normal polarity are consistent with a stronger virtual axial dipole moment (VADM) during normal polarity period as suggested previously (Tauxe and Yamazaki, 2007). The axial quadrupole contribution in the combined dataset is also smaller than that found in the TAFI dataset for reason stated above but agree with the dataset of Lawrence et al. (2006). However, the axial octupole of $g_3^0 = 0.01g_1^0$ is significantly lower than that found in Lawrence et al. (2006) ($g_3^0 = 0.06g_1^0$), but agrees with the g_3^0 derived from combined continental igneous and oceanic sediment data (McElhinny et al., 1996). The non-dipole components found in each study are summarised in Table 6.2.

Table 6.2: Summary of the non-dipole fields: $G2$ and $G3$ for normal polarity, reverse polarity and combined datasets. $G2$ and $G3$ are the ratios of g_2^0/g_1^0 and g_3^0/g_1^0. The non-dipole fields in Cromwell et al. (2018), Johnson et al. (2008), Lawrence et al. (2006) and McElhinny et al. (1996) datasets are also summarised in the table.

	Polarity	$G2$	$G3$
This study	All	0.04	0.01
	N	0.04	0.01
	R	0.06	0.02
Johnson et al. (2008)	All	0.03	0.03
	N	0.02	0.01
	R	0.04	0.05
Lawrence et al. (2006)	All	0.04	0.06
McElhinny et al. (1996)	Brunhes and Matuyama igneous and ocean sediment combined	0.04	0.01

6.7 Concluding remarks

- The modified TK03 model improves the S_F prediction at low- to mid- latitudes, but still fails to fit high-latitude data especially Iceland data for the combined dataset. This is likely due to non-dipole components that contribute to high-latitude data.
- The PSVL dataset shows that ~4% of axial quadrupole and 1% of axial octupole contributes to the TAF during normal polarity period. For the reverse polarity data, higher quadrupole and octupole components are required.
- The shallow inclinations during 2.5-8.5 Ma observed in northern Iceland are likely the result of non-dipole field that contributes to the GAD field, not from the tectonic effects.

Chapter 7

Palaeointensity results from Eyjafjardardalur

7.1 Overview

In this chapter, I investigate the Earth's magnetic field strength (palaeointensity) during three periods of volcanism in northern Iceland between 8.5 and 2.5 Ma. The lava flows in Eyjafjardardalur provide successful palaeomagnetic directions for approximately 150 sites and have been shown to record the palaeomagnetic field during the time of remanence acquisition (Chapter 5). Hence, the studied lava succession has the potential provide high quality palaeointensity data for determination of full-vector palaeomagnetic field behaviour at high latitudes. This prospect is supported by previous successful palaeointensity studies in Iceland (e.g., Døssing et al., 2016; Tanaka and Yamamoto, 2016): First, the topic of palaeointensity is reviewed. Second, details of rock magnetic studies are given. Following this the assessment of reliable samples and palaeointensity process are presented. Lastly, the results are presented and discussed and compared with the global palaeointensity dataset and a palaeointensity model.

7.2 Review of palaeointensity research

The Earth's magnetic field is a vector; described by both direction and strength. The departure of the palaeomagnetic field from the GAD theory can also be examined using palaeointensity data; a simple GAD field yields an intensity that is twice as strong at the poles than at the equator (Tauxe et al., 2010). However, most previous studies that have studied the GAD hypothesis from samples < 5 Ma in age have determined only the palaeodirection (e.g., Laj et al. (1999); Mejia et al. (2002); Opdyke et al. (2015); Chapter 5; Chapter 6). Few palaeointensity data sets, have been examined and in particular very few from high latitudes (Tauxe and Yamazaki, 2007). The general lack of palaeointensity data stems from low success rate of the palaeointensity experiments and their time-consuming nature. The lack of palaeointensity data at high latitudes is particularly important as data collected at the Earth's surface from high latitudes, better represents high latitude field behaviour compared to palaeodirectional data when downward continued to the Core Mantle Boundary (CMB) (Johnson and McFadden, 2007).

Trends in the palaeointensity record at high-southern latitudes during 0-8.5 Ma suggests that the long-term field was significantly weaker than the present-day field (Lawrence et al., 2009). High-northern latitude data from the same time window is also lower than the current Earth's field; however, the values are not as low as that from the southern hemisphere (Cromwell et al., 2015; Døssing et al., 2016; Tanaka and Yamamoto, 2016). This supports the suggestion of long-term hemispheric asymmetry of the palaeomagnetic field (Cromwell et al., 2013b). However, the age of the strata investigated in these northern high-latitude studies is generally in the time window 0-3.5 Ma and therefore might not have a sufficient age span to make direct comparison to high-southern latitude data (1-8.5 Ma). The lava succession in Eyjafjardardalur provides discrete time intervals that span 2.6-3.6, 4.5-6.0 and 7.0-8.5 Ma. Therefore, measurements of palaeointensity spanning 2.6-8.5 Ma are valuable for testing the hypothesis of the long-term hemispheric asymmetry of the palaeomagnetic field.

7.3 Rock magnetic methods

Small rock chips obtained from the bottom core during core cutting were used to study rock magnetic properties in order to determine domain states of the magnetic grains. A Princeton Measurements vibrating sample magnetometer (VSM) was used to measure hysteresis loops (with a maximum applied field of 500 mT) and backfield curves at room temperature. The strong field thermomagnetic measurements were performed by heating sampled from 50°C to 650°C with an increment of 1°C under an applied field of 100 mT. Helium was saturated in the furnace during heating and cooling processes in order to prevent alteration from oxidation.

7.3.1 Rock magnetic properties

Hysteresis loops and backfield curves were measured on rock chips from 156 sites to extract coercive force (H_c), coercivity of remanence (H_{cr}), saturation magnetisation (M_s) and remanent saturation (M_{rs}). The ratios of M_{rs}/Ms and H_{cr}/H_c are plotted on a Day-plot diagram (Day et al., 1977) as shown in Figure 7.1a. Most samples (~95%) from Eyjafjardardalur fell within the pseudo-single domain (PSD) region. Only one sample (GRB7) fell within the single domain range. Four types of hysteresis loop were found (Figure 7.1b-7.1e). Figure 7.1b shows hysteresis loop of GRB7 indicating single domain (SD) grain dominance. It is rare to find wasp-waisted hysteresis (Figure 7.1c) such as TOM3 which is indication of SD and superparamagnetic (SPM) assemblage (Tauxe et al., 1996) in the study area. The majority of samples exhibits pot-bellied hysteresis loop (Figure 7.1d), e.g., VA7 indicating pseudo-single domain (PSD) dominance (Tauxe et al., 1996). Few samples exhibit multidomain (MD) loop behaviour (Figure 7.1e).

The strong field thermomagnetic analysis shows variations of titanium (Ti) compositions in the samples, from Ti-rich titanomagnetite to iron-rich titanomagnetite. Five types of thermomagnetic curves were found. Figure 7.2a shows Type 1 curve indicating high Ti content in the sample. The Curie temperature of Type 1 curve is low. The curve is irreversible showing mineralogical change during heating. Figure 7.2b shows Type 2 curve representing titanomaghemite samples that is a result of low temperature oxidation. A hump at 400°C is a characteristic behaviour of a metastable form of magnetic mineral (Özdemir and O'Reilly, 1982). The final stable product occurs during cooling process and is irreversible (Özdemir, 1987). Type 2 curve is commonly found in VA, HS, GS and GR (Table-C1). Figure 7.2c shows Fe-rich titanomagnetite curve (Type 3) which is reversible. The Curie temperature is nearly 580°C (Ti composition $X \approx 0$) (Hunt et al., 1995). Type 4 curve (Figure 7.2d) also represents Fe-rich titanomagnetite samples but the curve is not completely reversible. There is a sign of mineralogical change on the cooling curve. Figure 7.2e represents two-phase titanomagnetite types. The first phase magnetic mineral has lower Curie temperature (~500°C) than the second phase (~580°C). The majority of samples in Eyjafjardardalur exhibits Type 4 curve. The thermomagnetic curve is one of the selection criteria for choosing samples for palaeointensity experiment. Lava flows that exhibit Type 3 and Type 4 curves are subjected to palaeointensity measurements. A summary of the thermomagnetic curve types for individual flow is given in Table C-1 (APPENDIX C).

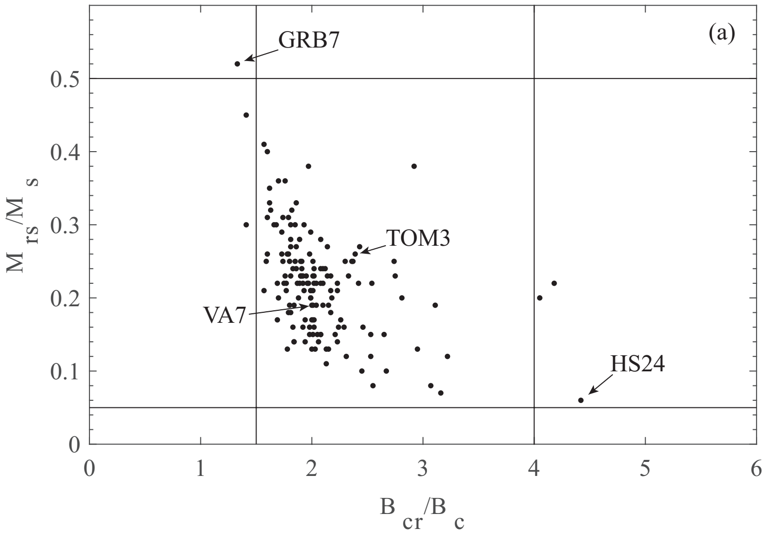

(b) GR7B

(c) TOM3

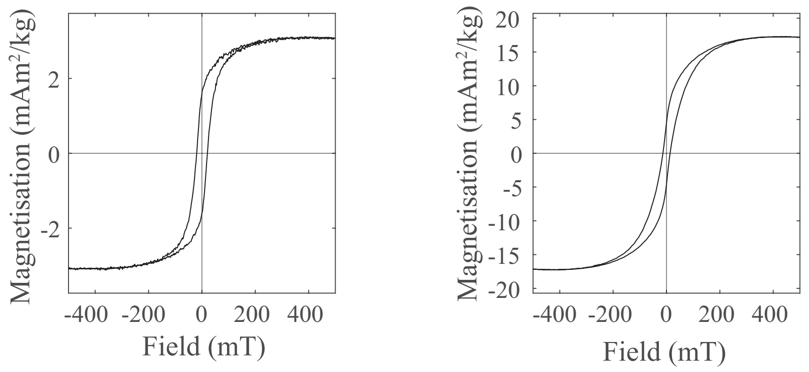

(d) VA7

(e) HS24

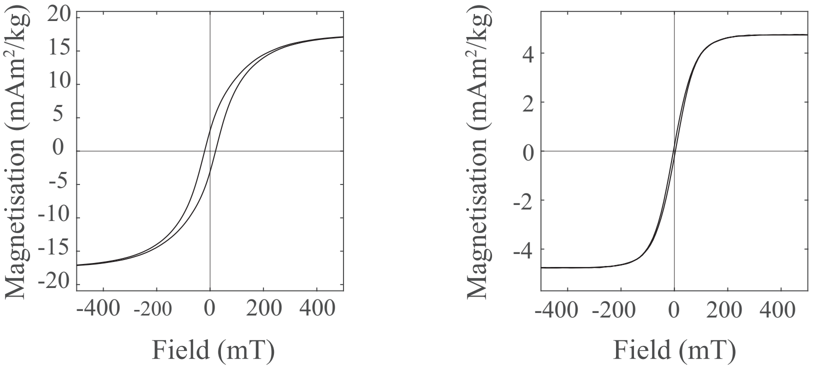

Figure 7.1: (a) A ‘Day plot’ diagram (Day et al, 1977) showing the domain state of samples from all sites. Majority of samples fell in pseudo-single domain (PSD) region. One sample fell in single domain (SD) region. (b)-(e) hysteresis loops representing (b) SD grain, (c) SD and superparamagnetic assemblage (wasp-waisted), (d) PSD grain (pot-bellied) and (e) multidomain (MD). The TOM3 fell in PSD region of Day’s plot but hysteresis loop is wasp-waisted. This suggests there could be mixture of PSD grain in the sample.

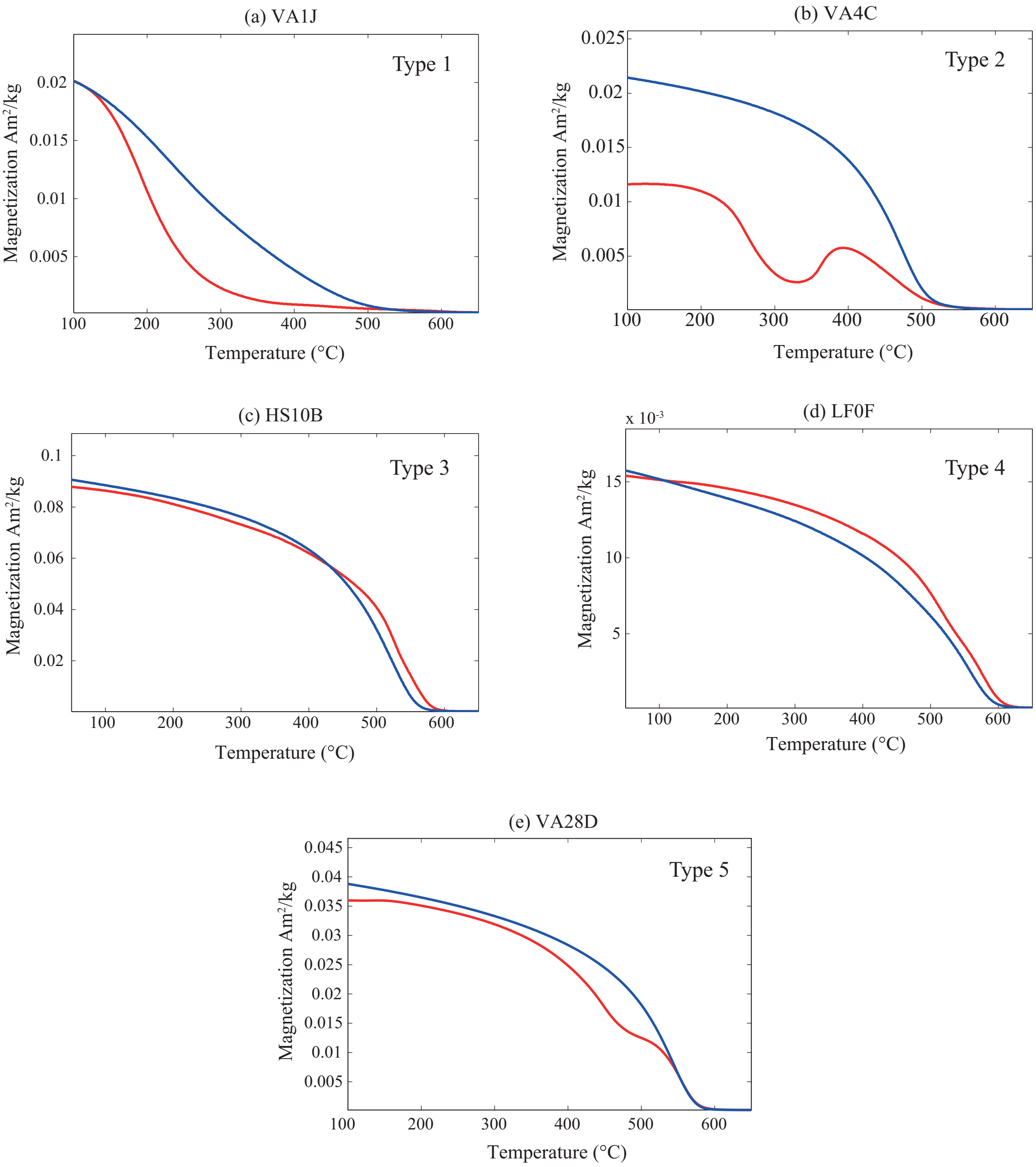

Figure 7.2: Thermomagnetic behaviour of the samples. Red and blue curves represent heating and cooling processes. (a) Type 1 irreversible curve showing low Curie temperature sample with small alteration during the cooling process, (b) Type 2 curve showing titanomaghemite sample resulting from low-temperature oxidation, (c) Type 3 reversible curve indicating Fe-rich titanomagnetite with high Curie temperature, (d) Type 4 nearly reversible curve indicating Fe-rich titanomagnetite with small alteration on the cooling curve and (e) Type 5 curve representing 2-phase magnetic minerals: low and high Curie temperature.

7.4 Palaeointensity experiment

7.4.1 Palaeointensity methods and assessment of reliable samples

A step-wise heating protocol by Thellier-Thellier (Thellier and Thellier, 1959) with modifications by Coe (1967) and Aitken et al. (1988) was used to determine the palaeointensity estimations. For the present study, I used the infield-zero field and zero field-infield (IZZI) protocol (Tauxe and Staudigel, 2004). The specimens' natural remanent magnetisations (NRM) were measured using an AGICO JR5A spinner magnetometer prior to the step-wise heating protocol. The normal and reverse polarity magnetisations of the specimens were used to decide sample alignments during the infield steps of the IZZI protocol, i.e., the applied field direction was < 90˚ from the NRM direction. This procedure was carried out to avoid effects of antiparallel angles between NRM direction and an applied laboratory field direction which cause the zig-zagging on palaeointensity data. Then, specimens were placed in quartz sample boats. One quartz boat can contain ~30 specimens. The quartz boat was placed in an ASC thermomagnetic oven and sealed within an attached furnace. Helium was saturated in the furnace ~10 minutes prior to the heating. This experiment was performed in the helium atmosphere in order to minimise chemical alteration of the samples. Subsequently, the samples were heated in a zero field (Z) environment, and then the specimens were heated to the same temperature with the previous heating step in an applied field (in-field, I) of 30 μT along the z-axis of the cores. The ZI was switched to IZ for the next elevated heating step (Tauxe and Staudigel, 2004). Partial thermoremanent magnetisation (pTRM) checks (Coe et al., 1978) and pTRM tail checks (Riisager and Riisager, 2001) were applied to the IZZI protocol to detect alteration of the samples and MD grains. It takes approximately three hours to complete one cycle of heating/cooling for one quartz boat, yielding two and a half to three months to complete determination of 60 samples in two batches.

In an assessment of reliable specimens for the palaeointensity experiment, a total 191 cores from 151 lava flows were chosen as pilot samples, i.e., all T_c types were tested in the pilot palaeointensity runs. Flows VA27, GR21, GR26, GR31 and BO14 were not included in the pilot experiment as all the specimens were used in the palaeodirection measurements. Fifteen samples with low Curie temperatures (T_c), were heated from 100°C to 300°C with a temperature interval of 25 °C. The remaining samples with high T_c were heated from 100°C to approximately 620°C or until the NRM drops below 5%. The NRM remaining was plotted against the pTRM gain on an Arai plot (Nagata et al., 1963). The palaeointensity was determined by determining the gradient of a fitted slope to the Arai plot. In order to select reliable palaeointensity estimates, selection criteria were applied to the palaeointensity data. There is currently no standard procedure for choosing the selection criteria; this is true for both the criteria themselves and the cut-off values for these criteria. The two sets of criteria are essentially (though not always) based around two commonly used palaeointensity programs: the ThellierTool program version 4.22 (Leonhardt et al., 2004a) (origin Munich), and the Thellier_GUI program (Tauxe et al., 2016) (origin SCRIPPS). The cut-off values also change with time, with constant modifications. Probably the most comprehensive current analysis of criteria and cut-off limits is that of Paterson et al. (2014). As a result many studies use different criteria suitable to their own dataset; for example, Selkin and Tauxe (2000) applied very strict SCRIPPS criteria to submarine basaltic glass data that is dominated by single domain (SD) magnetite. Døssing et al. (2016) used the same set of SCRIPPS criteria as other high-latitude studies have applied (e.g., Lawrence et al., 2009; Cromwell et al., 2013b) in order to compare Iceland data with those studies; these criteria are less strict than that of Selkin and Tauxe (2000). Stanton et al. (2011) applied Munich criteria to Icelandic lavas dominated by pseudo-single domain (PSD) grains. Stanton et al. (2011) showed that the Thellier criteria works well with the PSD samples from Iceland. As majority of samples in this study falls within PSD region on the Day's plot (Day et al., 1977), here I use the modified Munich criteria (Paterson et al., 2014), which are slightly looser than the original Munich criteria to evaluate data quality in this study (Table 7.1).

A total of 78 pilot specimens from 67 lava flows run using high-temperature protocol passed the selection criteria, however, all 15 samples measured using the low-temperature protocol (100 – 300°C) failed the palaeointensity experiment. Because palaeointensity measurements are very time-consuming, before continuing to the "production" run palaeointensity experiments, I considered both the pilot palaeointensity results and rock magnetic measurements to make a considered judgement of which samples to dedicate my time to. With these data, a simple selection method was designed to choose the most reliable samples. Samples that show Type 1 thermomagnetic curves were rejected. Titanomaghemite samples (Type 2 curves) were accepted if the degree of inversion on the thermomagnetic curves was small, i.e., nearly reversible curves. All iron-rich titanomagnetite samples (Type 3 reversible curves) were accepted. Iron-rich titanomagnetite samples (Type 4 irreversible curves) and two-phase magnetic minerals were rejected if the cooling curves showed large degree of inversions. In addition, samples that yielded successful results from the pilot palaeointensity runs and thermal demagnetisation experiments were also considered. The details of thermomagnetic curves, and successful pilot palaeointensity runs and thermal demagnetisation experiments are given in Table C-1 (Appendix C). Weighting scores were given to thermomagnetic curves (35%), pilot palaeointensity runs (40%) and thermal demagnetisation runs (25%). The pilot palaeointensity runs and thermomagnetic curves were given the highest and the second highest scores because these experiments were performed in the helium atmosphere, while thermal demagnetisation experiments were conducted in air; the thermal demagnetisation data had a higher risk of chemical alterations and deemed less reliable. If individual sites met 65% of the maximum score, they were selected for the production palaeointensity runs. List of accepted and rejected flows are summarised in Table C.1 (Appendix C). A total of 348 samples from 65 sites were chosen as potentially reliable samples for palaeointensity experiment. Of these, 81 samples were run in the neutral air environment because a transformer in the helium oven broke between March and April 2017; I had to use the larger dual chamber ASC oven for these experiments. It is not possible to heat in He using this oven. The high-temperature protocol was also modified from the pilot runs so that the majority of steps were concentrated in the region of bulk demagnetisation. A 100 °C step was applied from 100 °C to 400 °C, decreasing to 50 °C and 25 °C between 400 °C and 500 °C. Then, 10 °C step was applied above 500 °C until the NRM was completely removed. Six to seven pTRM checks and three pTRM tail checks were applied to the protocol. The palaeointensity experiment began in April 2015 and ended in August 2017, yielding a total of 17 batches of 539 specimens. The experiments were not conducted continuously.

Table 7.1: Palaeointensity selection criteria of modified Thellier Class A (TTA) and B (TTB), as in Paterson et al. (2014), where n is number of points used to estimate the best-fit line on the Arai plot, f is the NRM fraction used for the best-fit line, β is the ratio of standard error of the slope to absolute value of the slope, q is the quality factor used to measure the quality of the palaeointensity estimates. MAD_{ANC} represents the maximum angular deviation of the anchored best-fit line to the palaeomagnetic directions (Kirschvink, 1980) on the Zijderveld diagram (Zijderveld, 1967) and α represents the angular difference between the MAD_{ANC} and the MAD of the free-floating best-fit line. The criteria of δCK and δpal are the maximum absolute difference produced by the pTRM check normalised by the total TRM and the measurement of cumulative alteration. The variables δTR and δt* represent the maximum absolute difference produced by the pTRM-tail check normalised by the total TRM and the extent of the pTRM tail after correction for angular dependence (Leonhardt et al., 2004a).

Criterion	n	f	β	q	MAD_{ANC}	α	δCK	δpal	δTR	δt*
Modified TTA	5	0.35	0.10	5	6	15	7	10	10	9
Modified TTB	5	0.35	0.15	0	15	15	9	18	20	99

7.4.2 Palaeointensity results

After the high-temperature run, approximately 45% (242 samples) of the samples from 54 lava flows in seven rock sections yielded successful palaeointensity estimates. No samples from the BT section are represented here because none of the BT data met the minimum requirement of the sample selection criteria defined above. All BT data exhibit straight line behaviour on the Arai plot, but fail the pTRM checks, indicating that alterations occur during the step-wise heating process (e.g., Figure 7.8g). With regards to successful samples, there is diversity in sample behaviour as seen on the Arai plots due to non-ideal MD grains in the samples. Figure 7.3-7.6 represents examples of Arai plots, with inset figures showing vector end point diagrams (Zijderveld, 1967) and NRM decay plots. A total of 21 lava flows exhibited straight line or nearly straight line (Figure 7.3), which is ideal for palaeointensity estimate. The Zijderveld diagrams of these samples show linear or near-linear behaviour toward the origin indicating no overprint at high temperature steps, while the NRM was completely removed below 5% during the step-wise heating protocol. However, the difficulty of palaeointensity estimation arises when specimen behaviour departs from the ideal straight line, e.g., concave-up curve (Figure 7.4a-b), s-shaped curve (Figure 7.4c-d) and zigzag line (Figure 7.5). A total of 18 lava flows exhibits curved behaviour but passed all the selection criteria. MD grains are well-known in generating concave-up curves, convex curves and s-shape curves on the Arai plot (e.g., Levi, 1977; Biggin and Thomas, 2003; Leonhardt et al., 2004b; Xu and Dunlop, 2004). Fitting the low-temperature component yields high palaeointensity estimates, while fitting the high-temperature component results in low palaeointensity estimates. Here, I selected segments as large as possible to determine the ancient field even though the Arai plots are slightly curved or zig-zagged (e.g., Biggin and Thomas, 2003). Flow TO5 exhibits a concave-up curve with zig-zag behaviour (Figure 7.5c), while Flow GRA33 shows a convex-down curve with zig-zag behaviour (Figure 7.5d). It has been shown that laboratory conditions such as large angles between the NRM and the applied laboratory TRM can contribute to zig-zag behaviour on the Arai plot (e.g., Shaar et al., 2011; Paterson et al., 2015). Seven flows exhibited within-flow variations of sample behaviour; some specimens exhibit concave-up curves while some specimens displayed ideal straight lines (Figure 7.6). Table 7.2 summarises the diversity of the Arai plots observed in this study. Specimen-level palaeointensity data used in site-mean intensity calculation are given in Table 7.3.

Table 7.2: Summary of sample behaviour on the Arai plot for lava flows that passed the modified Thellier selection criteria.

Arai plot types	Flows	Total
Straight line	HS5, GRA25, GR29, GR32, GR33, TO3, BO1, BO5, BO10, BO13	10
Nearly straight line	VA5, HS3, HS13, GS1, GR19, GR22, LF1, LF7, TO1, TOM3, TO8	11
Concave-up curve	VA3, VA6, HS8, HSB18, GR4, LF0, LF2, LF4, TO6, TO7, TO11, TO12	12
S-shape	VA2, VA35	2
Zigzag	HSJ18, TOM1	2
Concave-up and zigzag	TO5	1
Convex and zigzag	GRA33	1
Two-behaviour within lava flows	VA7, VA30, VA31, HS11, GS3, TO9, BO12	7

In order to assess quality of site mean palaeointensity, the following criteria were applied:

- Site mean intensity is averaged over at least two samples per lava flow ($N \geq 2$).
- Per cent fraction of standard deviation $\left(d\sigma_B = \frac{\sigma_B}{B} \times 100\right)$, where σ_B is the standard deviation of the site mean intensity (B), must not exceed 15%. This criterion is set to be very strict because the results of this study will be compared with other high-latitude studies that used this same criterion (e.g., Lawrence et al., 2009; Cromwell et al., 2013b).

A word of caution of using the second criterion is that if the $d\sigma_B$ is set too high, the $d\sigma_B$ can cause bias to the high intensity data; for example, Selkin and Tauxe (2000) applied a $d\sigma_B = 25\%$ to omit outlier data, using a $d\sigma_B$ of 25% allows the mean intensity of 50 µT to vary from 37.5 µT to 62.5 µT, but only allows the mean intensity of 10 µT to vary from 7.5 µT to 12.5 µT. Given the errors in the method this absolute difference can be limiting, resulting in frequent rejection of weak intensity. A total of 46 lava flows passes the selection criteria defined above. Site-mean palaeointensities for 54 lava flows are presented in Table 7.4. Sites that are marked bold in the table are accepted sites with $d\sigma_B \leq 15\%$. The mean palaeointensity of this study, derived from 46 lava flows is 26.9 ± 1.8 µT. The virtual dipole moment (VDM) is calculated following Equation 7.1:

$$VDM = \frac{4\pi r^3}{\mu_0} B_{anc}(1 + 3\cos^2\theta)^{-1/2} \tag{7.1}$$

where r is the Earth's radius and θ is the magnetic co-latitudes. The virtual axial dipole moment (VADM) can be calculated from Equation 7.1. If site palaeolatitudes (Chapter 4) are entered instead of geographical latitudes, the virtual dipole moment (VDM) can be calculated. The VDM and VADM of this study are 41.4 ± 2.5 ZAm^2 and 37.4 ± 2.5 ZAm^2; slightly lower than the mean VADM of 42 ZAm^2 for the window 0-140 Myr data (Tauxe et al., 2013) and 46 ZAm^2 for window 0.3-300 Myr data (Selkin and Tauxe, 2000).

To put the new and robust palaeointensity data from high-latitudes to meet the standard of the palaeomagnetic community, the site-level mean intensities in Table 7.4 are graded using the Q_{PI} criteria: AGE, STAT, TRM, ALT, MD, CAN, TECH and LITH (Biggin and Paterson, 2014) (see Chapter 2 for descriptions and minimum requirements of each criterion). The Q_{PI} criteria are used in the community as a means of gauging the reliability of the dipole moment estimates. Here each Q_{PI} criterion is scored as ‘1’ if the site meets the requirement of that criterion and ‘0’ if the site fails the requirement of that criterion. The Q_{PI} criteria of this study are given in Table 7.4. The total Q_{PI} scores are also given in the last column of Table 7.4. Below shows an example how to grade the Q_{PI} criteria. For example, VA1 meets the requirements of AGE, STAT, ALT and MD:

AGE: VA1 was selected for the isotopic dating. Therefore, the reliable numerical age is confirmed. The Q_{PI} requires researchers to provide absolute or relative ages of the sites in order to tract palaeomagnetic dipole moment. This also extends to all sites in this study as the palaeodirections provide reliable data which coincide with the GTS2012 (Ogg, 2012).

STAT: VA1 meets this criterion as the site-mean intensity with $d\sigma_B \leq 15\%$ was averaged from 10 specimens. The STAT suggests the minimum number of specimens per site for averaging site-mean intensity must be at least five and the $d\sigma_B$ must be ≤ 25%. As the palaeointensity yields low successful rate, some sites in this study fail this criterion as the site-mean intensity is calculated from $N < 5$.

ALT and MD: VA1 and all other sites in this study pass these criteria as the pTRM check for checking alteration and pTRM-tail check for detecting non-ideal SD grain were measured in all heating protocols.

All sites in this study fail the TRM, ACN, TECH and LITH criteria (Table 7.4). The TRM criterion requires only microscopic study to confirm that the remanent component in the bulk of specimens is likely a TRM. The anisotropy of the TRM was not measured in this study to meet the ACN criterion. The TECH criterion requires at least two palaeointensity methods, e.g., Thellier-Thellier modified by Coe method (Coe, 1967) together with Shaw method (Shaw, 1974) to confirm consistency between two results from the same rock unit. As the palaeointensity is time-consuming, I performed only the Thellier-Thellier modified by Coe method which do not satisfy the TECH criterion. The most difficult criterion to meet is LITH. The LITH requires the palaeointensity estimates from more than one lithology or the same lithology that specimens have different unblocking temperature. As noticed by Biggin and Paterson (2014), ~30% and ~17% of palaeointensity studies pass the TRM and TECH, while only ~1% and 2% of the studies meet the ACN and LITH criteria (Biggin and Paterson, 2014).

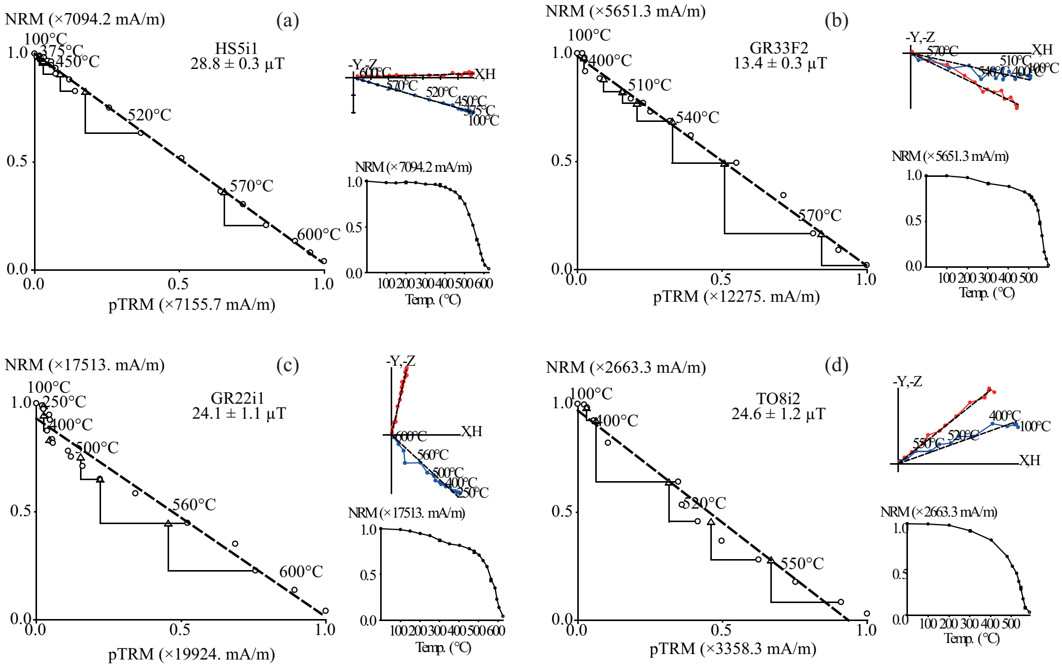

Figure 7.3: Examples of Arai plots with inset Zijderveld diagrams and NRM decay plots for (a)-(b) straight line and (c)-(d) nearly straight behaviour. The sample names are listed on the plot. Triangles on the Arai plots represent the pTRM checks and squares on the NRM decay plot show the pTRM-tail checks. Red (blue) lines on Zijderveld plots show the declination (inclination).

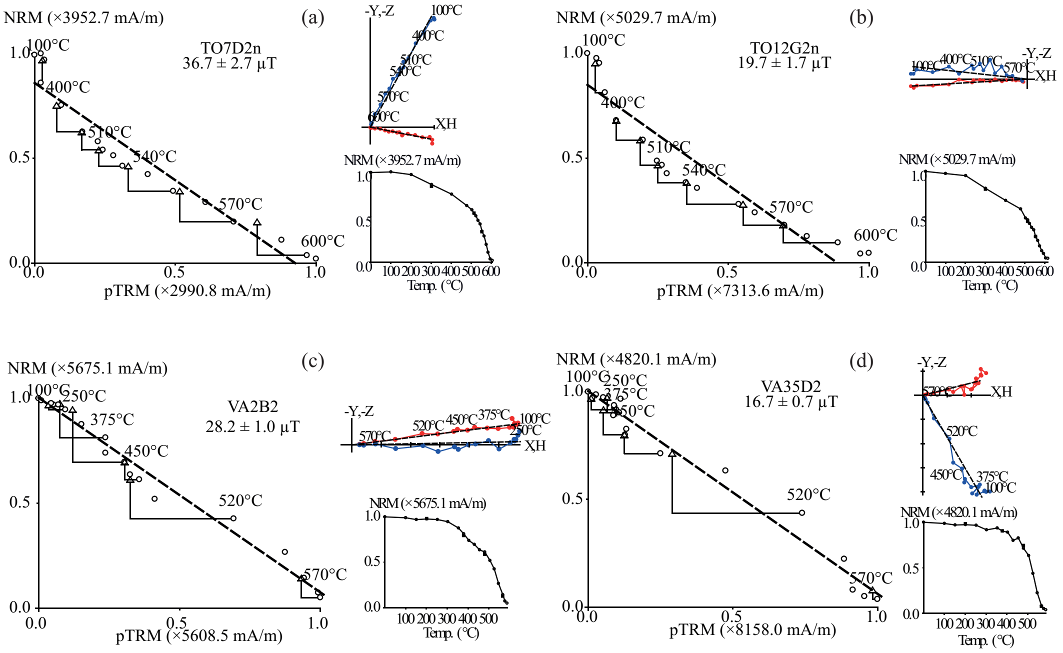

Figure 7.4: Examples of Arai plots with inset Zijderveld diagrams and NRM decay plots for (a)-(b) concave-up curves and (c)-(d) s-shape curves. The sample names are listed on the plot. Triangles on the Arai plots represent the pTRM checks and squares on the NRM decay plot show the pTRM-tail checks. Red (blue) lines on Zijderveld plots show the declination (inclination).

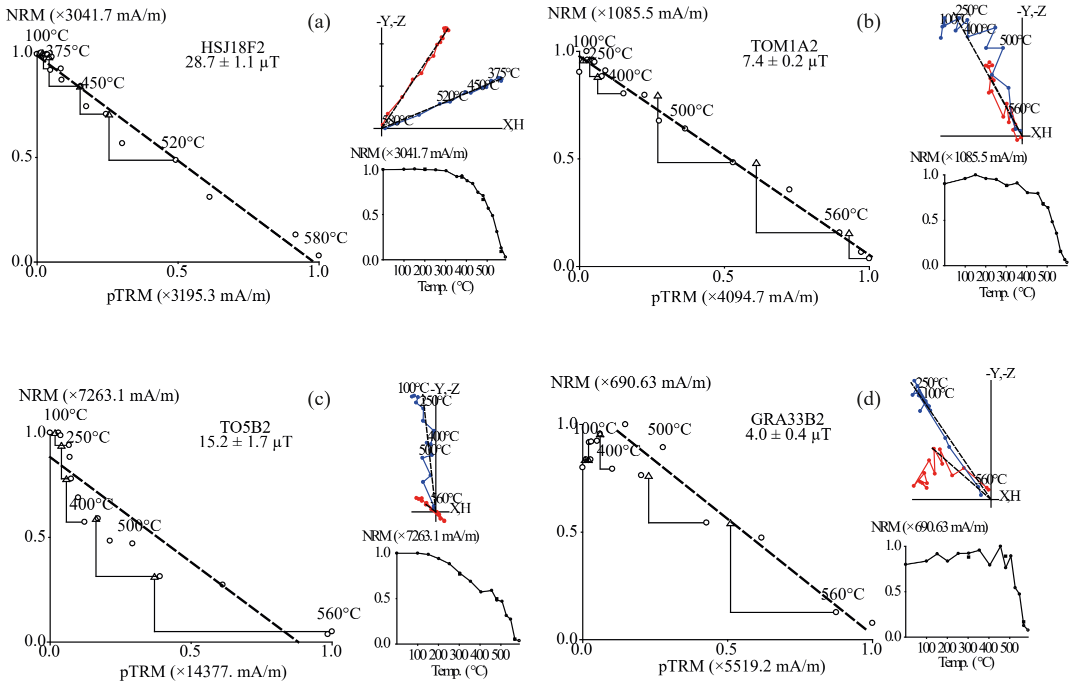

Figure 7.5: Examples of Arai plots with inset Zijderveld diagrams and NRM decay plots for (a)-(b) zigzag line, (c) concave-up curve + zigzag line, and (d) convex-down curve + zigzag line. The sample names are listed on the plot. Triangles on the Arai plots represent the pTRM checks and squares on the NRM decay plot show the pTRM-tail checks. Red (blue) lines on Zijderveld plots show the declination (inclination).

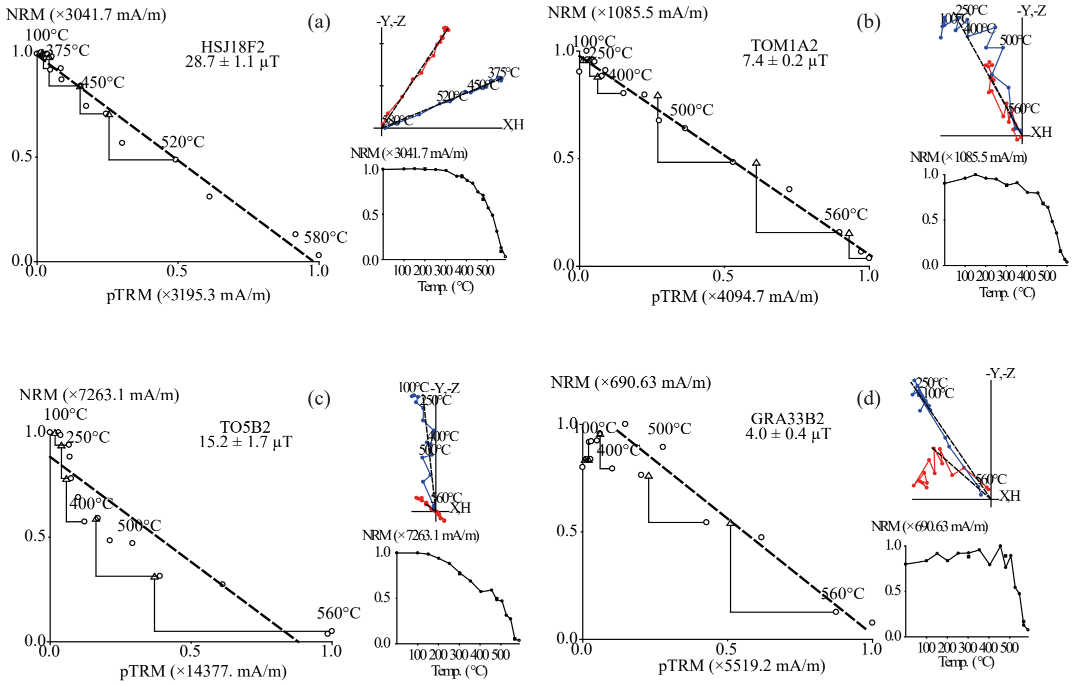

Figure 7.6: Examples of Arai plots with inset Zijderveld diagrams and NRM decay plots for samples that show variations within lava flows. (a) and (c) concave-up curves, and (b) and (d) straight lines. The sample names are listed on the plot. Triangles on the Arai plots represent the pTRM checks and squares on the NRM decay plot show the pTRM-tail checks. Red (blue) lines on Zijderveld plots show the declination (inclination).

Figure 7.7 shows the Arai plots of the pilot samples run in low-temperature protocol. All samples with low Curie temperature alter during step-wise heating and are deemed unreliable for palaeointensity estimates. Figure 7.8 shows representative samples that failed palaeointensity experiment from eight rock units in the pilot high-temperature run. Samples that failed the pilot palaeointensity experiment, usually showed signs of alteration during the step-wise heating experiment leading to scattered data points on the Arai plots (Figure 7.8a-d). Some samples exhibited different types of palaeointensity failure, having straight lines (Figure 7.8e-g) or concave-up curves (Figure 7.8h), but failing the pTRM checks, indicating the samples lost capability to acquire the laboratory thermoremanent magnetisation (TRM).

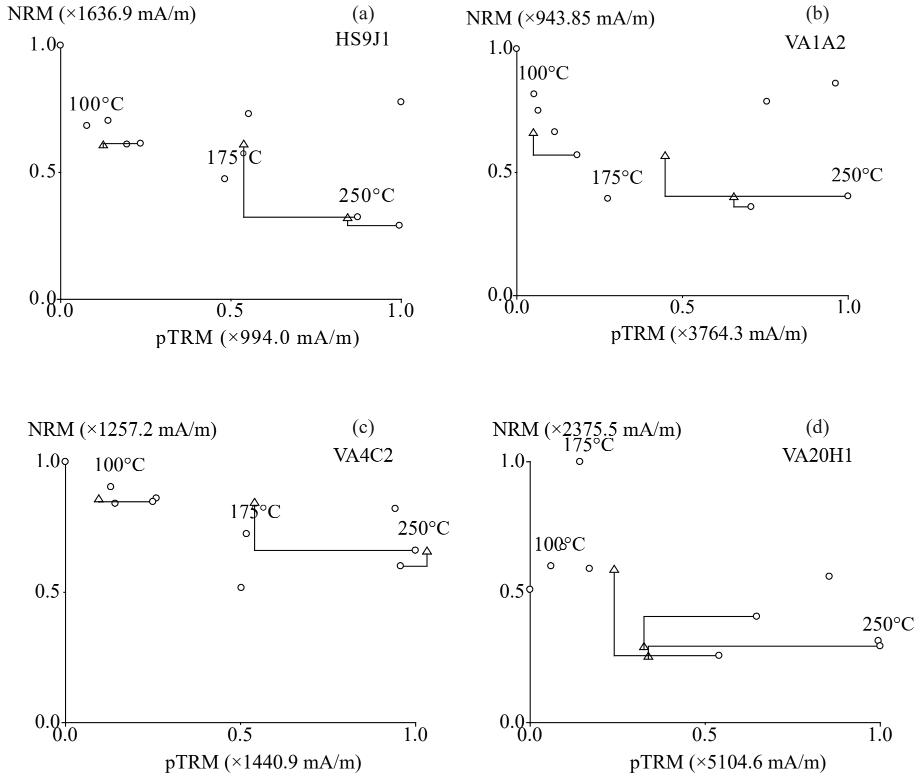

Figure 7.7: Examples of Arai plots representing samples that fail palaeointensity experiment during low-temperature pilot run, pTRM checks are given as triangles.

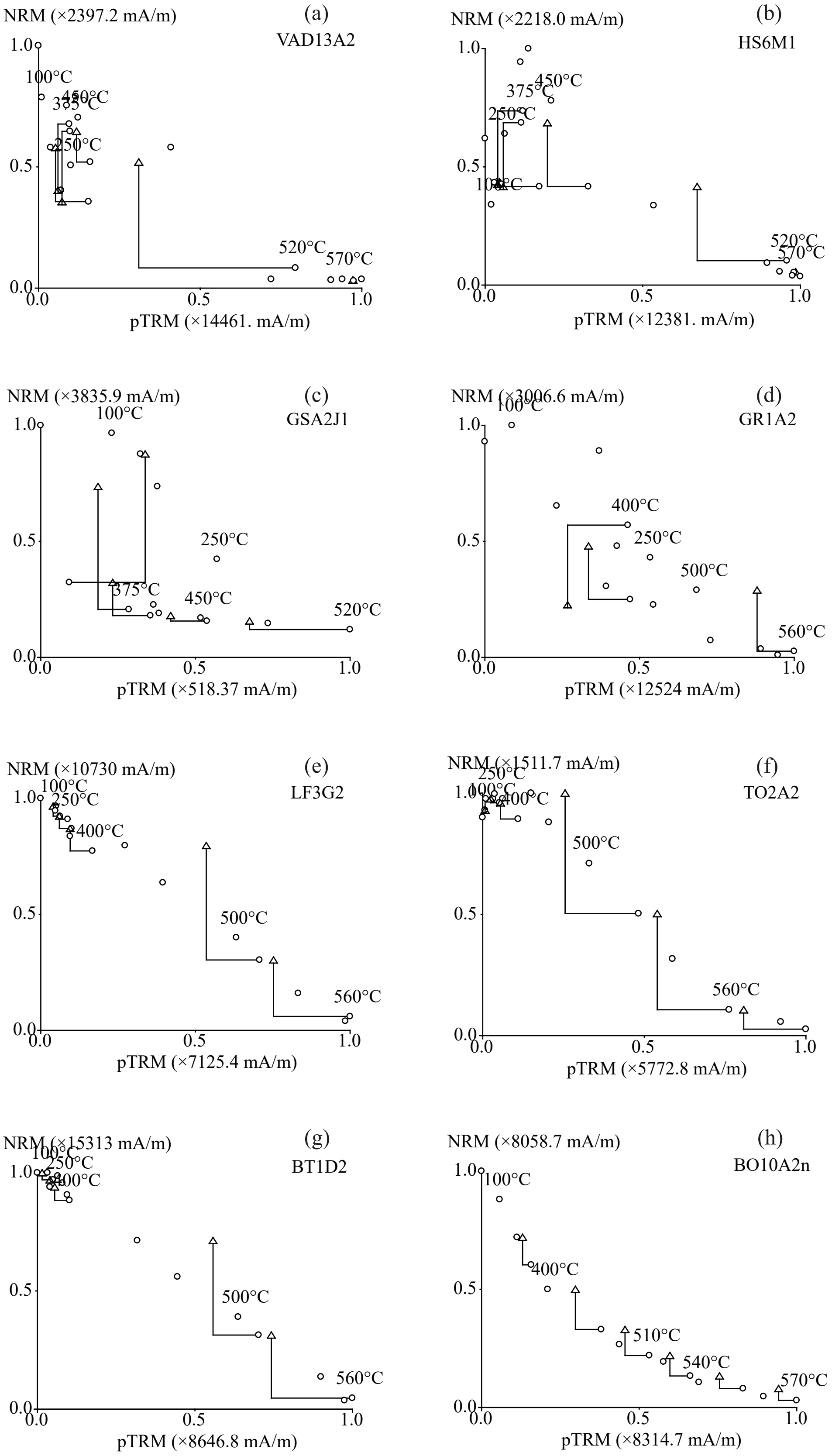

Figure 7.8: Examples of Arai plot for samples that fail palaeointensity experiment during high-temperature pilot runs, pTRM checks are represented as triangles.

Table 7.3: Individual sample palaeointensity estimates using the IZZI protocol. All listed samples pass the modified Thellier criteria of Paterson et al. (2014).

Name	B (μT)	σ (μT)	ΔT (°C)	N	f	β	k	q	MAD (°)	α	δCK	δpal	δTR	δt*	Class
VA2A2	23.4	0.8	0-590	19	0.98	0.88	0.17	25.1	2.7	1.8	3.8	8.0	2.0	3.0	A
VA2B2	28.2	1.0	0-580	18	0.94	0.90	0.13	24.8	2.4	1.8	3.0	1.1	2.5	4.3	A
VA2C2	34.2	1.6	0-580	18	0.99	0.89	0.39	19.3	2.1	1.5	3.2	2.1	2.3	4.3	A
VA2D2	34.9	1.6	0-580	18	0.99	0.89	0.39	19.0	2.5	1.5	2.7	1.9	2.7	4.0	A
VA2E2	29.4	1.3	0-580	18	1.00	0.88	0.42	19.7	2.7	2.0	7.1	7.1	5.6	3.3	B
VA2G2	28.4	1.2	0-580	18	1.00	0.87	0.38	21.3	2.6	2.0	5.2	6.4	5.6	2.7	A
VA2H1	30.4	1.3	0-580	18	1.00	0.88	0.42	20.1	2.2	1.7	3.4	3.8	6.2	3.2	A
VA2i1	28.9	1.2	0-580	18	1.00	0.87	0.39	21.1	2.5	1.7	3.8	2.9	2.9	3.0	A
VA2J1	30.1	1.3	0-580	18	1.00	0.88	0.39	21.0	2.5	1.7	3.6	5.2	5.9	4.5	A
VA2K2	31.3	1.2	0-570	17	1.00	0.88	0.32	23.3	2.0	1.6	6.7	6.8	1.2	0.0	A
VA3F2	34.8	1.7	0-580	17	1.00	0.85	0.45	17.5	1.4	1.1	2.3	5.9	5.4	4.1	A
VA3H2	34.1	1.7	0-580	17	1.00	0.85	0.46	17.2	1.7	1.4	2.5	4.6	5.6	3.4	A
VA3i1	36.0	2.2	0-540	10	0.85	0.84	0.48	11.8	2.0	3.1	8.4	6.9	0.9	2.5	B
VA3J1	39.3	3.1	0-540	10	0.86	0.84	0.58	9.0	2.4	3.4	6.9	0.2	1.3	4.2	A
VA5A2	16.3	1.0	0-580	17	0.99	0.84	0.57	13.0	5.8	5.2	5.2	3.8	3.3	2.5	A
VA5B2	15.3	1.0	0-590	19	1.00	0.85	0.68	13.3	5.5	3.3	7.7	2.8	1.3	3.3	B
VA5D2	12.7	0.7	0-580	17	0.98	0.82	0.44	14.1	6.3	3.5	5.6	3.6	3.4	2.0	B
VA5E2	13.4	0.9	0-580	17	0.98	0.85	0.40	12.9	5.8	4.0	5.4	2.1	3.3	2.1	A
VA5F2	12.4	0.4	0-600	15	0.97	0.89	-0.07	24.2	9.5	4.1	6.3	10.6	5.0	4.0	B
VA5G1	11.3	0.5	0-580	17	0.98	0.85	0.002	19.2	7.5	3.8	8.1	6.3	6.7	4.0	B
VA5J2	13.9	0.9	0-530	10	0.68	0.82	-0.16	8.3	6.4	7.5	8.8	4.4	4.2	4.5	B

…continue from previous page…

Name	B (μT)	σ (μT)	ΔT (°C)	N	f	β	k	q	MAD (°)	α	δCK	δpal	δTR	δt*	Class
VA6B2	29.0	1.3	0-590	19	1.00	0.86	0.48	19.7	2.5	1.6	3.8	6.9	2.2	4.6	A
VA6C2	21.0	0.6	300-580	13	0.92	0.83	0.39	26.3	3.7	1.6	9.0	11.3	3.7	5.6	B
VA6D2	24.2	1.2	0-580	18	1.00	0.86	0.49	17.8	3.6	2.5	7.3	9.4	3.6	5.8	B
VA6H2	26.8	1.8	0-580	18	1.00	0.85	0.70	12.6	2.9	2.1	4.6	8.0	2.3	4.7	A
VA6i2	25.2	1.9	0-580	18	1.00	0.85	0.78	11.4	3.3	2.4	5.3	6.9	2.1	5.3	A
VA7A2	22.8	0.9	0-600	20	1.00	0.89	0.49	22.9	2.1	1.5	5.2	0.0	1.5	6.2	A
VA7B2	24.7	1.5	0-580	18	1.00	0.88	0.62	15.0	2.2	1.9	6.5	1.3	1.4	4.2	A
VA7C2	23.5	1.1	0-580	18	1.00	0.88	0.50	19.3	2.3	2.1	7.0	5.4	1.6	3.8	A
VA7D2	22.0	1.1	0-580	18	1.00	0.89	0.55	17.8	2.6	2.1	8.2	12.8	0.9	5.3	B
VA7E2	23.6	1.5	0-580	18	1.00	0.89	0.67	14.0	2.4	2.3	6.3	4.8	2.1	2.2	A
VA7F2	23.7	1.5	0-590	19	1.00	0.90	0.69	14.2	2.2	2.3	6.0	0.9	2.3	2.5	A
VA7H2	20.0	0.4	0-590	19	0.96	0.88	0.19	41.3	2.3	1.9	3.9	1.3	3.0	2.5	A
VA7i2	17.6	1.4	0-540	10	0.91	0.83	0.60	9.4	6.0	5.0	8.0	10.1	3.4	5.2	B
VA11F1	17.0	0.6	0-600	20	0.95	0.89	-0.14	22.8	2.0	1.3	5.2	7.2	2.7	2.3	A
VA11H1	5.5	0.4	0-570	17	1.00	0.70	0.50	10.2	13.0	4.4	7.1	0.4	21.9	0.4	C
VA12B2	11.7	0.6	250-590	15	0.99	0.81	0.57	16.3	4.7	0.9	7.0	10.0	0.7	3.6	A
VA12J2	4.9	0.2	375-580	10	0.90	0.72	0.85	20.4	8.1	1.9	2.4	0.5	3.5	3.7	B
VA15C2	5.8	0.5	0-540	15	0.94	0.69	0	7.6	7.1	6.3	5.6	4.0	18.7	3.4	B
VA15E1	8.0	0.7	0-560	16	0.95	0.73	0.87	7.4	4.6	3.8	5.5	6.4	6.0	0.6	A
VA15G2	8.1	0.9	0-560	16	0.96	0.76	1.02	6.3	7.3	9.3	5.9	7.4	7.5	5.5	B

…continue from previous page…

Name	B (μT)	σ (μT)	ΔT (°C)	N	f	β	k	q	MAD (°)	α	δCK	δpal	δTR	δt*	Class
VA28A2	11.6	0.2	150-600	18	0.75	0.86	-0.14	43.5	2.4	5.2	1.7	0.2	2.0	1.7	A
VA28F1	7.7	0.3	0-580	15	0.89	0.85	-0.31	17.0	6.7	1.4	7.4	7.9	6.7	3.6	B
VA30B2	13.5	0.9	0-570	17	1.00	0.87	0.63	13.7	5.8	5.6	3.6	2.8	1.2	3.4	A
VA30C2	14.0	1.0	0-560	16	1.00	0.86	0.61	12.4	7.3	8.1	6.4	3.4	4.2	3.3	B
VA30D2	16.3	1.4	0-560	16	1.00	0.87	0.75	10.2	7.0	8.3	3.5	0.8	4.1	2.6	B
VA30E2	13.4	1.0	0-560	16	1.00	0.86	0.64	11.5	6.1	6.9	8.3	7.1	2.7	3.0	B
VA31A2	23.8	1.7	0-620	21	1.00	0.92	0.71	12.8	1.8	1.8	3.3	7.3	2.6	2.1	A
VA31B2	22.0	1.3	0-620	21	1.00	0.91	0.60	15.2	3.9	4.4	3.4	3.0	2.5	2.0	A
VA31C2	22.0	1.5	0-620	21	1.00	0.92	0.68	13.5	1.5	1.2	4.1	4.2	2.5	2.4	A
VA31D2	22.3	1.6	0-620	21	1.00	0.92	0.71	12.9	1.5	1.5	3.1	3.7	2.9	2.8	A
VA31F2	24.3	1.8	0-620	21	1.00	0.92	0.74	12.3	1.7	1.6	4.1	7.5	2.3	3.2	A
VA31H1	21.7	1.5	0-590	18	0.94	0.89	0.66	11.9	2.3	2.6	3.8	0.0	1.9	2.8	A
VA31i1	19.8	1.0	0-590	18	0.95	0.89	0.51	16.6	2.4	3.0	3.2	1.5	2.0	2.5	A
VA31K1	23.6	2.1	0-590	18	0.91	0.89	0.82	8.9	2.4	3.3	3.1	3.0	1.8	2.4	A
VA35A2	16.7	0.7	150-570	15	0.88	0.83	-0.20	16.4	5.1	1.9	5.4	1.1	1.6	5.3	A
VA35B2	15.8	0.8	0-580	18	0.90	0.83	-0.54	15.4	4.8	1.0	5.4	0.3	4.4	1.5	A
VA35D2	16.7	0.7	0-580	18	0.95	0.86	-0.22	20.6	4.5	1.4	6.2	5.3	3.3	9.3	B
VA35E2	15.0	0.8	150-580	16	0.95	0.84	-0.12	15.7	5.8	1.6	6.6	7.9	3.2	5.7	A
VA35H2	19.1	1.4	0-580	18	1.00	0.87	0.73	11.8	3.7	2.4	6.6	6.3	1.1	14.6	B

…continue from previous page…

Name	B (μT)	σ (μT)	ΔT (°C)	N	f	β	k	q	MAD (°)	α	δCK	δpal	δTR	δt*	Class
HS3B2	20.5	0.7	0-590	19	0.96	0.88	0.08	26.2	2.8	1.5	2.6	4.4	3.1	4.7	A
HS3C2	18.2	0.6	0-580	18	0.94	0.87	0	24.0	2.8	1.3	2.8	6.7	3.3	5.0	A
HS3D2	19.3	0.7	0-580	18	0.95	0.88	0.04	23.9	2.7	1.4	3.0	4.2	3.4	4.3	A
HS3i1	19.0	0.7	0-580	18	0.91	0.88	0.27	22.7	3.0	3.1	4.5	9.7	3.9	1.9	A
HS3J1	20.9	0.7	0-600	20	0.97	0.91	0.27	27.7	2.3	1.6	3.5	0.9	3.4	3.7	A
HS3K1	18.9	0.8	0-570	17	0.98	0.85	0.29	20.2	1.8	1.0	5.1	6.1	2.8	0.6	A
HS4C2	20.0	1.3	0-540	11	0.99	0.85	0.64	13.0	5.5	6.5	5.8	8.5	3.7	3.6	A
HS4J1	14.3	0.4	0-590	19	1.00	0.90	0.26	32.4	2.7	1.4	6.5	2.2	4.7	2.2	A
HS5i1	28.8	0.3	0-620	21	0.97	0.91	0.05	102.3	0.6	0.5	3.4	7.5	1.2	1.0	A
HS5J1	29.8	0.4	0-600	20	0.96	0.90	0.11	64.7	0.8	0.5	5.9	12.1	3.1	1.3	B
HS5K1	32.0	0.4	0-620	21	0.96	0.91	0.11	63.7	0.9	0.5	3.0	7.9	2.7	2.1	A
HS5L1	33.9	0.3	0-620	21	0.96	0.90	0	89.7	0.8	0.6	2.1	3.4	3.0	2.8	A
HS7A2	8.0	0.4	350-580	11	0.95	0.78	0.62	14.0	5.9	2.6	6.0	3.8	4.9	4.2	A
HS7C2	10.7	0.6	375-580	10	0.94	0.80	0.37	14.1	4.9	2.9	4.9	2.9	2.8	3.0	A
HS7J1	4.9	0.2	500-590	7	0.85	0.65	0.35	13.2	10.4	2.7	6.7	9.1	9.9	1.5	B
HS8A2	16.6	1.0	0-590	18	1.00	0.86	0.73	13.7	5.4	5.8	3.7	3.5	2.4	4.6	A
HS8B2	15.1	0.9	0-590	18	1.00	0.85	0.67	14.7	5.8	5.5	4.3	3.2	1.1	4.7	A
HS8C2	15.2	0.9	0-590	18	1.00	0.85	0.66	15.1	5.5	5.1	4.3	3.7	1.2	4.5	A
HS8D2	16.1	1.0	0-590	18	1.00	0.85	0.71	13.2	4.8	4.3	4.8	3.6	1.9	4.4	A
HS8G2	16.0	1.0	0-590	18	0.98	0.85	0.75	12.9	5.4	5.4	3.0	1.8	3.9	3.9	A
HS8i2	12.6	0.6	0-580	15	0.95	0.87	0.40	17.5	8.8	8.2	6.4	5.3	2.1	2.4	B
HS8K1	10.8	0.6	0-590	19	0.99	0.85	0.68	14.4	7.1	6.1	4.7	0.9	1.0	4.8	B

…continue from previous page…

Name	B (μT)	σ (μT)	ΔT (°C)	N	f	β	k	q	MAD (°)	α	δCK	δpal	δTR	δt*	Class
HS11B	61.2	4.2	0-590	19	0.99	0.87	0.68	12.5	1.2	1.0	3.8	2.5	3.0	4.9	A
HS11D2	58.1	2.6	0-600	20	0.97	0.89	0.51	19.4	1.1	1.0	1.8	2.1	2.9	5.9	A
HS11F	56.0	2.0	0-590	19	0.94	0.88	0.25	23.1	1.1	0.9	6.0	2.9	2.9	2.8	A
HS11J2	54.1	1.3	0-620	21	0.93	0.91	0.15	35.4	1.8	0.9	1.4	3.5	3.5	11.7	B
HS11K1	48.9	0.7	0-620	21	0.94	0.91	0.10	58.4	1.1	0.5	3.6	3.1	2.5	5.6	A
HS13D2	18.2	0.6	0-560	16	0.98	0.79	0.22	23.8	3.3	2.9	5.4	9.7	1.1	4.7	A
HS13E2	21.1	0.8	0-570	17	1.00	0.81	0.26	22.0	3.3	2.8	2.7	0.7	4.2	8.8	A
HSB18A2	22.0	2.1	0-580	17	1.00	0.81	0.87	8.5	1.8	2.0	2.9	3.2	3.4	3.8	A
HSB18H2	23.8	2.0	0-580	16	1.00	0.87	0.74	10.5	2.3	2.9	8.5	10.4	5.3	5.5	B
HSB18i2	24.9	2.1	0-580	17	1.00	0.87	0.76	10.2	2.3	3.5	6.9	5.3	4.4	4.5	A
HSJ18E2	29.4	1.3	0-580	17	1.00	0.86	0.35	20.0	1.1	1.3	3.5	0.4	4.1	1.2	A
HSJ18F2	28.7	1.1	0-580	17	1.00	0.87	0.33	21.9	1.3	0.9	1.2	2.1	4.2	1.0	A
HSJ18G2	29.5	1.3	0-580	17	1.00	0.87	0.34	20.5	1.3	1.2	2.0	1.3	4.7	6.0	A
HSJ18K2	21.3	1.1	0-580	17	1.00	0.86	0.48	16.3	1.5	1.2	4.2	3.8	6.8	0.3	A
GS1A1	26.4	0.6	400-600	12	0.78	0.83	-0.20	29.8	0.8	0.7	6.9	16.5	0.7	1.0	B
GS1B1	28.7	0.5	250-620	17	0.81	0.84	-0.13	39.2	1.4	1.0	3.6	6.9	1.2	0.0	A
GS1C1	26.1	0.4	250-620	17	0.82	0.84	-0.14	51.3	1.6	1.1	3.2	9.8	1.6	0.0	A
GS1D1	27.7	0.5	425-570	8	0.69	0.81	-0.21	28.9	1.4	1.1	3.8	10.0	1.5	0.0	A
GS1E1	30.9	0.8	450-600	10	0.75	0.79	-0.05	24.1	1.3	0.8	3.6	8.1	1.9	9.2	B
GS1F1	26.1	0.4	250-620	17	0.82	0.83	-0.07	50.5	1.7	1.2	4.3	6.7	1.7	7.2	A
GS1i1	22.1	0.5	450-560	6	0.68	0.79	-0.10	25.8	0.6	0.6	5.9	9.9	1.9	1.0	A
GS1J1	21.3	0.5	450-560	6	0.69	0.79	-0.08	23.5	0.5	0.4	5.7	9.9	1.4	1.0	A

…continue from previous page…

Name	B (μT)	σ (μT)	ΔT (°C)	N	f	β	k	q	MAD (°)	α	δCK	δpal	δTR	δt*	Class
GS3H1	31.9	0.9	375-620	14	0.94	0.89	0.32	30.4	0.7	0.7	4.7	0.6	1.1	4.2	A
GS3J1	42.8	3.0	475-590	11	0.63	0.79	0	7.0	2.0	3.5	6.5	9.8	0.6	0.0	A
GS3K1	33.7	3.6	0-550	12	0.98	0.87	0.72	8.0	2.7	3.3	7.0	7.0	2.6	0.6	B
GS3L1	35.5	3.8	0-550	12	1.00	0.87	0.77	8.1	3.3	3.1	8.3	11.6	2.8	1.9	B
GR4A2	15.2	0.8	100-590	17	0.97	0.88	0.41	16.9	2.8	1.0	2.7	0.4	3.8	3.8	A
GR4B2	17.6	0.8	100-590	15	0.92	0.86	0.12	18.3	3.9	0.9	6.8	8.9	4.1	3.0	A
GR19G1	25.8	0.9	0-580	15	0.94	0.82	0.08	22.8	1.9	1.0	4.0	4.2	3.4	2.1	A
GR19J1	30.6	3.3	520-590	8	0.55	0.80	-0.06	4.2	7.1	5.0	4.4	4.1	3.5	1.9	B
GR19K1	28.7	0.9	400-590	12	0.86	0.85	0.23	24.3	2.0	1.9	7.0	17.8	3.5	2.7	B
GR19M1	21.5	1.0	0-590	16	0.93	0.89	-0.11	17.5	4.0	0.8	4.9	7.0	4.4	2.8	A
GR22A2	19.6	0.7	0-560	13	0.95	0.87	0.22	21.8	2.4	1.6	8.3	13.3	4.3	5.4	B
GR22H1	25.2	1.2	0-620	18	0.98	0.90	0.40	18.2	3.3	4.3	6.6	6.7	1.8	2.2	A
GR22i1	24.1	1.1	0-620	18	0.97	0.90	0.34	19.6	3.2	4.2	6.5	4.8	2.1	2.8	A
GR22J1	24.6	1.4	0-590	16	0.91	0.90	0.40	14.9	2.6	2.8	5.9	6.8	2.9	3.4	A
GR22L1	24.7	1.2	0-590	16	0.93	0.91	0.36	17.7	2.9	2.2	7.1	2.5	2.2	4.3	B
GR24i1	30.3	2.1	400-580	11	0.81	0.85	0.40	10.0	2.7	0.9	8.1	13.4	6.9	5.5	B
GR24N1	45.1	2.4	475-580	6	0.63	0.77	0.40	9.0	1.3	1.2	3.6	17.8	3.5	7.9	B
GRA25A2	31.9	1.0	0-580	15	0.93	0.90	0	26.6	1.9	0.8	4.6	8.0	4.5	4.8	A
GRA25B2	29.5	0.8	0-560	13	0.83	0.87	0	25.6	1.7	1.0	7.7	10.6	3.8	5.0	B
GRA25E2	32.2	0.9	475-560	8	0.68	0.82	0.22	19.0	3.0	1.4	8.2	13.9	2.8	5.8	B
GRA25J1	25.6	0.6	0-590	16	0.96	0.91	0	34.9	3.1	1.8	4.9	5.0	3.0	4.2	A
GRA25K1	25.4	0.6	150-580	13	0.92	0.84	0.19	34.8	2.7	2.5	3.3	3.6	1.8	2.1	A

…continue from previous page…

Name	B (μT)	σ (μT)	ΔT (°C)	N	f	β	k	q	MAD (°)	α	δCK	δpal	δTR	δt*	Class
GR29B2	56.1	1.3	0-550	12	0.82	0.86	0	30.0	1.9	1.4	5.8	10.9	3.0	6.3	B
GR29E1	37.5	0.9	0-580	15	0.97	0.82	0.07	34.9	1.3	1.1	2.9	2.0	1.4	2.0	A
GR29H2	51.9	6.1	150-475	8	0.47	0.72	0.31	2.9	1.8	4.4	2.2	16.2	6.7	8.2	B
GR29i2	53.9	1.8	0-550	12	0.85	0.83	0.01	21.0	1.2	0.6	6.9	13.6	0.9	7.3	B
GR29K2	51.3	2.1	0-550	12	0.94	0.79	0	18.7	1.5	0.9	5.9	7.6	1.7	5.5	A
GR32D2	11.4	0.4	100-580	14	0.97	0.82	0.29	24.8	4.1	5.0	7.1	12.2	2.4	0.8	B
GR32E2	11.2	0.4	0-580	15	0.97	0.81	0.35	21.1	3.3	4.7	6.5	9.7	2.5	0.6	A
GRA33B2	4.0	0.4	450-580	7	0.84	0.75	-0.19	6.1	3.9	3.4	8.0	16.3	11.5	2.3	B
GRA33C2	4.7	0.6	450-580	7	0.80	0.66	1.51	4.3	2.9	1.4	2.9	3.9	11.1	2.1	B
GR33A2	11.1	0.4	200-570	12	0.86	0.84	-0.10	20.3	5.5	7.5	1.4	0.7	5.0	4.6	A
GR33C2	14.3	0.4	100-570	13	0.93	0.80	0	27.5	3.4	4.1	2.7	0.2	3.0	3.3	A
GR33D2	11.2	0.3	200-590	14	0.98	0.89	0.14	28.8	4.6	3.4	3.0	2.9	3.0	3.2	A
GR33F2	13.4	0.3	0-590	16	0.98	0.90	-0.04	42.3	3.5	3.3	4.1	4.2	1.8	4.1	A
GR33G2	13.1	0.7	0-560	14	0.65	0.64	0.18	8.3	1.6	2.7	1.6	0.2	4.8	1.6	A
GR33H2	12.1	0.2	100-580	14	0.96	0.68	0	39.7	1.8	1.2	2.9	3.4	5.1	1.1	A
LF0A2	15.3	1.8	0-560	14	1.00	0.77	0.75	6.7	4.7	7.0	4.0	3.4	1.5	4.4	B
LF0B2	14.6	0.9	0-580	15	1.00	0.75	0.53	12.0	3.6	3.3	4.9	4.6	1.8	0.2	A
LF0C2	14.7	1.0	0-580	15	1.00	0.79	0.55	11.4	3.4	4.0	2.2	4.6	6.8	0.5	A
LF0E2	17.6	1.6	0-560	14	0.85	0.71	0.52	6.8	5.3	10.7	0.7	0.9	1.5	3.1	A
LF0G2	18.6	1.4	0-580	15	0.93	0.76	0.59	9.5	4.8	7.6	3.1	2.8	5.6	9.3	B
LF0J2	19.7	1.9	0-560	14	0.83	0.73	0.53	6.4	4.4	9.7	4.3	3.8	3.0	5.9	A
LF0L2	17.4	1.4	0-580	15	0.96	0.78	0.62	9.6	4.1	6.7	3.1	3.9	10.1	5.7	B

…continue from previous page…

Name	B (μT)	σ (μT)	ΔT (°C)	N	f	β	k	q	MAD (°)	α	δCK	δpal	δTR	δt*	Class
LF1K1n	31.7	1.6	510-630	12	0.72	0.88	0.19	12.2	2.4	0.9	7.6	17.6	6.5	0.0	B
LF1L1n	34.3	2.4	520-610	10	0.60	0.85	0.08	7.3	2.2	1.7	7.4	16.3	6.4	0.0	B
LF1M1n	37.5	2.3	520-610	10	0.57	0.84	-0.01	7.8	2.5	1.9	8.4	11.8	6.1	0.3	B
LF2F2	56.7	4.3	0-580	15	1.00	0.87	0.72	11.6	2.0	1.7	7.0	9.6	4.4	4.5	B
LF2G2	54.1	4.3	0-580	15	1.00	0.88	0.73	11.1	1.9	2.1	7.9	7.6	4.0	3.8	B
LF2i2	58.1	4.5	0-580	15	1.00	0.88	0.74	11.2	1.5	0.9	6.6	6.8	4.0	3.8	A
LF2K2	63.9	6.5	0-580	15	1.00	0.87	0.75	8.6	1.9	0.5	5.7	12.0	1.5	2.0	B
LF4G2	34.8	1.8	500-580	5	0.66	0.71	0.30	9.3	1.6	0.4	8.5	16.2	1.5	5.6	B
LF4H2	33.3	1.7	520-590	5	0.58	0.68	0.25	7.6	1.6	0.9	9.0	13.5	1.8	3.9	B
LF4P2	31.1	2.1	300-520	7	0.51	0.77	-0.06	5.9	1.4	0.6	7.2	17.4	6.0	2.3	B
LF7B2	39.8	0.8	0-580	15	0.99	0.85	0.11	42.0	1.7	1.1	8.7	11.1	2.3	9.6	B
LF7C2	29.8	1.0	250-520	8	0.73	0.74	0.48	16.7	2.4	2.6	8.1	16.4	2.6	3.2	B
LF7F1	31.3	1.8	250-540	9	0.86	0.82	0.46	11.9	4.3	5.5	5.7	13.8	4.0	0.6	B
LF7i2	36.7	1.3	400-540	6	0.76	0.74	0.15	15.3	2.9	1.3	2.8	3.1	4.8	4.1	A
LF9A2	7.2	0.3	0-590	16	0.93	0.86	-0.16	18.2	7.6	4.2	5.9	17.5	3.0	0.0	B
LF9B2n	9.4	0.6	300-600	14	0.96	0.90	0.71	13.1	7.3	7.2	3.2	10.1	3.8	0.1	B
TOM3E2	32.3	1.2	0-580	13	0.96	0.88	0.31	23.7	2.0	1.8	5.9	16.0	1.6	5.7	B
TOM3F2	32.5	1.3	0-580	13	0.96	0.87	0.35	21.3	1.8	1.7	9.0	12.2	0.8	4.2	B
TOM3G2	29.3	1.2	400-580	9	0.88	0.82	0.31	18.0	3.0	1.5	9.0	16.8	0.7	4.1	B
TOM3i1	30.2	1.2	500-550	5	0.49	0.74	0.20	9.5	3.6	1.9	9.0	16.4	0.2	5.6	B

…continue from previous page…

Name	B (μT)	σ (μT)	ΔT (°C)	N	f	β	k	q	MAD (°)	α	δCK	δpal	δTR	δt*	Class
TOM1A2	7.4	0.2	0-590	16	0.95	0.87	0	31.7	8.2	6.1	7.5	17.8	0.7	0.0	B
TOM1B2	7.6	0.3	0-580	15	0.93	0.87	0.15	21.7	8.9	8.8	8.4	18.0	3.6	0.0	B
TOM1C2	8.7	0.4	350-580	9	0.86	0.83	-0.52	15.8	3.2	1.0	2.8	7.8	3.0	1.1	A
TOM1D2	8.2	0.2	250-580	11	0.88	0.83	-0.27	24.4	4.2	2.7	8.1	17.6	1.7	0.3	B
TOM1E2	7.9	0.5	0-580	15	0.88	0.82	-0.33	11.9	5.3	4.5	6.3	10.0	1.4	2.9	A
TOM1H2	9.6	0.1	150-580	13	0.92	0.88	0.01	62.6	5.4	4.9	8.3	17.2	2.1	0.8	B
TO1B2	12.4	0.4	0-600	15	0.99	0.81	0.27	23.3	3.7	3.9	2.2	2.5	1.7	2.5	A
TO1P	10.8	0.7	100-520	11	0.67	0.77	0.43	7.7	5.9	12.4	4.8	6.0	6.3	2.5	A
TO1Q1	9.5	0.6	200-550	10	0.97	0.84	0.42	13.2	6.4	4.9	6.8	17.8	1.3	0.8	B
TO3A2	40.8	1.5	0-600	17	0.95	0.81	0.40	20.5	1.3	0.7	8.4	9.2	2.2	15.8	B
TO3B2	41.6	1.6	0-580	15	0.91	0.87	0.27	20.7	0.8	0.4	5.9	9.3	2.8	2.4	A
TO3C1	38.6	2.0	0-580	15	0.95	0.84	0.39	15.7	1.3	1.8	7.2	14.5	2.5	1.8	B
TO3D1	41.4	1.9	0-580	15	0.94	0.82	0.33	17.1	1.3	0.9	5.5	4.8	2.2	0.6	A
TO3J2	38.0	1.3	0-600	17	0.97	0.80	0.40	22.7	1.1	0.7	6.5	17.0	1.7	6.9	B
TO3K2	40.3	1.2	0-600	17	0.94	0.82	0.27	25.9	1.0	0.3	8.3	15.8	1.8	0.0	B
TO5B2	15.2	1.7	0-580	15	1.00	0.84	0.88	7.3	6.8	8.3	3.2	5.0	1.7	1.9	B
TO5C2	17.5	2.5	0-560	14	1.00	0.83	0.94	5.8	6.7	11.1	1.8	2.0	2.4	0.0	B
TO5D2	17.1	2.0	0-540	10	0.74	0.72	0.76	4.6	5.0	11.4	4.2	11.4	10.1	0.0	B
TO5G2	19.5	1.9	0-540	10	0.76	0.80	0.71	6.1	6.4	13.9	3.9	12.2	19.8	7.8	B
TO6C2	25.1	3.5	0-590	16	0.96	0.87	0.62	6.0	3.2	2.6	6.9	7.9	1.1	1.4	B
TO6H1	26.6	1.9	0-600	14	0.97	0.89	0.55	12.1	2.0	1.6	4.8	5.0	7.7	7.9	A

…continue from previous page…

Name	B (μT)	σ (μT)	ΔT (°C)	N	f	β	k	q	MAD (°)	α	δCK	δpal	δTR	δt*	Class
TO7C2	35.3	4.8	250-580	11	0.87	0.85	0.38	5.5	1.9	2.4	6.7	16.4	3.1	0.0	B
TO7D2n	36.7	2.7	100-600	16	1.00	0.91	0.61	12.3	1.5	1.6	8.9	9.4	2.4	0.0	B
TO7E2n	32.0	1.4	475-570	9	0.57	0.85	0.60	10.8	1.3	2.1	2.5	3.2	2.9	0.0	A
TO7F2n	31.8	3.2	100-475	5	0.71	0.74	1.00	5.1	5.5	7.3	2.2	5.3	2.8	4.4	B
TO7G2n	39.3	5.9	0-475	6	0.39	0.73	0.47	1.9	2.5	4.7	6.7	13.9	1.5	0.7	B
TO8E2	20.7	3.0	0-590	16	1.00	0.84	0.60	5.8	2.0	2.0	7.9	10.8	2.2	0.7	B
TO8F2	24.0	1.0	100-560	13	0.98	0.87	0	19.9	2.4	3.1	3.4	5.3	2.9	1.0	A
TO8i2	24.6	1.2	0-580	13	1.00	0.88	0.36	17.9	2.9	2.5	4.7	6.6	2.2	6.2	A
TO8J2	27.7	1.3	0-580	13	1.00	0.84	0	17.6	2.1	1.8	7.2	2.7	2.7	5.2	B
TO8K2	26.9	0.8	0-530	9	0.63	0.77	0.26	15.9	1.7	2.5	5.8	17.3	0.4	4.5	B
TO8L2	18.9	1.0	400-580	9	0.90	0.84	0.34	14.8	3.1	2.1	8.7	16.8	2.7	6.2	B
TO9A2	25.0	3.4	0-590	16	0.97	0.83	0.52	6.0	1.8	1.8	4.2	9.4	4.2	0.0	B
TO9B2	25.0	3.2	0-590	16	0.96	0.83	0.47	6.2	1.6	1.5	4.8	12.3	4.2	0.0	B
TO9F2	23.4	0.7	0-580	13	0.99	0.88	0.26	29.1	1.6	1.5	1.3	0.3	1.2	3.9	A
TO9G2	21.2	0.4	0-580	13	0.97	0.88	0.13	46.0	2.5	2.0	1.6	3.2	1.2	3.8	A
TO11A2	33.4	3.9	0-580	15	0.88	0.86	0.31	6.5	1.6	2.4	7.3	5.3	2.0	0.0	B
TO11C2	28.1	3.2	0-580	15	0.81	0.87	0	6.1	1.5	2.3	2.4	6.5	1.5	0.0	B
TO11E2n	35.4	2.7	300-610	15	0.99	0.89	0.76	11.4	1.8	0.6	9.0	7.0	3.1	9.6	B
TO11F2n	37.9	3.0	300-610	15	0.99	0.89	0.81	11.0	1.6	1.0	8.8	12.7	2.4	9.6	B
TO11H2n	30.1	2.7	0-630	19	1.00	0.89	0.88	9.9	2.5	1.6	8.0	5.2	3.1	7.4	B
TO11J2n	40.0	3.4	400-570	10	0.51	0.85	0.30	5.1	0.9	2.1	6.6	5.6	2.9	2.4	A

…continue from previous page…

Name	B (μT)	σ (μT)	ΔT (°C)	N	f	β	k	q	MAD (°)	α	δCK	δpal	δTR	δt*	Class
TO12D2	16.6	0.4	0-580	15	0.93	0.81	0.02	35.6	2.1	1.8	7.2	8.7	2.0	0.8	B
TO12E2n	21.6	2.2	300-570	11	0.76	0.87	0.80	6.4	3.5	5.7	9.0	4.9	3.4	6.5	B
TO12G2n	19.7	1.7	0-610	18	1.00	0.92	0.81	10.4	5.7	3.8	1.7	1.6	2.3	4.7	A
TO12i2n	19.0	1.7	0-610	18	1.00	0.91	0.81	10.2	5.9	2.9	2.2	1.6	2.4	7.8	A
TO12K2n	23.9	3.0	475-550	7	0.47	0.79	0.71	2.9	2.5	2.3	4.8	0.6	4.4	5.1	B
TO12L2n	25.3	2.0	0-570	14	0.94	0.89	0.74	10.4	3.6	4.8	6.8	3.8	2.8	4.3	A
TO12M2n	21.9	1.8	0-600	17	1.00	0.91	0.72	10.8	3.5	4.2	8.0	8.2	1.8	5.5	B
BO1C2n	53.6	1.5	0-570	14	0.98	0.89	0.22	31.3	2.0	1.3	5.2	6.8	3.0	2.4	A
BO1E2	47.3	1.4	0-560	13	0.92	0.88	0	27.7	2.3	2.2	3.0	7.4	3.1	3.9	A
BO1F2n	55.9	1.9	0-570	14	0.97	0.87	0.20	25.3	2.2	1.5	8.4	0.2	4.4	1.1	B
BO1G2n	43.5	0.8	0-580	15	0.96	0.88	0.11	45.4	2.1	1.6	5.2	0.8	3.9	0.0	A
BO1H2n	42.6	1.2	0-570	14	0.96	0.88	0.18	29.9	2.1	1.6	8.7	12.6	4.2	0.7	B
BO1i2n	38.9	1.3	0-580	15	0.97	0.89	0.24	26.6	2.7	1.9	5.1	1.5	4.2	1.8	A
BO1N2	39.1	0.9	0-570	14	0.97	0.89	0.04	37.5	1.7	1.7	8.1	5.6	2.4	1.6	B
BO5E2n	26.7	1.2	500-570	8	0.49	0.83	0.54	9.2	2.3	1.4	5.2	9.0	1.8	3.1	A
BO5M2n	22.7	0.4	0-570	14	0.97	0.86	0.13	48.8	6.0	4.6	4.6	6.8	1.3	1.8	A
BO10C2n	47.3	2.3	0-550	12	0.75	0.87	0.37	13.6	2.2	2.2	4.5	11.5	2.1	3.7	B
BO10H1n	39.8	0.7	300-590	13	0.94	0.90	0.21	46.5	1.8	0.7	3.1	15.5	2.6	4.3	B
BO10i2n	38.8	0.7	400-590	12	0.86	0.88	0.17	40.8	1.6	0.7	4.5	14.4	2.6	5.0	B

…continue from previous page…

Name	B (μT)	σ (μT)	ΔT (°C)	N	f	β	k	q	MAD (°)	α	δCK	δpal	δTR	δt*	Class
BO12A2n	36.2	1.4	0-590	16	1.00	0.90	0.36	23.6	2.2	1.4	5.0	13.1	2.5	2.9	B
BO12B2n	38.4	2.0	0-590	16	1.00	0.90	0.46	17.7	1.9	0.7	4.6	9.8	3.5	6.1	A
BO12C2	44.1	1.2	300-580	11	0.91	0.76	0	25.4	1.7	1.4	4.4	0.4	1.4	4.1	A
BO12D1n	34.1	1.7	400-590	12	0.95	0.90	0.57	17.5	1.8	1.0	4.3	8.0	2.3	5.5	A
BO12F2n	48.6	1.2	475-600	12	0.82	0.90	0.22	30.7	1.2	0.1	7.0	3.0	3.0	2.6	A
BO12G2n	43.9	2.2	400-600	13	0.99	0.91	0.63	17.9	1.7	0.4	4.2	5.4	3.5	5.6	A
BO12i2n	33.5	1.0	200-590	14	0.99	0.90	0.25	31.5	2.3	1.7	3.3	1.1	1.7	3.9	A
BO13B2n	28.9	0.4	0-570	14	0.95	0.84	0.11	54.9	2.4	1.8	7.2	14.3	1.4	4.9	B
BO13D2n	35.7	1.3	0-590	16	0.98	0.91	0.33	23.9	1.0	0.4	3.4	3.4	2.4	1.6	A
BO13G1n	35.8	1.5	0-600	17	1.00	0.91	0.40	21.8	1.8	0.6	1.9	8.0	3.6	4.0	A
BO13H1	29.1	0.4	0-560	13	0.73	0.83	-0.16	43.6	1.4	2.5	2.9	3.1	2.4	1.6	A
BO13i2n	31.7	1.7	0-600	17	1.00	0.91	0.46	16.7	1.3	1.2	1.3	1.6	1.6	5.9	A
BO13K2	27.4	0.5	0-580	14	0.95	0.79	0.02	46.1	0.9	0.9	0.8	1.0	4.1	8.6	A

Table 7.4: Site mean palaeointensity data. Bold sites are those excluded in final mean palaeointensity estimates, because the per cent normalised standard deviation over the mean exceeds the critical value. The ages are estimated from the age model in Chapter 5. The Q_{PI} criteria: AGE, STAT, TRM, ALT, MD, ACN, TECH and LITH are graded with ‘1’ for rock units whose meet the criteria or ‘0’ for those whose fail the criteria (Biggin and Paterson, 2014). The Q_{PI} scores are summarised in the last column.

Site name	Ages (Ma)	Age σ (Ma)	B (μT)	σ_B (μT)	$d\sigma_B$ (%)	n	N	VADM (ZAm^2)	VDM (ZAm^2)	AGE	STAT	TRM	ALT	MD	ACN	TECH	LITH	Q_{PI} Score
VA2	**8.05**	**0.15**	**29.9**	**3.2**	**10.8**	**10**	**10**	**41.5**	**49.0**	**1**	**1**	**0**	**1**	**1**	**0**	**0**	**0**	**4**
VA3	**8.04**	**0.15**	**36.1**	**2.3**	**6.4**	**4**	**8**	**50.1**	**49.7**	**1**	**0**	**0**	**1**	**1**	**0**	**0**	**0**	**3**
VA5	**8.00**	**0.14**	**13.6**	**1.7**	**12.7**	**7**	**8**	**18.9**	**18.0**	**1**	**1**	**0**	**1**	**1**	**0**	**0**	**0**	**4**
VA6	**7.97**	**0.14**	**25.2**	**3.0**	**11.7**	**5**	**9**	**34.9**	**41.7**	**1**	**1**	**0**	**1**	**1**	**0**	**0**	**0**	**4**
VA7	**7.95**	**0.14**	**22.2**	**2.4**	**10.6**	**8**	**8**	**30.8**	**33.9**	**1**	**1**	**0**	**1**	**1**	**0**	**0**	**0**	**4**
VA11	7.86	0.14	11.2	8.1	72.6	2	2	15.5	18.6	1	0	0	1	1	0	0	0	3
VA12	7.86	0.14	8.3	4.8	58.3	2	2	11.5	15.2	1	0	0	1	1	0	0	0	3
VA15	7.82	0.14	7.3	1.3	17.5	3	3	10.1	12.3	1	0	0	1	1	0	0	0	3
VA28	7.68	0.13	9.6	2.7	28.3	2	2	13.3	17.1	1	0	0	1	1	0	0	0	3
VA30	**7.64**	**0.13**	**14.3**	**1.3**	**9.4**	**4**	**8**	**19.8**	**31.6**	**1**	**0**	**0**	**1**	**1**	**0**	**0**	**0**	**3**
VA31	**7.63**	**0.13**	**22.4**	**1.5**	**6.5**	**8**	**8**	**31.1**	**34.1**	**1**	**1**	**0**	**1**	**1**	**0**	**0**	**0**	**4**
VA35	**7.52**	**0.12**	**16.7**	**1.5**	**9.3**	**5**	**8**	**23.2**	**27.7**	**1**	**1**	**0**	**1**	**1**	**0**	**0**	**0**	**4**
HS3	**7.98**	**0.14**	**19.5**	**1.0**	**5.3**	**6**	**9**	**27.0**	**30.7**	**1**	**1**	**0**	**1**	**1**	**0**	**0**	**0**	**4**
HS4	7.96	0.14	17.1	4.0	23.6	2	5	23.7	22.3	1	0	0	1	1	0	0	0	3
HS5	**7.95**	**0.14**	**31.1**	**2.3**	**7.2**	**4**	**5**	**43.1**	**48.9**	**1**	**0**	**0**	**1**	**1**	**0**	**0**	**0**	**3**
HS7	7.81	0.14	7.9	2.9	36.9	3	4	11.0	10.7	1	0	0	1	1	0	0	0	3
HS8	**7.63**	**0.13**	**14.6**	**2.1**	**14.7**	**7**	**8**	**20.3**	**23.3**	**1**	**1**	**0**	**1**	**1**	**0**	**0**	**0**	**4**
HS11	**7.61**	**0.12**	**55.6**	**4.6**	**8.3**	**5**	**5**	**77.1**	**79.9**	**1**	**1**	**0**	**1**	**1**	**0**	**0**	**0**	**4**
HS13	**7.59**	**0.12**	**19.7**	**2.0**	**10.4**	**2**	**6**	**27.3**	**28.5**	**1**	**0**	**0**	**1**	**1**	**0**	**0**	**0**	**3**
HSB18	**7.41**	**0.12**	**23.5**	**1.5**	**6.4**	**3**	**7**	**32.6**	**33.7**	**1**	**0**	**0**	**1**	**1**	**0**	**0**	**0**	**3**
HSJ18	**7.41**	**0.12**	**27.2**	**4.0**	**14.5**	**4**	**9**	**37.7**	**41.2**	**1**	**0**	**0**	**1**	**1**	**0**	**0**	**0**	**3**

…continue from previous page…

Site name	Ages (Ma)	Age σ (Ma)	B (μT)	σB (μT)	%σB	n	N	VADM (ZAm^2)	VDM (ZAm^2)	AGE	STAT	TRM	ALT	MD	ACN	TECH	LITH	QPI
GS1	**7.05**	**0.10**	**26.2**	**3.2**	**12.3**	**8**	**8**	**36.3**	**41.0**	**1**	**1**	**0**	**1**	**1**	**0**	**0**	**0**	**4**
GS3	**5.65**	**0.12**	**36.0**	**4.8**	**13.4**	**4**	**4**	**49.9**	**47.0**	**1**	**0**	**0**	**1**	**1**	**0**	**0**	**0**	**3**
GR4	**5.56**	**0.12**	**16.4**	**1.7**	**10.6**	**2**	**4**	**22.8**	**30.4**	**1**	**0**	**0**	**1**	**1**	**0**	**0**	**0**	**3**
GR19	**5.30**	**0.12**	**26.7**	**4.0**	**15.0**	**4**	**5**	**37.0**	**44.8**	**1**	**0**	**0**	**1**	**1**	**0**	**0**	**0**	**3**
GR22	**5.23**	**0.12**	**23.6**	**2.3**	**9.7**	**5**	**5**	**32.7**	**37.3**	**1**	**1**	**0**	**1**	**1**	**0**	**0**	**0**	**4**
GR24	5.20	0.12	37.7	10.4	27.7	2	6	52.3	59.7	1	0	0	1	1	0	0	0	3
GRA25	**5.18**	**0.12**	**28.9**	**3.3**	**11.4**	**5**	**7**	**40.1**	**49.4**	**1**	**1**	**0**	**1**	**1**	**0**	**0**	**0**	**4**
GR29	**5.07**	**0.12**	**50.1**	**7.3**	**14.6**	**5**	**7**	**69.5**	**65.5**	**1**	**1**	**0**	**1**	**1**	**0**	**0**	**0**	**4**
GR32	**5.01**	**0.12**	**11.3**	**0.2**	**1.2**	**2**	**8**	**15.7**	**23.0**	**1**	**0**	**0**	**1**	**1**	**0**	**0**	**0**	**3**
GRA33	**4.96**	**0.12**	**4.4**	**0.5**	**10.5**	**2**	**2**	**6.1**	**9.1**	**1**	**0**	**0**	**1**	**1**	**0**	**0**	**0**	**3**
GR33	**4.99**	**0.12**	**12.5**	**1.3**	**10.2**	**6**	**8**	**17.3**	**16.8**	**1**	**1**	**0**	**1**	**1**	**0**	**0**	**0**	**4**
LF0	**5.27**	**0.12**	**16.8**	**2.0**	**11.8**	**7**	**7**	**23.3**	**26.1**	**1**	**1**	**0**	**1**	**1**	**0**	**0**	**0**	**4**
LF1	**5.23**	**0.12**	**34.5**	**2.9**	**8.3**	**3**	**7**	**47.9**	**50.3**	**1**	**0**	**0**	**1**	**1**	**0**	**0**	**0**	**3**
LF2	**5.22**	**0.12**	**58.2**	**4.1**	**7.1**	**4**	**7**	**80.8**	**95.2**	**1**	**0**	**0**	**1**	**1**	**0**	**0**	**0**	**3**
LF4	**5.18**	**0.12**	**33.1**	**1.8**	**5.6**	**3**	**8**	**45.9**	**47.9**	**1**	**0**	**0**	**1**	**1**	**0**	**0**	**0**	**3**
LF7	**5.15**	**0.12**	**34.4**	**4.7**	**13.6**	**4**	**8**	**47.7**	**47.4**	**1**	**0**	**0**	**1**	**1**	**0**	**0**	**0**	**3**
LF9	4.92	0.12	8.3	1.6	18.9	2	8	11.5	11.3	1	0	0	1	1	0	0	0	3
TOM3	**4.98**	**0.12**	**31.1**	**1.6**	**5.1**	**4**	**7**	**43.2**	**53.4**	**1**	**0**	**0**	**1**	**1**	**0**	**0**	**0**	**3**
TOM1	**4.92**	**0.12**	**8.2**	**0.8**	**10.0**	**6**	**8**	**11.4**	**11.1**	**1**	**1**	**0**	**1**	**1**	**0**	**0**	**0**	**4**
TO1	**4.85**	**0.12**	**10.9**	**1.5**	**13.3**	**3**	**6**	**15.1**	**20.2**	**1**	**0**	**0**	**1**	**1**	**0**	**0**	**0**	**3**
TO3	**4.79**	**0.12**	**40.1**	**1.5**	**3.7**	**6**	**8**	**55.6**	**54.7**	**1**	**1**	**0**	**1**	**1**	**0**	**0**	**0**	**4**
TO5	**4.76**	**0.12**	**17.3**	**1.8**	**10.0**	**4**	**8**	**24.0**	**22.5**	**1**	**0**	**0**	**1**	**1**	**0**	**0**	**0**	**3**
TO6	**4.74**	**0.12**	**25.8**	**1.1**	**4.1**	**2**	**3**	**35.8**	**33.8**	**1**	**0**	**0**	**1**	**1**	**0**	**0**	**0**	**3**

…continue from previous page…

Site name	Ages (Ma)	Age σ (Ma)	B (μT)	σB (μT)	%σB	n	N	VADM (ZAm2)	VDM (ZAm2)	AGE	STAT	TRM	ALT	MD	ACN	TECH	LITH	QPI
TO7	**4.73**	**0.12**	**35.0**	**3.2**	**9.2**	**5**	**8**	**48.6**	**45.7**	**1**	**1**	**0**	**1**	**1**	**0**	**0**	**0**	**4**
TO8	**4.71**	**0.12**	**23.8**	**3.5**	**14.5**	**6**	**8**	**33.0**	**39.8**	**1**	**1**	**0**	**1**	**1**	**0**	**0**	**0**	**4**
TO9	**4.69**	**0.12**	**23.6**	**1.8**	**7.7**	**4**	**8**	**32.8**	**39.2**	**1**	**0**	**0**	**1**	**1**	**0**	**0**	**0**	**3**
TO11	**4.66**	**0.12**	**34.1**	**4.5**	**13.3**	**6**	**8**	**47.3**	**58.9**	**1**	**1**	**0**	**1**	**1**	**0**	**0**	**0**	**4**
TO12	**4.59**	**0.12**	**21.1**	**3.0**	**14.0**	**7**	**8**	**29.3**	**39.5**	**1**	**1**	**0**	**1**	**1**	**0**	**0**	**0**	**4**
BO1	**3.24**	**0.11**	**45.9**	**6.8**	**14.7**	**7**	**8**	**63.7**	**62.2**	**1**	**1**	**0**	**1**	**1**	**0**	**0**	**0**	**4**
BO5	**3.01**	**0.12**	**24.7**	**2.9**	**11.6**	**2**	**14**	**34.3**	**47.1**	**1**	**0**	**0**	**1**	**1**	**0**	**0**	**0**	**3**
BO10	**2.80**	**0.12**	**42.0**	**4.7**	**11.1**	**3**	**8**	**58.3**	**59.5**	**1**	**0**	**0**	**1**	**1**	**0**	**0**	**0**	**3**
BO12	**2.67**	**0.13**	**39.8**	**5.8**	**14.4**	**7**	**7**	**55.2**	**56.4**	**1**	**1**	**0**	**1**	**1**	**0**	**0**	**0**	**4**
BO13	**2.64**	**0.13**	**31.4**	**3.6**	**11.5**	**6**	**8**	**43.6**	**56.6**	**1**	**1**	**0**	**1**	**1**	**0**	**0**	**0**	**4**

7.5 First order reversal curve

According to the Day plot diagram, a majority of samples fall within the pseudo-single domain (PSD) region. However, this is common for natural samples, and yields the use of the diagram slightly redundant (Tauxe et al., 2010). This happens because real samples consist of various combinations of mineral composition, grain size and inter-grain magnetic interactions producing the same net magnetic behaviour (Muxworthy and Roberts, 2007). In order to remove some of the ambiguity inherent to hysteresis measurements of some specimens yielding successful palaeointensity experiments, first-order reversal curve (FORC) was measured on some representative samples.

Figure 7.9 and 7.10 represents hysteresis loops (left column) and FORC diagrams (right column). Figure 7.9a and 7.9c represent hysteresis loops of PSD grains, while the FORC diagrams (Figure 7.9b and 7.9d) indicate the SD-like behaviour. All two samples exhibit straight lines on the Arai plot. With regards to BO13H (Figure 7.9e and 7.9f), the hysteresis loops indicate the SD-like behaviour while the FORC diagram show combinations of SD-like and PSD-like behaviour. These samples also show straight lines on the Arai plot. TO7I and TO12D yield successful palaeointensity results with slightly concave-up curve behaviour indicating MD dominance; the hysteresis loops display PSD behaviour (Figure 7.9g and 7.10a) while the FORC diagrams are typical for samples displaying large-PSD/multidomain behaviour (Figure 7.9h and 7.10b). Figure 7.10d and 7.10f shows the FORC diagrams of samples that failed palaeointensity experiment. The majority of grains are PSD and multidomain (MD) grains, respectively. With regard to BT6E (Figure 7.10g-h), both hysteresis loop and FORC diagram show nearly stable single domain (SD) magnetic behaviour, but the sample undergoes chemical alteration during step-wise heating. This suggests that room-temperature FORC measurements might not be a useful tool for assessing the reliability of samples for palaeointensity as suggested by Carvallo et al. (2006).

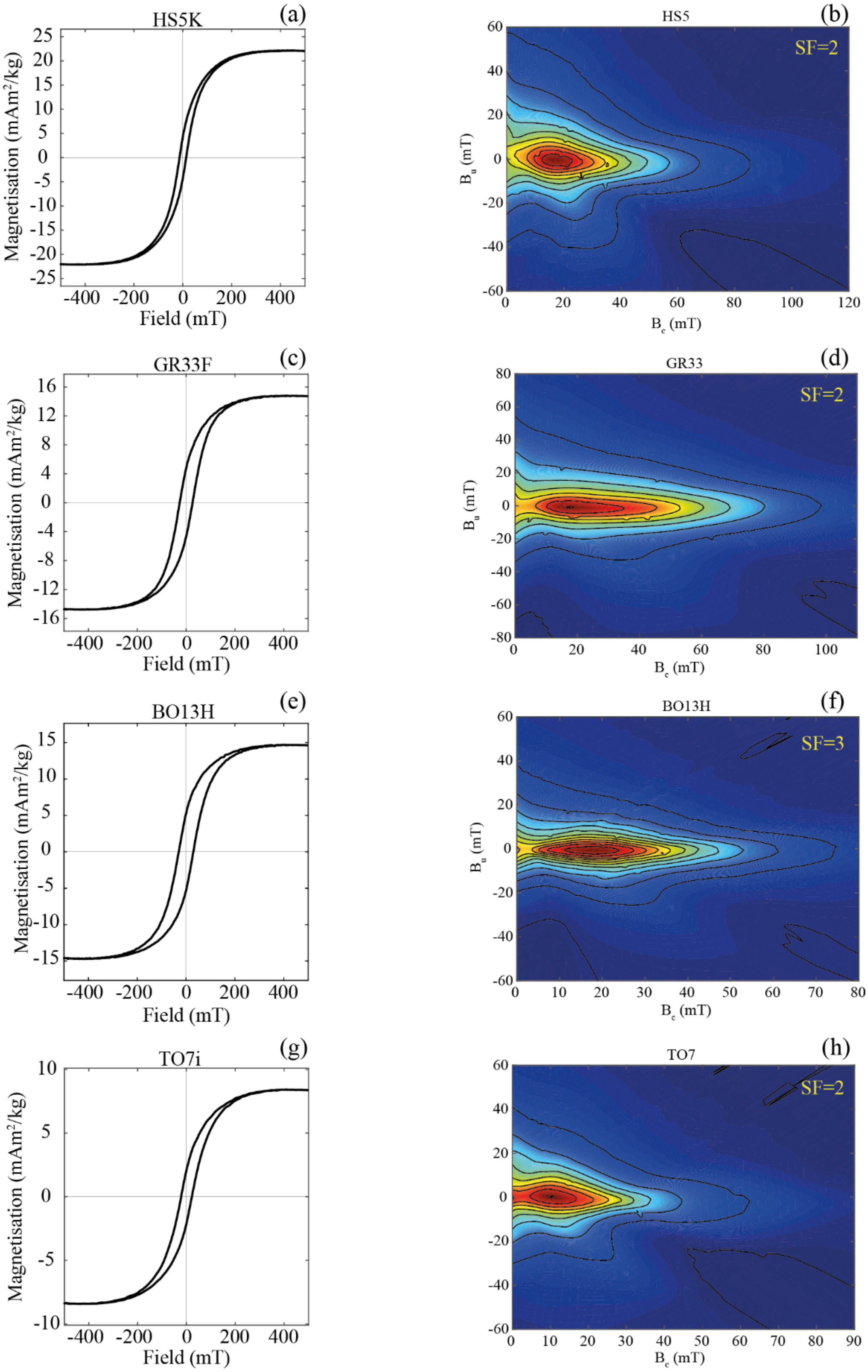

Figure 7.9: Examples of hysteresis loops (left column) and FORC diagrams (right column). (a)-(f) represent samples whose exhibit straight lines on the Arai plots. All samples exhibit high coercivity of the SD grains with characteristic of the PSD grain on the B_u axis. (g)-(h) represent samples showing the multi-domain concave-up curves on the Arai plot. It is seen that TO7i shows the PSD and MD bands.

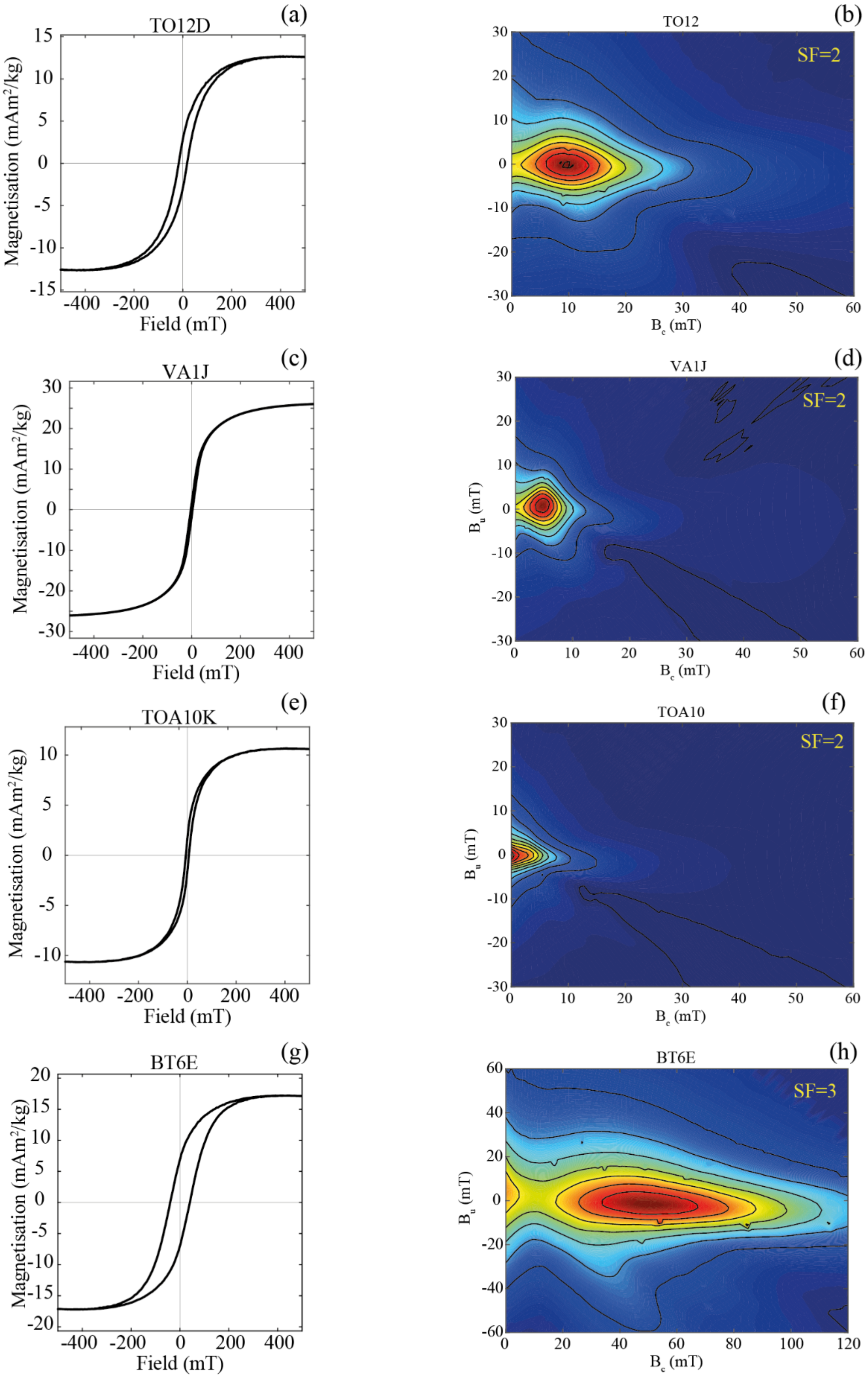

Figure 7.10: Examples of hysteresis loops (left column) and FORC diagrams (right column). (a)-(b) represent samples showing the multi-domain concave-up curves on the Arai plot. It is clearly seen that TO12D shows the PSD and MD bands. (c)-(h) represent samples whose alter during the palaeointensity experiment. It is clear that VA1J and TOA10 show characteristic of PSD and MD grains while BT6E show high coercivity band of the SD grain.

7.6 Palaeomagnetic field strength over the last 8.5 Myr

In order to compare this study with literature, the global palaeointensity data were collated from the absolute palaeointensity database 2015 (PINT15) (http://earth.liv.ac.uk/pint) (Biggin et al., 2009), which provides palaeointensity data from rock units older than 50 ka. The PINT15 data were screened using the following criteria:

1. Ages of sites must not exceed 8.5 Ma.
2. Site mean intensity must be calculated from at least two samples per site $(N \geq 2)$.
3. The fraction of standard deviation (σ_{perc}) of site mean intensity over the mean intensity must not exceed 15%.
4. All palaeointensity methods listed in the PINT15 database are accepted.

The palaeointensity data from Icelandic basalts that have not yet been included in the PINT15 database are also collated (Cromwell et al., 2015; Døssing et al., 2016; Tanaka and Yamamoto, 2016). Two recent studies in Iceland (e.g., Stanton et al., 2011; Tanaka et al., 2012) are not included because these studies focus on the palaeomagnetic field behaviour during the Holocene period, i.e., < 10 ka. A study by Camps et al. (2011) provides data from sites with ages that coincide with the chronologic framework for the present study; however, their study focused only on the field during polarity transitions. Therefore, I excluded Camps et al. (2011) data from the analysis in this study. A total of 940 data from the PINT15 database and literature passes the site selection criteria defined above, this dataset does not include the data from this study. Figure 7.11 presents the palaeointensity data from this study, literature and PINT15 against latitude. The individual-site mean intensity data from this study are shown as orange circles, while the mean palaeointensity of 26.9 ± 1.8 μT derived from 46 lava flows in Eyjafjardardalur, northern Iceland, is represented by a blue circle with the standard error of the mean. The global palaeointensity data (PINT15 and additional data from Iceland) are plotted as grey dots. The global data are grouped into 15° latitude bins and mean intensities for each bin (black circles) are calculated with the standard error of the mean. The mean intensity from the present study is approximately 50% lower than the current day intensity (blue line) predicted for Iceland (55 μT) using the current day VADM of 77.5 ZAm^2 (Tauxe et al., 2010). The data from the present study (26.9 ± 1.8 μT) are closer to an intensity of 30.3 μT predicted for Iceland (black line) using the 0-140 Myr VADM of 42 ZAm^2 (Tauxe et al., 2013). However, there is no overlap between the standard error of the mean of this study with the 0-140 Myr intensity. In comparison to the mean intensity from 60°-75° bin, it is clear that the data from the present study is significantly lower than the global 60°-75° bin data, and that the 60°-75° bin data shows a larger departure from the 0-140 Myr intensity than this study. As can be seen from the PINT15 dataset, the data from low latitudes tend towards the current day field (blue line) while mid- to high-latitudes data show significant deviations from the current day field. The mid- to high-latitudes data are tend towards the long-term time-averaged field during 0-140 Myr. It was reported by Selkin and Tauxe (2000) that palaeointensity data from 0-0.3 Ma rocks are biased toward the present day field. They suggested that data spanning from 0-0.3 Ma should be excluded from older data. Today the PINT15 database contains far more data than 17 years ago (Kono et al., 2000; Selkin and Tauxe, 2000) and includes a large proportion of new data that spans the period 0-1 Ma (c. ~570 data entries) (Figure 7.12). In comparison, merely 370 data entries comprise the palaeointensity record for 1-8.5 Ma (Figure 7.12). Here, I have separated the PINT15 data along with the additional Iceland data into two different time spans: 0-1 Ma (Figure 7.11b) and 1-8.5 Ma (Figure 7.11c) to illustrate how the ancient field behaves during different time intervals. It is clearly seen that palaeointensity data at low latitudes during 0-1 Ma especially between 15°N and 30°N tend toward the current day intensity (blue line) (Figure 7.11b and 7.12), while the data spanning from 1-8.5 Ma are significantly lower than the current day field but higher than 0-140 Ma field (black line) (Figure 7.11c). With regards to mid- to high-latitude data, data in both time spans show significant departure from the present-day field and tend towards the 0-140 Ma field especially at ~78°N (Figure 7.11b-c).

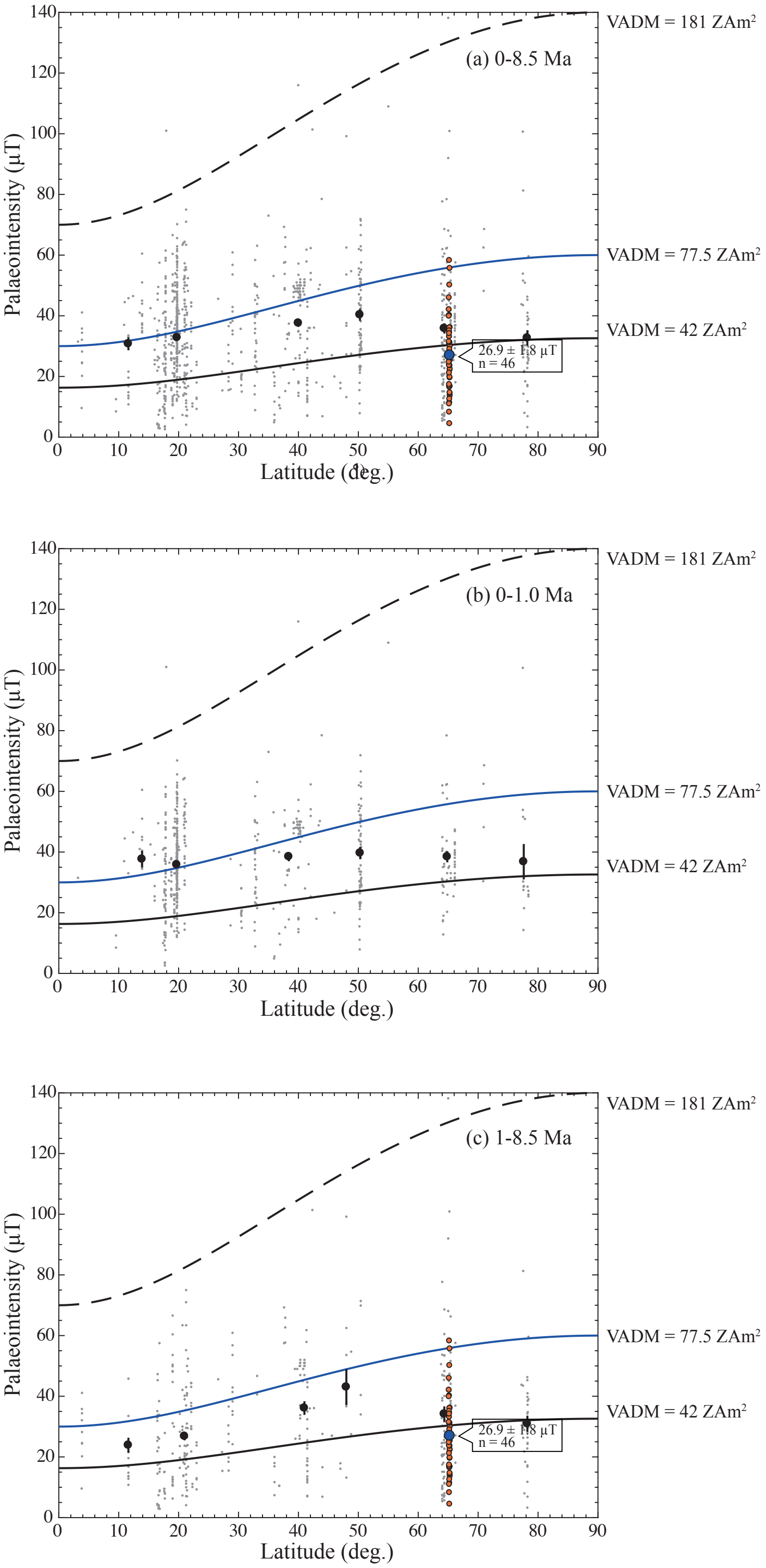

Figure 7.11: The variations of palaeointensity data with latitudes. Grey dots represent palaeointensity data from the PINT15 database (Biggin et al., 2009). Southern hemisphere data are scarce and were flipped to the northern hemisphere dimension. The PINT15 dataset is averaged into 15° latitude bins and illustrated as black circles with the standard error of the mean. The PINT15 data are categorized into three different time intervals: (a) 0-8.5 Ma, (b) 0-1 Ma and (c) 1-8.5 Ma. Orange and blue circles represent individual site mean intensity and mean intensity of this study. Blue, black and dash lines show the palaeointensity against latitudes drawn from the current day VADM of 77.5 ZAm^2, 0-140 Myr VADM of 42 ZAm^2 (Tauxe et al., 2013) and maximum VADM of 181 ZAm^2.

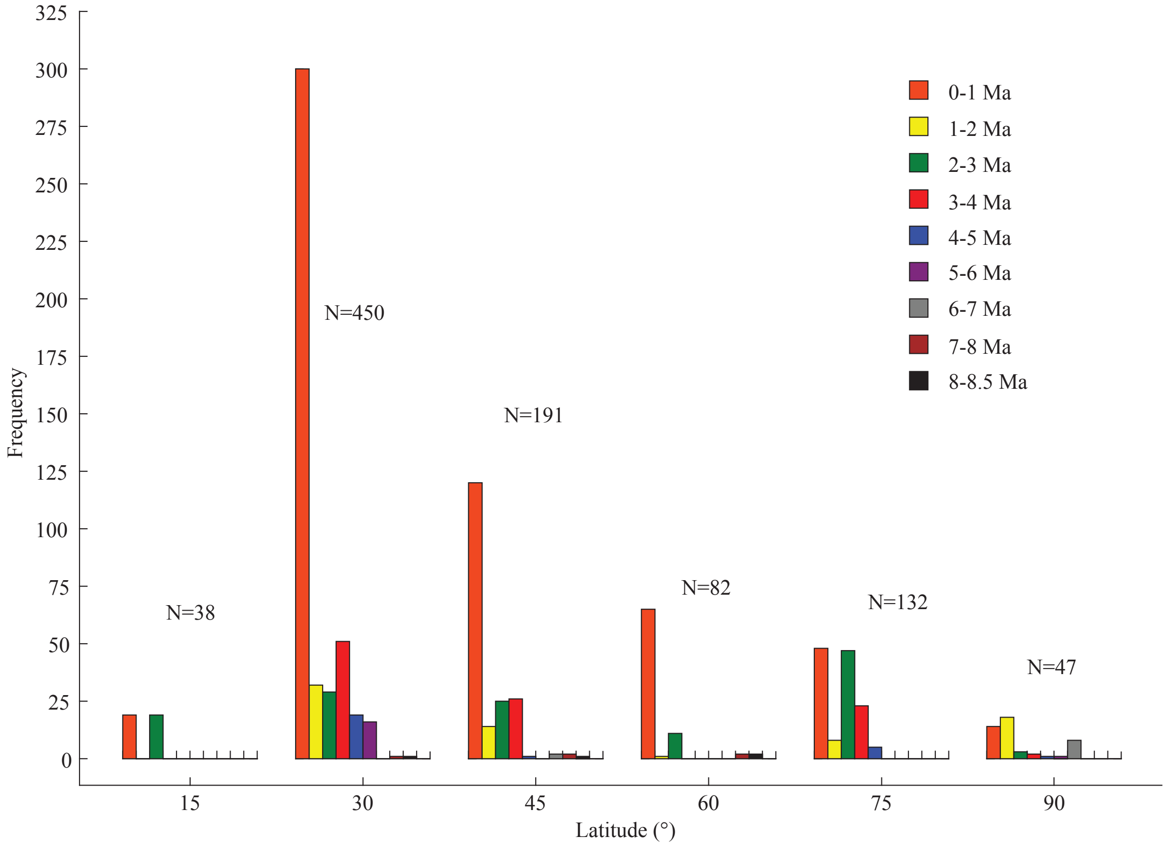

Figure 7.12: A histogram showing the age distribution of accepted PINT15 dataset (Biggin et al., 2009) and data from literature (Cromwell et al., 2015; Døssing et al., 2016; Tanaka and Yamamoto, 2016) between 0-8.5 Ma against latitude bins. The inset colour squares represent the age bands during different time intervals. The concentrations of the dataset fall within 0-1 Ma (orange stack) especially at latitude-bins of 15-30, 30-45 and 45-60°N. Approximately 300 data points spanning 0-1 Ma at 15-30°N yield the mean intensity toward the current day field as shown in Figure 7.11b.

Why is the intensity low at high-latitudes? I consider this here. One potential scenario is the long-term persistence of non-dipole contributions to the field since 8.5 Ma. This scenario was analysed by Muxworthy (2017). The author modified the statistical model TK03 (Tauxe and Kent, 2004) to fit the PINT15 data during the past 5 Myr. Muxworthy (2017) added the axial quadrupole and axial octupole to the model to fit the data. This modified model suggests that there is a persistent axial quadrupole (g_2^0) and the axial octupole (g_3^0) of ~10% and 15% in the 5 Ma dataset; both g_2^0 and g_3^0 are of the *opposite* sign with g_1^0. In order to re-examine the persistence of the non-dipole in the global dataset during the past 8.5 Myr, the palaeointensity data from 46 lava flows were combined with the PINT15 data and additional Iceland data. I modified the TK03 model (Tauxe and Kent, 2004) to vary g_1^0, g_2^0 and g_3^0 terms in a similar way to that described in Chapter 6 for the palaeodirection analysis. Here, the modified TK03 was adjusted with respect to the g_1^0, g_2^0 and g_3^0 terms in order to find the best non-dipole conditions to fit the global dataset. I kept the α and β terms of 7.8 μT and 4.0 the same as in Chapter 6.

In order to simulate the global dataset, c. 1000 intensity data were generated from the model for each latitude, from 90°S to 90°N. The intensity data in the southern hemisphere were flipped and binned with northern hemisphere data in order to average the field between hemispheres. Then, the mean intensity for 15° latitude bins was calculated. The weighted RMS misfit between the model and the global dataset for different portions of the non-dipole was calculated following Equation 7.2.

$$RMS = \sqrt{\frac{1}{N}\sum_{i=1}^{N}\left(B_{sim(i)} - B_{obs(i)}\right)^2} \tag{7.2}$$

where N is the number of data points used in the RMS calculation. B_{sim} and B_{obs} are the mean intensity for 15° latitude bin from the simulated data and the PINT15 dataset.

The modified TK03.GAD (α = 7.8 μT and β = 4.0) is presented in Figure 7.13a as a reference; note in this model $g_2^0 = 0$ and $g_3^0 = 0$. Then, the terms $g_2^0 = -0.10g_1^0$ and $g_3^0 = -0.20g_1^0$ were added to the modified TK03 (Figure 7.13b). It is clear that the modified TK03 underestimates the global dataset. This would be a result of low g_1^0 term in the model; therefore, the g_1^0 term is slightly adjusted to fit the dataset, i.e., different time interval has different g_1^0. The g_1^0 term was consistently between 20 and 24 μT which is larger than the original TK03 (Tauxe and Kent, 2004). The g_2^0 was set to $-0.05g_1^0$ and $-0.20g_1^0$, while the g_3^0 was varied from $-0.14g_1^0$ to $-0.23g_1^0$. Figure 7.14-7.19 represent the palaeointensity models during three different time intervals: 0-8.5 Ma (Figure 7.14-7.15), 0-1.0 Ma (Figure 7.16-7.17) and 1.0-8.5 Ma (Figure 7.18-7.19). The black lines in the figures represents the predicted intensity line for each non-dipole contribution. Here I found the g_2^0 around $-0.05g_1^0$ and $-0.10g_1^0$, and g_3^0 around $-0.19g_1^0$ to $-0.21g_1^0$ provide good estimates for global dataset during three time-intervals (Figure 7.14-7.19). Adding the $g_2^0 = -0.05g_1^0$ and $g_3^0 = -0.20g_1^0$ provides the best fit on the 0-8.5 Ma global dataset with root mean square (RMS) misfit of 1.25 μT (Figure 7.14c and Table 7.5). Regarding the 0-1.0 Ma and 1.0-8.5 Ma datasets, the g_2^0 around $-0.05g_1^0$ and $-0.10g_1^0$, and $g_3^0 = -0.20g_1^0$ provide the best estimate for these datasets (Figure 7.16-7.19 and Table 7.5). The RMS misfits for each non-dipole contribution are also given in Table 7.5.

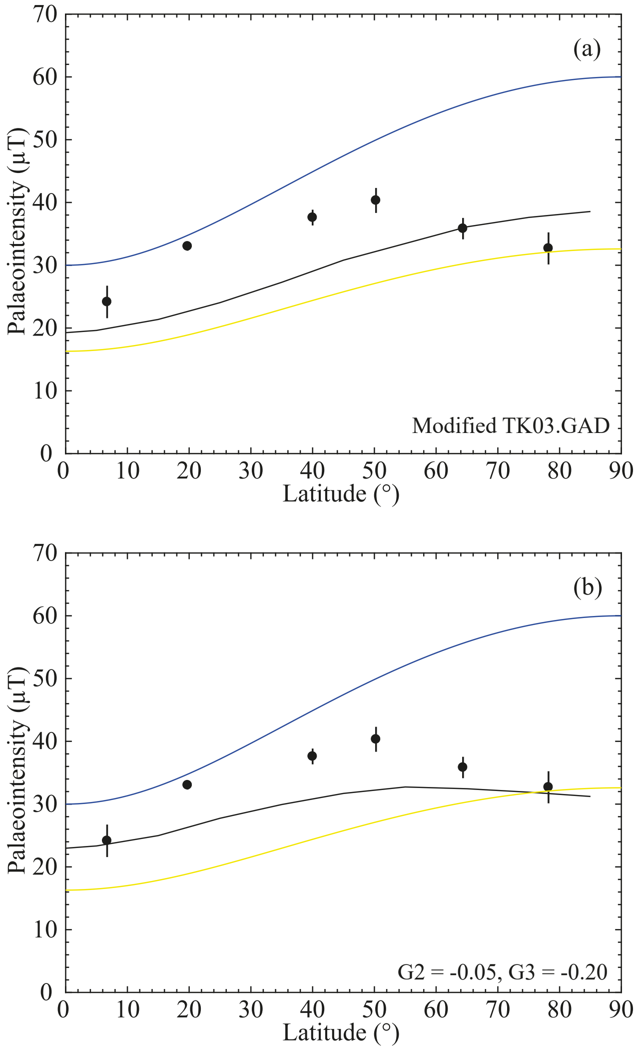

Figure 7.13: (a) The modified TK03.GAD (black line) (Chapter 6). The PINT15 data were binned into 15° latitude bin and plotted at black circles with standard errors. Yellow and blue lines show the reference palaeointensity against latitudes drawn from the current day VADM of 77.5 ZAm^2 and 0-140 Myr VADM of 42 ZAm^2 (Tauxe et al., 2013). (b) The modified TK03 with G2 = -0.10 and G3 = -0.20 contributions, where $\mathrm{G2} = g_2^0/g_1^0$ and $\mathrm{G3} = g_3^0/g_1^0$. (c) The modified TK03.GAD after g_1^0 was adjusted to -21 μT.

Table 7.5: The RMS misfit data indicating how the model predictions deviate from the global palaeointensity dataset. It is clear that the axial quadrupole and axial octupole terms of approximately -5% and -20% provide the lowest misfit (0-8.5 Ma), indicating smallest departure from the global dataset.

Non-dipole components	RMS misfit		
	0-8.5 Ma	0-1.0 Ma	1.0-8.5 Ma
$g_2^0 = -5\%, g_3^0 = -18\%$	1.38	2.04	3.97
$g_2^0 = -5\%, g_3^0 = -19\%$	1.25	1.96	3.99
$g_2^0 = -5\%, g_3^0 = -20\%$	1.25	1.91	3.96
$g_2^0 = -5\%, g_3^0 = -21\%$	1.30	1.91	4.06
$g_2^0 = -5\%, g_3^0 = -22\%$	1.42	2.02	4.06
$g_2^0 = -5\%, g_3^0 = -23\%$	1.65	2.12	4.16
$g_2^0 = -10\%, g_3^0 = -18\%$	1.62	2.06	3.88
$g_2^0 = -10\%, g_3^0 = -19\%$	1.59	1.92	3.85
$g_2^0 = -10\%, g_3^0 = -20\%$	1.52	1.88	3.96
$g_2^0 = -10\%, g_3^0 = -21\%$	1.56	1.88	3.95
$g_2^0 = -10\%, g_3^0 = -22\%$	1.71	1.91	4.01
$g_2^0 = -10\%, g_3^0 = -23\%$	2.54	1.99	4.02

0-8.5 Ma Dataset

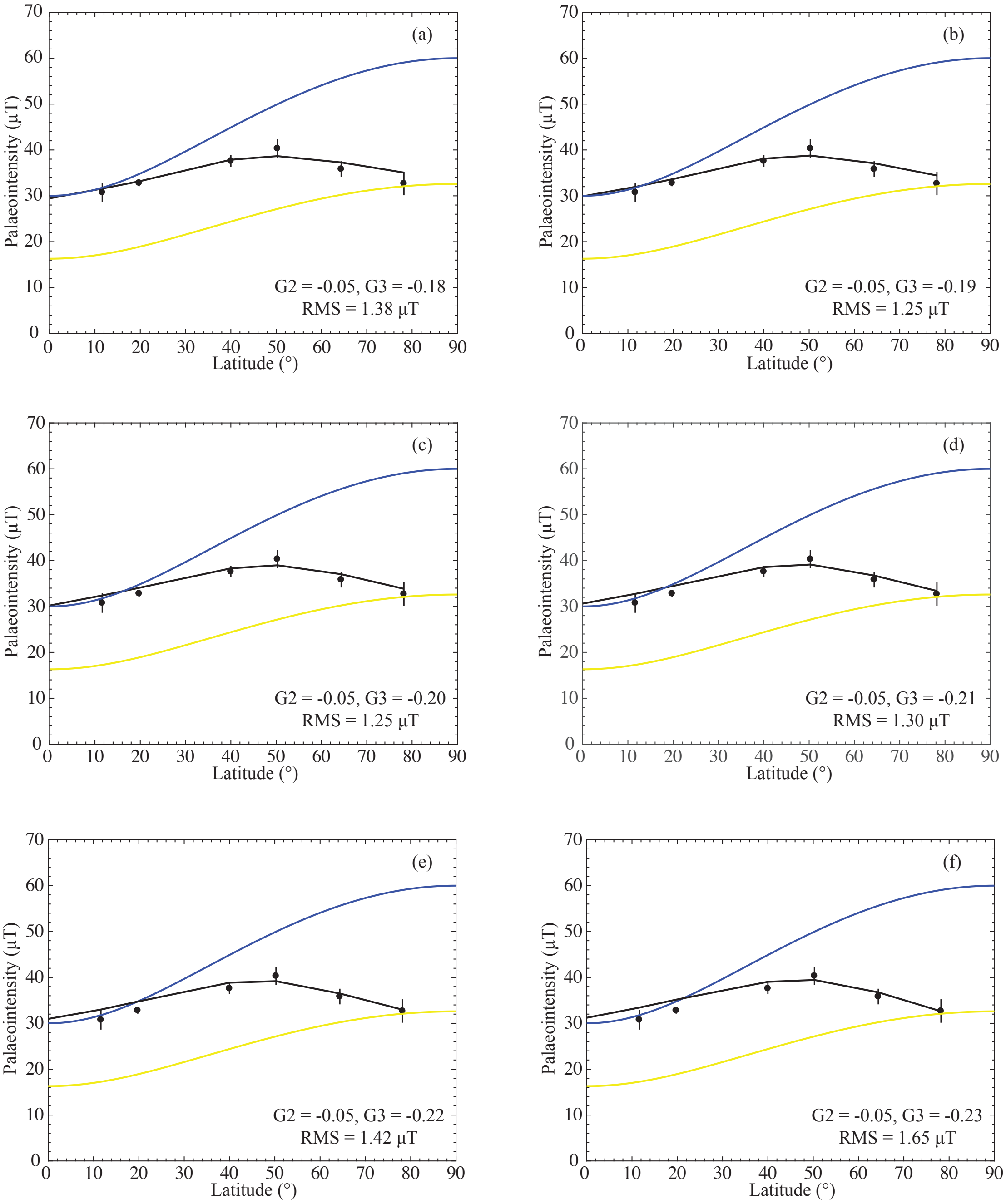

Figure 7.14: The modified TK03 model with the non-dipole contributions (black lines) to 0-8.5 Ma dataset. (a) G2 = -0.05, G3 = -0.18, (b) G2 = -0.05, G3 = -0.19, (c) G2 = -0.05, G3 = -0.20, (d) G2 = -0.05, G3 = -0.21, (e) G2 = -0.05, G3 = -0.22 and (f) G2 = -0.05, G3 = -0.23. Yellow and blue lines show the reference palaeointensity against latitudes drawn from the current day VADM of 77.5 ZAm^2 and 0-140 Myr VADM of 42 ZAm^2 (Tauxe et al., 2013).

0-8.5 Ma Dataset

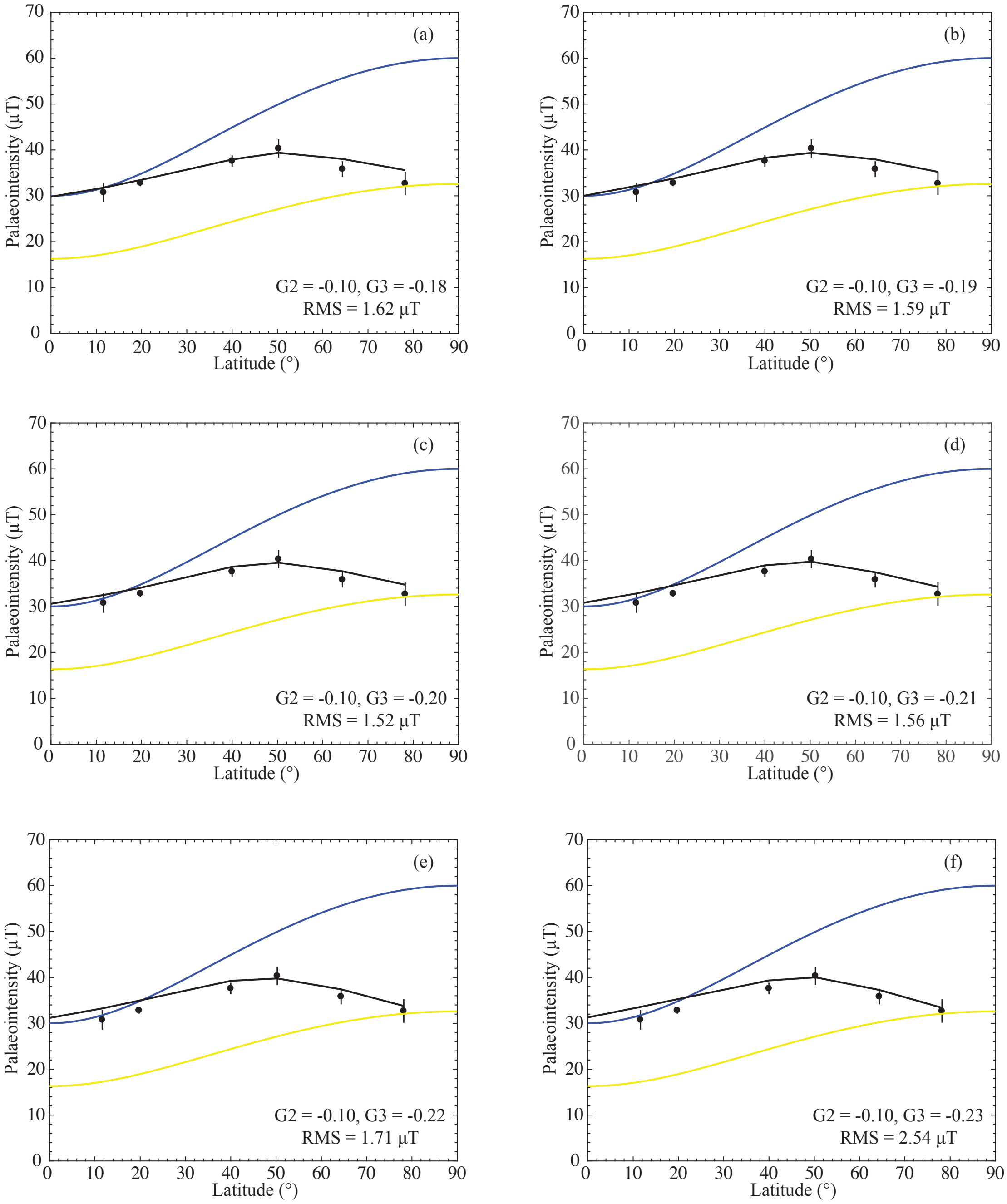

Figure 7.15: The modified TK03 model with the non-dipole contributions (black lines) to 0-8.5 Ma dataset. (a) G2 = -0.10, G3 = -0.18 (b) G2 = -0.10, G3 = -0.19, (c) G2 = -0.10, G3 = -0.20, (d) G2 = -0.10, G3 = -0.21, (e) G2 = -0.10, G3 = -0.22, and (f) G2 = -0.10, G3 = -0.23. Yellow and blue lines show the reference palaeointensity against latitudes drawn from the current day VADM of 77.5 ZAm^2 and 0-140 Myr VADM of 42 ZAm^2 (Tauxe et al., 2013).

0-1.0 Ma Dataset

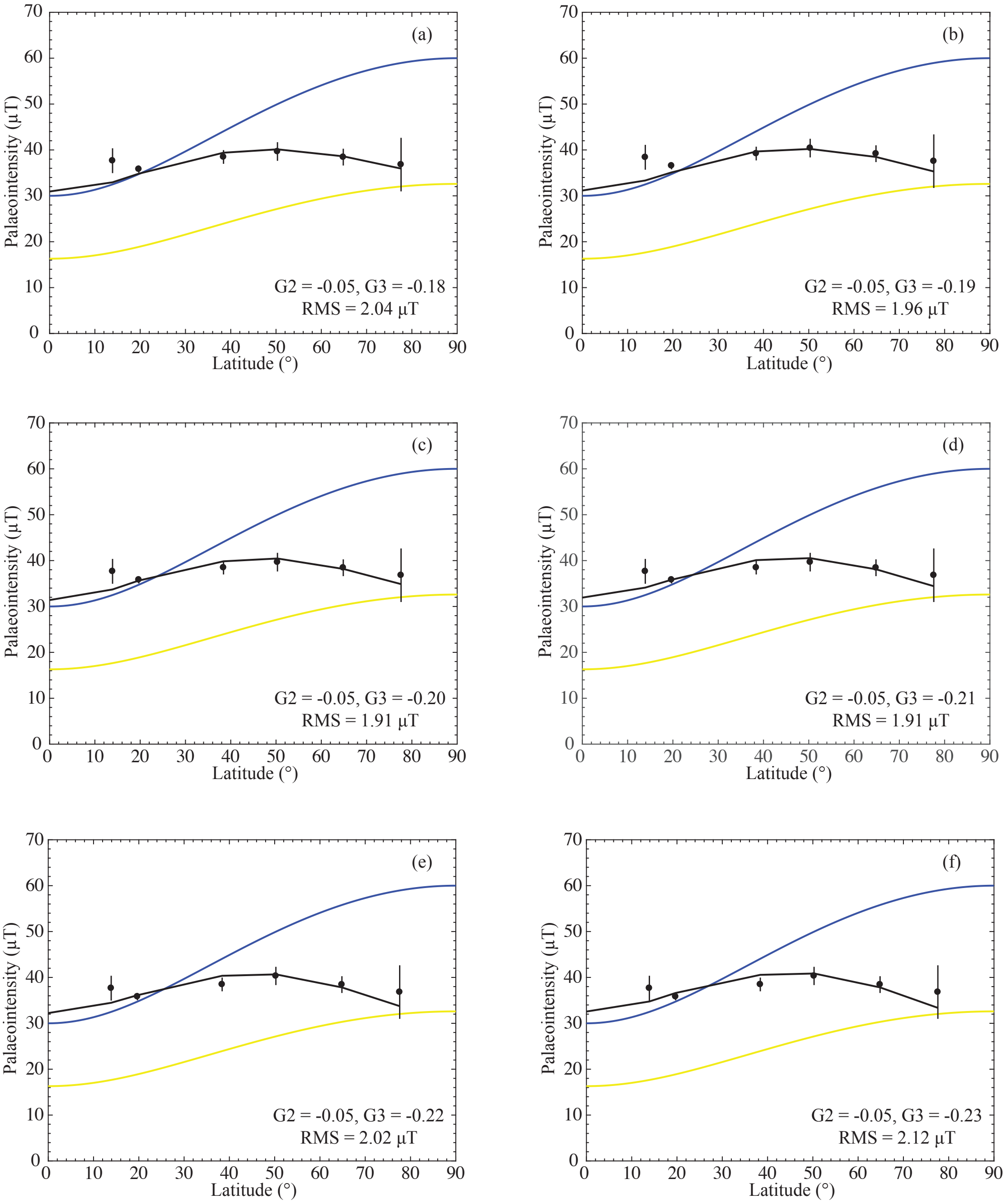

Figure 7.16: The modified TK03 model with the non-dipole contributions (black lines) to 0-1.0 Ma dataset. (a) G2 = -0.05, G3 = -0.18, (b) G2 = -0.05, G3 = -0.19, (c) G2 = -0.05, G3 = -0.20, (d) G2 = -0.05, G3 = -0.21, (e) G2 = -0.05, G3 = -0.22 and (f) G2 = -0.05, G3 = -0.23. Yellow and blue lines show the reference palaeointensity against latitudes drawn from the current day VADM of 77.5 ZAm^2 and 0-140 Myr VADM of 42 ZAm^2 (Tauxe et al., 2013).

0-1.0 Ma Dataset

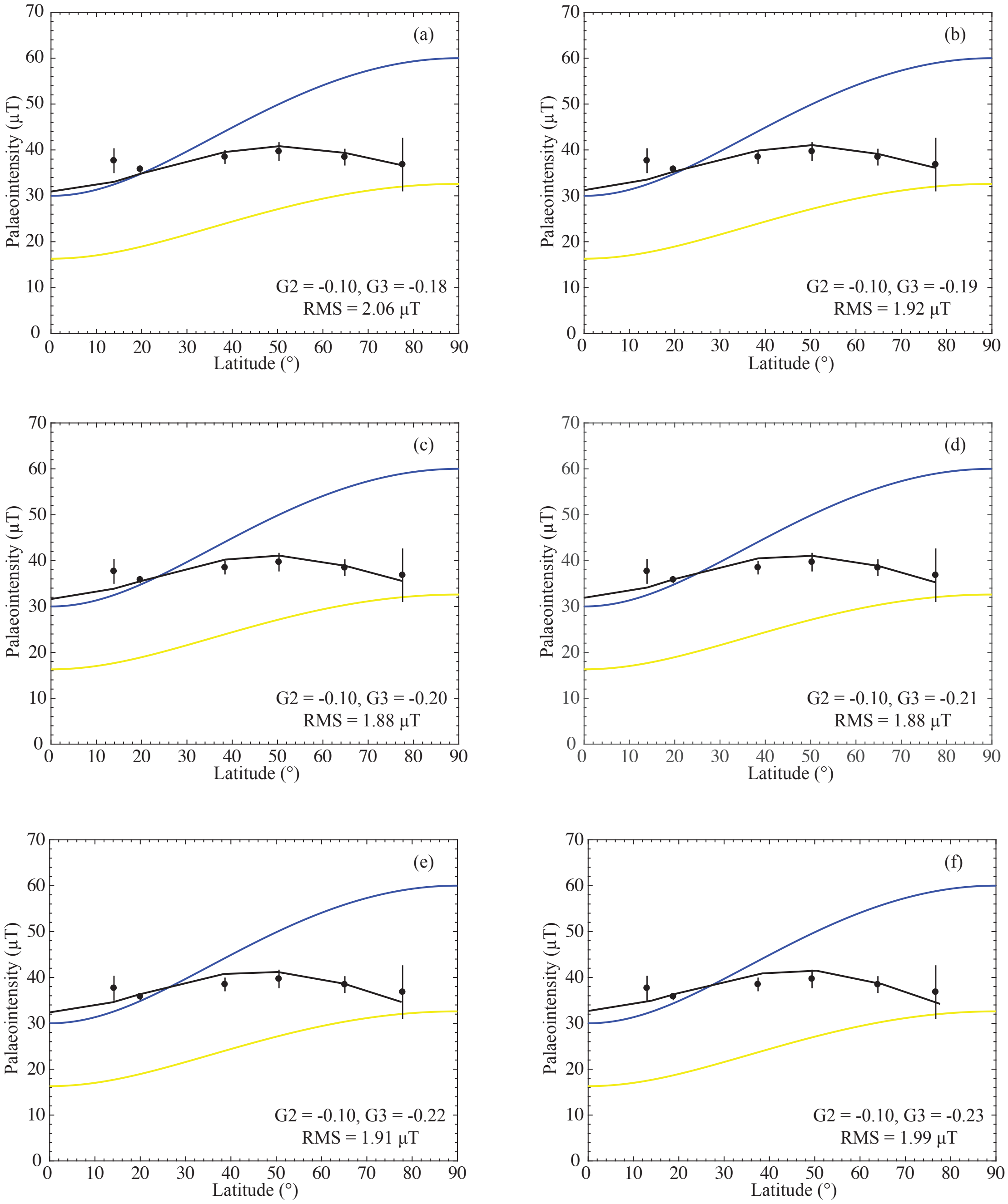

Figure 7.17: The modified TK03 model with the non-dipole contributions (black lines) to 0-1.0 Ma dataset. (a) G2 = -0.10, G3 = -0.18 (b) G2 = -0.10, G3 = -0.19, (c) G2 = -0.10, G3 = -0.20, (d) G2 = -0.10, G3 = -0.21, (e) G2 = -0.10, G3 = -0.22, and (f) G2 = -0.10, G3 = -0.23. Yellow and blue lines show the reference palaeointensity against latitudes drawn from the current day VADM of 77.5 ZAm^2 and 0-140 Myr VADM of 42 ZAm^2 (Tauxe et al., 2013).

1.0-8.5 Ma Dataset

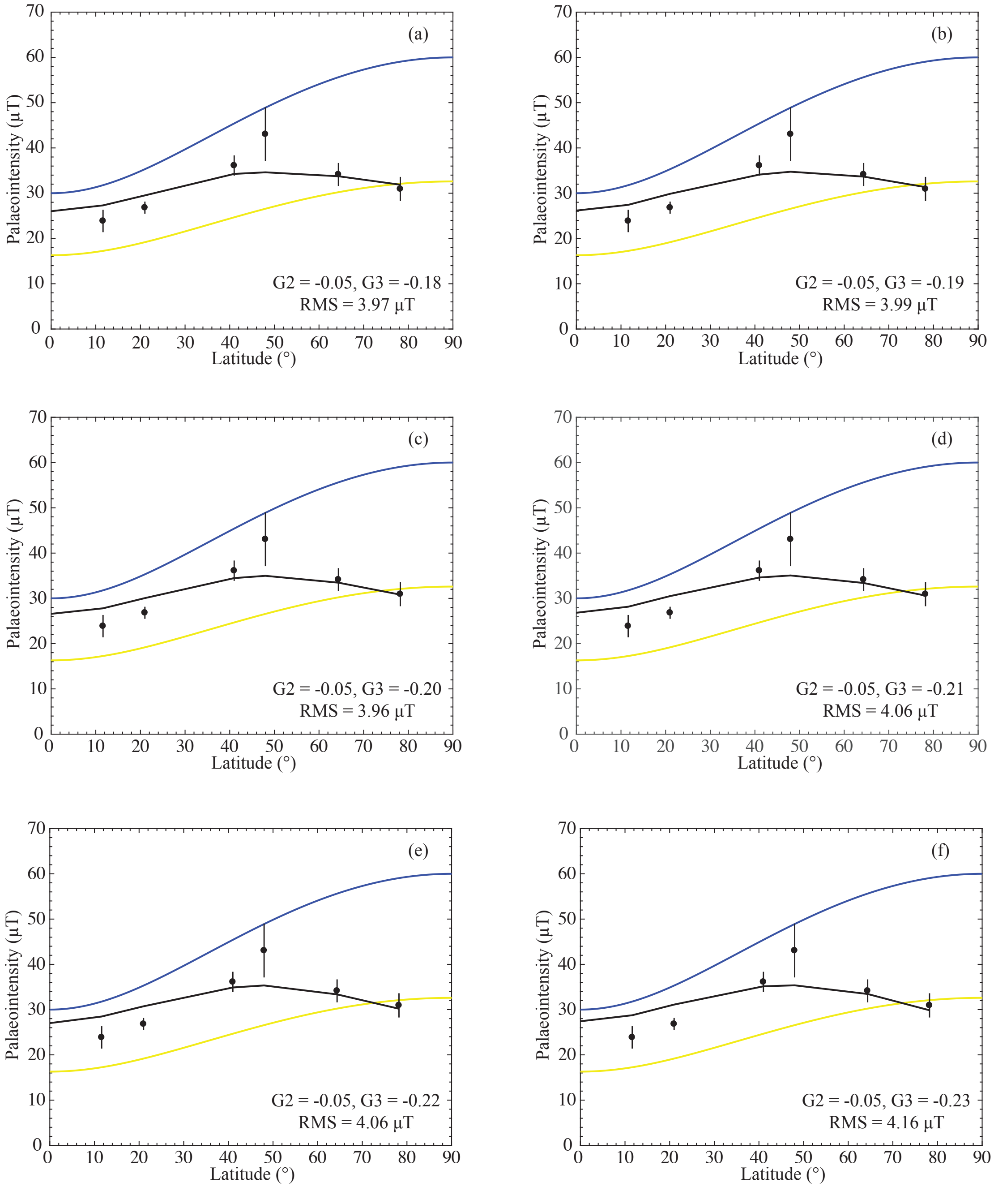

Figure 7.18: The modified TK03 model with the non-dipole contributions (black lines) to 1.0-8.5 Ma dataset. (a) G2 = -0.05, G3 = -0.18, (b) G2 = -0.05, G3 = -0.19, (c) G2 = -0.05, G3 = -0.20, (d) G2 = -0.05, G3 = -0.21, (e) G2 = -0.05, G3 = -0.22 and (f) G2 = -0.05, G3 = -0.23. Yellow and blue lines show the reference palaeointensity against latitudes drawn from the current day VADM of 77.5 ZAm^2 and 0-140 Myr VADM of 42 ZAm^2 (Tauxe et al., 2013).

1.0-8.5 Ma Dataset

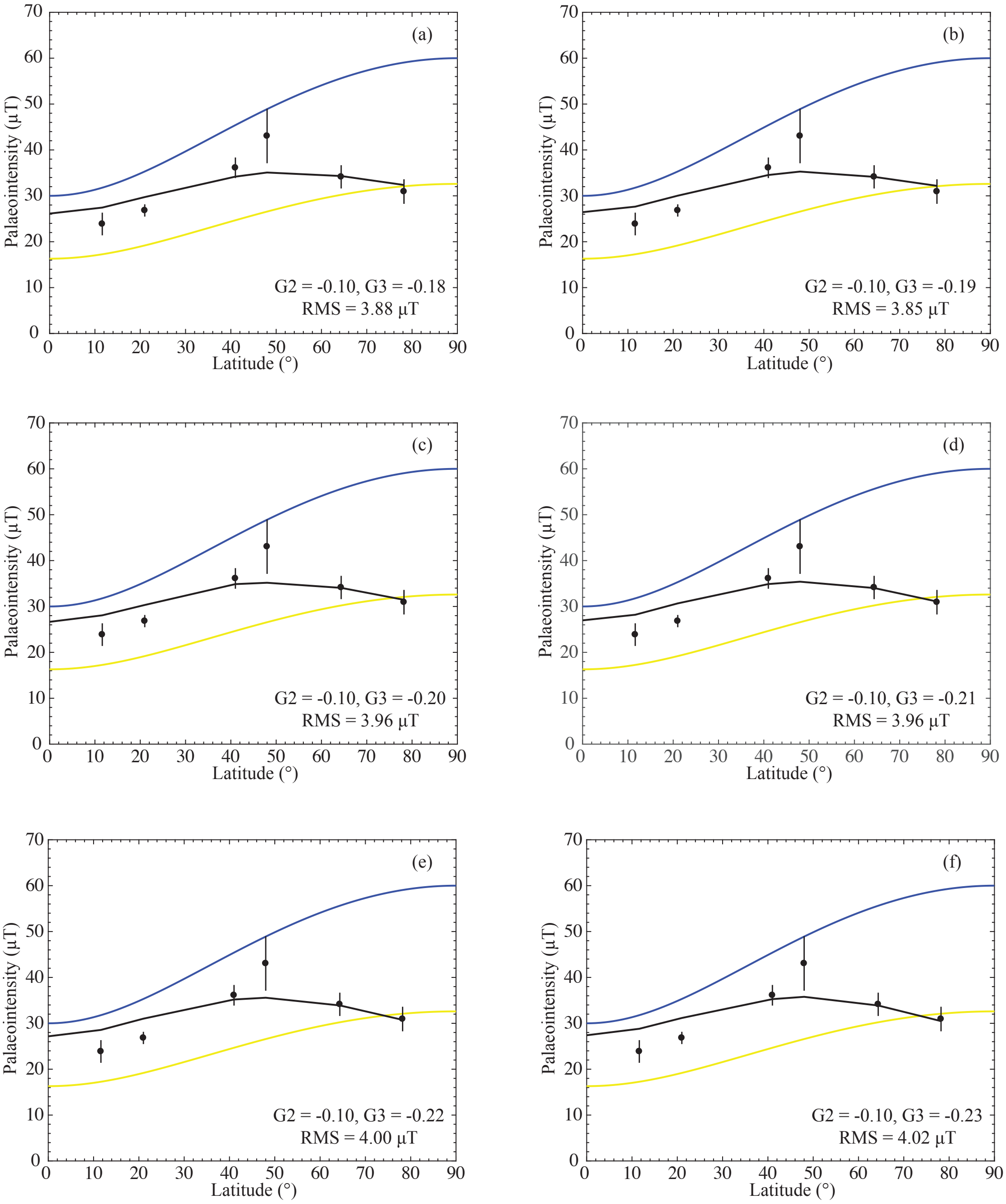

Figure 7.19: The modified TK03 model with the non-dipole contributions (black lines) to 1.0-8.5 Ma dataset. (a) G2 = -0.10, G3 = -0.18 (b) G2 = -0.10, G3 = -0.19, (c) G2 = -0.10, G3 = -0.20, (d) G2 = -0.10, G3 = -0.21, (e) G2 = -0.10, G3 = -0.22, and (f) G2 = -0.10, G3 = -0.23. Yellow and blue lines show the reference palaeointensity against latitudes drawn from the current day VADM of 77.5 ZAm^2 and 0-140 Myr VADM of 42 ZAm^2 (Tauxe et al., 2013).

To test the consistency between the palaeointensity and PSVL models (Chapter 6), firstly, the $g_2^0 = \pm 0.04 g_1^0$ and $g_3^0 = \pm 0.01 g_1^0$ were added to the modified TK03 to generate the intensity data for each latitude. The intensity data were plotted as the black lines in Figure 7.20. It is clear that the g_2^0 of $\pm 0.04 g_1^0$ and g_3^0 of $\pm 0.01 g_1^0$ can describe only the data from ~65°N but show the large mismatch in other latitude bands. This suggests that the proportion of g_2^0 and g_3^0 found in the PSVL dataset is not sufficient to describe the palaeointensity dataset. I also tested the proportion of g_2^0 and g_3^0 found in the palaeointensity dataset in the PSVL dataset. The g_2^0 of $\pm 0.05 g_1^0$ and g_3^0 of $\pm 0.20 g_1^0$ were added to the modified TK03 to simulate the declination and inclination data. Then, the inclination anomalies were calculated following Equation 1.6 and were plotted as the black lines in Figure 7.21. As can be seen from Figure 7.21 (left column), negative g_2^0 and g_3^0 yield positive inclination anomalies in the Northern Hemisphere and negative inclination anomalies in the Southern Hemisphere. There is a large mismatch between the PSVL dataset and simulated dataset. With regards to the positive g_2^0 and g_3^0, this condition provides negative inclination anomalies in the Northern Hemisphere and positive inclination anomalies in the Southern Hemisphere (Figure 7.21, right column). The large mismatch between the PSVL dataset and simulated dataset was also found in this positive g_2^0 and g_3^0 condition. The simulated inclination anomalies can only describe the reverse polarity data between 50°S and 80°S and all datasets (Figure 7.21, right column) between 10°S and 10°N. It is clear that the proportion of g_2^0 and g_3^0 found in the palaeointensity data cannot well describe the majority of the PSVL dataset. Further discussions for this inconsistency are given in the discussion section.

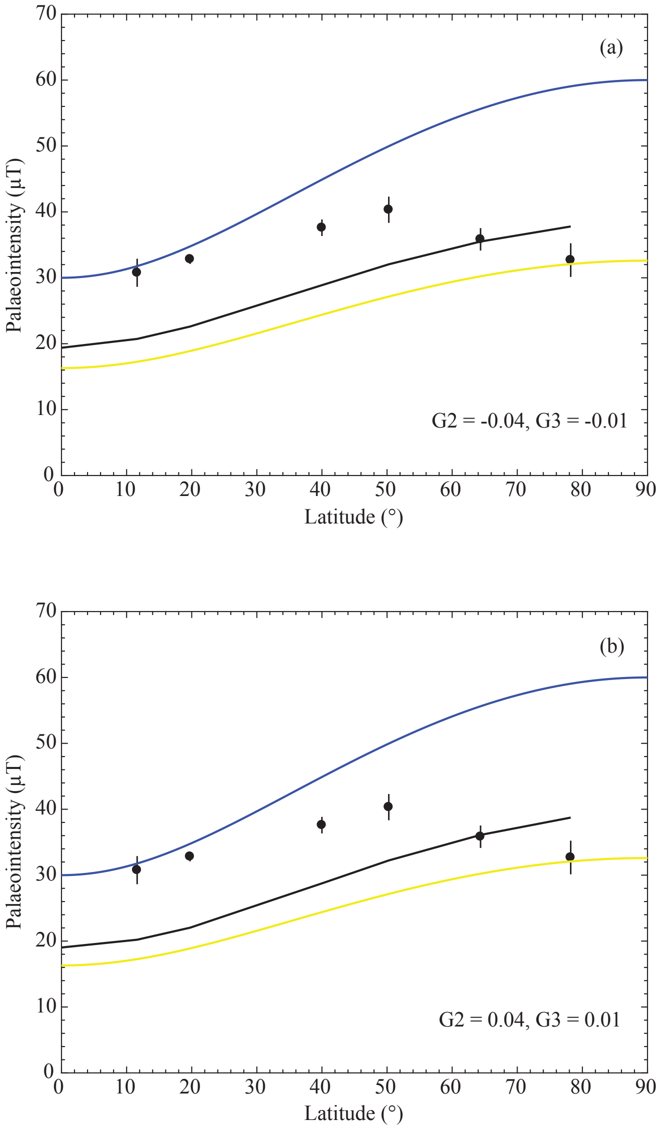

Figure 7.20: The modified TK03 (black lines) with (a) G2 = -0.04 and G3 = -0.01, and (b) G2 = 0.04 and G3 = 0.01 contributions, where $G2 = g_2^0/g_1^0$ and $G3 = g_3^0/g_1^0$. The PINT15 data were binned into 15° latitude bin and plotted at black circles with standard errors. Yellow and blue lines show the reference palaeointensity against latitudes drawn from the current day VADM of 77.5 ZAm^2 and 0-140 Myr VADM of 42 ZAm^2 (Tauxe et al., 2013). The proportion of G2 and G3 used in these models was obtained from PSVL dataset in Chapter 6.

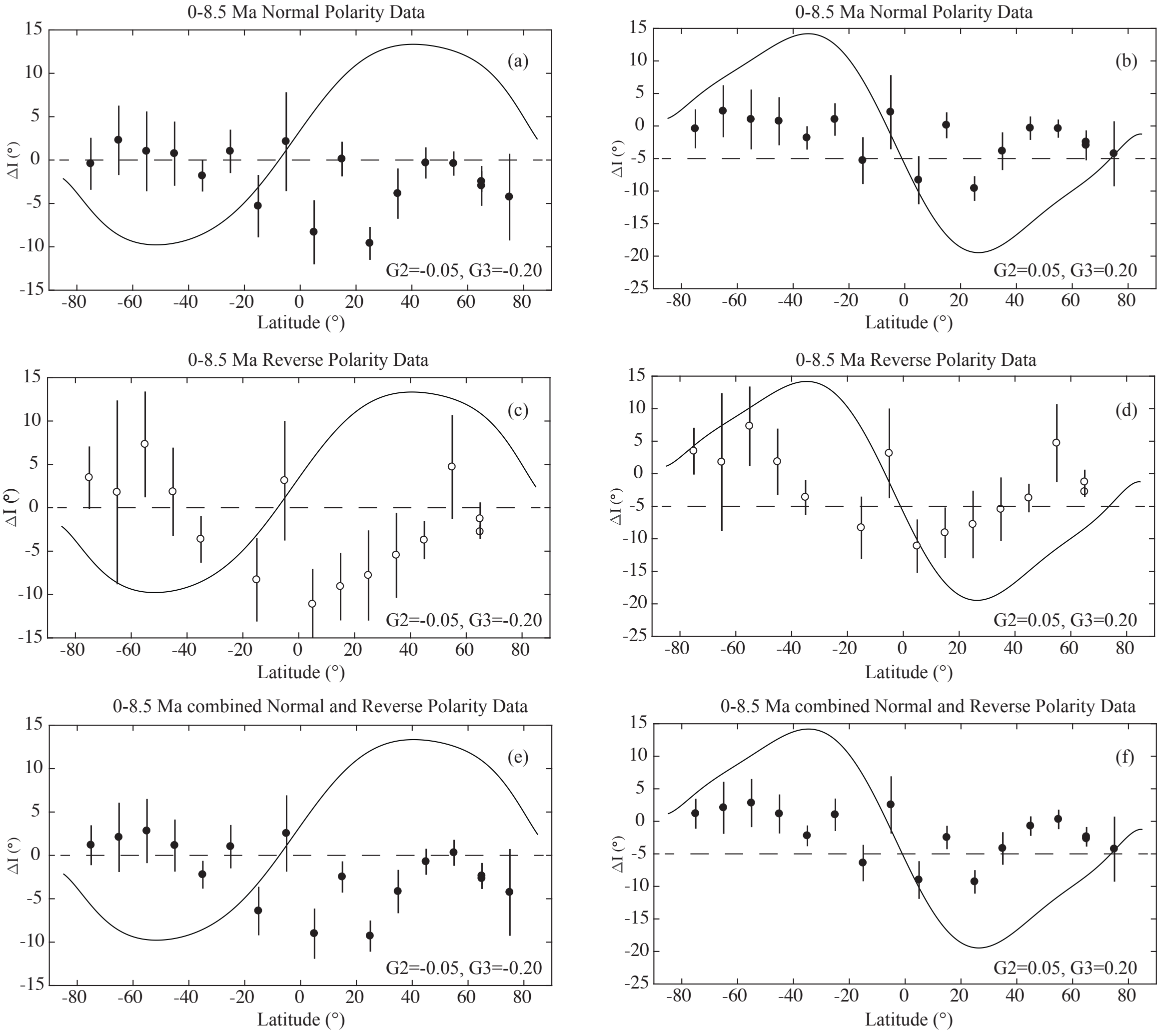

Figure 7.21: The observed inclination anomalies between simulated inclination data ($g_2^0 = \pm 0.05 g_1^0$ and $g_3^0 = \pm 0.20 g_1^0$) from modified TK03 (black lines) and the inclination data from the 0-8.5 Ma PSVL dataset (black circles) versus latitudes during (a)-(b) normal polarity interval, (c)-(d) reverse polarity interval and (e)-(f) combined normal and reverse polarity. (a), (c) and (e) show inclination anomalies with $g_2^0 = -0.045$ and $g_3^0 - 0.20 g_1^0$ while (b), (d) and (f) represent inclination anomalies with $g_2^0 = +0.05 g_1^0$ and $g_3^0 = +0.20 g_1^0$. The GAD inclination is presented as the dash lines ($y = 0$).

7.7 Discussions

7.7.1 Rock magnetic properties

Rock magnetic properties show variations of magnetic mineral compositions across Eyjafjardardalur valley. The main remanence carrier is predominantly titanomagnetite, as expected for volcanic rocks. The majority of samples fall within the pseudo-single domain region and exhibits thermomagnetic behaviours of iron-rich titanomagnetite. The high thermal resistance also reveals the possibility of obtaining robust palaeointensity estimates from northern Iceland. Even though, preliminarily screen for the promising specimens and flows were performed using these data; however, only 45% of the specimens yields reliable palaeointensity estimates.

7.7.2 Time-averaged field intensity

According to the time-averaged field equation (Equation 1.7), the GAD hypothesis predicts that the field strength at the equator is twice lower than the field strength at the pole, i.e., the time-averaged field intensity for 65°N is ~56 μT. The mean palaeointensity of 26.9 ± 1.9 μT from this study is significantly weaker than the GAD field. As the majority of the data covers time-span ~2.50-8.05 Ma, to improve the spatial coverage of the mean palaeointensity at 65°N, I included seven data points (~2.35-3.35 Ma) from Cromwell et al. (2015), 11 data points (~2.50-3.50 Ma) from Tanaka and Yamamoto (2016) and six data points (~1.10-1.83 Ma) from Døssing et al. (2016) in palaeointensity calculations. The inclusions of ~1.10-3.50 Ma data yields the mean palaeointensity of 31.7 ± 1.6 μT for ~1.10-8.05 Ma. This intensity is still low when compared to the GAD intensity of ~56 μT for Iceland. With regards to high-southern latitudes, the weak field strength of ~28.3 ± 2.9 μT was also observed by Lawrence et al. (2009), when compared to the GAD field intensity of ~59 μT for McMurdo station (~78°S).

The possible cause of weak field at high-latitudes concerning here is the persistence of the permanent non-dipole fields which contribute to the main field. This hypothesis was tested in the previous section. The models of palaeointensity during three different time intervals: 0-8.5 Ma, 0-1.0 Ma and 1.0-8.5 Ma show that there are the permanent axial quadrupole of -5% to -10% of g_1^0 and axial octupole of -20% of g_1^0 which cause the weak intensity at high-latitudes in the global palaeointensity dataset. Cromwell et al. (2013b) noticed that the axial quadrupole of ~20% would be required to describe the field at high-latitudes. However, I found that the axial quadrupole of ~5% would be needed for the high-latitude field. The portions of the g_2^0 and g_3^0 found in this study agree with Muxworthy (2017), but contradicts the Model K00 (Kono et al., 2000). Kono et al. (2000) inverted the palaeointensity data to determine the non-dipole components during 0-5 Ma. Their model (K00) found estimates for g_2^0 of $-0.06g_1^0$ and g_3^0 of $0.06g_1^0$. The present study proposes that g_3^0 terms are higher than the K00. I attempted to add the negative g_2^0 and positive g_3^0 as stated in K00 to the modified TK03 model. With these conditions, the model become worse. As stated above, the current PINT15 database has improved significantly since Kono et al. (2000) proposed their model. Veikkolainen et al. (2017) tested the GAD hypothesis using palaeointensity data spanning from 1-540 Ma and >540 Ma. They also proposed that an octupole term higher than ±10% of g_1^0 is needed to describe the global palaeointensity data. They also noticed that replacing axial octupole with ±10% quadrupole does not make their models fit the palaeointensity data. Therefore, I suggest that the long term non-dipole contributions are persistent and true.

A question arises why the contributions of g_2^0 and g_3^0 here are higher than those found for the palaeodirection dataset (e.g., Chapter 6 (section 6.5); Carlut and Courtillot, 1998; Johnson et al., 2008). The proportion of $g_2^0 = \pm 4\%$ and $g_3^0 = \pm 1\%$ determined from the PSVL data cannot described the weak intensity at high latitudes, while the g_2^0 of ±5% and g_3^0 of ±20% determined from palaeointensity dataset yield far too large inclination anomalies. This does not mean that the two models are inconsistent, because the palaeointensity data have higher sensitivity to high-latitude geomagnetic field behaviour than the palaeodirection data as stated in Constable (2007) and Johnson and McFadden (2007). While the palaeointensity is more sensitive to the high-latitudes field than the palaeodirection, ~180 data points from >°60N and >60°S were used in the palaeointensity model compilation. With regards to palaeodirection, the inclination has higher sensitivity to low-latitude geomagnetic field behaviour than the palaeointensity; however, the PSVL dataset contains more than 1,100 data points covering latitudes between 30°S and 30°N. Besides this, the PSVL data contains nearly 2,000 data points obtain from >°60N and >60°S. The larger amount of directional data could remove spatial bias due to low- and high-latitude fields in the PSVL dataset. In order to remove spatial bias of the palaeointensity, the palaeomagnetic community still needs more palaeointensity data at high-latitudes for the model compilation. Note that the process of merging data into latitude bins is also crucial for the model. Improper binning of data may lead to misrepresentation of the field. Muxworthy (2017) binned the PINT15 dataset into 10° latitude bins and found the mismatch between the model and the global dataset at mid-latitudes. This large mismatch is not detected in the present study as larger bins were used.

7.7.3 Virtual (Axial) dipole moment (V(A)DM) and hemispheric asymmetry of the field

The VDM and VADM were used here for comparison between this study and other high-latitude studies. The VDM data are preferred in this study as it is derived from magnetic co-latitudes that represent the "real" dipole moment during the recording time interval. However, for comparison with literature, the VADM data are used instead as many studies do not provide reliable palaeodirection data for calculating the VDM (e.g., Cromwell et al., 2015). Figure 7.22a-b shows the VDM and VADM from the PINT15 database (grey dots), this study and literature (Cromwell et al., 2013a; Cromwell et al., 2015; Døssing et al., 2016; Tanaka and Yamamoto, 2016) versus site ages. Regarding the mean VDM and VADM from the PINT15 database, It is seen that the mean VDM and VADM for 0-1 Ma data have a bias toward the current day VADM of ~77.5 ZAm^2 (blue line) while those for 5-8.5 Ma data show the bias toward the 0.3-140 Ma VADM of ~42 ZAm^2 (black line) (Tauxe et al., 2013). The mean VDM and VADM for the 1-4 Ma time period show the intermediate trend between the current day VADM and 0.3-140 Ma VADM. With the exception of the 4-5 Ma bin, data within this bin tends toward the current day VADM.

With regards to this study, the VDM and VADM during three different time intervals: 2.64-3.24 Ma, 4.60-5.65 Ma and 7.05-8.05 Ma were considered as there are two major hiatuses within the lava succession in the study area. It is clearly seen from Figure 7.22a-b that the mean VDM/VADM (blue circles) for the sites in Eyjafjardardalur increases over time from 38.2 ± 3.6/34.5 ± 3.6 ZAm^2 to 56.4 ± 2.5/51.0 ± 5.3 ZAm^2, while the mean VDM and VADM for the whole interval are 41.4 ± 2.5 ZAm^2 and 37.4 ± 2.5 ZAm^2 (yellow circles in Figure 7.22a-b). The mean VDM agrees well with the 0-140 Myr VADM of 42 ZAm^2 (Tauxe et al., 2013) while the mean VADM is slightly lower than the literature. The mean VDM and VADM of this study during three different time intervals are summarised in Table 7.6.

According to the PINT15 database, MAGIC database and literature search engine, not much palaeomagnetic data were studied at high-latitudes on both the northern and southern hemisphere. Lawrence et al. (2009) studied the palaeomagnetic field properties at high-southern latitudes during 0.03-7.25 Ma using materials from Erebus Volcanic Province (EVP) in the Antarctic. They found a low-field strength with a mean VADM of 37.3 ± 3.8 ZAm^2 for ~1.07-7.25 Ma. Cromwell et al. (2013b) presented palaeointensity data from young volcanic rocks from Jan Mayen, Arctic Ocean. Their data show a VADM of 76.8 ± 10.3 ZAm^2 derived from five sites younger than 0.45 Ma (Figure 7.22, upside down red triangle). Their VADM is significantly higher than the VADM found at the high-southern latitudes (44.0 ± 3.8 ZAm^2) during the same time interval, but agrees with the current day VADM of 77.5 ZAm^2. This clearly show the bias of the data spanning ca. 0-1 Ma toward the current day field as mentioned in Section 7.6. Their data supported the assumption of hemispheric asymmetry of the palaeomagnetic field. Cromwell et al. (2015) investigated the high-northern latitude field strength from rapidly cooled lava flows from several sites in Iceland during 0-3.35 Ma. Their mean VADM during 0.01-3.35 Ma is 50.8 ±3.6 ZAm^2. They also re-analysed the Antarctic data of Lawrence et al. (2009) from nine sites (2.46-7.25 Ma) and found that both Antarctic and Iceland data agree with the long-term palaeomagnetic field (Juárez et al., 1998; Selkin and Tauxe, 2000; Tauxe et al., 2013). They proposed that the assumption of the long-term hemispheric asymmetry of the field might not be valid; note however, their time window for the northern hemisphere data was only 50 kyr. Døssing et al. (2016) reported the VDM and VADM of approximately 59.5 ± 3.4 and 59.7 ± 3.6 ZAm^2 from Jökuldalur, eastern Iceland (~1.2-1.8 Ma). They also compared their data with high-southern latitude field during 0-2 Ma (Lawrence et al., 2009), however, using the longer timespan for the northern hemisphere data they concluded that the geomagnetic field is asymetric with higher field strengths in the northern hemisphere. Tanaka and Yamamoto (2016) sampled Icelandic basalts whose ages are around 2.5-3.5 Ma from Storutjarnir, central-north Iceland, which is located near the study area of the present research. Their data show high mean VDM and VADM values of 62.7 ± 4.2 ZAm^2 and 59.9 ± 4.3 ZAm^2. The VADM data (VDM if possible) of these studies during different time interval are presented in Table 7.6. Bold data represent the time interval which coincides with this study and are plotted in Figure 7.22. It is clear that the VADM from Jökuldalur shows an agreement with the VADM of 59.7 ± 3.6 ZAm^2 calculated from the global dataset during 1-2 Ma. With regards to 2-4 Ma time interval, the VADM of this study (51.0 ± 5.3 ZAm^2) agrees with Cromwell et al. (2015) study (49.1 ± 6.8 ZAm^2) and is lower than the VADM of the global dataset (60.3 ± 2.4 ZAm^2) during 2-4 Ma. The data from Tanaka and Yamamoto (2016) agree with the VADM of this study and the global dataset within the standard error.

Table 7.6: Revised VDM and VADM from high-latitude studies: this study, Jökuldalur (Døssing et al., 2016), Iceland (Cromwell et al., 2015), Storutjarnir (Tanaka and Yamamoto, 2016), Jan Mayen (Cromwell et al., 2013b) and McMurdo (Lawrence et al., 2009). Bold data represent selected time intervals for comparison with this study and are plotted in Figure 7.15.

	Ages (Ma)	N	VDM (ZAm^2)	VADM (ZAm^2)
This study	2.64-3.24	5	56.4 ± 2.5	51.0 ± 5.3
	4.60-5.65	25	40.4 ± 3.8	36.5 ± 3.6
	7.05-8.05	16	38.2 ± 3.6	34.5 ± 3.6
	All	46	41.4 ± 2.5	37.4 ± 2.5
All Iceland	**1.2-8.05**	**70**	**-**	**44.0 ± 2.2**
Jökuldalur, Iceland	1.2-1.8	6	59.5 ± 3.4	59.7 ± 3.6
Iceland	**2.35-3.35**	**7**	**-**	**49.1 ± 6.8**
Storutjarnir, Iceland	**2.5-3.5**	**11**	**62.7 ± 4.2**	**59.9 ± 4.3**
Jan Mayen, Norway	1732 CE-0.46	4	84.5 ± 13.8	76.8 ± 10.3
McMurdo, Antarctic	0.03-0.86	15	-	44.0 ± 3.8
	1.07-2.28	23	-	39.2 ± 4.2
	2.46-7.25	**9**	**-**	**32.2 ± 8.2**
	1.07-7.25	**32**	**-**	**37.3 ± 3.8**

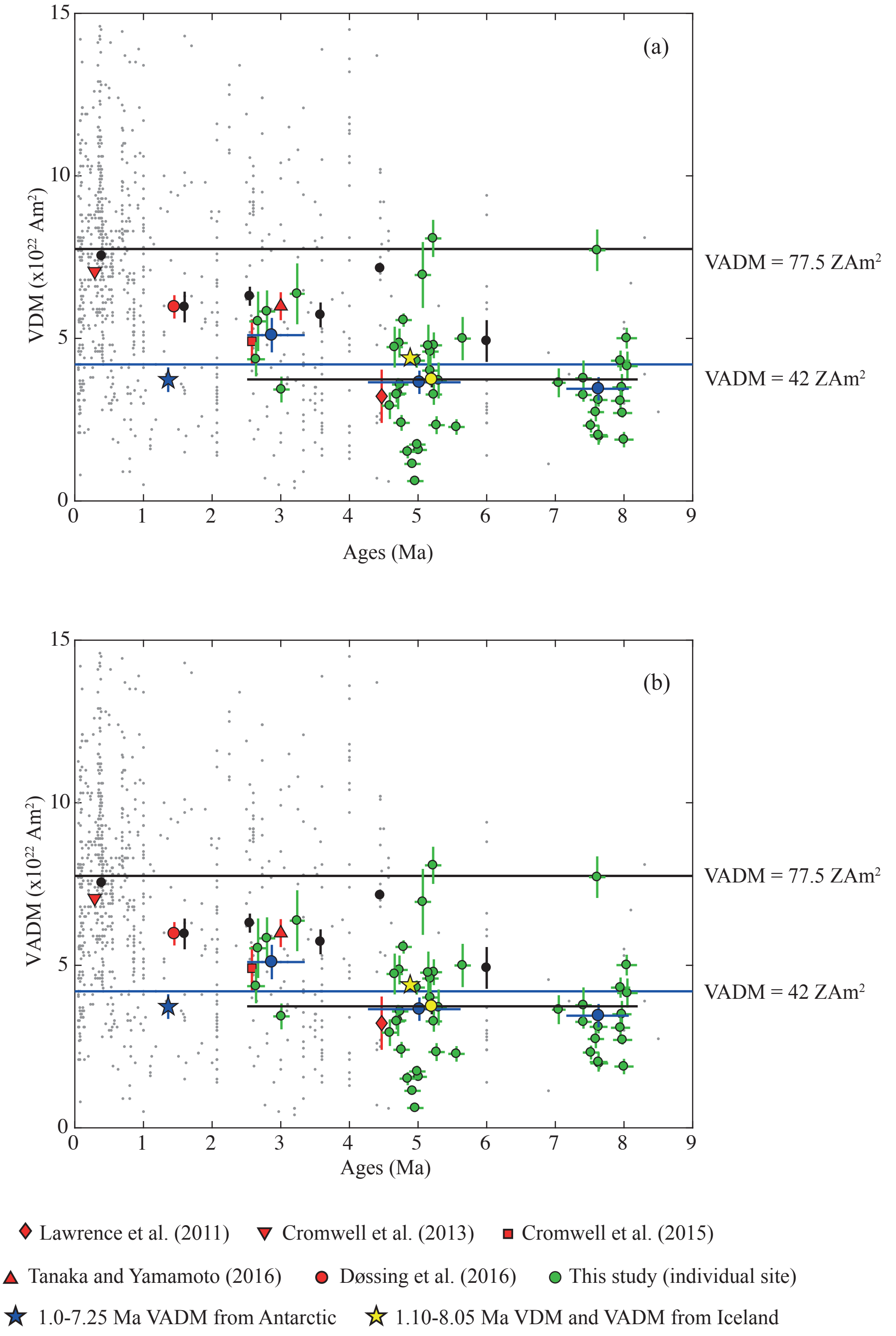

Figure 7.22: Plots of (a) VDM and (b) VADM data versus age for the last 9 Ma. Orange circles shows individual site mean VDM and VADM of this study. Blue circles represent mean VDM and VADM during three time intervals: 2.64-3.24 Ma, 4.6-5.65 Ma and 7.05-8.05 Ma and the yellow circle shows the mean VDM and VADM of this study. Grey dots represent PINT15 database (Biggin et al., 2009). The PINT15 data were grouped into 1 Myr bin for data whose ages lower than 5 Ma and data older than 5 Ma were grouped together in one bin. Black circles represent the mean VADM of each bin for the PINT15 data. Red symbols (diamond, downward triangle, square, upward triangle and circle) shows the VADM (or VDM if available) of the literature data from high-latitudes (these data are excluded from PINT15). Light blue and yellow stars represent the VADM from high-southern latitude sites during 0-7.5 Ma and from the combined data of this study and Døssing et al. (2016) study covering time span 0-8.5 Ma. The VADMs of the current day field and 0-140 Myr field average (Tauxe et al., 2013) are represented by black and blue lines respectively.

To evaluate the hemispheric asymmetry of the palaeomagnetic field, a comparison between this study and high-southern latitude study (Lawrence et al., 2009) was made. The Erebus Volcanic Province (EVP) sites in the Antarctic span 0.03-13 Ma in age, with 15 sites from 0.03-0.86 Ma rocks, 23 sites from 1.07-2.28 Ma rocks and 9 sites from 2.46-7.25 Ma old rocks. Note that the data during ca. 0.03-0.86 Ma from EVP sites are excluded from the discussions as Iceland data during ~1-8.5 Ma were used here for comparison. Overall, the mean VADM of this study (37.4 ± 2.5 ZAm^2, Table 7.6) for ca. 2.50-8.05 Ma (Figure 7.22b, yellow circle) seems to agree with the mean VADM from high-southern latitude (37.3 ± 3.8 ZAm^2) for ca. 1.07-7.25 Ma (Figure 7.22b, blue star) and supports that the hemispheric asymmetry of the field is invalid. However, the variations of the time interval should be taken into account, because the majority of sites at the Antarctic provide the ages around ca. 1.07-2.28 Ma as stated above. The VADM from the Antarctic sites during ca. 2.46-7.25 Ma (32.2 ± 8.2 ZAm^2) (Figure 7.22b, red diamond) is slightly lower than the VADM of this study (37.4 ± 2.5 ZAm^2). To improve temporal coverage of high-northern latitude data, six data from Jökuldalur, seven data from Cromwell et al. (2015), and 11 data from Storutjarnir were included to this study data. The inclusion of literature data to this study yields a total of 70 data points covering time span ~1.10-8.05 Ma. The mean VADM derived from 70 data points is ~44.0 ± 2.2 ZAm^2. This evidence clearly shows that there is a significant difference between the VADM observed at high-northern and southern latitudes.

The results from high-northern and high-southern latitudes suggest that there is the hemispheric asymmetry between the Antarctic and Iceland palaeointensity for the time span ~1.0-8.5 Ma. However, this assumption should be further tested because of the paucity of southern Hemisphere data. Only nine available sites from the Antarctic were used for comparison during ~2.5-8.5 Ma, compared to this study which provides 46 robust palaeointensity estimates. The low VADM of this study is not a function of poor quality of data as the strict selection criteria were applied to omit the outliers. Moreover, alteration of the sample and multidomain were monitored throughout the entire palaeointensity experiment. The low VADM from both hemispheres reflects a low axial dipole moment over geological time as stated in literature (e.g., Juárez et al., 1998; Selkin and Tauxe, 2000; Tauxe et al., 2013). Including low- to mid-latitude intensity data, the global dataset reflects the high contribution of the non-dipole term ($g_2^0 \approx 20\%$) required to fit the dataset as suggested by Cromwell et al. (2013b). However, this study proposes the $g_2^0 \approx 5\%$ and $g_3^0 \approx 20\%$ of the opposite sign to g_1^0 as discussed above. The persistence of the non-dipole fields results in the hemispheric asymmetry of the field, when observed the field at different hemispheres. Overall, this study improves palaeointensity data at high-northern latitudes with a total of 46 data points covering time span 2.5-8.5 Ma. However, further investigation of the palaeointensity in Iceland should also be considered for the missing time intervals including 3.24-4.60 Ma and 5.65-7.05 Ma in order to improve temporal coverage for the time span 0-8.5 Ma.

7.8 Concluding remarks

- A new, robust, mean palaeointensity of 26.9 ± 1.8 μT supports the idea of a permanent non-dipole component contributing to the geomagnetic field (Cromwell et al., 2013b), while the modified TK03 model shows the persistence of the axial quadrupole of -5% and the axial octupole of -20% in the global palaeointensity dataset.
- The VDM of this study supports the long-term low field strength over geological time.
- The comparison of the VADM observed between high-northern and high-southern latitudes supports the assumption of the long-term asymmetry of the field between Northern and Southern Hemispheres.
- The palaeointensity data at high latitudes are scarce and more globally distributed palaeointensity estimates at high latitudes are needed to capture the Earth's magnetic field through time. These values (46 data covering time span 2.5-8.5 Ma) will add crucial observations to limited high-latitude data.
- Further investigation of the field is still required, in particular the acquisition of additional high-southern and northern latitude data in order to better constrain the global palaeomagnetic field.

Chapter 8

Conclusions

8.1 Magnetostratigraphy

The investigation of palaeomagnetic directional data from Northern Iceland revealed that the Icelandic basalt is a reliable magnetic carrier for testing the GAD hypothesis, with primarily single component remanent magnetisations with only small viscous remanent magnetisations found in most samples. All the data were magnetically cleaned in the laboratory at Imperial College and no overprint was left in the data (McElhinny and McFadden, 1997). Using new 15 ^{40}Ar/^{39}Ar ages construct an age models with the use of GTS2012 (Ogg, 2012), I found that the ages of the lava pile in Eyjafjardardalur valley cover the time span ~2.6-8.5 Ma, with two major hiatuses covering time span ~6.05-7.15 Ma and ~3.60-4.5 Ma. The correlation of lava sections between this study and a previous study (Kristjansson et al., 2004) reveals that there are missing lava flows in the previous study and this study improves stratigraphic correlations in Eyjafjardardalur valley. This study also added a 1.6 km successive lava flows to Northern Iceland lava pile. With the results from previous Northern Iceland studies (Saemundsson et al., 1980; Kristjansson et al., 2004), a total of ~9.6 km lava succession now exists for Northern Iceland covering a time span from ~2.6 Ma at the basement of the Icelandic Highland Plateau to 12 Ma at the northern coast of the Tröllaskagi peninsular.

According to previous research in northern Iceland, not much details of geology of Eyjafjardardalur valley and Torfufell Central Volcano have been revealed (Hjartarson, 2003). This study is the first study that reveals the geology of the upper Eyjafjardardalur valley, near the basement of Iceland highland plateau. As the direct application of the palaeomagnetic data is to date the unknown age strata, combining palaeomagnetic data and $^{40}Ar/^{39}Ar$ ages of this study would be beneficial for future research that attempts to study Mt Torfufell or chronological evolution of central volcano in northern Iceland. The data of this study can also be used to date the spectacular phenomena in the study area such as volcanic conduits and fossil forests (Árnadóttir et al., 2018).

8.2 Palaeomagnetic direction

Overall, this study added more than 150 high-quality unique directional data at high-latitudes to the global dataset. These data meet the modern selection criteria of the TAF study (Johnson et al., 2008). The mean directions show shallow inclination of 71.4°, which is ~5.6° lower than the expected GAD inclination for Northern Iceland. The VGP of this study is located at ~80°N, which deviates from the geographic north by ~10°. The local magnetic anomalies in Eyjafjardardalur valley were avoided as more than 80% of the declinations were obtained via Sun readings. The shallow inclination and deviation of the VGP are likely a result of non-dipole fields which contribute to the GAD field in Northern Iceland. These non-dipole contributions were extensively analysed by examining a new compilation of the global dataset during the time span 0-8.5 Ma. The data from this study were also combined with this global dataset. The results of the compilation show that the time-averaged field during 0-8.5 Ma does not average to the GAD. It was found that around 4% of axial quadrupole and 1% of axial octupole terms are needed to explain the deviation from a GAD field during this time interval.

Even though this study proposes that the shallow inclinations observed in Iceland are an effect of the non-dipole field contributions to the GAD field. Several possibilities causing shallow inclination as discussed in Chapter 5 should not be avoided. (Though, several possibilities have been ruled out in Chapter 5). The effect of shape anisotropy and tectonic complications could be the major cause of shallow inclination in this study. Typically, Icelandic basalt has the magnetisation stronger than 200 mA/m. Coe (1979) modelled the effect of shape anisotropy in subaerial basalt with the magnetisation of 1 A/m. They found that the shape anisotropy can shallow the inclination with the maximum angle of 1.4°. Therefore, the effect of shape anisotropy could yield the GAD inclination of ~75° for Iceland. Furthermore, the study areas are located between the Kolbeinsey Ridge and North Volcanic Zone. There was the ridge jump process transferring from the Skagafjördur palaeo-rift in northern Iceland to the

North Volcanic Zone (NVZ) (Garcia et al., 2003). The NVZ began to form during ~8-8.5 Ma while the Skagafjördur palaeo-rift ceased during ~ 3 Ma (Garcia et al., 2003). The excess loading of basalt toward the palaeo-rift and the NVZ would cause the tectonic complication in the study areas. However, this problem cannot be resolved in this single study.

The direct application of the GAD hypothesis is to perform the plate tectonic reconstructions. The data of this study meet the standard requirement in palaeomagnetic community, e.g., the selection criteria for constructing the APW path require the data to have 1) at lease 6 sites and 36 samples per study, 2) a $\alpha_{95} < 10°$ in the Cenozoic and 15° in the Mesozoic, 3) evidence for successful AF/thermal demagnetisation (DMAG ≥ 2), 4) dating uncertainties < 15 Myr and 5) no re-magnetisation (e.g., Besse and Courtillot, 1991). However, the community requires only data from rigid plates and rejects the data from mobile zones (e.g., Besse and Courtillot, 2002) to construct the APW paths, i.e., Iceland data are omitted out (e.g., Torsvik et al., 2012) as Iceland is located on the active rift zone. However, the data of this study would benefit for regional reconstructions in Iceland.

The geodynamo community often explore geographic variations in the CMB heat flow that effect the time-averaged magnetic field. The geodynamo models show that lateral variations in the CMB heat flow influences the axial quadrupole and axial octupole to the long-term time averaged field (e.g., Olson and Christensen, 2002). Geodynamo simulations of ~150,000 years or greater are often used to test against the GAD field, by comparing the dynamo results with the field behavior obtained from the palaeomagnetic field models, e.g., 5-Ma model (e.g., Johnson and Constable, 1995). Adding ~150 high-quality data from Iceland would improve the resolutions of palaeomagnetic field model especially at high-latitudes. The better resolution of the field models would allow for a greater understanding of the CMB heat flows and core-mantle processes.

8.3 Palaeointensity

Even though careful sample selection methods were used to choose promising samples for palaeointensity experiment, only 45% of the samples yielded successful palaeointensity experiments. This per cent of successful results was improved from previous study from the Imperial group (~21%) in Eastern Iceland (Døssing et al., 2016), as I performed palaeointensity in controlled helium atmosphere in order to prevent alteration during step-wise heating while the previous study ran the experiment in l air. A mean intensity of 26.9 ± 1.8 μT was determined from 46 lava flows is lower than the expected GAD intensity at 65°N based on current-day field strengths. Combing my new data with the global palaeointensity data set found that that ~5% of axial quadrupole and ~20% of axial octupole are required to explain the palaeointensity record. The non-axial dipoles are of the opposite sign of the axial dipole. These per cents of non-dipoles are higher than palaeointensity model compiled by Kono et al. (2000) as this study included more high-latitude intensity data (e.g., this study (Chapter 7); Lawrence et al., 2009; Cromwell et al., 2013b; Døssing et al., 2016; Tanaka and Yamamoto, 2016), which did not exist in 2000. The high proportion of the non-dipole fields is because the observed palaeointensity at high-latitudes is sensitive to the radial field at the CMB. Any small changes of the radial field would much effect palaeointensity at high-latitudes (Johnson and Constable, 1997). Compared to the palaeodirection model, there is smaller proportion of the non-dipole fields which contributes to the PSV dataset. As discussed in Chapter 7, palaeodirection is not sensitive to the radial field at the CMB at high-latitudes. Compiling >2,000 directional data from high-latitudes would minimise the spatial bias of the field. However, only ~180 intensity data from high-latitudes were used in the palaeointensity model compilations. This could explain why the non-dipole fields are very strong in the palaeointensity dataset. The palaeointensity model compilations suggest that the palaeomagnetic community still requires more high-latitude intensity data to remove the spatial bias of the high-latitude field. The increasing number of the palaeointensity data in the future would allow the directional and intensity models to converge.

The combined palaeointensity data of this study and the other studies in Iceland (Cromwell et al., 2015; Døssing et al., 2016; Tanaka and Yamamoto, 2016) yields the VADM of 44.0 ± 2.2 ZAm^2 during time span 1.0-8.5 Ma, which is not in agreement with high-southern latitude VADM of 37.3 ± 3.8 ZAm^2 during time span 1.0-7.5 Ma (Lawrence et al., 2009). The results of this study suggested that the assumption of the long-term hemispheric asymmetry of the field between Northern and Southern Hemispheres is valid. However, due to the paucity of both high-northern and high-southern latitude data, we still require more high-latitude data to truly verify this assumption.

8.4 Future research

As there are two major hiatuses recorded in Eyjafjardardalur valley during ~6.05-7.15 Ma and ~3.60-4.5 Ma, future research should therefore concentrate on collecting more samples from sections covering these missing time intervals in order to improve temporal resolution of the palaeodirection and palaeointensity for the past 8.5 Myr for Iceland. Additionally, given importance to high-latitude data, more palaeomagnetic samples should be collected more from both high-northern and high-southern latitude regions especially areas above 65°N and 65°S in order to improve spatial bias of the palaeointensity at high-latitudes (Johnson and McFadden, 2007). More high-latitude data would also strongly confirm the hemispheric asymmetry assumption if it persists.

Bibliography

Abrajevitch, A., and Van der Voo, R., Incompatible Ediacaran paleomagnetic directions suggest an equatorial geomagnetic dipole hypothesis. *Earth Planet. Sci. Lett.*, 293: 164-170, 2010. doi: 10.1016/j.epsl.2010.02.038

Aitken, M.J., Allsop, A.L., Bussell, G.D., and Winter, M.B., Determination of the intensity of the Earth's magnetic field during archaeological times: Reliability of the Thellier Technique. *Rev. Geophys.*, 26: 3-12, 1988. doi: 10.1029/RG026i001p00003

Alva-Valdivia, L.M., Comprehensive paleomagnetic study of a succession of Holocene olivine-basalt flow: Xitle Volcano (Mexico) revisited. *Earth Planet Sp*, 57: 839-853, 2005. doi: 10.1186/bf03351862

Alva-Valdivia, L.M., Goguitchaichvili, A., and Urrutia-Fucugauchi, J., Further constraints for the Plio-Pleistocene geomagnetic field strength: New results from the Los Tuxtlas volcanic field (Mexico). *Earth Planet Sp*, 53: 873-881, 2001. doi: 10.1186/bf03351684

Argus, D.F., Gordon, R.G., and DeMets, C., Geologically current motion of 56 plates relative to the no-net-rotation reference frame. *Geochem. Geophys. Geosyst.*, 12: Q11001, 2011. doi: 10.1029/2011GC003751

Árnadóttir, S., Hjartarson, Á., Gautason, B., and Thordarson, T., The Neogene Torfufell Central Volcano: A gem in Northern Iceland, EGU General Assembly, 2018.

Aronson, J.L., and Saemundsson, K., Relatively old basalts from structurally high areas in central Iceland. *Earth Planet. Sci. Lett.*, 28: 83-97, 1975. doi: 10.1016/0012-821X(75)90077-1

Aubert, J., Tarduno, J., and Johnson, C., Observations and Models of the Long-Term Evolution of Earth's Magnetic Field. *Space Sci Rev*, 155: 337-370, 2010. doi: 10.1007/s11214-010-9684-5

Baag, C., and Helsley, C.E., Geomagnetic secular variation Model E. *J. Geophys. Res.*, 79: 4918-4922, 1974. doi: 10.1029/JB079i032p04918

Baag, C., Helsley, C.E., Xu, S.-z., and Lienert, B.R., Deflection of paleomagnetic directions due to magnetization of the underlying terrain. *J. Geophys. Res.: Solid Earth*, 100: 10013-10027, 1995. doi: 10.1029/95JB00148

Baraldo, A., Rapalini, A.E., Böhnel, H., and Mena, M., Paleomagnetic study of Deception Island, South Shetland Islands, Antarctica. *Geophys. J. Int.*, 153: 333-343, 2003. doi: 10.1046/j.1365-246X.2003.01881.x

Besse, J., and Courtillot, V., Revised and synthetic apparent polar wander paths of the African, Eurasian, North American and Indian Plates, and true polar wander since 200 Ma. *J. Geophys. Res.: Solid Earth*, 96: 4029-4050, 1991. doi: 10.1029/90JB01916

Besse, J., and Courtillot, V., Apparent and true polar wander and the geometry of the geomagnetic field over the last 200 Myr. *J. Geophys. Res.: Solid Earth*, 107: EPM 6-1-EPM 6-31, 2002. doi: 10.1029/2000JB000050

Biggin, A., Strik, G.M.A., and Langereis, C., The intensity of the geomagnetic field in the late-Archaean: new measurements and an analysis of the updated IAGA palaeointensity database. *Earth Planet Sp*, 61: 9-22, 2009. doi: 10.1186/BF03352881

Biggin, A.J., and Paterson, G.A., A new set of qualitative reliability criteria to aid inferences on palaeomagnetic dipole moment variations through geological time. *Frontiers in Earth Science*, 2, 2014. doi: 10.3389/feart.2014.00024

Biggin, A.J., and Thomas, D.N., The application of acceptance criteria to results of Thellier palaeointensity experiments performed on samples with pseudo-single-domain-like characteristics. *Phys. Earth Planet. In.*, 138: 279-287, 2003. doi: 10.1016/S0031-9201(03)00127-4

Blakely, R.J., Potential theory in gravity and magnetic applications / Richard J. Blakely. Cambridge : Cambridge University Press, 1995., Cambridge, 1995.

Blakemore, R.P., Frankel, R.B., and Kalmijn, A.J., South-seeking magnetotactic bacteria in the Southern Hemisphere. *Nature*, 286: 384, 1980. doi: 10.1038/286384a0

Bloxham, J., Sensitivity of the geomagnetic axial dipole to thermal core-mantle interactions. *Nature*, 405: 63-65, 2000. doi:

Boven, A., Pasteels, P., Kelley, S.P., Punzalan, L., Bingen, B., and Demaiffe, D., 40Ar/39Ar study of plagioclases from the Rogaland anorthosite complex (SW Norway); an attempt to understand argon ages in plutonic plagioclase. *Chemical Geology*, 176: 105-135, 2001. doi: 10.1016/S0009-2541(00)00372-7

Bowles, J.A., Tatsumi-Petrochilos, L., Hammer, J.E., and Brachfeld, S.A., Multicomponent cubic oxide exsolution in synthetic basalts: Temperature dependence and implications for magnetic properties. *J. Geophys. Res.: Solid Earth*, 117: B03202, 2012. doi: 10.1029/2011JB008867

Braginsky, S.I., Structure of the F layer and reasons for convection in the Earth's core. *Dokl. Akad. Nauk SSSR*, 149: 8-10, 1963. doi:

Brassart, J., Tric, E., Valet, J.-P., and Herrero-Bervera, E., Absolute paleointensity between 60 and 400 ka from the Kohala Mountain (Hawaii). *Earth Planet. Sci. Lett.*, 148: 141-156, 1997. doi: 10.1016/S0012-821X(97)00024-1

Brooks, C., Hart, S.R.H., and Wendt, I., Realistic use of two-error regression treatments as applied to rubidium-strontium data. *Rev. Geophys.*, 10: 551-577, 1972. doi: 10.1029/RG010i002p00551

Brown, L.L., Singer, B.S., and Gorring, M.L., Paleomagnetism and 40Ar/39Ar Chronology of Lavas from Meseta del Lago Buenos Aires, Patagonia. *Geochem. Geophys. Geosyst.*, 5: Q01H04, 2004. doi: 10.1029/2003GC000526

Brown, M.C., Singer, B.S., Knudsen, M.F., Jicha, B.R., Finnes, E., and Feinberg, J.M., No evidence for Brunhes age excursions, Santo Antão, Cape Verde. *Earth Planet. Sci. Lett.*, 287: 100-115, 2009. doi: 10.1016/j.epsl.2009.07.039

Buffett, B.A., 8.08 - Core–Mantle Interactions, in: Schubert, G. (Ed.), Treatise on Geophysics (Second Edition). Elsevier, Oxford, pp. 213-224, 2015.

Butler, R.F., Paleomagnetism : magnetic domains to geologic terranes. Blackwell Scientific, Oxford, 1992.

Cai, S., Chen, W., Tauxe, L., Deng, C., Qin, H., Pan, Y., Yi, L., and Zhu, R., New constraints on the variation of the geomagnetic field during the late Neolithic period: Archaeointensity results from Sichuan, southwestern China. *J. Geophys. Res.: Solid Earth*, 120: 2056-2069, 2015. doi: 10.1002/2014JB011618

Cai, S., Jin, G., Tauxe, L., Deng, C., Qin, H., Pan, Y., and Zhu, R., Archaeointensity results spanning the past 6 kiloyears from eastern China and implications for extreme behaviors of the geomagnetic field. *Proceedings of the National Academy of Sciences*, 114: 39-44, 2017. doi: 10.1073/pnas.1616976114

Cai, S., Tauxe, L., Deng, C., Pan, Y., Jin, G., Zheng, J., Xie, F., Qin, H., and Zhu, R., Geomagnetic intensity variations for the past 8 kyr: New archaeointensity results from Eastern China. *Earth Planet. Sci. Lett.*, 392: 217-229, 2014. doi: 10.1016/j.epsl.2014.02.030

Calvo-Rathert, M., Bógalo, M.F., Gogichaishvili, A., Sologashvili, J., and Vashakidze, G., New paleomagnetic and paleointensity data from Pliocene lava flows from the Lesser Caucasus. *J. Asian Earth Sci.*, 73: 347-361, 2013a. doi: 10.1016/j.jseaes.2013.04.039

Calvo-Rathert, M., Goguitchaichvili, A., Bógalo, M.-F., Vegas-Tubía, N., Carrancho, Á., and Sologashvili, J., A paleomagnetic and paleointensity study on Pleistocene and Pliocene basaltic flows from the Djavakheti Highland (Southern Georgia, Caucasus). *Phys. Earth Planet. In.*, 187: 212-224, 2011. doi: 10.1016/j.pepi.2011.03.008

Calvo-Rathert, M., Goguitchaichvili, A., and Vegas-Tubía, N., A paleointensity study on middle Miocene to Pliocene volcanic rocks from south-eastern Spain. *Earth Planet Sp*, 61: 61-69, 2009. doi: 10.1186/bf03352885

Calvo-Rathert, M., Reyes, B.A., Goguitchaichvili, A., Elguera, J.R., Franco, H., Morales, J., Soto, R., Carrancho, Á., and Delgado, H., Rock-magnetic and paleomagnetic results from the Tepic-Zacoalco rift region (western Mexico). *Stud Geophys Geod*, 57: 309-331, 2013b. doi: 10.1007/s11200-012-0239-y

Camps, P., Henry, B., Prévot, M., and Faynot, L., Geomagnetic paleosecular variation recorded in Plio-Pleistocene volcanic rocks from Possession Island (Crozet Archipelago, southern Indian Ocean). *J. Geophys. Res.: Solid Earth*, 106: 1961-1971, 2001. doi: 10.1029/2000JB900370

Camps, P., Singer, B.S., Carvallo, C., Goguitchaichvili, A., Fanjat, G., and Allen, B., The Kamikatsura event and the Matuyama–Brunhes reversal recorded in lavas from Tjörnes Peninsula, northern Iceland. *Earth Planet. Sci. Lett.*, 310: 33-44, 2011. doi: 10.1016/j.epsl.2011.07.026

Carlut, J., and Courtillot, V., How complex is the time-averaged geomagnetic field over the past 5 Myr? *Geophys. J. Int.*, 134: 527-544, 1998. doi: 10.1046/j.1365-246x.1998.00577.x

Carlut, J., and Quidelleur, X., Absolute paleointensities recorded during the Brunhes chron at La Guadeloupe Island. *Phys. Earth Planet. In.*, 120: 255-269, 2000. doi: 10.1016/S0031-9201(99)00170-3

Carlut, J., Quidelleur, X., Courtillot, V., and Boudon, G., Paleomagnetic directions and K/Ar dating of 0 to 1 Ma lava flows from La Guadeloupe Island (French West Indies): Implications for time-averaged field models. *J. Geophys. Res.: Solid Earth*, 105: 835-849, 2000. doi: 10.1029/1999JB900238

Carlut, J., Valet, J.-P., Quidelleur, X., Courtillot, V., Kidane, T., Gallet, Y., and Gillot, P.-Y., Paleointensity across the Réunion event in Ethiopia. *Earth Planet. Sci. Lett.*, 170: 17-34, 1999. doi: 10.1016/S0012-821X(99)00094-1

Carvallo, C., Özdemir, Ö., and Dunlop, D.J., Palaeointensity determinations, palaeodirections and magnetic properties of basalts from the Emperor seamounts. *Geophys. J. Int.*, 156: 29-38, 2004. doi: 10.1111/j.1365-246X.2004.02110.x

Carvallo, C., Roberts, A.P., Leonhardt, R., Laj, C., Kissel, C., Perrin, M., and Camps, P., Increasing the efficiency of paleointensity analyses by selection of samples using first-order reversal curve diagrams. *J. Geophys. Res.: Solid Earth*, 111: B12103, 2006. doi: 10.1029/2005JB004126

Castro, J., and Brown, L., Shallow paleomagnetic directions from historic lava flows, Hawaii. *Geophys. Res. Lett.*, 14: 1203-1206, 1987. doi: 10.1029/GL014i012p01203

Ceja, M.R., Goguitchaichvili, A., Calvo-Rathert, M., Morales-Contreras, J., Alva-Valdivia, L., Elguera, J.R., Fucugauchi, J.U., and Granados, H.D., Paleomagnetism of the Pleistocene Tequila Volcanic Field (Western Mexico). *Earth Planet Sp*, 58: 1349-1358, 2006. doi: 10.1186/bf03352631

Chauvin, A., Gillot, P.-Y., and Bonhommet, N., Paleointensity of the Earth's magnetic field recorded by two Late Quaternary volcanic sequences at the Island of La Réunion (Indian Ocean). *J. Geophys. Res.: Solid Earth*, 96: 1981-2006, 1991. doi: 10.1029/90JB02223

Chenet, A.-L., Fluteau, F., Courtillot, V., Gérard, M., and Subbarao, K.V., Determination of rapid Deccan eruptions across the Cretaceous-Tertiary boundary using paleomagnetic secular variation: Results from a 1200-m-thick section in the Mahabaleshwar escarpment. *J. Geophys. Res.: Solid Earth*, 113, 2008. doi: 10.1029/2006JB004635

Coe, R.S., Paleo-intensities of the Earth's magnetic field determined from Tertiary and Quaternary rocks. *J. Geophys. Res.*, 72: 3247-3262, 1967. doi: 10.1029/JZ072i012p03247

Coe, R.S., The effect of shape anisotropy on TRM direction. *Geophysical Journal of the Royal Astronomical Society*, 56: 369-383, 1979. doi: 10.1111/j.1365-246X.1979.tb00170.x

Coe, R.S., Grommé, S., and Mankinen, E.A., Geomagnetic paleointensities from radiocarbon-dated lava flows on Hawaii and the question of the Pacific nondipole low. *J. Geophys. Res.: Solid Earth*, 83: 1740-1756, 1978. doi: 10.1029/JB083iB04p01740

Coe, R.S., Zhao, X.X., Lyons, J.J., Pluhar, C.J., and Mankinen, E.A., Revisiting the 1964 collection of Nunivak lava flows, Eos Trans. AGU, pp. Abstract GP62A-06, 2000.

Conrad, C.P., and Hager, B.H., Effects of plate bending and fault strength at subduction zones on plate dynamics. *J. Geophys. Res.: Solid Earth*, 104: 17551-17571, 1999. doi: 10.1029/1999JB900149

Constable, C., 5.09 - Centennial- to Millennial-Scale Geomagnetic Field Variations, in: Schubert, G. (Ed.), Treatise on Geophysics. Elsevier, Amsterdam, pp. 337-372, 2007.

Constable, C., Korte, M., and Panovska, S., Persistent high paleosecular variation activity in southern hemisphere for at least 10 000 years. *Earth Planet. Sci. Lett.*, 453: 78-86, 2016. doi: 10.1016/j.epsl.2016.08.015

Constable, C.G., and Johnson, C.L., Anisotropic paleosecular variation models: implications for geomagnetic field observables. *Phys. Earth Planet. In.*, 115: 35-51, 1999. doi: 10.1016/S0031-9201(99)00065-5

Constable, C.G., Johnson, C.L., and Lund, S.P., Global geomagnetic field models for the past 3000 years: transient or permanent flux lobes? , 358: 991-1008, 2000. doi: 10.1098/rsta.2000.0570

Constable, C.G., and Parker, R.L., Statistics of the geomagnetic secular variation for the past 5 m.y. *J. Geophys. Res.: Solid Earth*, 93: 11569-11581, 1988. doi: 10.1029/JB093iB10p11569

Conte-Fasano, G., Urrutia-Fucugauchi, J., Goguitchaichvili, A., and Morales-Contreras, J., Low-latitude paleosecular variation and the time-averaged field during the late Pliocene and Quaternary—Paleomagnetic study of the Michoacan-Guanajuato volcanic field, Central Mexico. *Earth Planet Sp*, 58: 1359-1371, 2006. doi: 10.1186/bf03352632

Cox, A., Analysis of Present Geomagnetic Field for Comparison with Paleomagnetic Results. *Journal of geomagnetism and geoelectricity*, 13: 101-112, 1962. doi: 10.5636/jgg.13.101

Cox, A., Confidence Limits for the Precision Parameter k. *Geophysical Journal of the Royal Astronomical Society*, 17: 545-549, 1969. doi: 10.1111/j.1365-246X.1969.tb00257.x

Cox, A., Latitude Dependence of the Angular Dispersion of the Geomagnetic Field*. *Geophysical Journal of the Royal Astronomical Society*, 20: 253-269, 1970. doi: 10.1111/j.1365-246X.1970.tb06069.x

Creer, K.M., The dispersion of the geomagnetic field due to secular variation and its determination for remote times from paleomagnetic data. *J. Geophys. Res.*, 67: 3461-3476, 1962. doi: 10.1029/JZ067i009p03461

Creer, K.M., Computer synthesis of geomagnetic palaeosecular variations. *Nature*, 304: 695, 1983. doi: 10.1038/304695a0

Creer, K.M., Irving, E., and Nairn, A.E.M., Palaeomagnetism of the Great Whin Sill. *Geophys. J. Int.*, 2: 306-323, 1959. doi: 10.1111/j.1365-246X.1959.tb05802.x

Creer, K.M., Irving, E., and Runcorn, S.K., The Direction of the Geomagnetic Field in Remote Epochs in Great Britain. *Journal of geomagnetism and geoelectricity*, 6: 163-168, 1954. doi: 10.5636/jgg.6.163

Cromwell, G., Constable, C.G., Staudigel, H., Tauxe, L., and Gans, P., Revised and updated paleomagnetic results from Costa Rica. *Geochem. Geophys. Geosyst.*, 14: 3379-3388, 2013a. doi: 10.1002/ggge.20199

Cromwell, G., Johnson, C.L., Tauxe, L., Constable, C.G., and Jarboe, N.A., PSV10: A Global Data Set for 0–10 Ma Time-Averaged Field and Paleosecular Variation Studies. *Geochem. Geophys. Geosyst.*, 0: 1-26, 2018. doi: 10.1002/2017GC007318

Cromwell, G., Tauxe, L., and Halldórsson, S.A., New paleointensity results from rapidly cooled Icelandic lavas: Implications for Arctic geomagnetic field strength. *J. Geophys. Res.: Solid Earth*, 120: 2913-2934, 2015. doi: 10.1002/2014JB011828

Cromwell, G., Tauxe, L., Staudigel, H., Constable, C.G., Koppers, A.A.P., and Pedersen, R.B., In search of long-term hemispheric asymmetry in the geomagnetic field: Results from high northern latitudes. *Geochem. Geophys. Geosyst.*, 14: 3234-3249, 2013b. doi: 10.1002/ggge.20174

Dalrymple, B.G., Lanphere, M.A., and Pringle, M.S., Correlation diagrams in 40Ar/39Ar dating: Is there a correct choice? *Geophys. Res. Lett.*, 15: 589-591, 1988. doi: 10.1029/GL015i006p00589

Day, R., Fuller, M., and Schmidt, V.A., Hysteresis properties of titanomagnetites: Grain-size and compositional dependence. *Phys. Earth Planet. In.*, 13: 260-267, 1977. doi: 10.1016/0031-9201(77)90108-X

DeMets, C., Gordon, R.G., Argus, D.F., and Stein, S., Effect of recent revisions to the geomagnetic reversal time scale on estimates of current plate motions. *Geophys. Res. Lett.*, 21: 2191-2194, 1994. doi: 10.1029/94GL02118

Di Chiara, A., Tauxe, L., and Speranza, F., Paleointensity determination from São Miguel (Azores Archipelago) over the last 3 ka. *Phys. Earth Planet. In.*, 234: 1-13, 2014. doi: 10.1016/j.pepi.2014.06.008

Dickin, A.P., Radiogenic Isotope Geology, 3 ed. Cambridge University Press, Cambridge, 2018.

Dodd, S.C., Mac Niocaill, C., and Muxworthy, A.R., Long duration (>4 Ma) and steady-state volcanic activity in the early Cretaceous Paraná–Etendeka Large Igneous Province: New palaeomagnetic data from Namibia. *Earth Planet. Sci. Lett.*, 414: 16-29, 2015. doi: 10.1016/j.epsl.2015.01.009

Domeier, M., Van der Voo, R., Tomezzoli, R.N., Tohver, E., Hendriks, B.W.H., Torsvik, T.H., Vizan, H., and Dominguez, A., Support for an "A-type" Pangea reconstruction from high-fidelity Late Permian and Early to Middle Triassic paleomagnetic data from Argentina. *J. Geophys. Res.: Solid Earth*, 116, 2011. doi: 10.1029/2011JB008495

Døssing, A., Muxworthy, A.R., Supakulopas, R., Riishuus, M.S., and Mac Niocaill, C., High northern geomagnetic field behavior and new constraints on the Gilsá event: Paleomagnetic and 40Ar/39Ar results of ~0.5–3.1 Ma basalts from Jökuldalur, Iceland. *Earth Planet. Sci. Lett.*, 456: 98-111, 2016. doi: 10.1016/j.epsl.2016.09.022

Driscoll, P., and Olson, P., Superchron cycles driven by variable core heat flow. *Geophys. Res. Lett.*, 38, 2011. doi: 10.1029/2011GL046808

Dunlop, D.J., and Özdemir, Ö., 5.08 - Magnetizations in Rocks and Minerals, in: Schubert, G. (Ed.), Treatise on Geophysics. Elsevier, Amsterdam, pp. 277-336, 2007.

Dunlop, D.J., and Özdemir, Ö., Rock Magnetism: Fundamentals and Frontiers, Cambridge Studies in Magnetism. Cambridge University Press, New York, 1997.

Eiríksson, J., Gudmundsson, A.I., KristjÁNsson, L., and Gunnarsson, K., Palaeomagnetism of Pliocene-Pleistocene sediments and lava flows on Tjörnes and Flatey, North Iceland. *Boreas*, 19: 39-55, 1990. doi: 10.1111/j.1502-3885.1990.tb00420.x

Elmaleh, A., Valet, J.P., Quidelleur, X., Solihin, A., Bouquerel, H., Tesson, T., Mulyadi, E., Khokhlov, A., and Wirakusumah, A.D., Palaeosecular variation in Java and Bawean Islands (Indonesia) during the Brunhes chron. *Geophys. J. Int.*, 157: 441-454, 2004. doi: 10.1111/j.1365-246X.2004.02197.x

Elming, S.A., Kravchenko, S.N., Layer, P., Rusakov, O.M., Glevasskaya, A.M., Mikhailova, N.P., and Bachtadse, V., Palaeomagnetism and 40Ar/39Ar age determinations of the Ediacaran traps from the southwestern margin of the East European Craton, Ukraine: relevance to the Rodinia break-up. *Journal of the Geological Society*, 164: 969-982, 2007. doi: 10.1144/0016-76492005-163

Esser, R.P., McIntosh, W.C., Heizler, M.T., and Kyle, P.R., Excess argon in melt inclusions in zero-age anorthoclase feldspar from Mt. Erebus, Antarctica, as revealed by the 40Ar39Ar method. *Geochimica et Cosmochimica Acta*, 61: 3789-3801, 1997. doi: 10.1016/S0016-7037(97)00287-1

Fabian, K., and Hubert, A., Shape-induced pseudo-single-domain remanence. *Geophys. J. Int.*, 138: 717-726, 1999. doi: 10.1046/j.1365-246x.1999.00916.x

Fisher, R., Dispersion on a Sphere. *" Proc. R. Soc. London, Ser. A"*, 217: 295-305, 1953. doi: 10.1098/rspa.1953.0064

Fleck, R.J., Sutter, J.F., and Elliot, D.H., Interpretation of discordant 40Ar/39Ar age-spectra of mesozoic tholeiites from antarctica. *Geochimica et Cosmochimica Acta*, 41: 15-32, 1977. doi:

Foster, J., and Symons, D.T.A., Defining a paleomagnetic polarity pattern in the Monteregian intrusives. *Canadian Journal of Earth Sciences*, 16: 1716-1725, 1979. doi: 10.1139/e79-159

Garcia, S., Arnaud, N.O., Angelier, J., Bergerat, F., and Homberg, C., Rift jump process in Northern Iceland since 10 Ma from 40Ar/39Ar geochronology. *Earth Planet. Sci. Lett.*, 214: 529-544, 2003. doi: 10.1016/S0012-821X(03)00400-X

Gilbert, W., On the magnet (De Magnete). Peter Short, London, 1600.

Globerman, B.R., and Irving, E., Mid-Cretaceous paleomagnetic reference field for North America: Restudy of 100 Ma intrusive rocks from Arkansas. *J. Geophys. Res.: Solid Earth*, 93: 11721-11733, 1988. doi: 10.1029/JB093iB10p11721

Goguitchaichvili, A., Calvo, M., Sologashvili, D., Alva, L., and Urrutia, J., Palaeomagnetism of Georgian Plio-Quaternary volcanic provinces (Southern Caucasus): a pilot study. *Comptes Rendus de l'Académie des Sciences - Series IIA - Earth and Planetary Science*, 331: 683-690, 2000. doi: 10.1016/S1251-8050(00)01471-3

Goguitchaichvili, A., Petronille, M., Henry, B., Valdivia, L.A., Morales, J., and Urrutia-Fucugauchi, J., Paleomagnetism of the Eastern Alkaline Province (Mexico): contribution to the time-averaged field global database and geomagnetic instability time scale. *Earth Planet Sp*, 59: 775-783, 2007. doi: 10.1186/bf03352740

Gonzalez, S., Sherwood, G., Böhnel, H., and Schnepp, E., Palaeosecular variation in Central Mexico over the last 30000 years: the record from lavas. *Geophys. J. Int.*, 130: 201-219, 1997. doi: 10.1111/j.1365-246X.1997.tb00999.x

Gubbins, D., and Kelly, P., Persistent patterns in the geomagnetic field over the past 2.5 Myr. *Nature*, 365: 829, 1993. doi: 10.1038/365829a0

Gubbins, D., Thomson, C.J., and Whaler, K.A., Stable regions in the Earth's liquid core. *Geophysical Journal of the Royal Astronomical Society*, 68: 241-251, 1982. doi: 10.1111/j.1365-246X.1982.tb06972.x

Gubbins, D., Willis, A.P., and Sreenivasan, B., Correlation of Earth's magnetic field with lower mantle thermal and seismic structure. *Phys. Earth Planet. In.*, 162: 256-260, 2007. doi: 10.1016/j.pepi.2007.04.014

Hagstrum, J.T., Fleck, R.J., Evarts, R.C., and Calvert, A.T., Paleomagnetism and 40Ar/39Ar geochronology of the Plio-Pleistocene Boring Volcanic Field: Implications for the geomagnetic polarity time scale and paleosecular variation. *Phys. Earth Planet. In.*, 262: 101-115, 2017. doi: 10.1016/j.pepi.2016.07.008

Hale, C.J., and Dunlop, D.J., Evidence for an Early Archean Geomagnetic Field: A paleomagnetic study of the Komati Formation, Barberton Greenstone Belt, South Africa. *Geophys. Res. Lett.*, 11: 97-100, 1984. doi: 10.1029/GL011i002p00097

Hanzlik, M., Heunemann, C., Holtkamp-Rötzler, E., Winklhofer, M., Petersen, N., and Fleissner, G., Superparamagnetic Magnetite in the Upper Beak Tissue of Homing Pigeons. *Biometals*, 13: 325-331, 2000. doi: 10.1023/A:1009214526685

Hardarson, B.S., Fitton, G., and Hjartarson, A., Tertiary volcanism in Iceland. *Jokull*, 58: 161-178, 2008. doi:

Hardarson, B.S., Pringle, M.S., Kristjansson, L., Gudmundsson, A., and Johannesson, H., Stratigraphy and paleomagnetism of a 2.8 km lava succession in central northern Iceland, GA1.15/E/03-B4 presented at the XXII General Assembly, International Union of Geodesy and Geophysics, Birmingham, p. 326, 1999.

Hatakeyama, T., and Kono, M., Geomagnetic field model for the last 5 My: time-averaged field and secular variation. *Phys. Earth Planet. In.*, 133: 181-215, 2002. doi: 10.1016/S0031-9201(02)00084-5

Hebeda, E.H., Hantelmann, J.J., and Priem, H.N.A., K-Ar and paleomagnetic investigations of a series of lava flows on the eastern side of Eyjafjordur, Northern Iceland., International Meeting for Geochronology, Cosmochronology and Isotope Geology, Paris, p. 3, 1974.

Helgason, J., and Duncan, R.A., Glacial-interglacial history of the Skaftafell region, southeast Iceland, 0–5 Ma. *Geology*, 29: 179-182, 2001. doi:

Herrero-Bervera, E., and Valet, J.-P., Paleomagnetic secular variation of the Honolulu Volcanic Series (33–700 ka), O'ahu (Hawaii). *Phys. Earth Planet. In.*, 133: 83-97, 2002. doi: 10.1016/S0031-9201(02)00092-4

Herrero-Bervera, E., and Valet, J.-P., Persistent anomalous inclinations recorded in the Koolau volcanic series on the island of Oahu (Hawaii, USA) between 1.8 and 2.6 Ma. *Earth Planet. Sci. Lett.*, 212: 443-456, 2003. doi: 10.1016/S0012-821X(03)00168-7

Herrero-Bervera, E., and Valet, J.-P., Holocene paleosecular variation from dated lava flows on Maui (Hawaii). *Phys. Earth Planet. In.*, 161: 267-280, 2007. doi: 10.1016/j.pepi.2007.02.008

Hjartarson, Á., The Skagafjörður Unconformity, North Iceland, and its Geological History, Geological Museum. University of Copenhagen, p. 248, 2003.

Hjartarson, Á., and Sæmundsson, K., Geological Map of Iceland. Bedrock. 1:600,000. Iceland GeoSurvey, 2014.

Hunt, C.P., Moskowitz, B.M., and Banerjee, S.K., Magnetic Properties of Rocks and Minerals, Rock Physics & Phase Relations : A Handbook of Physical Constants. American Geophysical Union, pp. 189-204, 1995.

Irving, E., and Ward, M.A., A statistical model of the geomagnetic field. *pure and applied geophysics*, 57: 47-52, 1964. doi: 10.1007/bf00879707

Jackson, A., Jonkers, A.R.T., and Walker, M.R., Four centuries of geomagnetic secular variation from historical records. *Philos. Trans. R. Soc. A*, 358: 957-990, 2000. doi: 10.1098/rsta.2000.0569

Jakobsson, S.P., Jónasson, K., and Sigurdsson, I.A., The three igneous rock series of Iceland. *Jökull*, 58: 117-138, 2008. doi:

Johannesson, H., Yfirlit um jardfraedi Tröllaskaga (Overview of the geology of the Tröllaskagi penninsular, in Iceland). Yearbook of the Iceland Touring Association 1991, 1991.

Johannesson, H., and Saemundsson, K., Geological Map of Iceland in scale 1:500,000. Tectonics, Tectonics. Icelandic Institute of Natural History, Reykjavik, 1998.

Johannesson, H., and Sæmundsson, K., Geological Map of Iceland: Tectonics, 1:600 000. Iceland Institute of Natural History, 2009.

Johnson, C.L., and Constable, C.G., The time-averaged geomagnetic field as recorded by lava flows over the past 5 Myr. *Geophys. J. Int.*, 122: 489-519, 1995. doi: 10.1111/j.1365-246X.1995.tb07010.x

Johnson, C.L., and Constable, C.G., Palaeosecular variation recorded by lava flows over the past five million years. *Philosophical Transactions of the Royal Society of London. Series A: Mathematical, Physical and Engineering Sciences*, 354: 89, 1996. doi:

Johnson, C.L., and Constable, C.G., The time-averaged geomagnetic field: global and regional biases for 0–5 Ma. *Geophys. J. Int.*, 131: 643-666, 1997. doi: 10.1111/j.1365-246X.1997.tb06604.x

Johnson, C.L., Constable, C.G., Tauxe, L., Barendregt, R., Brown, L.L., Coe, R.S., Layer, P., Mejia, V., Opdyke, N.D., Singer, B.S., Staudigel, H., and Stone, D.B., Recent investigations of the 0–5 Ma geomagnetic field recorded by lava flows. *Geochem. Geophys. Geosyst.*, 9: Q04032, 2008. doi: 10.1029/2007GC001696

Johnson, C.L., and McFadden, P., Time-Averaged Field and Paleosecular Variation, in: Schubert, G. (Ed.), Treatise on Geophysics. Elsevier, Amsterdam, pp. 417-453, 2007.

Johnson, C.L., Wijbrans, J.R., Constable, C.G., Gee, J., Staudigel, H., Tauxe, L., Forjaz, V.-H., and Salgueiro, M., 40Ar/39Ar ages and paleomagnetism of São Miguel lavas, Azores. *Earth Planet. Sci. Lett.*, 160: 637-649, 1998. doi: 10.1016/S0012-821X(98)00117-4

Juárez, M.T., Tauxe, L., Gee, J.S., and Pick, T., The intensity of the Earth's magnetic field over the past 160 million years. *Nature*, 394: 878, 1998. doi: 10.1038/29746

Kelley, S., Excess argon in K–Ar and Ar–Ar geochronology. *Chemical Geology*, 188: 1-22, 2002. doi: 10.1016/S0009-2541(02)00064-5

Kelly, P., and Gubbins, D., The geomagnetic field over the past 5 million years. *Geophys. J. Int.*, 128: 315-330, 1997. doi: 10.1111/j.1365-246X.1997.tb01557.x

Kent, D.V., Wang, H., and Rochette, P., Equatorial paleosecular variation of the geomagnetic field from 0 to 3 Ma lavas from the Galapagos Islands. *Phys. Earth Planet. In.*, 183: 404-412, 2010. doi: 10.1016/j.pepi.2010.08.010

Kidane, T., Courtillot, V., Manighetti, I., Audin, L., Lahitte, P., Quidelleur, X., Gillot, P.-Y., Gallet, Y., Carlut, J., and Haile, T., New paleomagnetic and geochronologic results from Ethiopian Afar: Block rotations linked to rift overlap and propagation and determination of a ~2 Ma reference pole for stable Africa. *J. Geophys. Res.: Solid Earth*, 108: 2102, 2003. doi: 10.1029/2001JB000645

Kirschvink, J.L., The least-squares line and plane and the analysis of palaeomagnetic data. *Geophys. J. Int.*, 62: 699-718, 1980. doi: 10.1111/j.1365-246X.1980.tb02601.x

Kissel, C., Rodriguez-Gonzalez, A., Laj, C., Perez-Torrado, F., Carracedo, J.C., Wandres, C., and Guillou, H., Paleosecular variation of the earth magnetic field at the Canary Islands over the last 15 ka. *Earth Planet. Sci. Lett.*, 412: 52-60, 2015. doi: 10.1016/j.epsl.2014.12.031

Knight, K.B., Nomade, S., Renne, P.R., Marzoli, A., Bertrand, H., and Youbi, N., The Central Atlantic Magmatic Province at the Triassic–Jurassic boundary: paleomagnetic and 40Ar/39Ar evidence from Morocco for brief, episodic volcanism. *Earth Planet. Sci. Lett.*, 228: 143-160, 2004. doi: 10.1016/j.epsl.2004.09.022

Kono, M., Tanaka, H., and Tsunakawa, H., Spherical harmonic analysis of paleomagnetic data: The case of linear mapping. *J. Geophys. Res.: Solid Earth*, 105: 5817-5833, 2000. doi: 10.1029/1999JB900050

Korte, M., and Constable, C., Continuous global geomagnetic field models for the past 3000 years. *Phys. Earth Planet. In.*, 140: 73-89, 2003. doi: 10.1016/j.pepi.2003.07.013

Korte, M., and Constable, C., Improving geomagnetic field reconstructions for 0–3 ka. *Phys. Earth Planet. In.*, 188: 247-259, 2011. doi: 10.1016/j.pepi.2011.06.017

Korte, M., Constable, C., Donadini, F., and Holme, R., Reconstructing the Holocene geomagnetic field. *Earth Planet. Sci. Lett.*, 312: 497-505, 2011. doi: 10.1016/j.epsl.2011.10.031

Korte, M., and Constable, C.G., Continuous geomagnetic field models for the past 7 millennia: 2. CALS7K. *Geochem. Geophys. Geosyst.*, 6: Q02H16, 2005. doi: 10.1029/2004GC000801

Kristjansson, L., Analyses of primary remanence vector data from a large collection of lava flows: towards improved methodology in paleo-geomagnetism. *Stud Geophys Geod*, 57: 543-564, 2013. doi: 10.1007/s11200-012-0480-4

Kristjánsson, L., Paleomagnetic observations at three locations in the Pleistocene lava sequences of southwest and south Iceland. *Jökull*, 60: 149-164, 2010. doi:

Kristjánsson, L., Duncan, R.A., and GuĐMundsson, Á., Stratigraphy, palaeomagnetism and age of volcanics in the upper regions of Þjórsárdalur valley, central southern Iceland. *Boreas*, 27: 1-13, 1998. doi: 10.1111/j.1502-3885.1998.tb00863.x

Kristjansson, L., Fridleifsson, I.B., and Watkins, N.D., Stratigraphy and paleomagnetism of the Esja, Eyrarfjall and Akrafjall mountains, SW- Iceland. *Journal of Geophysics - Zeitschrift fur Geophysik*, 47: 31-42, 1980. doi:

Kristjánsson, L., and Guðmundsson, Á., Paleomagnetic studies in Skarðsheiði, South-Western Iceland. *Jökull*, 50: 33-48, 2001. doi:

Kristjansson, L., Gudmundsson, A., and Hardarson, B., Stratigraphy and paleomagnetism of a 2.9-km composite lava section in Eyjafjördur, Northern Iceland: a reconnaissance study. *Int J Earth Sci (Geol Rundsch)*, 93: 582-595, 2004. doi: 10.1007/s00531-004-0409-4

Kristjansson, L., Gudmundsson, M.T., Smellie, J.L., McIntosh, W.C., and Esser, R., Palaeomagnetic, 40Ar/39Ar, and stratigraphical correlation of Miocene–Pliocene basalts in the Brandy Bay area, James Ross Island, Antarctica. *Antarctic Science*, 17: 409-417, 2005. doi: 10.1017/S0954102005002853

Kristjansson, L., Hardarson, B.S., and Audunsson, H., A detailed palaeomagnetic study of the oldest (≈15 Myr) lava sequences in Northwest Iceland. *Geophys. J. Int.*, 155: 991-1005, 2003. doi: 10.1111/j.1365-246X.2003.02111.x

Kristjánsson, L., and Jóhannesson, H., Secular variation and reversals in a composite 2.5 km thick lava section in central Western Iceland. *Earth Planet Sp*, 51: 261-276, 1999. doi: 10.1186/bf03352230

Kristjánsson, L., Jóhannesson, H., Eiríksson, J., and Gudmundsson, A.I., Brunhes–Matuyama paleomagnetism in three lava sections in Iceland. *Canadian Journal of Earth Sciences*, 25: 215-225, 1988. doi: 10.1139/e88-024

Kristjansson, L., Johannesson, H., and Fridleifsson, I.B., Paleomagnetic stratigraphy of the Mosfellssveit area, SW-Iceland : a pilot study. *Jokull*, 41: 47-60, 1991. doi:

Kristjansson, L., and Sigurgeirsson, M., The R3-N3 and R5-N5 Palaeomagnetic Transition Zones in SW-Iceland Revisited. *Journal of geomagnetism and geoelectricity*, 45: 275-288, 1993. doi: 10.5636/jgg.45.275

Laj, C., Guillou, H., Szeremeta, N., and Coe, R., Geomagnetic paleosecular variation at Hawaii around 3 Ma from a sequence of 107 lava flows at Kaena Point (Oahu). *Earth Planet. Sci. Lett.*, 170: 365-376, 1999. doi: 10.1016/S0012-821X(99)00119-3

Laj, C., Raïs, A., Surmont, J., Gillot, P.-Y., Guillou, H., Kissel, C., and Zanella, E., Changes of the geomagnetic field vector obtained from lava sequences on the island of Vulcano (Aeolian Islands, Sicily). *Phys. Earth Planet. In.*, 99: 161-177, 1997. doi: 10.1016/S0031-9201(96)03221-9

Lanphere, M.A., and Dalrymple, B.G., Identification of excess 40Ar by the 40Ar/39Ar age spectrum technique. *Earth Planet. Sci. Lett.*, 32: 141-148, 1976. doi: 10.1016/0012-821X(76)90052-2

Lapointe, P.L., Paleomagnetism of the Notre Dame Bay lamprophyre dikes, Newfoundland, and the opening of the North Atlantic Ocean. *Canadian Journal of Earth Sciences*, 16: 1823-1831, 1979. doi: 10.1139/e79-166

Lawrence, K.P., Constable, C.G., and Johnson, C.L., Paleosecular variation and the average geomagnetic field at ±20° latitude. *Geochem. Geophys. Geosyst.*, 7: Q07007, 2006. doi: 10.1029/2005GC001181

Lawrence, K.P., Tauxe, L., Staudigel, H., Constable, C.G., Koppers, A., McIntosh, W., and Johnson, C.L., Paleomagnetic field properties at high southern latitude. *Geochem. Geophys. Geosyst.*, 10: Q01005, 2009. doi: 10.1029/2008GC002072

Lee, J.K.W., Ar–Ar and K–Ar Dating, in: Rink, W.J., Thompson, J. (Eds.), Encyclopedia of Scientific Dating Methods. Springer Netherlands, Dordrecht, pp. 1-27, 2013.

Lee, S., A study of the time-averaged paleomagnetic field for the last 195 million years. Australian National University, 1983.

Leó Kristjánsson, and Ágúst Guðmundsson, Stratigraphy and paleomagnetism of lava sequences in the Suðurdalur area, Fljótsdalur, Eastern Iceland. *Jökull*, 55: 17-32, 2005. doi:

Leonhardt, R., Heunemann, C., and Krása, D., Analyzing absolute paleointensity determinations: Acceptance criteria and the software ThellierTool4.0. *Geochem. Geophys. Geosyst.*, 5: 1-11, 2004a. doi: 10.1029/2004GC000807

Leonhardt, R., Krása, D., and Coe, R.S., Multidomain behavior during Thellier paleointensity experiments: a phenomenological model. *Phys. Earth Planet. In.*, 147: 127-140, 2004b. doi: 10.1016/j.pepi.2004.01.009

Leonhardt, R., Matzka, J., and Menor, E.A., Absolute paleointensities and paleodirections of miocene and pliocene lavas from Fernando de Noronha, Brazil. *Phys. Earth Planet. In.*, 139: 285-303, 2003. doi: 10.1016/j.pepi.2003.09.008

Leonhardt, R., and Soffel, H.C., The growth, collapse and quiescence of Teno volcano, Tenerife: new constraints from paleomagnetic data. *Int J Earth Sci (Geol Rundsch)*, 95: 1053-1064, 2006. doi: 10.1007/s00531-006-0089-3

Levi, S., The effect of magnetite particle size on paleointensity determinations of the geomagnetic field. *Phys. Earth Planet. In.*, 13: 245-259, 1977. doi: 10.1016/0031-9201(77)90107-8

Lurcock, P.C., and Wilson, G.S., PuffinPlot: A versatile, user-friendly program for paleomagnetic analysis. *Geochem. Geophys. Geosyst.*, 13: Q06Z45, 2012. doi: 10.1029/2012GC004098

Mankinen, E.A., Prévot, M., Grommé, C.S., and Coe, R.S., The Steens Mountain (Oregon) geomagnetic polarity transition: 1. Directional history, duration of episodes, and rock magnetism. *J. Geophys. Res.: Solid Earth*, 90: 10393-10416, 1985. doi: 10.1029/JB090iB12p10393

Mark, D.F., Barfod, D., Stuart, F.M., and Imlach, J., The ARGUS multicollector noble gas mass spectrometer: Performance for 40Ar/39Ar geochronology. *Geochem. Geophys. Geosyst.*, 10: 1-13, 2009. doi: 10.1029/2009GC002643

McCausland, P.J.A., Van der Voo, R., and Hall, C.M., Circum-Iapetus paleogeography of the Precambrian–Cambrian transition with a new paleomagnetic constraint from Laurentia. *Precambrian Research*, 156: 125-152, 2007. doi: 10.1016/j.precamres.2007.03.004

McClelland, E., and Briden, J.C., An improved methodology for Thellier-type paleointensity determination in igneous rocks and its usefulness for verifying primary thermoremanence. *J. Geophys. Res.: Solid Earth*, 101: 21995-22013, 1996. doi: 10.1029/96JB02113

McDougall, I., and Harrison, T.M., Geochronology and Thermochronology by the 40Ar/39Ar Method. Oxford University Press, New York, 1999.

McDougall, I., and Roksandic, Z., Total fusion 40Ar/39Ar ages using Hifar reactor. *J. Geol. Soc. Aust.*, 21: 81-89, 1974. doi: 10.1080/00167617408728836

McDougall, I., Saemundsson, K., Johannesson, H., Watkins, N.D., and Kristjansson, L., Extension of the geomagnetic polarity time scale to 6.5 m.y.: K-Ar dating, geological and paleomagnetic study of a 3,500-m lava succession in western Iceland. *GSA Bulletin*, 88: 1-15, 1977. doi: 10.1130/0016-7606(1977)88<1:EOTGPT>2.0.CO;2

McDougall, I., Watkins, N.D., and Kristjansson, L., Geochronology and paleomagnetism of a Miocene-Pliocene lava sequence at Bessastadaa, eastern Iceland. *American Journal of Science*, 276: 1078-1095, 1976. doi: 10.2475/ajs.276.9.1078

McElhinny, M.W., and McFadden, P.L., Palaeosecular variation over the past 5 Myr based on a new generalized database. *Geophys. J. Int.*, 131: 240-252, 1997. doi: 10.1111/j.1365-246X.1997.tb01219.x

McElhinny, M.W., McFadden, P.L., and Merrill, R.T., The time-averaged paleomagnetic field 0–5 Ma. *J. Geophys. Res.: Solid Earth*, 101: 25007-25027, 1996. doi: 10.1029/96JB01911

McElhinny, M.W., and Merrill, R.T., Geomagnetic secular variation over the past 5 m.y. *Rev. Geophys.*, 13: 687-708, 1975. doi: 10.1029/RG013i005p00687

McFadden, P.L., and McElhinny, M.W., A physical model for palaeosecular variation. *Geophysical Journal of the Royal Astronomical Society*, 78: 809-830, 1984. doi: 10.1111/j.1365-246X.1984.tb05072.x

McFadden, P.L., and McElhinny, M.W., Classification of the reversal test in palaeomagnetism. *Geophys. J. Int.*, 103: 725-729, 1990. doi: 10.1111/j.1365-246X.1990.tb05683.x

McFadden, P.L., Merrill, R.T., and McElhinny, M.W., Dipole/quadrupole family modeling of paleosecular variation. *J. Geophys. Res.: Solid Earth*, 93: 11583-11588, 1988. doi: 10.1029/JB093iB10p11583

Meert, J.G., Voo, R.V.d., Powell, C.M., Li, Z.-X., McElhinny, M.W., Chen, Z., and Symons, D.T.A., A plate-tectonic speed limit? *Nature*, 363: 216, 1993. doi: 10.1038/363216a0

Meert, J.G., Walderhaug, H.J., Torsvik, T.H., and Hendriks, B.W.H., Age and paleomagnetic signature of the Alnø carbonatite complex (NE Sweden): Additional controversy for the Neoproterozoic paleoposition of Baltica. *Precambrian Research*, 154: 159-174, 2007. doi: 10.1016/j.precamres.2006.12.008

Mejia, V., Barendregt, R.W., and Opdyke, N.D., Paleosecular variation of brunhes age lava flows from British Columbia, Canada. *Geochem. Geophys. Geosyst.*, 3: 1-14, 2002. doi: 10.1029/2002GC000353

Mejia, V., Böhnel, H., Opdyke, N.D., Ortega-Rivera, M.A., Lee, J.K.W., and Aranda-Gomez, J.J., Paleosecular variation and time-averaged field recorded in late Pliocene–Holocene lava flows from Mexico. *Geochem. Geophys. Geosyst.*, 6: Q07H19, 2005. doi: 10.1029/2004GC000871

Mejia, V., Opdyke, N.D., Vilas, J.F., Singer, B.S., and Stoner, J.S., Plio-Pleistocene time-averaged field in southern Patagonia recorded in lava flows. *Geochem. Geophys. Geosyst.*, 5: Q03H08, 2004. doi: 10.1029/2003GC000633

Merrihue, C., and Turner, G., Potassium-argon dating by activation with fast neutrons. *J. Geophys. Res.*, 71: 2852-2857, 1966. doi: 10.1029/JZ071i011p02852

Merrill, R.T., The magnetic field of the earth : paleomagnetism, the core, and the deep mantle / Ronald T. Merrill, Michael W. McElhinny, Phillip L. McFadden. San Diego ; London : Academic Press, c1996., San Diego ; London, 1996.

Merrill, R.T., McElhinny, M.W., and McFadden, P.L., The magnetic field of the earth : paleomagnetism, the core, and the deep mantle / Ronald T. Merrill, Michael W. McElhinny, Phillip L. McFadden. San Diego ; London : Academic Press, c1996., San Diego ; London, 1996.

Michalk, D.M., Böhnel, H.N., Nowaczyk, N.R., Aguírre-Diaz, G.J., López-Martínez, M., Ownby, S., and Negendank, J.F.W., Evidence for geomagnetic excursions recorded in Brunhes and

Matuyama Chron lavas from the trans-Mexican volcanic belt. *J. Geophys. Res.: Solid Earth*, 118: 2648-2669, 2013. doi: 10.1002/jgrb.50214

Miki, M., Inokuchi, H., Yamaguchi, S., Matsuda, J.-i., Nagao, K., Isezaki, N., and Yaskawa, K., Geomagnetic paleosecular variation in Easter Island, the southeast Pacific. *Phys. Earth Planet. In.*, 106: 93-101, 1998. doi: 10.1016/S0031-9201(97)00106-4

Mitchell, J.G., The argon-40argon-39 method for potassium-argon age determination. *Geochimica et Cosmochimica Acta*, 32: 781-790, 1968. doi: 10.1016/0016-7037(68)90012-4

Mitchell, R.J., Jaeger, D.J., Diehl, J.F., and Hammond, P.E., Palaeomagnetic Results From the Indian Heaven Volcanic Field, South-Central Washington. *Geophys. J. Int.*, 97: 381-390, 1989. doi: 10.1111/j.1365-246X.1989.tb00509.x

Mochizuki, N., Tsunakawa, H., Shibuya, H., Cassidy, J., and Smith, I.E.M., Palaeointensities of the Auckland geomagnetic excursions by the LTD-DHT Shaw method. *Phys. Earth Planet. In.*, 154: 168-179, 2006. doi: 10.1016/j.pepi.2005.09.005

Morales, J., Goguitchaichvili, A., and Urrutia-Fucugauchi, J., A rock-magnetic and paleointensity study of some Mexican volcanic lava flows during the Latest Pleistocene to the Holocene. *Earth Planet Sp*, 53: 893-902, 2001. doi: 10.1186/BF03351686

Moskowitz, B.M., Methods for estimating Curie temperatures of titanomaghemites from experimentalJs-T data. *Earth Planet. Sci. Lett.*, 53: 84-88, 1981. doi: 10.1016/0012-821X(81)90028-5

Muxworthy, A.R., Considerations for Latitudinal Time-Averaged-Field Palaeointensity Analysis of the Last Five Million Years. *Frontiers in Earth Science*, 5, 2017. doi: 10.3389/feart.2017.00079

Muxworthy, A.R., and Roberts, A.P., First-Order Reversal Curve (FORC) Diagrams, in: Gubbins, D., Herrero-Bervera, E. (Eds.), Encyclopedia of Geomagnetism and Paleomagnetism. Springer Netherlands, Dordrecht, pp. 266-272, 2007.

Nagata, T., Rock Magnetism, 2nd ed. Maruzen, Tokyo, 1961.

Nagata, T., Arai, Y., and Momose, K., Secular variation of the geomagnetic total force during the last 5,000 years. *J. Geophys. Res.*, 68: 5,277-275,281, 1963. doi:

Nagy, L., Williams, W., Muxworthy, A.R., Fabian, K., Almeida, T.P., Conbhuí, P.Ó., and Shcherbakov, V.P., Stability of equidimensional pseudo–single-domain magnetite over billion-year timescales. *Proceedings of the National Academy of Sciences*, 114: 10356-10360, 2017. doi: 10.1073/pnas.1708344114

Néel, L., Théorie du traînage magnétique des ferromagnétiques en grains fins avec applications aux terres cuites. *Ann. Géophys*, 5: 99–136, 1949. doi:

Nier, A.O., A Redetermination of the Relative Abundances of the Isotopes of Carbon, Nitrogen, Oxygen, Argon, and Potassium. *Physical Review*, 77: 789-793, 1950. doi: 10.1103/PhysRev.77.789

Niespolo, E.M., Rutte, D., Deino, A.L., and Renne, P.R., Intercalibration and age of the Alder Creek sanidine 40Ar/39Ar standard. *Quat. Geochronol.*, 39: 205-213, 2017. doi: 10.1016/j.quageo.2016.09.004

Ogg, J.G., Chapter 5 - Geomagnetic Polarity Time Scale, The Geologic Time Scale. Elsevier, Boston, pp. 85-113, 2012.

Oliva-Urcia, B., and Kontny, A., Remanent magnetization of maghemitized basalts from Krafla drill cores, NE-Iceland. *Stud Geophys Geod*, 56: 641-657, 2012. doi: 10.1007/s11200-011-9013-9

Olson, P., and Christensen, U.R., The time-averaged magnetic field in numerical dynamos with non-uniform boundary heat flow. *Geophys. J. Int.*, 151: 809-823, 2002. doi: 10.1046/j.1365-246X.2002.01818.x

Opdyke, N.D., Hall, M., Mejia, V., Huang, K., and Foster, D.A., Time-averaged field at the equator: Results from Ecuador. *Geochem. Geophys. Geosyst.*, 7: Q11005, 2006. doi: 10.1029/2005GC001221

Opdyke, N.D., and Henry, K.W., A test of the dipole hypothesis. *Earth Planet. Sci. Lett.*, 6: 139-151, 1969. doi: 10.1016/0012-821X(69)90132-0

Opdyke, N.D., Kent, D.V., Foster, D.A., and Huang, K., Paleomagnetism of Miocene volcanics on Sao Tome: Paleosecular variation at the Equator and a comparison to its latitudinal dependence over the last 5 Myr. *Geochem. Geophys. Geosyst.*, 16: 3870-3882, 2015. doi: 10.1002/2015GC005901

Opdyke, N.D., Kent, D.V., Huang, K., Foster, D.A., and Patel, J.P., Equatorial paleomagnetic time-averaged field results from 0–5 Ma lavas from Kenya and the latitudinal variation of angular dispersion. *Geochem. Geophys. Geosyst.*, 11: Q05005, 2010. doi: 10.1029/2009GC002863

Opdyke, N.D., and Musgrave, R., Paleomagnetic results from the Newer Volcanics of Victoria: Contribution to the Time Averaged Field Initiative. *Geochem. Geophys. Geosyst.*, 5: Q03H09, 2004. doi: 10.1029/2003GC000632

Óskarsson, B.V., Riishuus, M.S., and Arnalds, Ó., Climate-dependent chemical weathering of volcanic soils in Iceland. *Geoderma*, 189-190: 635-651, 2012. doi: 10.1016/j.geoderma.2012.05.030

Otake, H., Tanaka, H., Kono, M., and Saito, K., Paleomagnetic Study of Pleistocene Lavas and Dikes of the Zao Volcano Group, Japan. *Journal of geomagnetism and geoelectricity*, 45: 595-612, 1993. doi: 10.5636/jgg.45.595

Özdemir, Ö., Inversion of titanomaghemites. *Phys. Earth Planet. In.*, 46: 184-196, 1987. doi: 10.1016/0031-9201(87)90181-6

Özdemir, Ö., and O'Reilly, W., Magnetic hysteresis properties of synthetic monodomain titanomaghemites. *Earth Planet. Sci. Lett.*, 57: 437-447, 1982. doi: 10.1016/0012-821X(82)90162-5

Ozima, M., and Ozima, M., Characteristic thermomagnetic curve in submarine basalts. *J. Geophys. Res.*, 76: 2051-2056, 1971. doi: 10.1029/JB076i008p02051

Panaiotu, C.G., Jicha, B.R., Singer, B.S., Ţugui, A., Seghedi, I., Panaiotu, A.G., and Necula, C., 40Ar/39Ar chronology and paleomagnetism of Quaternary basaltic lavas from the Perşani Mountains (East Carpathians). *Phys. Earth Planet. In.*, 221: 1-14, 2013. doi: 10.1016/j.pepi.2013.06.007

Panaiotu, C.G., Vişan, M., Ţugui, A., Seghedi, I., and Panaiotu, A.G., Palaeomagnetism of the South Harghita volcanic rocks of the East Carpathians: implications for tectonic rotations and palaeosecular variation in the past 5 Ma. *Geophys. J. Int.*, 189: 369-382, 2012. doi: 10.1111/j.1365-246X.2012.05394.x

Paterson, G.A., Biggin, A.J., Hodgson, E., and Hill, M.J., Thellier-type paleointensity data from multidomain specimens. *Phys. Earth Planet. In.*, 245: 117-133, 2015. doi: 10.1016/j.pepi.2015.06.003

Paterson, G.A., Tauxe, L., Biggin, A.J., Shaar, R., and Jonestrask, L.C., On improving the selection of Thellier-type paleointensity data. *Geochem. Geophys. Geosyst.*, 15: 1180-1192, 2014. doi: 10.1002/2013GC005135

Peña, R.M., Goguitchaichvili, A., Guilbaud, M.-N., Martínez, V.C.R., Rathert, M.C., Siebe, C., Reyes, B.A., and Morales, J., Paleomagnetic secular variation study of Ar–Ar dated lavas flows from Tacambaro area (Central Mexico): Possible evidence of Intra-Jaramillo geomagnetic excursion in volcanic rocks. *Phys. Earth Planet. In.*, 229: 98-109, 2014. doi: 10.1016/j.pepi.2014.01.005

Peña, R.M., Goguitchaichvili, A., Henry, B., Sánchez-Bettucci, L., Morales, J., Reyes, B.A., Soler-Arechalde, A.M., and Calvo-Rathert, M., Plio-pleistocene paleomagnetic record from the Michoacán-Guanajuato Monogenetic Volcanic Field (Western Mexico). *Stud Geophys Geod*, 55: 311-328, 2011. doi: 10.1007/s11200-011-0017-2

Petronille, M., Goguitchaichvili, A., Henry, B., Alva-Valdivia, L.M., Rosas-Elguera, J., Urrutia-Fucugauchi, J., Rodriguez Cejá, M., and Calvo-Rathert, M., Paleomagnetism of Ar-Ar dated lava flows from the Ceboruco-San Pedro volcanic field (western Mexico): Evidence for the Matuyama-Brunhes transition precursor and a fully reversed geomagnetic event in the Brunhes chron. *J. Geophys. Res.: Solid Earth*, 110: B08101, 2005. doi: 10.1029/2004JB003321

Phillips, B.R., Bunge, H.-P., and Schaber, K., True polar wander in mantle convection models with multiple, mobile continents. *Gondwana Research*, 15: 288-296, 2009. doi: 10.1016/j.gr.2008.11.007

Prasad, J.N., Paleomagnetism of the Mesozoic lamprophyric dikes in north-central Newfoundland. Memorial University of Newfoundland, p. 119, 1981.

Pullaiah, G., Irving, E., Buchan, K.L., and Dunlop, D.J., Magnetization changes caused by burial and uplift. *Earth Planet. Sci. Lett.*, 28: 133-143, 1975. doi: 10.1016/0012-821X(75)90221-6

Quidelleur, X., Carlut, J., Tchilinguirian, P., Germa, A., and Gillot, P.Y., Paleomagnetic directions from mid-latitude sites in the southern hemisphere (Argentina): Contribution to time averaged field models. *Phys. Earth Planet. In.*, 172: 199-209, 2009. doi: 10.1016/j.pepi.2008.09.012

Quidelleur, X., and Courtillot, V., On low-degree spherical harmonic models of paleosecular variation. *Phys. Earth Planet. In.*, 95: 55-77, 1996. doi: 10.1016/0031-9201(95)03115-4

Quidelleur, X., Valet, J.-P., Courtillot, V., and Hulot, G., Long-term geometry of the geomagnetic field for the last five million years: An updated secular variation database. *Geophys. Res. Lett.*, 21: 1639-1642, 1994. doi: 10.1029/94GL01105

Raïs, A., Laj, C., Surmont, J., Gillot, P.-Y., and Guillou, H., Geomagnetic field intensity between 70 000 and 130 000 years B.P. from a volcanic sequence on La Réunion, Indian Ocean. *Earth Planet. Sci. Lett.*, 140: 173-189, 1996. doi: 10.1016/0012-821X(96)00024-6

Riisager, P., and Riisager, J., Detecting multidomain magnetic grains in Thellier palaeointensity experiments. *Phys. Earth Planet. In.*, 125: 111-117, 2001. doi: 10.1016/S0031-9201(01)00236-9

Riisager, P., Riisager, J., Abrahamsen, N., and Waagstein, R., New paleomagnetic pole and magnetostratigraphy of Faroe Islands flood volcanics, North Atlantic igneous province. *Earth Planet. Sci. Lett.*, 201: 261-276, 2002. doi: 10.1016/S0012-821X(02)00720-3

Roperch, P., Chauvin, A., Lara, L.E., and Moreno, H., Secular variation of the Earth's magnetic field and application to paleomagnetic dating of historical lava flows in Chile. *Phys. Earth Planet. In.*, 242: 65-78, 2015. doi: 10.1016/j.pepi.2015.03.005

Ruiz-Martínez, V.C., Urrutia-Fucugauchi, J., and Osete, M.L., Palaeomagnetism of the Western and Central sectors of the Trans-Mexican volcanic belt—implications for tectonic rotations and palaeosecular variation in the past 11 Ma. *Geophys. J. Int.*, 180: 577-595, 2010. doi: 10.1111/j.1365-246X.2009.04447.x

Saemundsson, K., Kristjansson, L., McDougall, I., and Watkins, N.D., K-Ar dating, geological and paleomagnetic study of a 5-km lava succession in northern Iceland. *J. Geophys. Res.: Solid Earth*, 85: 3628-3646, 1980. doi: 10.1029/JB085iB07p03628

Sánchez-Duque, A., Mejia, V., Opdyke, N.D., Huang, K., and Rosales-Rivera, A., Plio-Pleistocene paleomagnetic secular variation and time-averaged field: Ruiz-Tolima volcanic chain, Colombia. *Geochem. Geophys. Geosyst.*, 17: 538-549, 2016. doi: 10.1002/2015GC006149

Sarson, G.R., Jones, C.A., and Longbottom, A.W., The influence of boundary region heterogeneities on the geodynamo. *Phys. Earth Planet. In.*, 101: 13-32, 1997. doi: 10.1016/S0031-9201(96)03248-7

Sbarbori, E., Tauxe, L., Goguitchaichvili, A., Urrutia-Fucugauchi, J., and Bohrson, W.A., Paleomagnetic behavior of volcanic rocks from Isla Socorro, Mexico. *Earth Planet Sp*, 61: 191-204, 2009. doi: 10.1186/bf03352899

Selkin, P.A., and Tauxe, L., Long-term variations in palaeointensity. *Philosophical Transactions of the Royal Society of London. Series A: Mathematical, Physical and Engineering Sciences*, 358: 1065-1088, 2000. doi: 10.1098/rsta.2000.0574

Shaar, R., Ron, H., Tauxe, L., Kessel, R., and Agnon, A., Paleomagnetic field intensity derived from non-SD: Testing the Thellier IZZI technique on MD slag and a new bootstrap procedure. *Earth Planet. Sci. Lett.*, 310: 213-224, 2011. doi: 10.1016/j.epsl.2011.08.024

Shaar, R., Tauxe, L., Ben-Yosef, E., Kassianidou, V., Lorentzen, B., Feinberg, J.M., and Levy, T.E., Decadal-scale variations in geomagnetic field intensity from ancient Cypriot slag mounds. *Geochem. Geophys. Geosyst.*: 1-20, 2015. doi: 10.1002/2014GC005455

Shah, J., Koppers, A.A.P., Leitner, M., Leonhardt, R., Muxworthy, A.R., Heunemann, C., Bachtadse, V., Ashley, J.A.D., and Matzka, J., Palaeomagnetic evidence for the persistence or recurrence of geomagnetic main field anomalies in the South Atlantic. *Earth Planet. Sci. Lett.*, 441: 113-124, 2016. doi: 10.1016/j.epsl.2016.02.039

Shaw, J., A New Method of Determining the Magnitude of the Palaeomagnetic Field: Application to five historic lavas and five archaeological samples. *Geophysical Journal of the Royal Astronomical Society*, 39: 133-141, 1974. doi: 10.1111/j.1365-246X.1974.tb05443.x

Shcherbakov, V.P., and Shcherbakova, V.V., On the suitability of the Thellier method of palaeointensity determinations on pseudo-single-domain and multidomain grains. *Geophys. J. Int.*, 146: 20-30, 2001. doi: 10.1046/j.0956-540x.2001.01421.x

Shive, P.N., and Frerichs, W.E., Paleomagnetism of the Niobrara Formation in Wyoming, Colorado, and Kansas. *J. Geophys. Res.*, 79: 3001-3007, 1974. doi: 10.1029/JB079i020p03001

Smirnov, A.V., and Tarduno, J.A., Magnetic hysteresis monitoring of Cretaceous submarine basaltic glass during Thellier paleointensity experiments: evidence for alteration and attendant low field bias. *Earth Planet. Sci. Lett.*, 206: 571-585, 2003. doi: 10.1016/S0012-821X(02)01123-8

Smirnov, A.V., and Tarduno, J.A., Secular variation of the Late Archean–Early Proterozoic geodynamo. *Geophys. Res. Lett.*, 31: L16607, 2004. doi: 10.1029/2004GL020333

Smith, P.E., Evensen, N.M., and York, D., First successful 40Ar-39Ar dating of glauconies: Argon recoil in single grains of cryptocrystalline material. *Geology*, 21: 41-44, 1993. doi: 10.1130/0091-7613(1993)021<0041:FSAADO>2.3.CO;2

Sparks, R.S.J., Folkes, C.B., Humphreys, M.C.S., Barfod, B.N., Jorge Clavero, J., Mayel Sunagua, C., McNutt, S.R., and Pritchard, M.E., Uturuncu Volcano, Bolivia: Volcanic unrest due to mid-crustal magma intrusion. *American Journal of Science*, 308: 727-769, 2011. doi: 10.2475/06.2008.01

Speranza, F., Branca, S., Coltelli, M., D'Ajello Caracciolo, F., and Vigliotti, L., How accurate is “paleomagnetic dating”? New evidence from historical lavas from Mount Etna. *J. Geophys. Res.: Solid Earth*, 111: B12S33, 2006. doi: 10.1029/2006JB004496

Speranza, F., Pompilio, M., D'Ajello Caracciolo, F., and Sagnotti, L., Holocene eruptive history of the Stromboli volcano: Constraints from paleomagnetic dating. *J. Geophys. Res.: Solid Earth*, 113: B09101, 2008. doi: 10.1029/2007JB005139

Stanton, T., Riisager, P., Knudsen, M.F., and Thordarson, T., New palaeointensity data from Holocene Icelandic lavas. *Phys. Earth Planet. In.*, 186: 1-10, 2011. doi: 10.1016/j.pepi.2011.01.006

Steiger, R.H., and Jäger, E., Subcommission on geochronology: Convention on the use of decay constants in geo- and cosmochronology. *Earth Planet. Sci. Lett.*, 36: 359-362, 1977. doi: 10.1016/0012-821X(77)90060-7

Stoenner, R.W., Schaeffer, O.A., and Katcoff, S., Half-Lives of Argon-37, Argon-39, and Argon-42. *Science*, 148: 1325-1328, 1965. doi: 10.1126/science.148.3675.1325

Stone, D.B., and Layer, P.W., Paleosecular variation and GAD studies of 0–2 Ma flow sequences from the Aleutian Islands, Alaska. *Geochem. Geophys. Geosyst.*, 7: Q04H22, 2006. doi: 10.1029/2005GC001007

Sumita, I., and Olson, P., A Laboratory Model for Convection in Earth's Core Driven by a Thermally Heterogeneous Mantle. *Science*, 286: 1547-1549, 1999. doi: 10.1126/science.286.5444.1547

Sumita, I., and Olson, P., Rotating thermal convection experiments in a hemispherical shell with heterogeneous boundary heat flux: Implications for the Earth's core. *J. Geophys. Res.: Solid Earth*, 107: ETG 5-1-ETG 5-18, 2002. doi: 10.1029/2001JB000548

Suttie, N., Biggin, A.J., and Holme, R., Correlation of palaeomagnetic directions constrains eruption rate of large igneous provinces. *Earth Planet. Sci. Lett.*, 387: 4-9, 2014. doi: 10.1016/j.epsl.2013.11.011

Tanaka, H., Hashimoto, Y., and Morita, N., Palaeointensity determinations from historical and Holocene basalt lavas in Iceland. *Geophys. J. Int.*, 189: 833-845, 2012. doi: 10.1111/j.1365-246X.2012.05412.x

Tanaka, H., Kamizaki, R., and Yamamoto, Y., Palaeomagnetism of the Older Ontake Volcano, Japan: Contributions to the palaeosecular variation for 750–400 Ka, the lower half of the Brunhes Chron. *Geophys. J. Int.*, 169: 81-90, 2007. doi: 10.1111/j.1365-246X.2006.03306.x

Tanaka, H., Kawamura, K.i., Nagao, K., and Houghton, B.F., K-Ar Ages and Paleosecular Variation of Direction and Intensity from Quaternary Lava Sequences in the Ruapehu Volcano, New Zealand. *Journal of geomagnetism and geoelectricity*, 49: 587-599, 1997. doi: 10.5636/jgg.49.587

Tanaka, H., and Kobayashi, T., Paleomagnetism of the late Quaternary Ontake Volcano, Japan: directions, intensities, and excursions. *Earth Planet Sp*, 55: 189-202, 2003. doi: 10.1186/bf03351748

Tanaka, H., Komuro, N., and Turner, G.M., Palaeosecular variation for 0.1-21 Ka from the Okataina Volcanic Centre, New Zealand. *Earth Planet Sp*, 61: 213-225, 2009. doi: 10.1186/bf03352901

Tanaka, H., Turner, G.M., Houghton, B.F., Tachibana, T., Kono, M., and McWilliams, M.O., Palaeomagnetism and chronology of the central Taupo Volcanic Zone, New Zealand. *Geophys. J. Int.*, 124: 919-934, 1996. doi: 10.1111/j.1365-246X.1996.tb05645.x

Tanaka, H., and Yamamoto, Y., Palaeointensities from Pliocene lava sequences in Iceland: emphasis on the problem of Arai plot with two linear segments. *Geophys. J. Int.*, 205: 694-714, 2016. doi: 10.1093/gji/ggw031

Tanguy, J.C., An archaeomagnetic strudy of Mount Etna: the magnetic direction recorded in lava flows subsequent to the twelfth century. *Archaeometry*, 12: 115-128, 1970. doi: 10.1111/j.1475-4754.1970.tb00014.x

Tanguy, J.C., Abnormal shallow palaeomagnetic inclinations from the 1950 and 1972 lava flows, Hawaii. *Geophys. J. Int.*, 103: 281-283, 1990. doi: 10.1111/j.1365-246X.1990.tb01769.x

Tanty, C., Carlut, J., Valet, J.-P., and Germa, A., Palaeosecular variation recorded by 9 ka to 2.5-Ma-old lavas from Martinique Island: new evidence for the La Palma aborted reversal ∼617 ka ago. *Geophys. J. Int.*, 200: 917-934, 2015. doi: 10.1093/gji/ggu423

Tarduno, J.A., Blackman, E.G., and Mamajek, E.E., Detecting the oldest geodynamo and attendant shielding from the solar wind: Implications for habitability. *Phys. Earth Planet. In.*, 233: 68-87, 2014. doi: 10.1016/j.pepi.2014.05.007

Tarduno, J.A., Cottrell, R.D., Watkeys, M.K., and Bauch, D., Geomagnetic field strength 3.2 billion years ago recorded by single silicate crystals. *Nature*, 446: 657, 2007. doi: 10.1038/nature05667

Tauxe, L., Paleomagnetic Principles and Practice. Kluwer Academic Publishers, 2003.

Tauxe, L., Butler, R.F., Voo, R.V.d., and Banerjee, S.K., Essentials of paleomagnetism. University of California Press, Berkeley, 2010.

Tauxe, L., Constable, C., Johnson, C.L., Koppers, A.A.P., Miller, W.R., and Staudigel, H., Paleomagnetism of the southwestern U.S.A. recorded by 0–5 Ma igneous rocks. *Geochem. Geophys. Geosyst.*, 4: 8802, 2003. doi: 10.1029/2002GC000343

Tauxe, L., Gee, J.S., Steiner, M.B., and Staudigel, H., Paleointensity results from the Jurassic: New constraints from submarine basaltic glasses of ODP Site 801C. *Geochem. Geophys. Geosyst.*, 14: 4718-4733, 2013. doi: 10.1002/ggge.20282

Tauxe, L., and Kent, D.V., A Simplified Statistical Model for the Geomagnetic Field and the Detection of Shallow Bias in Paleomagnetic Inclinations: was the Ancient Magnetic Field Dipolar?, Timescales Of The Paleomagnetic Field. American Geophysical Union, pp. 101-115, 2004.

Tauxe, L., Luskin, C., Selkin, P., Gans, P., and Calvert, A., Paleomagnetic results from the Snake River Plain: Contribution to the time-averaged field global database. *Geochem. Geophys. Geosyst.*, 5: Q08H13, 2004. doi: 10.1029/2003GC000661

Tauxe, L., Mullender, T.A.T., and Pick, T., Potbellies, wasp-waists, and superparamagnetism in magnetic hysteresis. *J. Geophys. Res.: Solid Earth*, 101: 571-583, 1996. doi: 10.1029/95JB03041

Tauxe, L., Shaar, R., Jonestrask, L., Swanson-Hysell, N.L., Minnett, R., Koppers, A.A.P., Constable, C.G., Jarboe, N., Gaastra, K., and Fairchild, L., PmagPy: Software package for paleomagnetic data analysis and a bridge to the Magnetics Information Consortium (MagIC) Database. *Geochem. Geophys. Geosyst.*, 17: 2450-2463, 2016. doi: 10.1002/2016GC006307

Tauxe, L., and Staudigel, H., Strength of the geomagnetic field in the Cretaceous Normal Superchron: New data from submarine basaltic glass of the Troodos Ophiolite. *Geochem. Geophys. Geosyst.*, 5: 1-16, 2004. doi: 10.1029/2003GC000635

Tauxe, L., Staudigel, H., and Wijbrans, J.R., Paleomagnetism and 40Ar/39Ar ages from La Palma in the Canary Islands. *Geochem. Geophys. Geosyst.*, 1: 2000GC000063, 2000. doi: 10.1029/2000GC000063

Tauxe, L., and Watson, G.S., The fold test: an eigen analysis approach. *Earth Planet. Sci. Lett.*, 122: 331-341, 1994. doi: 10.1016/0012-821X(94)90006-X

Tauxe, L., and Yamazaki, T., 5.13 - Paleointensities, in: Schubert, G. (Ed.), Treatise on Geophysics. Elsevier, Amsterdam, pp. 509-563, 2007.

Thellier, E., Sur l'aimantationdes terres cuites et ses applications geophysique. *Annales Institut Physique du Globe de Paris*, 16: 157-302, 1938. doi:

Thellier, E., and Thellier, O., Sur l'intensité du champ magnétique terrestre dans le passé historique et géologique. *Annales de Geophysique*, 15: 285, 1959. doi:

Thordarson, T., and Larsen, G., Volcanism in Iceland in historical time: Volcano types, eruption styles and eruptive history. *J. Geodyn.*, 43: 118-152, 2007. doi: 10.1016/j.jog.2006.09.005

Torsvik, T.H., Müller, D.R., Van der Voo, R., Steinberger, B., and Gaina, C., Global plate motion frames: Toward a unified model. *Rev. Geophys.*, 46, 2008a. doi: 10.1029/2007RG000227

Torsvik, T.H., Smethurst, M.A., Burke, K., and Steinberger, B., Long term stability in deep mantle structure: Evidence from the ~300 Ma Skagerrak-Centered Large Igneous Province (the SCLIP). *Earth Planet. Sci. Lett.*, 267: 444-452, 2008b. doi: 10.1016/j.epsl.2007.12.004

Torsvik, T.H., Van der Voo, R., Preeden, U., Mac Niocaill, C., Steinberger, B., Doubrovine, P.V., van Hinsbergen, D.J.J., Domeier, M., Gaina, C., Tohver, E., Meert, J.G., McCausland, P.J.A., and Cocks, L.R.M., Phanerozoic polar wander, palaeogeography and dynamics. *Earth-Science Reviews*, 114: 325-368, 2012. doi: 10.1016/j.earscirev.2012.06.007

Tsai, V.C., and Stevenson, D.J., Theoretical constraints on true polar wander. *J. Geophys. Res.: Solid Earth*, 112, 2007. doi: 10.1029/2005JB003923

Turner, G., The Distribution of Potassium and Argon in Chondrites† A2 - AHRENS, L.H, Origin and Distribution of the Elements. Pergamon, pp. 387-398, 1968.

Turner, G., and Cadogan, P.H., Possible effects of 39Ar recoil in 40Ar-39Ar dating. *Proceedings of the Fifth Lunar Science Conference*, 2: 1601 - 1615, 1974. doi:

Ubangoh, R.U., Pacca, I.G., and Nyobe, J.B., Palaeomagnetism of the continental sector of the Cameroon Volcanic Line, West Africa. *Geophys. J. Int.*, 135: 362-374, 1998. doi: 10.1046/j.1365-246X.1998.00635.x

Udagawa, S., Kitagawa, H., Gudmundsson, A., Hiroi, O., Koyaguchi, T., Tanaka, H., Kristjansson, L., and Kono, M., Age and magnetism of lavas in Jökuldalur area, Eastern Iceland: Gilsá event revisited. *Phys. Earth Planet. In.*, 115: 147-171, 1999. doi: 10.1016/S0031-9201(99)00073-4

Urrutia-Fucugauchi, J., Alva-Valdivia, L.M., Goguitchaichvili, A., Rivas, M.L., and Morales, J., Palaeomagnetic, rock-magnetic and microscopy studies of historic lava flows from the Paricutin volcano, Mexico: implications for the deflection of palaeomagnetic directions. *Geophys. J. Int.*, 156: 431-442, 2004. doi: 10.1111/j.1365-246X.2004.02166.x

Valet, J.-P., and Soler, V., Magnetic anomalies of lava fields in the Canary islands. Possible consequences for paleomagnetic records. *Phys. Earth Planet. In.*, 115: 109-118, 1999. doi: 10.1016/S0031-9201(99)00071-0

Valet, J.-P., Tric, E., Herrero-Bervera, E., Meynadier, L., and Lockwood, J.P., Absolute paleointensity from Hawaiian lavas younger than 35 ka. *Earth Planet. Sci. Lett.*, 161: 19-32, 1998. doi: 10.1016/S0012-821X(98)00133-2

Van der Voo, R., The reliability of paleomagnetic data. *Tectonophysics*, 184: 1-9, 1990. doi: 10.1016/0040-1951(90)90116-P

Vandamme, D., A new method to determine paleosecular variation. *Phys. Earth Planet. In.*, 85: 131-142, 1994. doi: 10.1016/0031-9201(94)90012-4

Veikkolainen, T., Heimpel, M., Evans, M.E., Pesonen, L.J., and Korhonen, K., A paleointensity test of the geocentric axial dipole (GAD) hypothesis. *Phys. Earth Planet. In.*, 265: 54-61, 2017. doi: 10.1016/j.pepi.2017.02.008

Verhoogen, J., Heat Balance of the Earth's Core. *Geophys. J. Int.*, 4: 276-281, 1961. doi: 10.1111/j.1365-246X.1961.tb06819.x

Walker, G.P.L., Zeolite Zones and Dike Distribution in Relation to the Structure of the Basalts of Eastern Iceland. *The Journal of Geology*, 68: 515-528, 1960. doi:

Wang, H., Kent, D.V., and Rochette, P., Weaker axially dipolar time-averaged paleomagnetic field based on multidomain-corrected paleointensities from Galapagos lavas. *Proceedings of the National Academy of Sciences*, 112: 15036-15041, 2015. doi: 10.1073/pnas.1505450112

Watkins, N.D., McDougall, I., and Kristjansson, L., Upper Miocene and Pliocene geomagnetic secular variation in the Borgarfjördur area of Western Iceland. *Geophysical Journal of the Royal Astronomical Society*, 49: 609-632, 1977. doi: 10.1111/j.1365-246X.1977.tb01307.x

Watkins, N.D., and Walker, G.P.L., Magnetostratigraphy of eastern Iceland. *American Journal of Science*, 277: 513-584, 1977. doi: 10.2475/ajs.277.5.513

Watson, G.S., Large sample theory of the Langevin distribution. *Journal of Statistical Planning and Inference*, 8: 245-256, 1983. doi: 10.1016/0378-3758(83)90043-5

Xu, S., and Dunlop, D.J., Thellier paleointensity theory and experiments for multidomain grains. *J. Geophys. Res.: Solid Earth*, 109: B07103, 2004. doi: 10.1029/2004JB003024

Yamamoto, Y., Shimura, K., Tsunakawa, H., Kogiso, T., Uto, K., Barsczus, H.G., Oda, H., Yamazaki, T., and Kikawa, E., Geomagnetic paleosecular variation for the past 5 Ma in the Society Islands, French Polynesia. *Earth Planet Sp*, 54: 797-802, 2002. doi: 10.1186/bf03351733

Yamamoto, Y., Tsunakawa, H., Shaw, J., and Kono, M., Paleomagnetism of the Datong monogenetic volcanoes in China: paleodirection and paleointensity during the middle to early Brunhes Chron. *Earth Planet Sp*, 59: 727-746, 2007. doi: 10.1186/bf03352736

York, D., Cooling Histories from Ar/Ar Age Spectra: Implications for Precambrian Plate Tectonics. *Annual Review of Earth and Planetary Sciences*, 12: 383-409, 1984. doi: 10.1146/annurev.ea.12.050184.002123

Yu, Y., and Tauxe, L., Testing the IZZI protocol of geomagnetic field intensity determination. *Geochem. Geophys. Geosyst.*, 6: Q05H17, 2005. doi: 10.1029/2004GC000840

Zhang, K., and Gubbins, D., Convection in a rotating spherical fluid shell with an inhomogeneous temperature boundary condition at infinite Prandtl number. *J. Fluid Mech.*, 250: 209-232, 1993. doi: 10.1017/S0022112093001430

Zhang, K., and Gubbins, D., Convection in a rotating spherical fluid shell with an inhomogeneous temperature boundary condition at finite Prandtl number. *Phys. Fluids*, 8: 1141-1148, 1996. doi: 10.1063/1.868914

Zijderveld, J.D.A., The natural remanent magnetizations of the exeter volcanic traps (Permian, Europe). *Tectonophysics*, 4: 121 - 153, 1967. doi:

APPENDICES

APPENDIX A

This section summarises some studies from the TAFI project:

Stone and Layer (2006) collected lava flow samples from six localities of Aleutian Islands, Alaska. The study was initiated in 1968 to investigate the persistence of the low secular variation in the Pacific Ocean over geological time. Samples are normally magnetised and the ^{40}Ar/^{39}Ar dating yields numerical ages of 50 ka to 2 Ma. One study area shows significantly high secular variation and was excluded from the mean direction determination. The mean direction of Dec = 356.3°, Inc = 68.7° with α_{95} of 2.0° derived from 49 lava flows shows an agreement with the GAD inclination of 70.0° predicted for 54°N.

Mejia et al. (2002) performed palaeomagnetic measurements on lava flow samples from five volcanic fields located in British Columbia, Canada (51.5°N). They improved the number of samples used in palaeodirection calculation by collecting approximately 8 to 10 cores per lava flow. This number satisfies the minimum requirement of the modern time-averaged field study (Tauxe et al., 2010). More than five specimens per site were used to determine the site mean direction. They found the mean direction of Dec = 356.9°, Inc = 70.2° with α_{95} of 2.8°, which deviate approximate 1.9° from the GAD field at British Columbia during 0.76 Ma.

Tauxe et al. (2004) sampled the Pliocene to Recent basaltic lava flows of the Snake River Plain in northwest US. All 23 sites were normally magnetised and the ^{40}Ar/^{39}Ar ages are approximately 0-5 Ma. The mean direction of the study is Dec = 4.4°, Inc = 59.2° with and α_{95} of 5.0°. These directions are slightly shallower than a GAD field of 62°.

Johnson et al. (1998) conducted a palaeomagnetic experiment on 28 lava flows in the São Miguel, Azores. Rock were dated using ^{40}Ar/^{39}Ar geochronology. All sites are of 0.78-0.88 Ma age, and are normally magnetised. The mean direction for normal polarity data is Dec = 359.1°, Inc = 52.6°, with α_{95} of 7.2°. These directions are indistinguishable from a GAD field of 57.2°. However, the mean direction for reverse polarity is Dec = 175.8°, Inc = -43.7°, with α_{95} of 7.6°. These directions show a large deviation from the reverse GAD (-57.2°) at Azores.

Tauxe et al. (2000) collected samples from the La Palma in the Canary Islands. The time span of their data is approximately 0-2 Ma. The mean normal directions derived from 9 sites are Dec = 355.1° and Inc = 46.6°, with α_{95} of 9.6°. The GAD inclination predicted for La Palma is approximately 47.0°. It is clear that the normal polarity data is indistinguishable with the GAD field. With regards to the reverse polarity data, the mean direction derived from a total of 12 sites is Dec = 180.9°, Inc = -39.1°, with α_{95} of 8.4°. It is clearly seen that the reverse inclination is significantly lower than the reverse GAD.

Mejia et al. (2005) sampled the Pliocene-Holocene lava flows from the Trans-Mexican Volcanic Belt (TMVB) areas in Mexico. All 13 sites were normally magnetised and the ^{40}Ar/^{39}Ar ages are approximately 0-2 Ma. They combined their dataset with several studies in the TMVB to improve spatial coverage of the data. The mean direction derived from 187 sites yields Dec = 358.8°, Inc = 31.6°, with α_{95} of 2.0°. The GAD inclination for the TMVB areas is approximately 34.9°. It is clear that their results show significant departure from the GAD hypothesis with no overlap of 95% confidence limit. They reported a 5% of axial quadrupole field which contributes to the time-averaged field during 0-2 Ma recorded in the TMVB areas.

Opdyke et al. (2006) performed a palaeomagnetic experiment on 70 lava flows from Ecuador. Rock were dated using the ^{40}Ar/^{39}Ar method. All sites are of 0-2.6 Ma age, and are normally magnetised. The mean direction for normal polarity data is Dec = 359.9°, Inc = -5.4°, with α_{95} of 4.2°. These directions are distinguishable from the GAD inclination of ~-0.3° near the equator and in agreement with the GAD field with 5% of the axial quadrupole.

Opdyke and Musgrave (2004) conducted a palaeomagnetic experiment on 42 lava flows from Newer Volcanic Province of Victoria, Australia. The K/Ar dating indicates the ages of their samples are approximately 0-5 Ma, with a high concentration at 2.0-2.75 Ma. Of these, 33 sites yielded successful palaeomagnetic measurements and provided the mean direction of Dec = 356.3°, Inc = -57.7°, with α_{95} of 3.5°, which is in agreement of the GAD inclination of approximately -57°.

Brown et al. (2004) sampled the late Miocene to late Pleistocene lava flows of Meseta del Lago Buenos Aires in Patagonia. All sites were normally magnetised and the ^{40}Ar/^{39}Ar ages are approximately 0-3.3 Ma. The mean direction for 26 sites is Dec = 3.4°, Inc = -63.0° with α_{95} of 5.4°, which is indistinguishable from the GAD inclination for Patagonia (~-65°)

Mejia et al. (2004) performed a palaeomagnetic measurement on 53 lava flows of the Pali-Aike Volcanic Field and the Meseta Vischas plateau lavas. A total of 33 lava flows provide discrete ages during the time span of 0-4 Ma. The mean direction derived from 33 lava flows is Dec = 358.7°, Inc = -68.2° with α_{95} of 5.0°. This result is in an agreement with the GAD inclination of -68.1° at Patagonia.

Opdyke et al. (2010) sampled the Pliocene-Pleistocene lavas of Mount Kenya and Loiyangalani in Kenya. A total of 132 sites from two study areas provides the discrete ages of 0-5.78 Ma. Of these, a total of 69 sites in Mount Kenya yielded the mean direction of Dec = 1.4°, Inc = -0.7° and α_{95} = 3.2°. With regards to the Loiyangalani site, the mean direction determined from 32 sites is Dec = 1.1°, Inc =

-1.0° with α_{95} of 4.1°. The expected GAD inclination for these localities are approximately 0°. These mean directions are indistinguishable from the GAD field.

Opdyke et al. (2015) compiled palaeomagnetic directions from a total of 42 Miocene lava flows of Sao Tome. The $^{40}Ar/^{39}Ar$ shows the time span of these 42 sites are approximately 0-5 Ma. The mean direction of the study is Dec = 358.4°, Inc = -6.3° with $\alpha_{95}$of 4.1°. This direction shows significant departure from the GAD inclination of 0.6°.

APPENDIX B

Figure B-1 to B-10 present isochron and age spectrum (lower Figure) diagrams of dated 10 samples. Raw data are given in the tables on page 268-293.

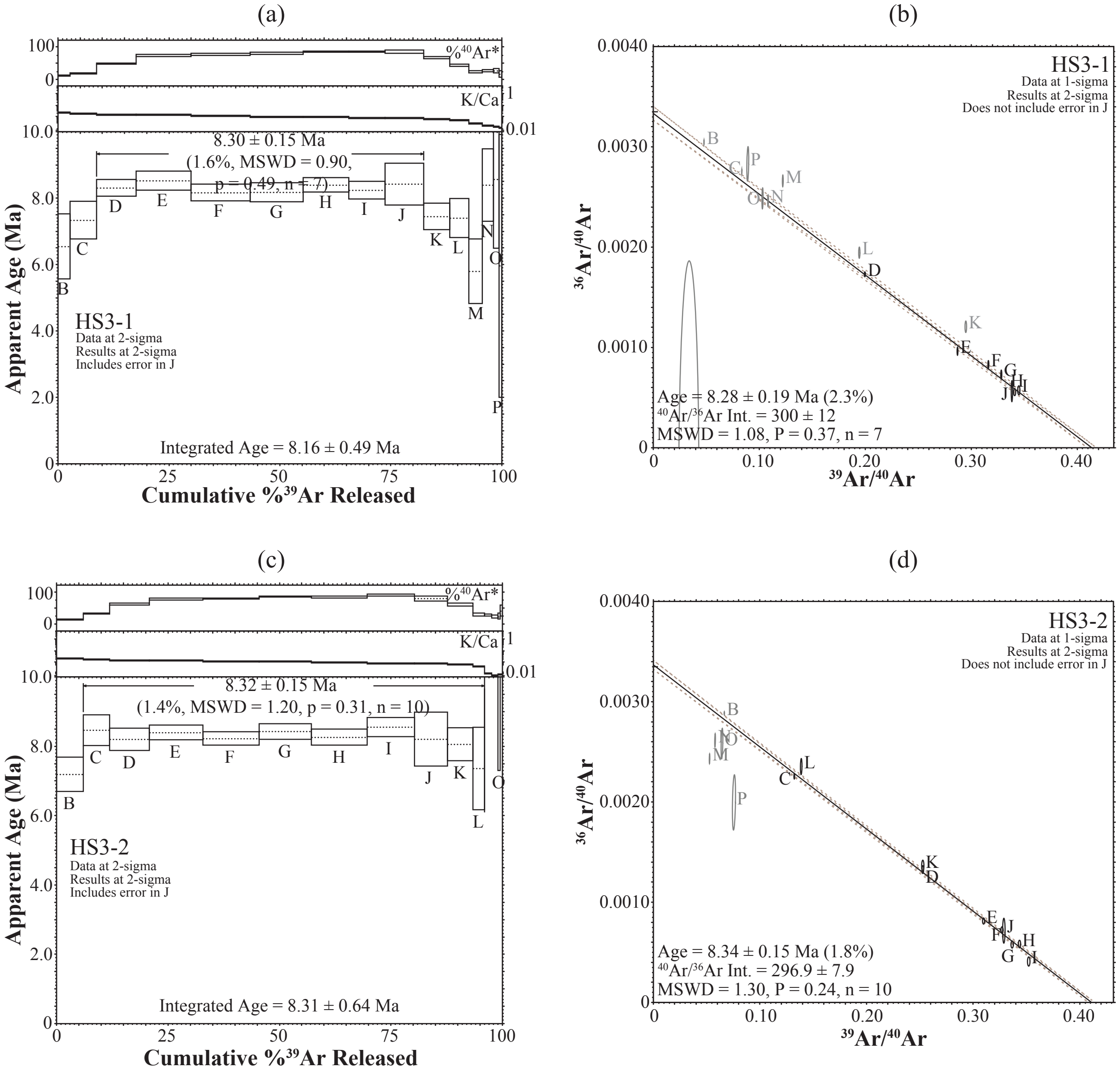

Figure B-1: (a) and (b) isochron and age spectrum diagrams for sample HS3 from step-up heating. (c) and (d) replicated isochron and age spectrum diagrams for sample HS3. Integrated age (total fusion age) is also marked in the age spectrum diagrams.

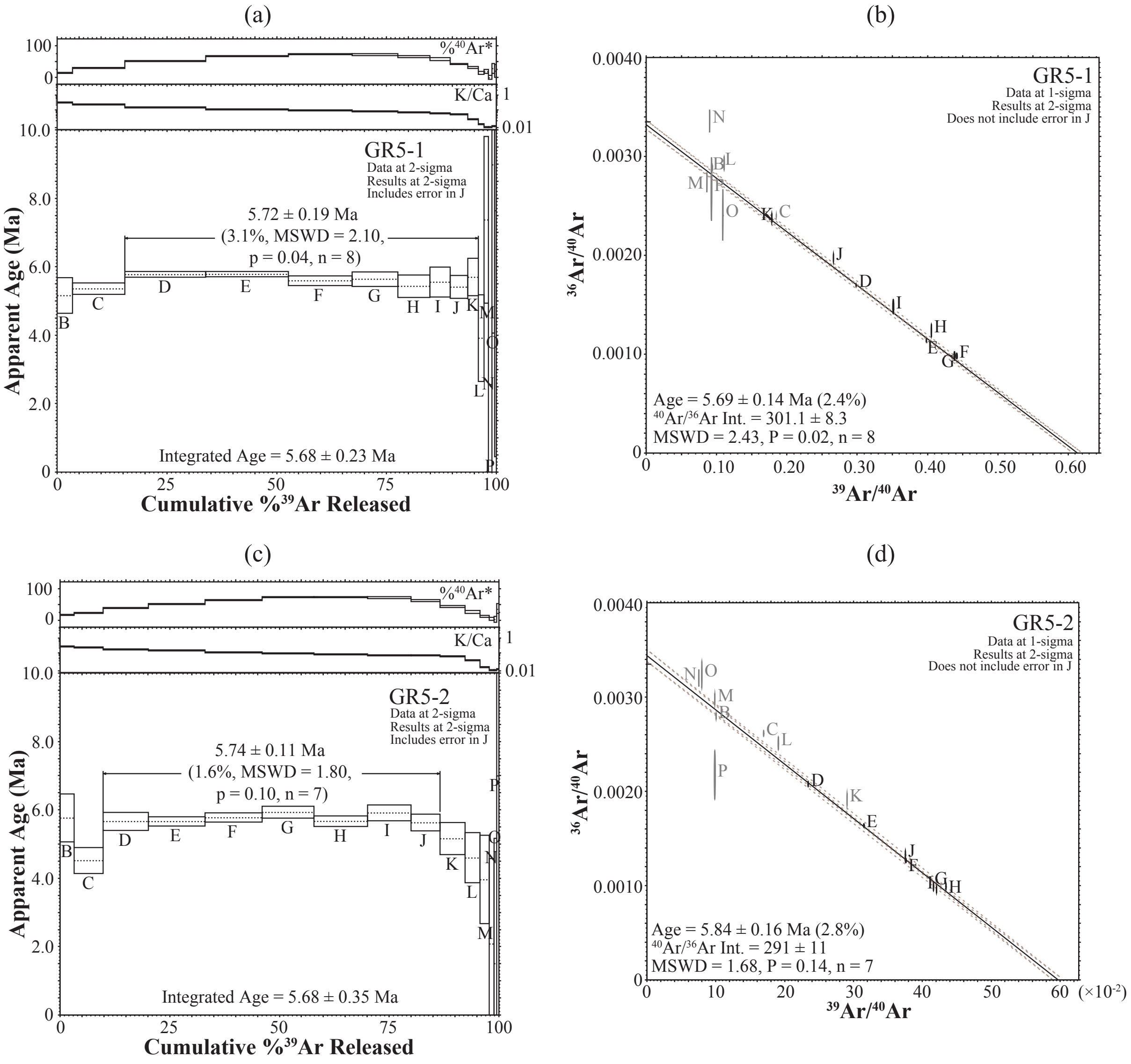

Figure B-2: (a) and (b) isochron and age spectrum diagrams for sample GR5 from step-up heating. (c) and (d) replicated isochron and age spectrum diagrams for sample GR5. Integrated age (total fusion age) is also marked in the age spectrum diagrams.

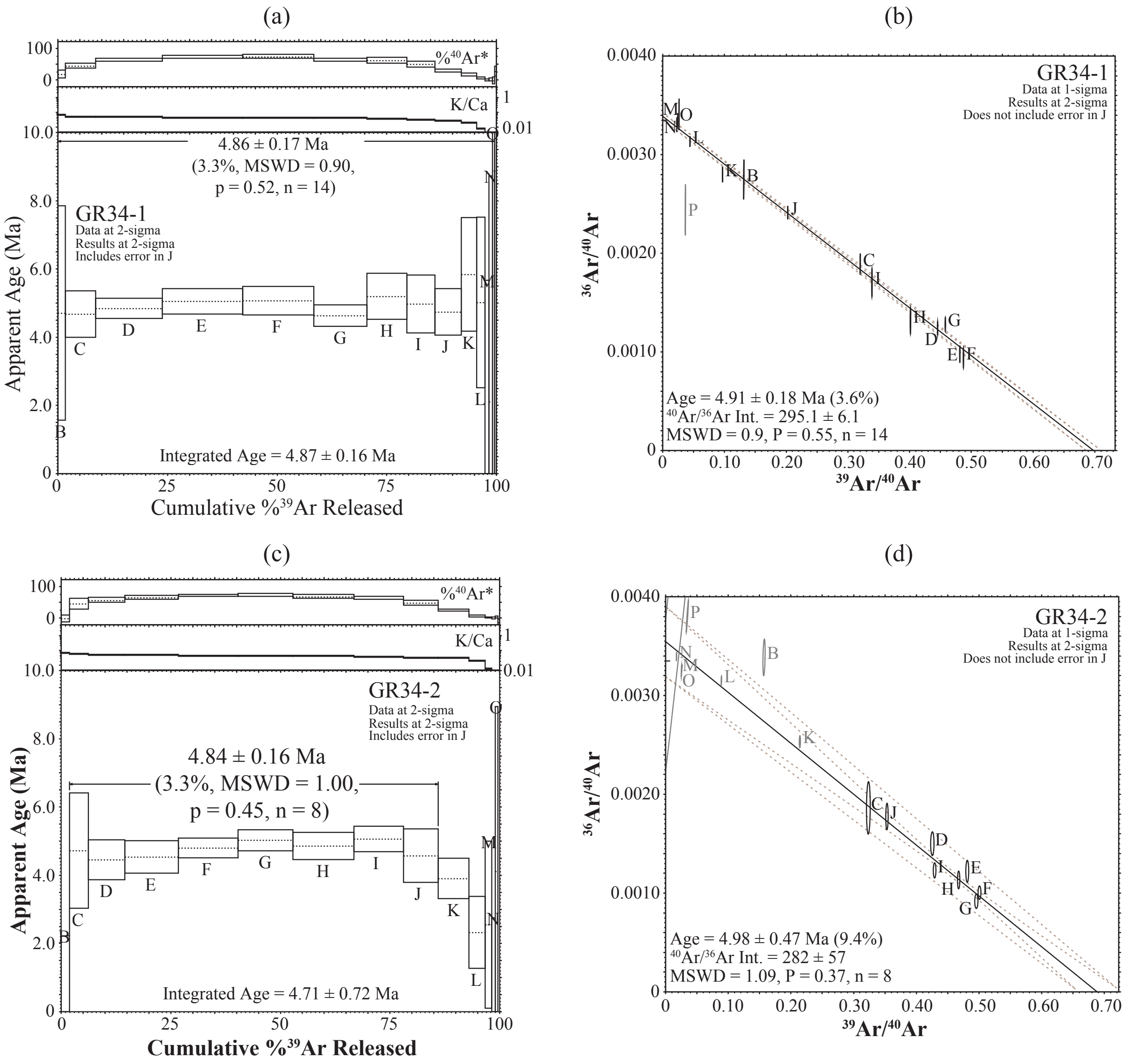

Figure B-3: (a) and (b) isochron and age spectrum diagrams for sample GR34 from step-up heating. (c) and (d) replicated isochron and age spectrum diagrams for sample GR34. Integrated age (total fusion age) is also marked in the age spectrum diagrams.

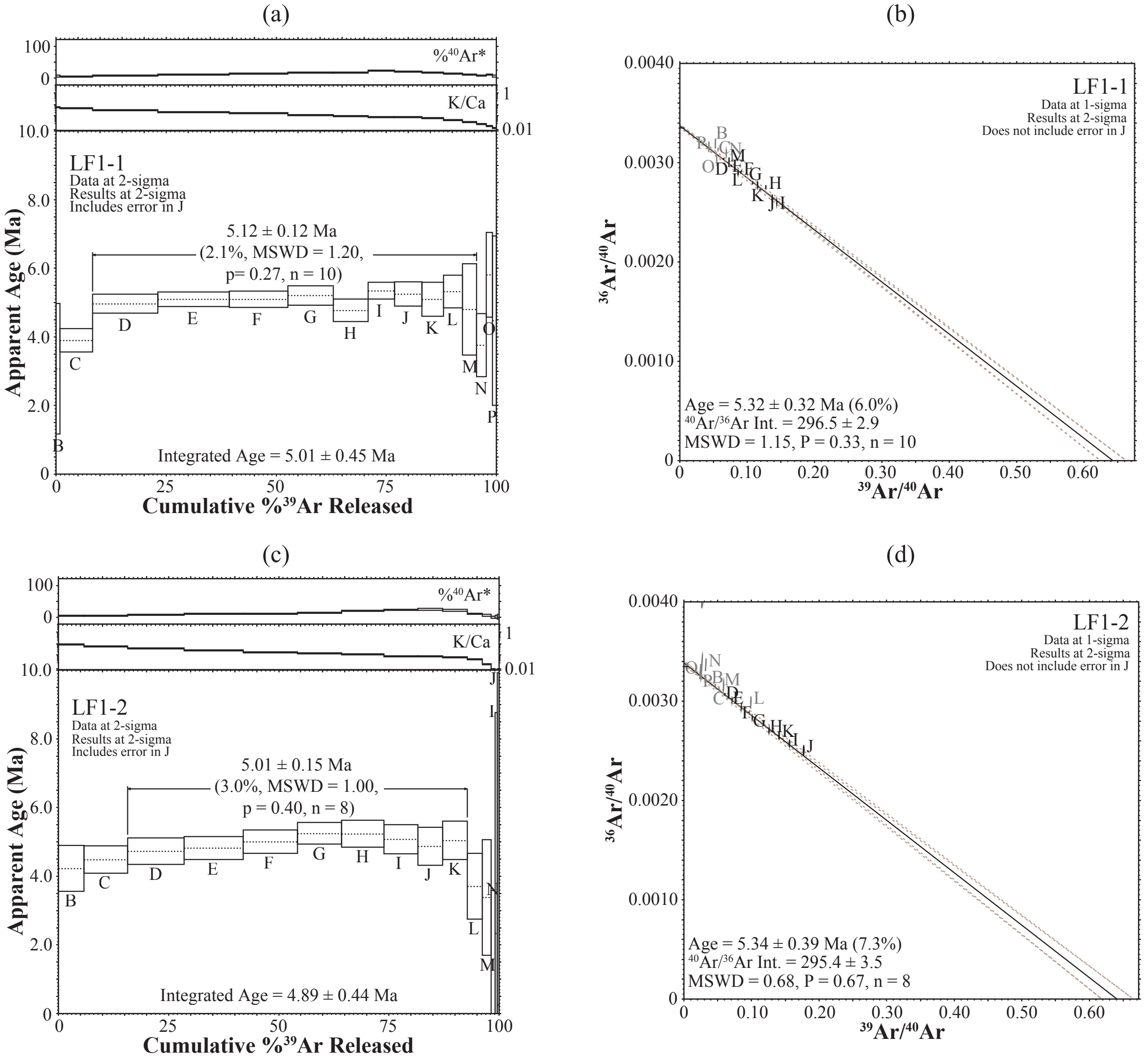

Figure B-4: (a) and (b) isochron and age spectrum diagrams for sample LF1 from step-up heating. (c) and (d) replicated isochron and age spectrum diagrams for sample LF1. Integrated age (total fusion age) is also marked in the age spectrum diagrams.

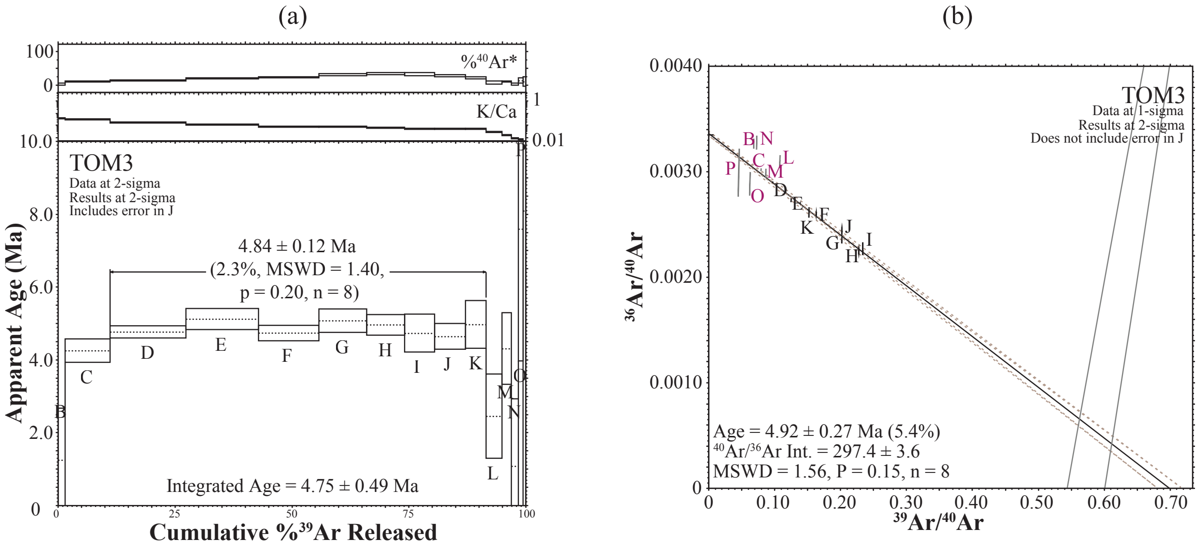

Figure B-5: (a) and (b) isochron and age spectrum diagrams for sample TO-3 from step-up heating. Integrated age (total fusion age) is also marked in the age spectrum diagram.

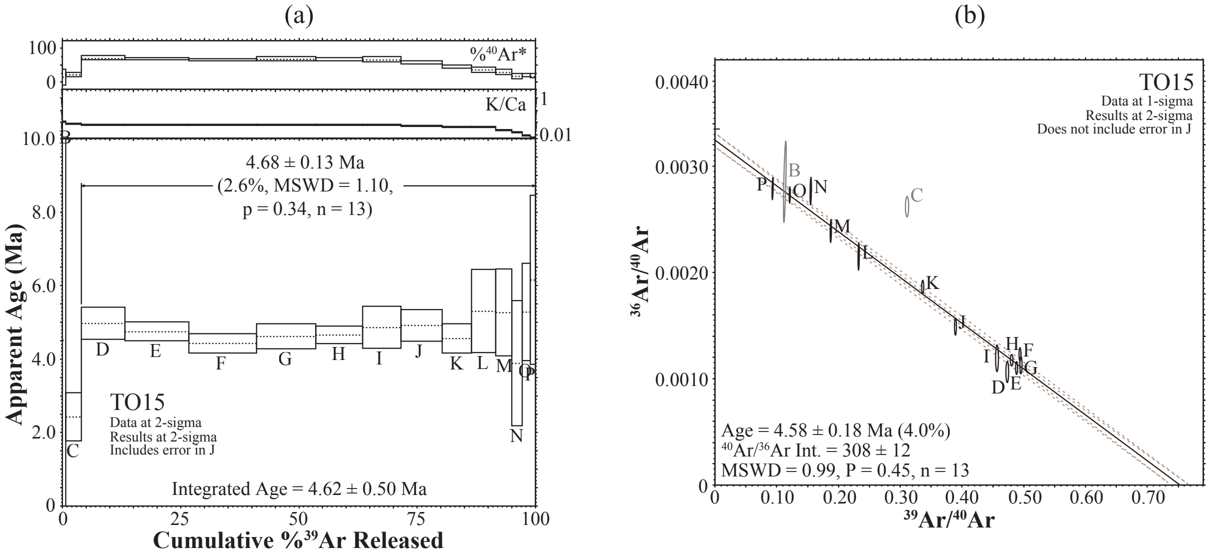
(a) (b)

Figure B-6: (a) and (b) isochron and age spectrum diagrams for sample TO15 from step-up heating. Integrated age (total fusion age) is also marked in the age spectrum diagram.

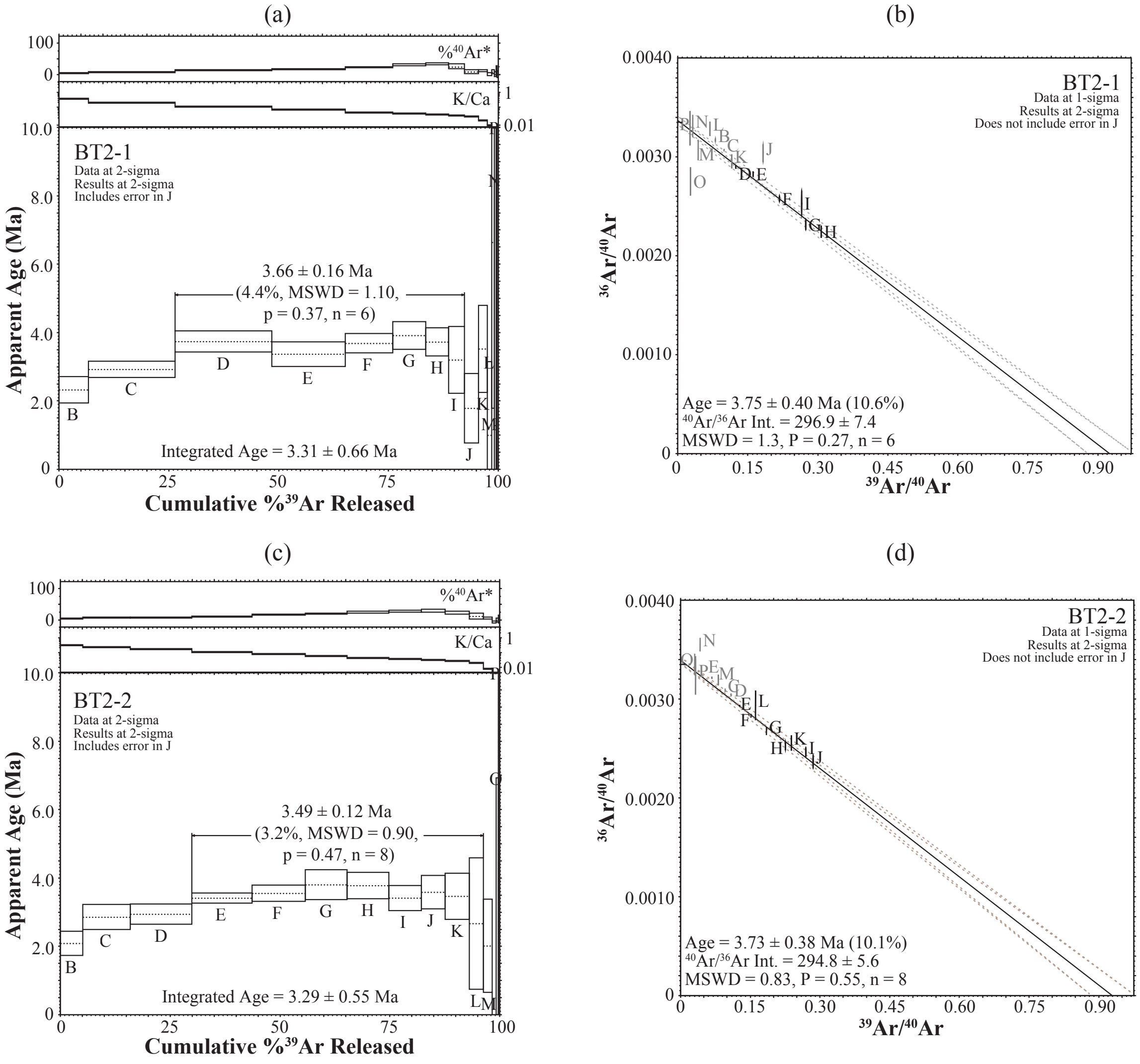
(a)

(b)

(c)

(d)

Figure B-7: (a) and (b) isochron and age spectrum diagrams for sample BT2 from step-up heating. (c) and (d) replicated isochron and age spectrum diagrams for sample BT2. Integrated age (total fusion age) is also marked in the age spectrum diagrams.

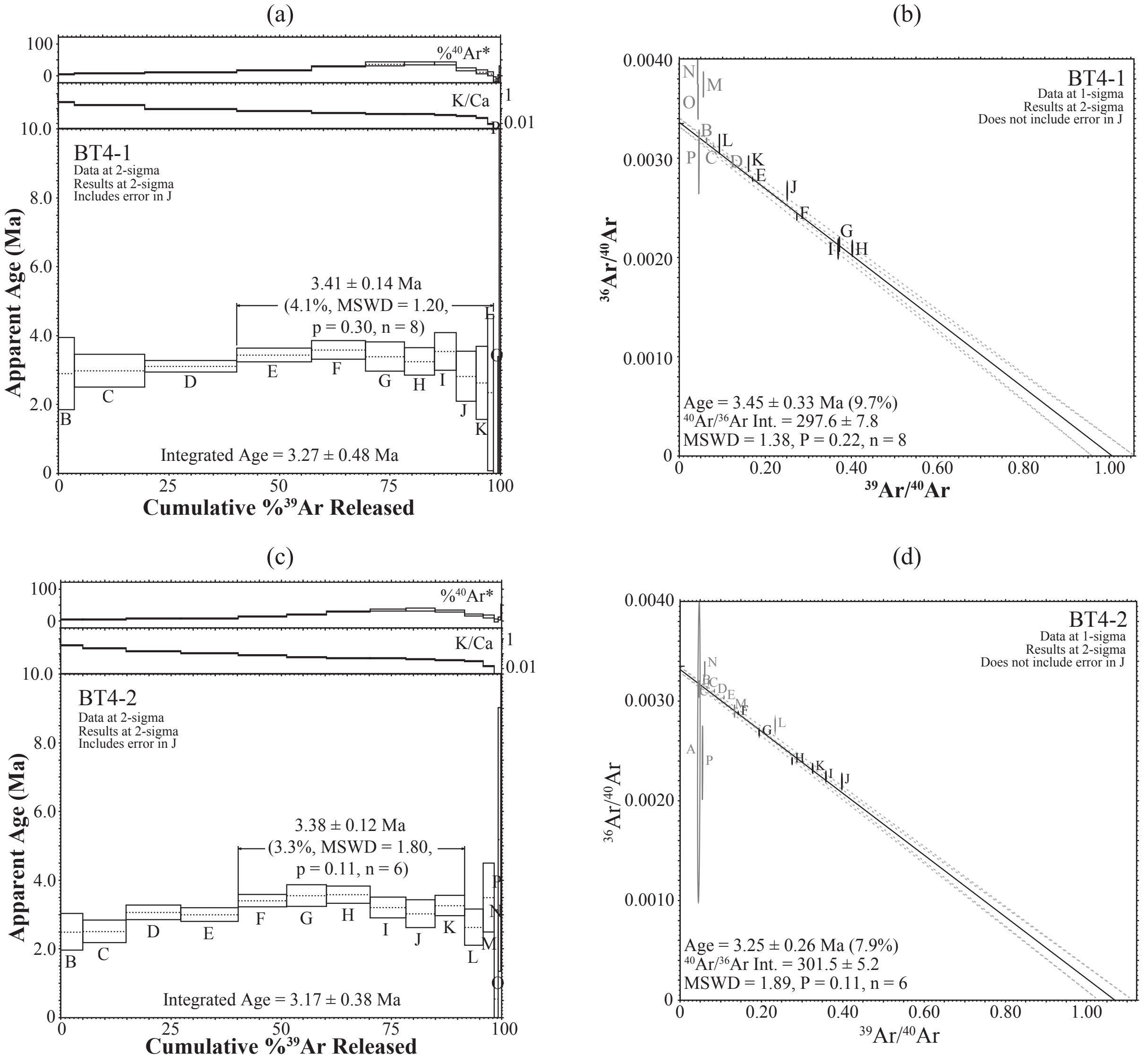

Figure B-8: (a) and (b) isochron and age spectrum diagrams for sample BT4 from step-up heating. (c) and (d) replicated isochron and age spectrum diagrams for sample BT4. Integrated age (total fusion age) is also marked in the age spectrum diagrams.

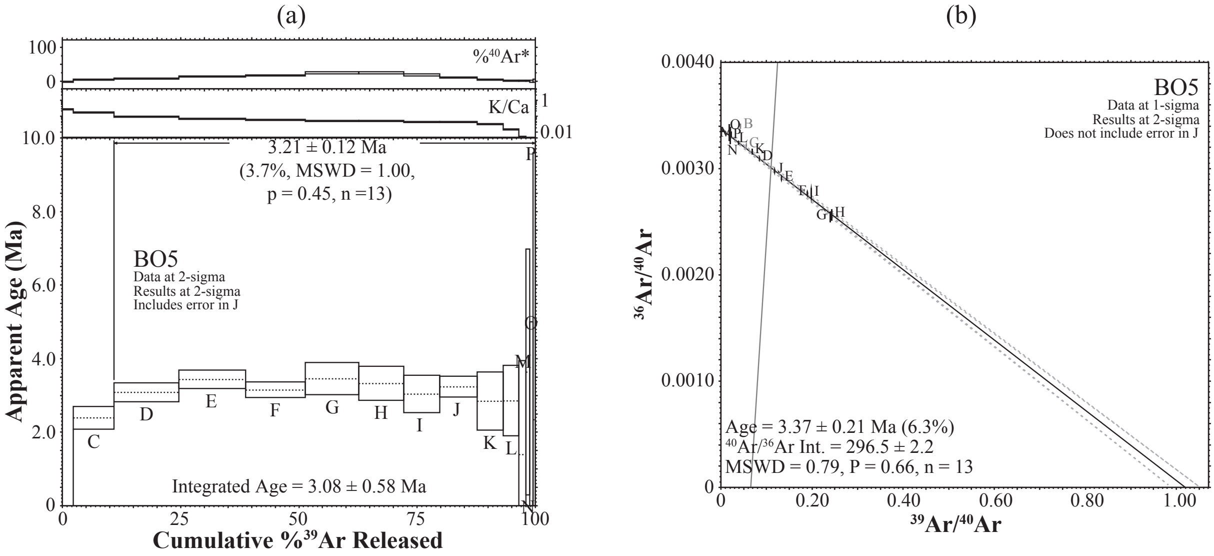

Figure B-9: (a) and (b) isochron and age spectrum diagrams for sample BO5 from step-up heating. Integrated age (total fusion age) is also marked in the age spectrum diagram.

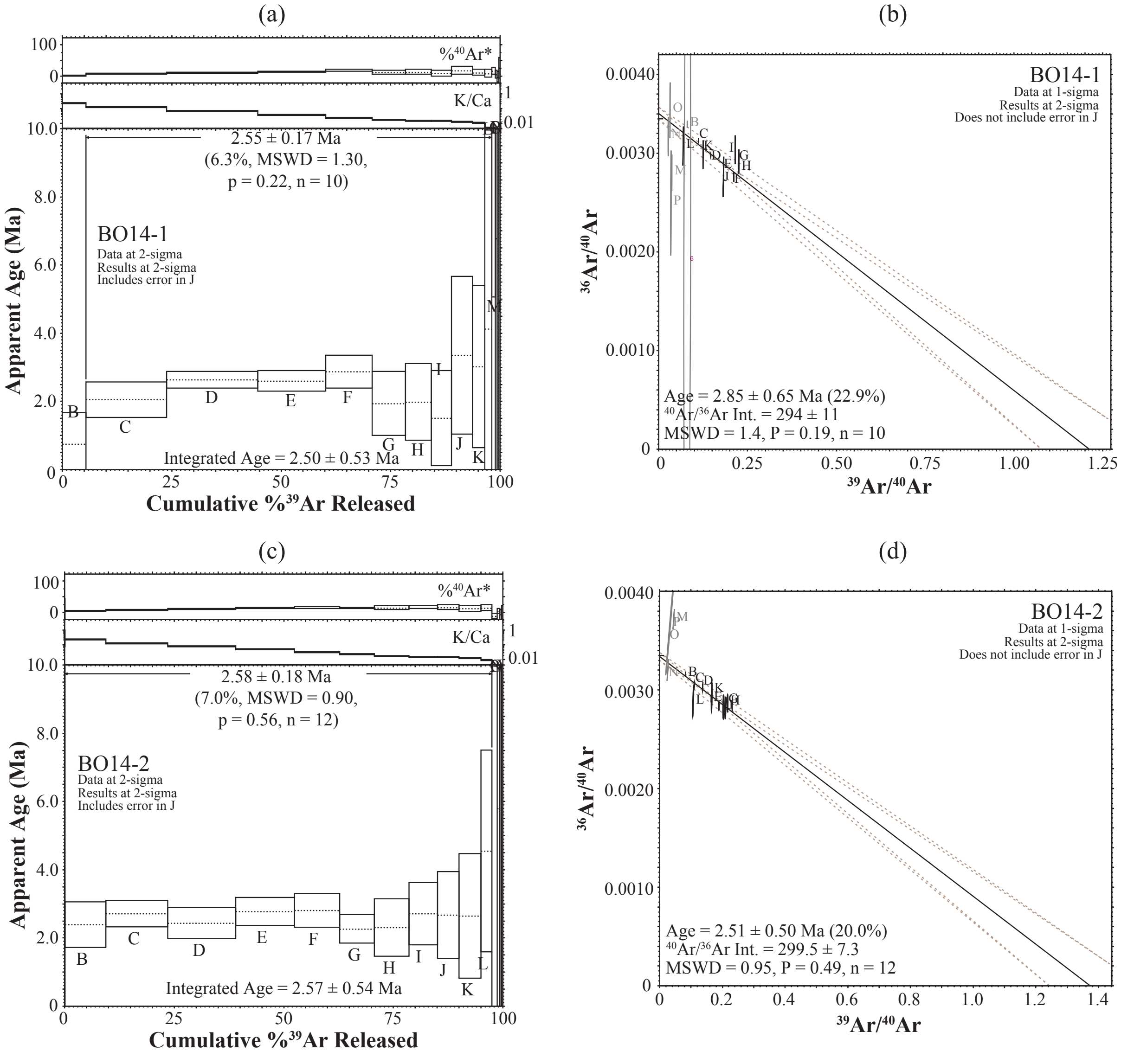

Figure B-10: (a) and (b) isochron and age spectrum diagrams for sample BO14 from step-up heating. (c) and (d) replicated isochron and age spectrum diagrams for sample BO14. Integrated age (total fusion age) is also marked in the age spectrum diagrams.

VA1 Raw Data

Plateau Age

Run_ID	^{36}Ar/^{39}Ar	^{37}Ar/^{39}Ar	Ca/K	Cl/K	^{38}Ar/^{39}Ar	^{40}Ar/^{39}Ar	^{40}Ar*/^{39}Ar	^{40}Ar* (%)	Age (Ma)	±2σ (Ma)	^{39}Ar (×10^{-17} mol)
93016-1A	-0.12128	13.29565	26.30207	2.049435	0.68896	-3.2428	34.38046	-1050.18	115.3656	115.37	115.37
93016-1B	0.037058	2.79169	5.48191	-0.01802	0.012876	12.00213	1.159989	9.646695	4.014811	4.01	4.01
93016-1C	0.013439	3.234692	6.353841	-0.00029	0.014508	5.632505	1.879627	33.30037	6.50106	6.50	6.50
93016-1D	0.004263	3.667511	7.20625	-0.00085	0.012568	3.235892	2.258372	69.62913	7.808198	7.81	7.81
93016-1E	0.003186	4.103451	8.065327	-0.00041	0.0125	2.834048	2.213192	77.89027	7.652319	7.65	7.65
93016-1F	0.002785	4.42604	8.701366	-0.00231	0.011758	2.660475	2.18502	81.89872	7.555115	7.56	7.56
93016-1G	0.002434	4.659619	9.162084	-0.0008	0.012202	2.617138	2.265564	86.31016	7.833011	7.83	7.83
93016-1H	0.002588	4.817417	9.473417	-0.00089	0.012197	2.613571	2.22879	85.01571	7.706135	7.71	7.71
93016-1I	0.002638	4.910704	9.657502	-0.00076	0.012247	2.603667	2.21147	84.67053	7.646378	7.65	7.65
93016-1J	0.002368	5.015699	9.864718	0.000494	0.012621	2.622591	2.319921	88.17524	8.020528	8.02	8.02
93016-1K	0.00293	5.187258	10.20337	0.002272	0.013332	2.746156	2.28927	83.0842	7.914793	7.91	7.91
93016-1L	0.00486	6.836009	13.4621	0.00048	0.013015	3.156044	2.256044	71.16004	7.800165	7.80	7.80
93016-1M	0.010467	16.01955	31.75138	0.000509	0.013725	3.918586	2.083354	52.58373	7.204286	7.20	7.20
93016-1N	0.015814	33.61803	67.46724	0.002556	0.014736	4.590305	2.588587	55.08347	8.947078	8.95	8.95
93016-1O	0.019627	40.8589	82.42358	-0.00498	0.012644	4.605153	2.03491	42.9395	7.037092	7.04	7.04
93016-1P	0.023682	45.86132	92.84712	-0.01392	0.010236	4.65563	1.252622	26.05192	4.335037	4.34	4.34

Plateau calculation

Steps	N	Ca/K	MSWD	^{39}Ar (%)	^{39}Ar (mol)	Age (Ma)	±2σ (Ma)
D-O	12	28.28 ± 20.34	1.5	95.4	6.73 × 10^{-16}	7.77	0.15

Isochron Age

Isochron age (Ma)	±2σ w/o J	±2σ w/J	n	MSWD	p	^{40}Ar/^{36}Ar$_{(i)}$	±2σ
7.788497	0.147576	0.17217	12	1.673	0.081	294.5	22.8

VA15 Raw Data

Plateau Age

Run_ID	^{36}Ar/^{39}Ar	^{37}Ar/^{39}Ar	Ca/K	Cl/K	^{38}Ar/^{39}Ar	^{40}Ar/^{39}Ar	^{40}Ar*/^{39}Ar	^{40}Ar* (%)	Age (Ma)	±2σ (Ma)	^{39}Ar (×10^{-17} mol)
93015-1A	0.333630	-4.86967	-9.51279	-0.09744	0.041581	18.40456	-81.3172	-443.345	-307.27	116.61	0.01
93015-1B	0.043979	0.734864	1.44063	0.003260	0.021587	15.59961	2.527867	16.19716	8.76	0.51	2.03
93015-1C	0.025915	0.865898	1.697743	0.003241	0.018169	9.949511	2.281671	22.92038	7.91	0.13	11.80
93015-1D	0.016694	1.230676	2.413751	0.002803	0.016265	7.193255	2.30788	32.05976	8.00	0.05	19.70
93015-1E	0.012956	2.065046	4.052868	0.002903	0.015562	6.016323	2.314208	38.41494	8.02	0.06	16.86
93015-1F	0.011128	3.366375	6.613128	0.003523	0.015379	5.370168	2.31891	43.08616	8.04	0.08	11.49
93015-1G	0.010028	4.773588	9.386936	0.002934	0.014914	4.901216	2.291873	46.61309	7.95	0.10	7.46
93015-1H	0.009587	5.960353	11.73045	0.004752	0.015408	4.564423	2.182122	47.61672	7.57	0.18	5.26
93015-1I	0.00925	6.683895	13.16113	0.00277	0.014635	4.471164	2.248066	50.05378	7.80	0.14	3.90
93015-1J	0.009896	7.335482	14.45078	0.002476	0.014631	4.398523	2.034025	46.01521	7.05	0.15	3.83
93015-1K	0.009439	8.417738	16.59542	0.003325	0.014792	4.477493	2.338477	51.93026	8.11	0.25	2.81
93015-1L	0.013964	12.50654	24.7273	0.008218	0.017156	4.945788	1.781182	35.70631	6.18	0.46	2.27
93015-1M	0.018526	24.7814	49.42232	0.003687	0.015980	5.501654	1.964378	35.09486	6.81	0.56	1.50
93015-1N	0.025706	39.23791	79.06191	0.005319	0.017307	5.554701	1.011204	17.7103	3.51	0.64	1.22
93015-1O	0.023434	44.20564	89.3889	0.011989	0.018908	5.099532	1.650984	31.38491	5.73	0.94	1.06
93015-1P	0.024148	47.04622	95.32707	0.013760	0.019515	5.085038	1.651177	31.41393	5.73	1.05	0.81
Plateau calculation											
Steps	N	Ca/K		MSWD	^{39}Ar (%)	^{39}Ar (mol)			Age (Ma)	±2σ (Ma)	
N-I	8	10.26 ± 5.49		1.6	85.5	7.85 × 10^{-16}			7.98	0.15	

Isochron Age

Isochron age (Ma)	±2σ w/o J	±2σ w/J	n	MSWD	p	^{40}Ar/^{36}Ar$_{(i)}$	±2σ
7.876818	0.194381	0.215228	8	1.586	0.147	300.8	3.9

HS3-1 Raw Data

Plateau Age

Run_ID	$^{36}Ar/^{39}Ar$	$^{37}Ar/^{39}Ar$	Ca/K	Cl/K	$^{38}Ar/^{39}Ar$	$^{40}Ar/^{39}Ar$	$^{40}Ar^{*}/^{39}Ar$	$^{40}Ar^{*}$ (%)	Age (Ma)	±2σ (Ma)	^{39}Ar (×10^{-17} mol)
93009-1A	-0.010342	3.128303	6.144394	0.4873468	0.1778074	29.6892	33.1059	111.2685	110.30	70.87	0.01
93009-1B	0.0637344	2.066749	4.056215	-0.000647	0.0239137	20.76908	1.906041	9.164442	6.54	0.49	1.86
93009-1C	0.0334777	2.778323	5.455608	0.0022528	0.0191794	11.90891	2.137047	17.91138	7.33	0.28	3.95
93009-1D	0.0095269	3.422747	6.72414	-0.002032	0.0131643	4.990201	2.421637	48.41948	8.30	0.13	5.87
93009-1E	0.0043312	3.770373	7.408906	-0.001583	0.0123257	3.474436	2.485346	71.35988	8.52	0.15	8.15
93009-1F	0.0037638	4.349181	8.549799	-0.002565	0.0118589	3.152986	2.379774	75.26608	8.16	0.13	8.83
93009-1G	0.0035573	5.085179	10.00186	-0.000950	0.0123467	3.035113	2.383047	78.2572	8.17	0.14	7.88
93009-1H	0.0031471	5.766634	11.34764	-0.001308	0.0121202	2.921098	2.44677	83.44707	8.39	0.11	6.79
93009-1I	0.0033417	6.373629	12.54746	-0.000557	0.0123914	2.884959	2.401416	82.89135	8.23	0.13	5.45
93009-1J	0.0034615	6.810103	13.41084	0.0002266	0.0126659	2.93974	2.455977	83.16917	8.42	0.31	5.77
93009-1K	0.0060521	7.517545	14.81133	0.0013512	0.0135126	3.371383	2.169863	64.03873	7.44	0.20	3.87
93009-1L	0.0124734	9.648053	19.0374	0.0021215	0.0149037	5.103369	2.156402	41.97712	7.39	0.29	2.86
93009-1M	0.0268526	20.64132	41.04537	0.0014211	0.0169441	8.048677	1.688176	20.67553	5.79	0.48	2.05
93009-1N	0.0309332	33.04629	66.29284	0.0055643	0.0186232	9.012108	2.446855	26.52928	8.39	0.54	1.71
93009-1O	0.034398	41.52993	83.81748	0.0098819	0.0203815	9.409737	2.497193	25.77436	8.56	1.04	0.83
93009-1P	0.0426931	45.25372	91.57708	0.0052695	0.0202516	10.84908	1.737038	15.50837	5.96	1.98	0.40
Plateau calculation											
Steps	N	Ca/K		MSWD	^{39}Ar (%)	^{39}Ar (mol)			Age (Ma)	±2σ (Ma)	
D-J	7	10.66 ± 2.49		0.9	73.7	4.88×10^{-16}			8.3	0.15	

Isochron Age

Isochron age (Ma)	±2σ w/o J	±2σ w/J	n	MSWD	p	$^{40}Ar/^{36}Ar_{(i)}$	±2σ
8.282795	0.172149	0.189908	7	1.079	0.369	300	12.4

HS3-2 Raw Data

Plateau Age

Run_ID	^{36}Ar/^{39}Ar	^{37}Ar/^{39}Ar	Ca/K	Cl/K	^{38}Ar/^{39}Ar	^{40}Ar/^{39}Ar	^{40}Ar*/^{39}Ar	^{40}Ar* (%)	Age (Ma)	±2σ (Ma)	^{39}Ar (×10^{-17} mol)
93009-2A	-0.031172	1.812181	3.555914	-0.017144	0.0003484	24.26762	33.75915	138.9409	112.41	16.00	0.05
93009-2B	0.0439134	2.517572	4.94265	0.0018798	0.0210289	15.00443	2.095795	13.94408	7.19	0.25	3.50
93009-2C	0.0178705	3.281514	6.446031	0.0007115	0.0156867	7.539467	2.46857	32.67046	8.46	0.22	3.49
93009-2D	0.0061791	3.59573	7.064848	-0.001540	0.0126956	3.946304	2.391165	60.45226	8.20	0.16	5.19
93009-2E	0.003637	3.893429	7.651385	-0.002199	0.0119785	3.219989	2.448005	75.83672	8.39	0.10	6.99
93009-2F	0.0033448	4.301952	8.45667	-0.001993	0.0119786	3.049218	2.397317	78.40437	8.22	0.10	7.36
93009-2G	0.0030104	4.914159	9.664319	-0.002749	0.0116319	2.96027	2.457873	82.76544	8.42	0.11	6.80
93009-2H	0.0031805	5.668758	11.15427	-0.002258	0.0118038	2.900735	2.40837	82.71982	8.25	0.12	7.33
93009-2I	0.002865	6.462376	12.72296	-0.001441	0.0119946	2.828359	2.494702	87.82959	8.55	0.14	6.21
93009-2J	0.0040838	7.275488	14.33199	0.0026689	0.013603	3.024537	2.392332	78.71641	8.20	0.39	4.33
93009-2K	0.007531	8.249879	16.26257	0.0050112	0.0150175	3.932252	2.349362	59.41438	8.05	0.24	3.29
93009-2L	0.0202442	13.04578	25.80325	0.0078795	0.0182025	7.138734	2.145703	29.78769	7.36	0.60	1.53
93009-2M	0.0565302	45.87538	92.87652	-0.001078	0.0207166	18.26453	5.180892	27.46254	17.71	0.95	0.99
93009-2N	0.0608778	68.78845	141.5943	0.0037492	0.0222372	16.33527	3.782229	22.04777	12.95	1.17	0.81
93009-2O	0.0551163	63.63924	130.5046	0.0101525	0.0234658	14.81725	3.553467	22.92233	12.17	2.44	0.36
93009-2P	0.0406537	58.40143	119.309	0.0243687	0.0256581	12.64088	5.340558	40.53575	18.25	3.74	0.25

Plateau calculation

Steps	N	Ca/K	MSWD	^{39}Ar (%)	^{39}Ar (mol)	Age (Ma)	±2σ (Ma)
C-L	17	13.96 ± 3.65	1.2	90	5.25×10^{-16}	8.32	0.15
Composite plateau age (HS3 (1) and HS3 (2))							
C-L	17	11.96 ± 1.96	1.0	100	1.01×10^{-15}	8.31	0.13

Isochron Age

Isochron age (Ma)	±2σ w/o J	±2σ w/J	n	MSWD	p	^{40}Ar/^{36}Ar$_{(i)}$	±2σ
8.33945	0.122279	0.146525	10	1.301	0.238	296.9	7.9
Composite isochron age (HS3 (1) and HS3 (2))							
8.320193	0.098662	0.127365	17	1.073	0.376	297.8	6.7

HS15-1 Raw Data

Plateau Age

Run_ID	^{36}Ar/^{39}Ar	^{37}Ar/^{39}Ar	Ca/K	Cl/K	^{38}Ar/^{39}Ar	^{40}Ar/^{39}Ar	^{40}Ar*/^{39}Ar	^{40}Ar* (%)	Age (Ma)	±2σ (Ma)	^{39}Ar (×10^{-17} mol)
93008-1A	-0.438382	1.208714	2.370631	4.794383	1.581281	-31.8982	99.26527	-310.925	312.54	361.59	0.00
93008-1B	0.0365977	1.930486	3.788396	-0.003241	0.0179092	12.00179	1.22876	10.22502	4.22	0.48	1.01
93008-1C	0.012195	3.020517	5.932227	-0.000617	0.0141697	5.322303	1.923621	36.07172	6.60	0.11	3.22
93008-1D	0.0061779	4.643346	9.129983	-0.003989	0.0118135	3.552096	2.080889	58.40493	7.14	0.15	5.43
93008-1E	0.0053447	6.511367	12.81986	-0.003032	0.0119142	3.165068	2.09319	65.84999	7.18	0.12	6.43
93008-1F	0.0048978	8.312458	16.38665	-0.001494	0.0122885	2.929165	2.136107	72.52212	7.33	0.14	6.38
93008-1G	0.0062547	9.636961	19.01536	-0.002723	0.0120723	3.208703	2.117142	65.55414	7.26	0.17	5.52
93008-1H	0.0054386	10.52989	20.79029	0.0013384	0.0132745	2.879077	2.103119	72.53205	7.21	0.11	4.44
93008-1I	0.0061441	11.26241	22.24803	-0.000722	0.012674	2.972091	2.044002	68.2515	7.01	0.25	3.27
93008-1J	0.0071206	11.90141	23.52087	0.0000588	0.0131004	3.30316	2.135768	64.13758	7.33	0.40	3.27
93008-1K	0.0096627	13.76855	27.24664	0.0027392	0.0144225	4.053538	2.279115	55.69725	7.82	0.29	2.19
93008-1L	0.0188199	21.0133	41.79603	0.0143117	0.019795	6.039128	2.113217	34.48517	7.25	0.60	1.71
93008-1M	0.0324525	39.21859	79.02188	0.0058603	0.018761	8.381771	1.845356	21.41802	6.33	0.61	1.22
93008-1N	0.041283	59.13123	120.8638	-0.004820	0.0160931	10.00539	2.458524	23.56384	8.43	1.21	0.81
93008-1O	0.0523449	77.42365	160.3799	0.0095677	0.0221835	11.54431	2.157437	17.68377	7.40	1.39	0.46
93008-1P	0.064089	92.39254	193.5151	0.0026413	0.0215471	13.00407	1.259846	9.066467	4.33	2.73	0.25
Plateau calculation											
Steps	N	Ca/K		MSWD	^{39}Ar (%)	^{39}Ar (mol)			Age (Ma)	±2σ (Ma)	
D-P	13	42.73 ± 24.43		0.9	90.7	4.14 × 10^{-16}			7.23	0.15	

Isochron Age

Isochron age (Ma)	±2σ w/o J	±2σ w/J	n	MSWD	p	^{40}Ar/^{36}Ar$_{(i)}$	±2σ
7.257883	0.188856	0.200939	13	0.929	0.51	296.4	11.6

HS15-2 Raw Data

Plateau Age

Run_ID	$^{36}Ar/^{39}Ar$	$^{37}Ar/^{39}Ar$	Ca/K	Cl/K	$^{38}Ar/^{39}Ar$	$^{40}Ar/^{39}Ar$	$^{40}Ar*/^{39}Ar$	$^{40}Ar*$ (%)	Age (Ma)	±2σ (Ma)	^{39}Ar (×10^{-17} mol)
93008-2A	-0.087695	-4.90388	-9.57940	-0.005268	-0.005967	28.35204	53.96153	190.9804	176.56	156.58	0.01
93008-2B	0.0202001	2.344069	4.601432	-0.000126	0.0158741	7.287267	1.443386	19.77668	4.95	0.43	2.51
93008-2C	0.0084058	3.541946	6.958905	-0.001630	0.0130865	4.135471	1.909997	46.08015	6.55	0.21	3.52
93008-2D	0.0051056	4.744161	9.328876	-0.001691	0.0123973	3.252039	2.109228	64.65925	7.24	0.15	4.99
93008-2E	0.0046796	6.087116	11.98099	-0.001864	0.0122059	3.026173	2.118804	69.7365	7.27	0.13	5.93
93008-2F	0.0045717	7.54577	14.86724	-0.002127	0.0120392	2.900338	2.142877	73.51464	7.35	0.12	6.41
93008-2G	0.0046034	8.839112	17.4313	-0.000078	0.0126978	2.797876	2.135198	75.86581	7.32	0.12	5.76
93008-2H	0.0050212	9.855811	19.45018	-0.001219	0.0123465	2.816656	2.110994	74.45262	7.24	0.13	6.23
93008-2I	0.005348	10.93905	21.60435	0.0010391	0.013139	2.890103	2.174692	74.69286	7.46	0.15	4.86
93008-2J	0.0067531	12.14292	24.00225	0.0013381	0.0134591	3.161057	2.122781	66.60267	7.28	0.20	3.04
93008-2K	0.012491	14.87179	29.45269	0.0022215	0.0147356	4.328167	1.793322	41.01235	6.15	0.37	2.39
93008-2L	0.0255787	26.7777	53.47913	0.000242	0.0160645	7.288501	1.803174	24.28196	6.19	0.64	1.19
93008-2M	0.0716444	89.83302	187.7972	0.0241077	0.0300124	16.22553	2.072043	11.97347	7.11	1.01	0.74
93008-2N	0.1073908	170.3221	378.6536	0.0275688	0.0342129	20.29328	1.935319	8.408115	6.64	2.26	0.48
93008-2O	0.0973653	166.5236	369.1035	-0.012337	0.0203277	16.95333	1.196593	6.241531	4.11	3.70	0.31
93008-2P	0.0712554	144.4189	314.6415	0.0073274	0.0222981	13.24045	3.770579	25.62065	12.91	5.09	0.21
Plateau calculation											
Steps	N	Ca/K		MSWD	^{39}Ar (%)	^{39}Ar (mol)			Age (Ma)	±2σ (Ma)	
D-J	7	18.81 ± 3.01		0.3	76.9	3.72×10^{-16}			7.31	0.14	
Composite plateau age (HS15 (1) and HS15 (2))											
D-P	20	32.49 ± 11.59		0.7	100	7.86×10^{-16}			7.27	0.12	

Isochron Age

Isochron age (Ma)	±2σ w/o J	±2σ w/J	n	MSWD	p	$^{40}Ar/^{36}Ar_{(i)}$	±2σ
7.452748	0.519236	0.523996	7	0.313	0.905	283.7	54.3
Composite isochron age (HS15 (1) and HS15 (2))							
7.31856	0.142296	0.158231	20	0.713	0.801	294.6	10.9

HS22-1 Raw Data

Plateau Age

Run_ID	^{36}Ar/^{39}Ar	^{37}Ar/^{39}Ar	Ca/K	Cl/K	^{38}Ar/^{39}Ar	^{40}Ar/^{39}Ar	^{40}Ar*/^{39}Ar	^{40}Ar* (%)	Age (Ma)	±2σ (Ma)	^{39}Ar (×10^{-17} mol)
93005-1A	0.2499011	2.47	4.849085	-0.112775	0.020402	29.45135	-45.04418	-152.6856	-161.99	53.41	0.04
93005-1B	0.0389699	0.542349	1.062966	0.0086141	0.0224956	12.41123	0.8190339	6.597035	2.82	0.31	6.07
93005-1C	0.0164182	0.6145302	1.204555	0.0118117	0.0193428	5.861544	1.008281	17.19642	3.47	0.14	16.83
93005-1D	0.004159	0.7098193	1.391493	0.0026279	0.0138623	3.213149	2.027912	63.09613	6.96	0.08	23.42
93005-1E	0.0015313	0.7086547	1.389208	-0.002316	0.0116629	2.651495	2.250697	84.86561	7.73	0.06	34.80
93005-1F	0.000974	0.7444925	1.459521	-0.002835	0.0113778	2.474376	2.24284	90.62249	7.70	0.05	40.88
93005-1G	0.0007466	0.8167341	1.601269	-0.002566	0.0114246	2.384051	2.22622	93.3553	7.64	0.04	40.99
93005-1H	0.0006175	0.9029743	1.770502	-0.002663	0.0113637	2.323242	2.21091	95.13504	7.59	0.05	36.13
93005-1I	0.0006952	0.9777924	1.917337	-0.002536	0.0114192	2.294158	2.164625	94.31965	7.43	0.06	28.69
93005-1J	0.0006584	1.08989	2.137365	-0.001670	0.0117063	2.289546	2.180072	95.17676	7.48	0.07	28.99
93005-1K	0.0006373	1.214767	2.382516	-0.001147	0.0118779	2.313009	2.219962	95.92649	7.62	0.16	21.32
93005-1L	0.0012081	1.645896	3.22921	-0.000146	0.0123136	2.376531	2.147755	90.29786	7.37	0.11	17.10
93005-1M	0.0015693	2.083994	4.090113	-0.000450	0.0122599	2.497219	2.195982	87.83539	7.54	0.14	13.20
93005-1N	0.0024496	2.149867	4.219605	-0.000817	0.0122972	2.657675	2.098797	78.87483	7.21	0.19	9.32
93005-1O	0.0024105	2.305507	4.525605	0.0011852	0.012973	2.793044	2.258672	80.75928	7.75	0.36	5.71
93005-1P	0.0032271	2.723071	5.346899	0.0015963	0.0132521	3.036162	2.291746	75.35692	7.87	0.54	3.14
Plateau calculation											
Steps	N	Ca/K		MSWD	^{39}Ar (%)	^{39}Ar (mol)			Age (Ma)	±2σ (Ma)	
H-P	9	3.30 ± 0.96		1.2	50.1	1.64 × 10^{-15}			7.50	0.11	

Isochron Age

Isochron age (Ma)	±2σ w/o J	±2σ w/J	n	MSWD	p	^{40}Ar/^{36}Ar$_{(i)}$	±2σ
7.516043	0.109986	0.129498	9	1.374	0.211	291.5	55.7

HS22-2 Raw Data

Plateau Age

Run_ID	$^{36}Ar/^{39}Ar$	$^{37}Ar/^{39}Ar$	Ca/K	Cl/K	$^{38}Ar/^{39}Ar$	$^{40}Ar/^{39}Ar$	$^{40}Ar^{*}/^{39}Ar$	$^{40}Ar^{*}$ (%)	Age (Ma)	±2σ (Ma)	^{39}Ar ($\times10^{-17}$ mol)
93005-2A	0.0682962	0.7633274	1.496477	0.0291855	0.0351054	22.3718	2.042726	9.126262	7.01	9.55	0.25
93005-2B	0.0286025	0.6735046	1.320248	0.0106204	0.021227	9.352888	0.8665384	9.261316	2.98	0.18	14.33
93005-2C	0.0094258	0.654104	1.282188	0.0091767	0.0171146	4.199782	1.437502	34.2184	4.94	0.15	16.34
93005-2D	0.0024696	0.7117624	1.395306	0.0006475	0.0128612	2.85397	2.173299	76.13184	7.46	0.12	20.92
93005-2E	0.000869	0.7083283	1.388568	-0.002553	0.0114565	2.550382	2.347318	92.01896	8.06	0.08	29.74
93005-2F	0.0005924	0.7390253	1.448795	-0.003540	0.011063	2.43129	2.313258	95.12497	7.94	0.06	36.16
93005-2G	0.0005128	0.8007835	1.56997	-0.003478	0.0110669	2.354316	2.265011	96.18305	7.77	0.07	38.11
93005-2H	0.0005071	0.8908832	1.746774	-0.003076	0.011201	2.29842	2.218066	96.47485	7.61	0.05	45.51
93005-2I	0.0004618	0.9927057	1.946607	-0.002523	0.0113792	2.256604	2.197972	97.36609	7.54	0.06	36.63
93005-2J	0.000644	1.091915	2.141339	-0.002544	0.0114025	2.250868	2.145815	95.29133	7.37	0.09	26.16
93005-2K	0.0007722	1.323323	2.59566	-0.000507	0.0121196	2.268196	2.143561	94.44858	7.36	0.10	21.90
93005-2L	0.001329	1.92277	3.773232	-0.000241	0.012293	2.363819	2.121233	89.6453	7.28	0.20	12.86
93005-2M	0.0026439	3.351372	6.583585	0.0006405	0.0127887	2.704243	2.184397	80.61023	7.50	0.33	7.15
93005-2N	0.0052514	3.783908	7.435575	0.0035674	0.01427	3.337916	2.07423	61.99156	7.12	0.54	4.29
93005-2O	0.0072013	3.979047	7.820119	0.0023001	0.0141941	3.689668	1.858925	50.25249	6.38	0.91	2.69
93005-2P	0.0061388	4.082688	8.024399	-0.002488	0.0123433	3.643475	2.138954	58.55156	7.34	1.72	1.28
Plateau calculation											
Steps	N	Ca/K		MSWD	^{39}Ar (%)	^{39}Ar (mol)			Age (Ma)	±2σ (Ma)	
H-P	9	4.95 ± 2.45		1.5	50.5	1.58×10^{-15}			7.51	0.12	
Composite plateau age (HS22 (1) and HS22 (2))											
H-P	18	4.02 ± 1.04		1.3	100	3.22×10^{-15}			7.51	0.11	

Isochron Age

Isochron age (Ma)	±2σ w/o J	±2σ w/J	n	MSWD	p	$^{40}Ar/^{36}Ar_{(i)}$	±2σ
7.543253	0.082931	0.10763	9	1.59	0.133	273.3	48.4
Composite isochron age (HS22 (1) and HS22 (2))							
7.532889	0.066533	0.095501	18	1.312	0.179	281.9	35.6

HS24 Raw Data

Plateau Age

Run_ID	^{36}Ar/^{39}Ar	^{37}Ar/^{39}Ar	Ca/K	Cl/K	^{38}Ar/^{39}Ar	^{40}Ar/^{39}Ar	^{40}Ar*/^{39}Ar	^{40}Ar* (%)	Age (Ma)	±2σ (Ma)	^{39}Ar (×10^{-17} mol)
93023-1A	0.0830687	-1.464522	-2.867983	0.0840581	0.0569329	14.9539	-9.951764	-66.6206	-34.31	77.43	0.01
93023-1B	0.0199796	0.0992408	0.1940863	0.0073152	0.0184854	7.237545	1.279779	17.68306	4.37	0.24	3.02
93023-1C	0.0032146	0.0703303	0.1374152	0.0052465	0.0146123	2.659675	1.704936	64.11762	5.81	0.07	14.79
93023-1D	0.0007287	0.0606688	0.1184769	0.00105	0.0126971	2.293369	2.079978	90.72039	7.09	0.04	37.60
93023-1E	0.0004108	0.0565941	0.1104897	-0.001227	0.0118523	2.215944	2.097096	94.66414	7.15	0.02	64.60
93023-1F	0.0002018	0.0548926	0.1071546	-0.001669	0.0116606	2.149498	2.092878	97.39526	7.13	0.02	82.98
93023-1G	0.0001408	0.0559892	0.109304	-0.001509	0.011704	2.128841	2.090548	98.23111	7.13	0.02	92.50
93023-1H	0.0001031	0.0570752	0.1114327	-0.001443	0.0117198	2.113422	2.086475	98.75513	7.11	0.02	93.54
93023-1I	0.0000687	0.0589237	0.1150561	-0.001386	0.0117326	2.094806	2.078277	99.24148	7.08	0.02	84.78
93023-1J	0.0000638	0.0599714	0.1171098	-0.001254	0.0117772	2.096052	2.081056	99.315	7.09	0.02	92.85
93023-1K	0.0002557	0.0603014	0.1177567	-0.001217	0.0118264	2.163559	2.091303	96.68893	7.13	0.02	65.03
93023-1L	0.0001902	0.0644015	0.1257935	-0.000897	0.0119242	2.139901	2.087534	97.58174	7.12	0.02	48.24
93023-1M	0.0004915	0.0730601	0.142766	-0.000405	0.0121503	2.208364	2.06674	93.61313	7.04	0.02	33.57
93023-1N	0.0009367	0.0762109	0.1489422	-0.000154	0.0123207	2.312001	2.037715	88.15957	6.95	0.03	21.00
93023-1O	0.0015612	0.0731662	0.1429739	0.0002916	0.0125921	2.508696	2.047736	81.64513	6.98	0.06	11.13
93023-1P	0.0031929	0.0825214	0.1613121	0.0003271	0.0129116	2.955658	2.008297	67.96044	6.85	0.25	6.31
Plateau calculation											
Steps	N	Ca/K		MSWD	^{39}Ar (%)	^{39}Ar (mol)			Age (Ma)	±2σ (Ma)	
D-L	9	0.1143 ± 0.0043		1.2	88.1	6.62×10^{-15}			7.12	0.10	

Isochron Age

Isochron age (Ma)	±2σ w/o J	±2σ w/J	n	MSWD	p	^{40}Ar/^{36}Ar$_{(i)}$	±2σ
7.103855	0.021312	0.071806	9	0.948	0.468	321.2	27.4

GR5-1 Raw Data

Plateau Age

Run_ID	^{36}Ar/^{39}Ar	^{37}Ar/^{39}Ar	Ca/K	Cl/K	^{38}Ar/^{39}Ar	^{40}Ar/^{39}Ar	^{40}Ar/^{39}Ar	^{40}Ar* (%)	Age (Ma)	±2σ (Ma)	^{39}Ar (×10^{-17} mol)
92985-1A	0.2348364	-1.39639	-2.73472	-0.469381	-0.1054754	3.229945	-66.93852	-2074.916	-250.38	134.06	0.01
92985-1B	0.030974	1.606022	3.150881	0.003953	0.0193391	10.597	1.477462	13.92766	5.15	0.26	2.60
92985-1C	0.0135421	2.263689	4.443382	-0.001936	0.0139989	5.39704	1.534647	28.39408	5.35	0.08	8.83
92985-1D	0.0065433	3.356704	6.594084	-0.001209	0.0128874	3.338886	1.653991	49.43243	5.77	0.04	13.59
92985-1E	0.004033	4.497363	8.84203	-0.000848	0.0124943	2.500408	1.656568	66.06407	5.78	0.04	13.96
92985-1F	0.0036936	5.603383	11.02513	-0.001669	0.0121054	2.256282	1.602323	70.76235	5.59	0.07	10.71
92985-1G	0.0039636	6.585188	12.96587	0.0003763	0.0128207	2.271161	1.615464	70.82657	5.63	0.11	7.71
92985-1H	0.0049888	7.404192	14.58684	-0.003265	0.0117329	2.45249	1.556028	63.1391	5.43	0.16	5.39
92985-1I	0.0063504	8.190958	16.14575	0.0000693	0.0131029	2.830177	1.590579	55.89511	5.55	0.22	3.42
92985-1J	0.0100944	10.40175	20.53544	0.0051274	0.0154544	3.729263	1.549017	41.24455	5.40	0.16	3.02
92985-1K	0.0182682	19.52487	38.79474	0.0032838	0.0160029	5.519463	1.631561	29.16283	5.69	0.27	1.77
92985-1L	0.0369048	42.99463	86.86465	0.0003623	0.0176093	8.704658	1.120789	12.49202	3.91	0.63	1.03
92985-1M	0.048177	68.80831	141.6372	0.0015917	0.0191334	10.95247	2.11313	18.37215	7.37	1.22	0.76
92985-1N	0.0536168	69.65741	143.4739	0.0117688	0.023465	10.47768	-0.020428	-0.185540	-0.07	1.31	0.59
92985-1O	0.0370009	59.9798	122.6737	-0.005189	0.015132	8.770877	2.575943	28.14723	8.98	2.46	0.47
92985-1P	0.0441199	62.97012	129.0696	-0.004565	0.0165676	10.28589	2.190625	20.36669	7.64	3.59	0.28

Plateau calculation

Steps	N	Ca/K	MSWD	^{39}Ar (%)	^{39}Ar (mol)	Age (Ma)	±2σ (Ma)
D-K	8	18.82 ± 10.33	2.1	80.5	5.96×10^{-16}	5.72	0.19

Isochron Age

Isochron age (Ma)	±2σ w/o J	±2σ w/J	n	MSWD	p	^{40}Ar/^{36}Ar$_{(i)}$	±2σ
5.686481	0.124066	0.138117	8	2.429	0.024	301.1	8.3

GR5-2 Raw Data

Plateau Age

Run_ID	^{36}Ar/^{39}Ar	^{37}Ar/^{39}Ar	Ca/K	Cl/K	^{38}Ar/^{39}Ar	^{40}Ar/^{39}Ar	^{40}Ar*/^{39}Ar	^{40}Ar* (%)	Age (Ma)	±2σ (Ma)	^{39}Ar (×10^{-17} mol)
92985-2A	0.4180091	1.889528	3.707906	-0.853004	-0.202800	37.30919	-87.47838	-234.165	-334.73	151.48	0.01
92985-2B	0.0282963	1.97414	3.87419	0.0002259	0.0175362	9.941677	1.65125	16.5878	5.76	0.35	2.10
92985-2C	0.0159881	2.317392	4.548976	0.0013416	0.0155863	5.882183	1.293505	21.95753	4.51	0.19	4.33
92985-2D	0.0096203	3.02787	5.946701	-0.000961	0.0135658	4.252393	1.622357	38.07788	5.66	0.13	6.79
92985-2E	0.0061661	3.716653	7.303066	-0.002153	0.0124777	3.165487	1.621976	51.1188	5.66	0.07	8.45
92985-2F	0.0045404	4.48109	8.809934	-0.001206	0.0124673	2.650528	1.653865	62.22035	5.77	0.07	8.52
92985-2G	0.0036662	5.296364	10.41878	-0.003315	0.0115468	2.368834	1.698731	71.46967	5.92	0.09	7.74
92985-2H	0.0038867	6.138239	12.08205	0.0000653	0.0127168	2.292118	1.623534	70.55137	5.66	0.08	8.05
92985-2I	0.0042121	6.988847	13.76456	0.0010512	0.0130834	2.391429	1.694312	70.52664	5.91	0.12	6.49
92985-2J	0.0055573	7.771948	15.3153	0.0010301	0.0132992	2.647967	1.611685	60.55284	5.62	0.12	4.34
92985-2K	0.0089569	9.177005	18.10195	-0.002298	0.012745	3.417145	1.477682	42.9765	5.15	0.24	3.77
92985-2L	0.0170457	15.38474	30.47954	0.0048748	0.0164792	5.174514	1.316027	25.16445	4.59	0.37	2.25
92985-2M	0.0409741	45.01065	91.0693	0.006312	0.0202854	9.770699	1.133537	11.23928	3.96	0.64	1.43
92985-2N	0.0588374	70.40738	145.0981	-0.00138	0.0201056	12.56238	0.5947818	4.503195	2.08	1.25	0.75
92985-2O	0.0559049	65.36979	134.2223	0.0016166	0.0207335	11.93001	0.4298468	3.439579	1.50	1.83	0.42
92985-2P	0.035789	55.45729	113.0532	0.0113682	0.0205625	9.713855	3.552869	35.16811	12.37	2.69	0.28
Plateau calculation											
Steps	N	Ca/K		MSWD	^{39}Ar (%)	^{39}Ar (mol)			Age (Ma)	±2σ (Ma)	
D-J	7	12.59 ± 2.21		1.8	76.8	5.04 × 10^{-16}			5.74	0.11	
Composite plateau age (GR5 (1) and GR5 (2))											
D-K	15	15.96 ± 4.40		1.8	100	1.10 × 10^{-15}			5.73	0.14	

Isochron Age

Isochron age (Ma)	±2σ w/o J	±2σ w/J	n	MSWD	p	^{40}Ar/^{36}Ar$_{(i)}$	±2σ
5.839572	0.151032	0.163387	7	1.683	0.135	290.7	10.6
Composite isochron age (GR5 (1) and GR5 (2))							
5.743835	0.095866	0.113792	15	1.96	0.02	297.4	6.5

GRC7 Raw Data

Plateau Age

Run_ID	^{36}Ar/^{39}Ar	^{37}Ar/^{39}Ar	Ca/K	Cl/K	^{38}Ar/^{39}Ar	^{40}Ar/^{39}Ar	^{40}Ar*/^{39}Ar	^{40}Ar* (%)	Age (Ma)	±2σ (Ma)	^{39}Ar (×10^{-17} mol)
92984-1A	0.1744761	1.556881	3.054352	0.2418029	0.0414723	53.15646	1.188391	2.233259	4.16	12.60	0.12
92984-1B	0.1011313	1.657675	3.252352	0.0050171	0.0318366	30.94857	0.8862812	2.860491	3.10	0.26	5.60
92984-1C	0.0298726	2.274963	4.46555	0.0054037	0.0178913	10.05197	1.314545	13.05776	4.60	0.14	10.90
92984-1D	0.0028653	2.869405	5.634831	0.0042185	0.0120486	2.403027	1.777363	73.83841	6.22	0.07	15.36
92984-1E	0.0016839	3.224583	6.333939	0.0043382	0.0114661	2.054382	1.81002	87.93909	6.33	0.05	18.00
92984-1F	0.0016005	3.454698	6.787065	0.0040462	0.0113653	2.013825	1.812862	89.83719	6.34	0.09	15.50
92984-1G	0.0018742	3.563437	7.001236	0.005591	0.011909	2.02924	1.755174	86.31091	6.14	0.12	12.28
92984-1H	0.0021064	3.566398	7.00707	0.0048136	0.0119621	2.107653	1.764545	83.54224	6.17	0.15	8.38
92984-1I	0.0027928	3.487923	6.8525	0.0075938	0.0122983	2.261848	1.70736	75.32646	5.97	0.14	5.28
92984-1J	0.0033194	3.526161	6.927814	0.0087954	0.0138164	2.548094	1.83987	72.04939	6.44	0.38	3.86
92984-1K	0.0062666	5.816284	11.44575	0.0174082	0.0132364	3.146932	1.74246	55.15904	6.10	0.57	2.20
92984-1L	0.0132563	13.75637	27.2223	0.0333084	0.0142405	3.590909	0.72771	20.07563	2.55	0.66	2.14
92984-1M	0.0129092	17.65487	35.03297	0.0475789	0.014774	3.767197	1.325424	34.75823	4.64	0.44	2.39
92984-1N	0.0138222	17.48104	34.68378	0.0655289	0.0180865	3.746989	1.01513	26.76788	3.55	1.05	1.34
92984-1O	0.0144554	17.18188	34.08304	0.0804335	0.0112307	3.832986	0.8862602	22.85012	3.10	1.48	1.01
92984-1P	0.0100087	16.86368	33.44435	0.0926091	0.0202848	3.750879	2.121446	55.90651	7.42	1.76	0.88

Plateau calculation

Steps	N	Ca/K	MSWD	^{39}Ar (%)	^{39}Ar (mol)	Age (Ma)	±2σ (Ma)
D-K	8	6.93 ± 0.92	1.3	76.9	8.09×10^{-16}	6.27	0.11

Isochron Age

Isochron age (Ma)	±2σ w/o J	±2σ w/J	n	MSWD	p	^{40}Ar/^{36}Ar$_{(i)}$	±2σ
6.359638	0.135817	0.150724	8	1.218	0.293	276.4	29.6

GR31 Raw Data

Plateau Age

Run_ID	^{36}Ar/^{39}Ar	^{37}Ar/^{39}Ar	Ca/K	Cl/K	^{38}Ar/^{39}Ar	^{40}Ar/^{39}Ar	^{40}Ar*/^{39}Ar	^{40}Ar* (%)	Age (Ma)	±2σ (Ma)	^{39}Ar (×10^{-17} mol)
93012-1A	0.0800112	0.32806	0.642705	-0.017611	0.0212019	17.16744	-6.697375	-39.00484	-23.13	18.89	0.03
93012-1B	0.0263279	0.7680315	1.505706	-0.000023	0.0171262	9.230428	1.430751	15.49333	4.90	0.19	3.89
93012-1C	0.0218328	0.9327408	1.828919	0.001710	0.0169004	7.911634	1.467268	18.53539	5.03	0.10	12.30
93012-1D	0.0184151	1.669141	3.274876	0.002205	0.0163666	6.852333	1.487411	21.68376	5.10	0.07	14.72
93012-1E	0.0155265	3.018092	5.927455	0.002151	0.0157505	5.903517	1.509182	25.51365	5.17	0.07	11.45
93012-1F	0.0140486	5.334634	10.49435	0.000909	0.0149537	5.188807	1.421058	27.28927	4.87	0.10	7.53
93012-1G	0.0135447	8.223081	16.20944	0.001423	0.0149223	4.839975	1.454269	29.8798	4.98	0.14	4.95
93012-1H	0.0135671	10.68936	21.10753	0.000872	0.0146413	4.590618	1.395389	30.17548	4.78	0.20	3.67
93012-1I	0.0135121	12.34632	24.40777	0.002399	0.015088	4.571382	1.526426	33.10963	5.23	0.35	2.95
93012-1J	0.0167368	14.72493	29.15884	0.004785	0.0164167	4.893065	1.071455	21.67653	3.67	0.23	3.21
93012-1K	0.0214688	21.11083	41.9929	0.010620	0.0190361	6.172894	1.454233	23.21543	4.98	0.37	2.38
93012-1L	0.0309789	39.36072	79.31632	0.011820	0.0204763	7.281463	1.178314	15.74124	4.04	0.50	1.97
93012-1M	0.0410873	59.63637	121.941	0.008962	0.0205925	8.324701	0.8089874	9.315919	2.77	0.67	1.49
93012-1N	0.0471366	77.1524	159.7861	0.005358	0.0198388	8.842118	0.9220294	9.869328	3.16	0.88	1.06
93012-1O	0.0484598	87.41495	182.4152	-0.003235	0.0168937	8.968129	1.506897	15.78319	5.16	1.40	0.66
93012-1P	0.0441254	94.03711	197.2005	0.022116	0.0239943	8.565364	3.029049	33.05533	10.36	1.90	0.41

Plateau calculation

Steps	N	Ca/K	MSWD	^{39}Ar (%)	^{39}Ar (mol)	Age (Ma)	±2σ (Ma)
B-I	8	17.10 ± 11.32	1.4	84.9	6.15×10^{-16}	5.05	0.10

Isochron Age

Isochron age (Ma)	±2σ w/o J	±2σ w/J	n	MSWD	p	^{40}Ar/^{36}Ar$_{(i)}$	±2σ
4.965251	0.327346	0.331254	8	1.578	0.149	300	5.7

GR34-1 Raw Data

Plateau Age

Run_ID	^{36}Ar/^{39}Ar	^{37}Ar/^{39}Ar	Ca/K	Cl/K	^{38}Ar/^{39}Ar	^{40}Ar/^{39}Ar	^{40}Ar*/^{39}Ar	^{40}Ar* (%)	Age (Ma)	±2σ (Ma)	^{39}Ar (×10^{-17} mol)
93011-1A	4.25913	61.71208	126.3755	16.88995	6.38695	625.3942	-669.7177	-102.4945	NaN	-92064.99	0.00
93011-1B	0.0227307	7.609991	14.99445	-0.006950	0.0138063	7.548965	1.370955	18.06652	4.70	1.57	0.73
93011-1C	0.0083655	9.484295	18.71212	0.0011448	0.013801	3.101744	1.362778	43.65648	4.67	0.34	2.96
93011-1D	0.005485	10.25899	20.25158	-0.001945	0.0121698	2.227393	1.410753	62.90539	4.84	0.15	6.51
93011-1E	0.0048615	10.76327	21.25457	-0.001050	0.0123393	2.062379	1.472744	70.90068	5.05	0.19	7.82
93011-1F	0.0049071	11.31828	22.35928	0.0000848	0.0127146	2.03622	1.47752	72.01675	5.07	0.21	6.91
93011-1G	0.0059961	12.17088	24.05798	-0.000591	0.0126557	2.166137	1.34953	61.7949	4.63	0.16	5.20
93011-1H	0.0067471	13.25136	26.21364	-0.001029	0.0126059	2.466423	1.513614	60.82144	5.19	0.34	3.89
93011-1I	0.008829	14.60814	28.92518	-0.002286	0.0125171	2.915736	1.449465	49.2193	4.97	0.42	2.75
93011-1J	0.0162335	17.03447	33.78712	0.0016947	0.0151765	4.86377	1.380461	28.05068	4.73	0.34	2.59
93011-1K	0.0350676	25.49585	50.87287	0.0061044	0.0198891	10.12522	1.70218	16.51457	5.83	0.83	1.50
93011-1L	0.0826247	57.91087	118.2648	-0.001644	0.024985	21.49054	1.462032	6.529545	5.01	1.25	0.85
93011-1M	0.1600613	146.7756	320.3594	-0.006770	0.0345815	36.14947	-0.0296059	-0.0735455	-0.10	2.88	0.45
93011-1N	0.1786099	211.8285	486.8592	0.0183959	0.0430571	37.08904	0.6126899	1.408767	2.10	3.31	0.36
93011-1O	0.165686	224.442	521.2077	-0.049085	0.020436	31.17765	-0.6321782	-1.711409	-2.17	6.08	0.25
93011-1P	0.1127042	212.4102	488.4279	0.0127451	0.028945	23.12851	7.373158	27.17366	25.14	7.11	0.19
Plateau calculation											
Steps	N	Ca/K		MSWD	^{39}Ar (%)	^{39}Ar (mol)			Age (Ma)	±2σ (Ma)	
B-O	14	67.92 ± 49.96		0.9	99.6	4.28 × 10^{-16}			4.86	0.17	

Isochron Age

Isochron age (Ma)	±2σ w/o J	±2σ w/J	n	MSWD	p	^{40}Ar/^{36}Ar$_{(i)}$	±2σ
4.911255	0.17085	0.1777	14	0.901	0.545	295.1	6.1

GR34-2 Raw Data

Plateau Age

Run_ID	^{36}Ar/^{39}Ar	^{37}Ar/^{39}Ar	Ca/K	Cl/K	^{38}Ar/^{39}Ar	^{40}Ar/^{39}Ar	^{40}Ar*/^{39}Ar	^{40}Ar* (%)	Age (Ma)	±2σ (Ma)	^{39}Ar (×10^{-17} mol)
93011-2A	0.1376473	-0.891176	-1.74606	1.141022	0.4318696	26.41575	-14.71492	-55.7412	-51.24	153.28	0.01
93011-2B	0.0234271	7.793932	15.35886	-0.002740	0.0153748	6.313099	-0.065833	-1.03728	-0.23	1.22	0.79
93011-2C	0.0081457	9.209273	18.16601	-0.004987	0.0116695	3.071235	1.375818	44.52071	4.72	0.85	1.73
93011-2D	0.0061637	10.05319	19.84244	0.0022344	0.0137367	2.334246	1.297796	55.22677	4.45	0.29	3.32
93011-2E	0.0052927	10.51476	20.76021	0.0003678	0.0129154	2.060832	1.321486	63.67771	4.53	0.24	4.95
93011-2F	0.0048916	10.96405	21.6541	-0.000345	0.0125784	1.981598	1.398528	70.06363	4.80	0.14	5.46
93011-2G	0.0048425	11.37807	22.47833	-0.000394	0.0125362	2.000197	1.46548	72.71375	5.02	0.15	5.04
93011-2H	0.0055755	11.97726	23.67204	-0.002893	0.011797	2.121496	1.415464	66.18731	4.85	0.20	5.65
93011-2I	0.0062719	13.00003	25.71193	-0.000180	0.012816	2.30682	1.475422	63.40114	5.06	0.19	4.54
93011-2J	0.0087903	14.46318	28.63523	0.0000912	0.0133267	2.799363	1.331875	47.11171	4.57	0.39	3.21
93011-2K	0.016075	16.7206	33.15726	0.0001067	0.0146177	4.60076	1.136778	24.42519	3.90	0.30	2.85
93011-2L	0.0408355	23.06499	45.94342	-0.003741	0.0177341	11.03265	0.6756712	6.026507	2.32	0.53	1.47
93011-2M	0.138664	78.15781	161.988	-0.004704	0.0337745	35.91765	0.7413033	1.951824	2.54	1.23	0.67
93011-2N	0.2184369	215.2785	496.1836	0.0371768	0.055924	47.57266	-0.718807	-1.28492	-2.47	2.61	0.34
93011-2O	0.1651707	225.2141	523.3334	-0.026129	0.0269947	32.50615	1.197659	3.107771	4.11	2.41	0.29
93011-2P	0.1468909	205.228	469.165	0.0013358	0.0323186	24.35033	-3.812504	-13.4240	-13.14	4.83	0.18
Plateau calculation											
Steps	N	Ca/K		MSWD	^{39}Ar (%)	^{39}Ar (mol)			Age (Ma)	±2σ (Ma)	
C-J	15	23.01 ± 2.52		1.0	84.1	3.39×10^{-16}			4.84	0.16	
Composite plateau age (GR5 (1) and GR5 (2))											
B-O	22	55.83 ± 27.39		0.9	100	7.67×10^{-16}			4.85	0.13	

Isochron Age

Isochron age (Ma)	±2σ w/o J	±2σ w/J	n	MSWD	p	^{40}Ar/^{36}Ar$_{(i)}$	±2σ
4.980184	0.463638	0.466278	8	1.087	0.367	282	56.6
Composite isochron age (GR34 (1) and GR34 (2))							
4.890244	0.123139	0.132402	22	0.884	0.609	295.1	6

LF1-1 Raw Data

Plateau Age

Run_ID	^{36}Ar/^{39}Ar	^{37}Ar/^{39}Ar	Ca/K	Cl/K	^{38}Ar/^{39}Ar	^{40}Ar/^{39}Ar	^{40}Ar*/^{39}Ar	^{40}Ar* (%)	Age (Ma)	±2σ (Ma)	^{39}Ar (×10^{-17} mol)
93022-1A	2.115952	-21.52431	-41.5663	-8.604981	-2.599515	-33.3831	-657.1857	1998.023	NaN	-22383.69	0.00
93022-1B	0.060612	0.9378576	1.838961	0.0060823	0.0256875	18.918	0.8958629	4.732603	3.07	0.95	0.76
93022-1C	0.0551177	1.193826	2.341402	-0.000581	0.0223455	17.49858	1.137274	6.494119	3.89	0.17	5.79
93022-1D	0.0469559	1.622907	3.184049	0.0019315	0.0216555	15.33893	1.4491	9.437002	4.96	0.14	11.61
93022-1E	0.0391917	2.321005	4.556081	-0.000435	0.0193494	13.00388	1.488082	11.42555	5.09	0.11	12.73
93022-1F	0.0325909	3.232319	6.349169	0.0001137	0.0182584	10.95918	1.487173	13.54053	5.09	0.12	10.49
93022-1G	0.0268035	4.340056	8.531806	-0.001294	0.0166402	9.175992	1.520722	16.52416	5.20	0.14	8.15
93022-1H	0.0228386	5.473985	10.76954	-0.000457	0.0161365	7.774	1.392948	17.85154	4.77	0.16	6.18
93022-1I	0.0196631	6.473216	12.7444	0.0025476	0.0165304	6.911762	1.559613	22.46547	5.34	0.12	4.72
93022-1J	0.0210957	7.239715	14.26116	-0.000972	0.015563	7.250407	1.531813	21.02307	5.24	0.18	4.93
93022-1K	0.0259603	8.012683	15.79236	0.0007878	0.0170536	8.596671	1.487474	17.20801	5.09	0.25	3.86
93022-1L	0.0362745	11.70632	23.13215	0.0029686	0.0195999	11.44581	1.553837	13.466	5.32	0.24	3.41
93022-1M	0.0456359	19.95987	39.67122	0.0029652	0.0210373	13.42901	1.401928	10.29528	4.80	0.67	2.51
93022-1N	0.0511378	27.20142	54.34168	0.0038348	0.0220825	14.19232	1.096823	7.582569	3.76	0.46	1.79
93022-1O	0.0646352	43.32172	87.54602	-0.01328	0.0182626	17.51638	1.69652	9.394103	5.80	0.62	1.14
93022-1P	0.0849605	60.28646	123.3284	-0.001368	0.0254253	21.84839	1.306347	5.72881	4.47	1.23	0.67

Plateau calculation

Steps	N	Ca/K	MSWD	^{39}Ar (%)	^{39}Ar (mol)	Age (Ma)	±2σ (Ma)
D-M	10	17.43 ± 11.80	1.2	87.2	6.86 × 10^{-16}	5.12	0.12

Isochron Age

Isochron age (Ma)	±2σ w/o J	±2σ w/J	n	MSWD	p	^{40}Ar/^{36}Ar$_{(i)}$	±2σ
5.324668	0.315315	0.319853	10	1.147	0.327	296.5	2.9

LF1-2 Raw Data

Plateau Age

Run_ID	^{36}Ar/^{39}Ar	^{37}Ar/^{39}Ar	Ca/K	Cl/K	^{38}Ar/^{39}Ar	^{40}Ar/^{39}Ar	^{40}Ar*/^{39}Ar	^{40}Ar* (%)	Age (Ma)	±2σ (Ma)	^{39}Ar (×10^{-17} mol)
93022-2A	0.1131891	1.098476	2.154218	0.2017485	0.1030107	20.6847	-13.02775	-62.9367	-45.21	33.33	0.07
93022-2B	0.0673415	0.6788978	1.330829	0.0039078	0.0262173	21.28488	1.233049	5.79054	4.22	0.34	5.90
93022-2C	0.0600668	0.9231658	1.810127	0.0005044	0.0236632	19.16874	1.308335	6.82124	4.48	0.20	9.89
93022-2D	0.0503909	1.424632	2.794606	0.0013285	0.0221032	16.31137	1.380017	8.452459	4.72	0.19	12.77
93022-2E	0.0425179	2.012825	3.950224	0.0012127	0.0205559	13.94111	1.407468	10.08222	4.82	0.17	13.51
93022-2F	0.0351169	2.789757	5.478107	0.0009287	0.0190323	11.72212	1.460458	12.43561	5.00	0.17	12.30
93022-2G	0.0287585	3.6945	7.259421	0.0009347	0.0178002	9.821453	1.530829	15.54772	5.24	0.16	10.03
93022-2H	0.0226063	4.960999	9.75676	0.0007676	0.0165334	7.879839	1.527544	19.32042	5.23	0.19	9.64
93022-2I	0.0179756	6.268982	12.34053	-0.000108	0.0153088	6.347072	1.48197	23.24982	5.07	0.21	7.76
93022-2J	0.0160028	7.471906	14.72094	0.001389	0.0154035	5.601934	1.421984	25.25527	4.87	0.28	5.63
93022-2K	0.0210721	9.011464	17.77334	-0.000722	0.0155757	7.041265	1.471397	20.76803	5.04	0.28	5.58
93022-2L	0.0334724	13.42417	26.55871	0.0006344	0.0182063	10.00292	1.080857	10.70538	3.70	0.48	3.46
93022-2M	0.0605368	31.81325	63.76336	-0.000624	0.0221679	16.52277	0.9869875	5.841678	3.38	0.84	2.09
93022-2N	0.1194008	84.47743	175.9029	0.0022789	0.0321706	28.84055	-0.132445	-0.432281	-0.45	2.02	0.93
93022-2O	0.1535385	105.5754	223.313	-0.004293	0.0356762	38.11896	0.6805952	1.654473	2.33	3.21	0.56
93022-2P	0.1407231	92.92759	194.7131	0.0110902	0.0387	34.73019	0.0724168	0.1950497	0.25	4.84	0.35
Plateau calculation											
Steps	N	Ca/K		MSWD	^{39}Ar (%)	^{39}Ar (mol)			Age (Ma)	±2σ (Ma)	
D-K	8	12.63 ± 4.81		1.0	77	7.72×10^{-16}			5.01	0.15	
Composite plateau age (LF1 (1) and LF1 (2))											
D-M	18	16.79 ± 7.28		1.2	100	1.46×10^{-15}			5.08	0.11	

Isochron Age

Isochron age (Ma)	±2σ w/o J	±2σ w/J	n	MSWD	p	^{40}Ar/^{36}Ar$_{(i)}$	±2σ
5.338889	0.386838	0.390565	8	0.681	0.665	295.4	3.5
Composite isochron age (LF1 (1) and LF1 (2))							
5.342208	0.243507	0.249392	18	0.941	0.52	296	2.2

TOM3 Raw Data

Plateau Age

Run_ID	$^{36}Ar/^{39}Ar$	$^{37}Ar/^{39}Ar$	Ca/K	Cl/K	$^{38}Ar/^{39}Ar$	$^{40}Ar/^{39}Ar$	$^{40}Ar^{*}/^{39}Ar$	$^{40}Ar^{*}$ (%)	Age (Ma)	±2σ (Ma)	^{39}Ar ($\times 10^{-17}$ mol)
93020-1A	-0.171448	6.368354	12.53702	0.4904513	0.1479929	9.846585	61.82166	625.1161	201.11	231.67	0.01
93020-1B	0.0476381	1.337619	2.623734	0.0086928	0.0241245	14.4785	0.3612863	2.493135	1.24	0.71	1.03
93020-1C	0.0381739	1.843693	3.617835	0.0018193	0.0199524	12.48648	1.236018	9.886741	4.25	0.16	6.59
93020-1D	0.0303933	3.023783	5.938655	0.0006587	0.0180397	10.21857	1.385764	13.5337	4.76	0.09	11.03
93020-1E	0.0229198	4.569281	8.98388	0.000878	0.0166457	7.96625	1.48883	18.63158	5.12	0.15	10.64
93020-1F	0.0174988	6.216321	12.23642	0.000256	0.0153457	6.105074	1.377682	22.47136	4.73	0.11	8.80
93020-1G	0.0135496	7.518164	14.81256	0.0016113	0.0150154	4.919381	1.475828	29.84793	5.07	0.16	6.98
93020-1H	0.0120446	8.505919	16.7703	0.0000959	0.0141734	4.358408	1.443134	32.92124	4.96	0.14	5.60
93020-1I	0.0120729	9.233043	18.2132	0.0013858	0.0145924	4.241202	1.375346	32.22563	4.73	0.26	4.36
93020-1J	0.0146046	9.936818	19.61116	0.0025293	0.0154337	4.914619	1.34909	27.26501	4.64	0.18	4.51
93020-1K	0.0199091	11.02926	21.78389	0.0046682	0.0171227	6.506007	1.444998	22.04242	4.97	0.33	3.02
93020-1L	0.0328701	17.30182	34.32387	0.0056979	0.0196665	9.148628	0.7117688	7.687115	2.45	0.58	2.33
93020-1M	0.0420741	32.95834	66.11227	0.0134712	0.0233913	11.17774	1.251948	10.94451	4.30	0.49	1.41
93020-1N	0.0579489	57.25274	116.8651	-0.000374	0.0207782	13.07236	0.3125934	2.296229	1.08	0.92	1.05
93020-1O	0.0642622	79.06923	163.9868	0.0039196	0.0225222	15.01931	2.209838	13.90541	7.59	1.81	0.78
93020-1P	0.0889818	109.5072	232.3147	0.0357741	0.03612	20.07836	2.355298	10.83812	8.09	5.06	0.37
Plateau calculation											
Steps	N	Ca/K		MSWD	^{39}Ar (%)	^{39}Ar (mol)			Age (Ma)	±2σ (Ma)	
D-K	8	15.34 ± 4.98		1.4	80.3	5.49×10^{-16}			4.84	0.12	

Isochron Age

Isochron age (Ma)	±2σ w/o J	±2σ w/J	n	MSWD	p	$^{40}Ar/^{36}Ar_{(i)}$	±2σ
4.916162	0.260295	0.265428	8	1.562	0.154	297.4	3.6

TO15 Raw Data

Plateau Age

Run_ID	^{36}Ar/^{39}Ar	^{37}Ar/^{39}Ar	Ca/K	Cl/K	^{38}Ar/^{39}Ar	^{40}Ar/^{39}Ar	^{40}Ar*/^{39}Ar	^{40}Ar* (%)	Age (Ma)	±2σ (Ma)	^{39}Ar (×10^{-17} mol)
93019-1A	2.019879	-39.4712	-75.2983	-3.933745	-0.999048	54.74357	-536.7998	-1007.49	NaN	-251829.5	0.00
93019-1B	0.0262991	4.873249	9.583588	0.0120127	0.0210974	8.770222	1.307877	14.86343	4.51	3.47	0.36
93019-1C	0.010126	6.686521	13.16633	0.0012869	0.0142912	3.194391	0.7027383	21.90189	2.42	0.33	1.62
93019-1D	0.0042688	7.713	15.19851	0.0015252	0.0132284	2.098831	1.441596	68.34112	4.97	0.22	4.47
93019-1E	0.0043018	7.812256	15.39517	-0.000097	0.0126745	2.035732	1.376209	67.25963	4.74	0.13	6.54
93019-1F	0.0045163	7.739843	15.25169	-0.000633	0.0125339	2.013603	1.283716	63.43214	4.42	0.13	6.93
93019-1G	0.0043133	7.740242	15.25249	-0.001327	0.0122575	2.007641	1.338689	66.34499	4.61	0.17	6.09
93019-1H	0.0045631	8.064787	15.89564	-0.000091	0.0127157	2.067638	1.350181	64.95745	4.65	0.12	4.81
93019-1I	0.0049096	8.756533	17.26745	0.0002548	0.0128729	2.17434	1.409185	64.43686	4.86	0.28	3.92
93019-1J	0.0064427	9.994253	19.72531	-0.002113	0.0123031	2.54963	1.425945	55.55485	4.91	0.21	4.24
93019-1K	0.0085339	11.52364	22.76825	0.0038015	0.0146617	2.948608	1.322397	44.49993	4.56	0.20	3.03
93019-1L	0.012631	13.2468	26.20455	-0.000839	0.0137803	4.24731	1.537674	35.8763	5.30	0.57	2.48
93019-1M	0.0179723	20.46939	40.69856	0.0016015	0.0153378	5.252692	1.527422	28.6691	5.26	0.59	1.66
93019-1N	0.0265182	34.70553	69.70369	0.0076778	0.0184353	6.270769	1.125933	17.52417	3.88	0.85	1.09
93019-1O	0.0370212	58.26495	119.0184	0.0071801	0.0192925	7.913422	1.531665	18.57315	5.28	0.66	0.85
93019-1P	0.05139	88.88459	185.684	0.014181	0.0230245	9.985792	1.785073	16.77299	6.15	1.15	0.55
Plateau calculation											
Steps	N	Ca/K		MSWD	^{39}Ar (%)	^{39}Ar (mol)			Age (Ma)	±2σ (Ma)	
D-P	13	39.51		1.1	95.9	4.66 × 10^{-16}			4.68	0.13	

Isochron Age

Isochron age (Ma)	±2σ w/o J	±2σ w/J	n	MSWD	p	^{40}Ar/^{36}Ar$_{(i)}$	±2σ
4.577344	0.177023	0.183943	13	0.988	0.454	308.1	12.4

BT2-1 Raw Data

Plateau Age

Run_ID	^{36}Ar/^{39}Ar	^{37}Ar/^{39}Ar	Ca/K	Cl/K	^{38}Ar/^{39}Ar	^{40}Ar/^{39}Ar	^{40}Ar*/^{39}Ar	^{40}Ar* (%)	Age (Ma)	±2σ (Ma)	^{39}Ar (×10^{-17} mol)
92989-1A	0.1149051	1.121055	2.198541	-0.392332	-0.101356	16.71219	-17.52731	-104.800	-61.84	29.91	0.03
92989-1B	0.0393257	1.439218	2.823252	0.0017411	0.0201585	12.29671	0.6694405	5.43894	2.32	0.20	3.62
92989-1C	0.0313208	2.489144	4.886737	0.0027198	0.0189449	9.99546	0.8420158	8.410024	2.92	0.12	10.52
92989-1D	0.0243728	4.643393	9.130076	0.0017986	0.0172332	7.983765	1.077168	13.44966	3.73	0.15	11.85
92989-1E	0.0193814	7.682779	15.13864	0.0020126	0.0162461	6.145439	0.9712644	15.72211	3.37	0.18	8.94
92989-1F	0.0146835	11.18685	22.09759	0.0000706	0.0145581	4.553281	1.061963	23.14539	3.68	0.14	5.85
92989-1G	0.0121142	14.24307	28.19508	0.002517	0.0147901	3.607846	1.128394	30.97273	3.91	0.20	4.05
92989-1H	0.0114849	16.17823	32.06948	0.000641	0.0139555	3.211042	1.073448	33.06144	3.72	0.21	2.79
92989-1I	0.0139798	17.25251	34.22486	0.0016968	0.0147438	3.720469	0.9220029	24.48951	3.20	0.49	1.97
92989-1J	0.0219623	21.38447	42.54544	0.0011066	0.0158861	5.37214	0.5138917	9.424958	1.78	0.51	1.76
92989-1K	0.0340249	35.22556	70.77434	0.0088168	0.0202127	8.362312	1.015126	11.84312	3.52	0.63	1.06
92989-1L	0.0647992	76.49589	158.3501	0.007647	0.0239428	13.56596	0.2864119	1.999112	0.99	1.07	0.59
92989-1M	0.1050341	162.4332	358.8833	0.0164202	0.0307169	20.20711	1.915445	8.409237	6.63	2.43	0.34
92989-1N	0.1519028	258.6625	618.093	0.0151833	0.0350874	25.18977	0.3685303	1.200037	1.28	3.59	0.25
92989-1O	0.1538472	282.0021	687.46	-0.028931	0.0222324	28.77993	6.415096	17.92186	22.12	5.24	0.19
92989-1P	0.1730621	280.0112	681.4339	0.0021658	0.0345548	30.06918	0.6869175	1.83992	2.38	6.73	0.14
Plateau calculation											
Steps	N	Ca/K		MSWD	^{39}Ar (%)	^{39}Ar (mol)			Age (Ma)	±2σ (Ma)	
D-I	6	18.95 ± 11.67		1.1	65.9	3.54 × 10^{-16}			3.66	0.16	

Isochron Age

Isochron age (Ma)	±2σ w/o J	±2σ w/J	n	MSWD	p	^{40}Ar/^{36}Ar$_{(i)}$	±2σ
3.745754	0.394421	0.396759	6	1.302	0.267	296.9	7.4

BT2-2 Raw Data

Plateau Age

Run_ID	^{36}Ar/^{39}Ar	^{37}Ar/^{39}Ar	Ca/K	Cl/K	^{38}Ar/^{39}Ar	^{40}Ar/^{39}Ar	^{40}Ar/^{39}Ar	^{40}Ar* (%)	Age (Ma)	±2σ (Ma)	^{39}Ar (×10^{-17} mol)
92989-2A	0.1807838	-0.379371	-0.743811	-0.070253	0.0220699	8.379013	-45.6162	-544.6012	-165.58	55.31	0.02
92989-2B	0.0475082	1.76839	3.469869	-0.000521	0.0209094	14.64514	0.6009784	4.098763	2.08	0.18	2.86
92989-2C	0.0326851	2.165591	4.250517	0.0015959	0.0188279	10.40883	0.8222423	7.888137	2.85	0.18	6.03
92989-2D	0.0286286	3.223863	6.332521	0.0014291	0.0179642	9.138496	0.8474014	9.252837	2.94	0.15	7.83
92989-2E	0.0240763	4.716557	9.274413	0.0018447	0.0171902	7.795582	0.9830471	12.57015	3.41	0.07	7.70
92989-2F	0.0202744	6.572988	12.94174	0.0005335	0.0159504	6.552568	1.023438	15.54925	3.55	0.12	6.75
92989-2G	0.0167423	8.901218	17.55455	0.0030503	0.0160562	5.384203	1.09597	20.23209	3.80	0.22	5.37
92989-2H	0.0141077	11.42892	22.5796	0.0001009	0.0144505	4.388883	1.089037	24.62051	3.77	0.20	5.31
92989-2I	0.0126666	13.80513	27.31973	0.0016667	0.0146212	3.664467	0.9837097	26.59224	3.41	0.18	4.15
92989-2J	0.0123091	15.52175	30.75396	0.0002788	0.014013	3.46956	1.033012	29.45851	3.58	0.24	3.07
92989-2K	0.0152237	17.52221	34.76647	0.0030863	0.015441	4.146197	0.998825	23.80092	3.46	0.34	3.08
92989-2L	0.024171	23.68525	47.19962	0.0072884	0.0183091	6.098801	0.7683228	12.39202	2.66	0.96	1.85
92989-2M	0.053962	61.65155	126.246	0.0036323	0.0211783	11.78862	0.5797004	4.707034	2.01	0.68	1.13
92989-2N	0.1187852	171.6375	381.9739	-0.003955	0.0267282	20.6601	-1.391432	-5.931669	-4.83	1.66	0.57
92989-2O	0.1595127	259.8402	621.5272	0.0058443	0.0338334	27.04163	-0.0303048	-0.091831	-0.11	3.51	0.34
92989-2P	0.1474425	249.8414	592.5851	-0.012683	0.0266811	25.08505	1.005369	3.312001	3.48	6.08	0.19
Plateau calculation											
Steps	N	Ca/K		MSWD	^{39}Ar (%)	^{39}Ar (mol)			Age (Ma)	±2σ (Ma)	
E-L	8	26.84 ± 12.97		0.9	66.4	3.73 × 10^{-16}			3.49	0.12	
Composite plateau age (BT2 (1) and BT2 (2))											
D-L	14	22.81 ± 7.83		1.2	100	7.27 × 10^{-16}			3.55	0.10	

Isochron Age

Isochron age (Ma)	±2σ w/o J	±2σ w/J	n	MSWD	p	^{40}Ar/^{36}Ar$_{(i)}$	±2σ
3.729291	0.373266	0.375714	8	0.825	0.551	294.8	5.6
Composite isochron age (BT2 (1) and BT2 (2))							
3.779731	0.262576	0.266139	14	1.013	0.433	294.7	4.2

BT4-1 Raw Data

Plateau Age

Run_ID	^{36}Ar/^{39}Ar	^{37}Ar/^{39}Ar	Ca/K	Cl/K	^{38}Ar/^{39}Ar	^{40}Ar/^{39}Ar	^{40}Ar*/^{39}Ar	^{40}Ar* (%)	Age (Ma)	±2σ (Ma)	^{39}Ar (×10^{-17} mol)
92988-1A	0.161705	7.10539	13.99524	-0.358685	-0.080657	16.26243	-31.61804	-193.472	-113.46	131.76	0.01
92988-1B	0.0498036	2.001048	3.927076	0.0023996	0.0223387	15.54376	0.8331865	5.353062	2.90	0.53	1.95
92988-1C	0.0395858	2.991529	5.875173	0.0012343	0.0199722	12.43781	0.8568054	6.8748	2.98	0.24	8.58
92988-1D	0.028386	5.152836	10.13542	0.0012966	0.0177974	8.958666	0.8938933	9.943049	3.11	0.09	11.26
92988-1E	0.0182552	7.543464	14.86267	0.0008429	0.015638	5.837041	0.9880493	16.84058	3.43	0.10	9.15
92988-1F	0.0112436	9.403222	18.55111	-0.000827	0.0136714	3.637416	1.030472	28.15027	3.58	0.14	6.59
92988-1G	0.0085239	10.73326	21.19486	-0.001187	0.0129839	2.663769	0.9745792	36.32344	3.39	0.21	4.83
92988-1H	0.0083106	11.94368	23.60511	-0.000694	0.0130658	2.462307	0.933051	37.58988	3.24	0.20	3.65
92988-1I	0.0090632	13.11335	25.93812	-0.000769	0.0131368	2.678545	1.018681	37.6947	3.54	0.27	2.70
92988-1J	0.0145195	15.16353	30.03662	-0.000483	0.0141839	3.936911	0.8094664	20.34801	2.81	0.36	2.46
92988-1K	0.0237262	21.89712	43.58116	-0.002862	0.0148512	6.095983	0.7554518	12.20546	2.63	0.53	1.38
92988-1L	0.0461558	51.52691	104.7433	0.0054484	0.0207124	10.35444	0.6744305	6.280618	2.34	1.14	0.74
92988-1M	0.0940564	129.7792	279.5843	-0.002750	0.0240301	15.95775	-2.040594	-11.6346	-7.11	2.39	0.38
92988-1N	0.1341478	219.8922	508.736	0.0069236	0.030974	19.60039	-3.60465	-15.5806	-12.58	3.13	0.26
92988-1O	0.1313833	237.0839	556.3566	-0.022227	0.0213612	19.22719	-1.486901	-6.45929	-5.18	4.28	0.20
92988-1P	0.1152546	232.9207	544.7001	-0.007858	0.0226122	18.08949	2.513526	11.64604	8.72	7.22	0.14

Plateau calculation

Steps	N	Ca/K	MSWD	^{39}Ar (%)	^{39}Ar (mol)	Age (Ma)	±2σ (Ma)
E-L	8	25.63 ± 10.15	1.2	58	3.15 × 10^{-16}	3.41	0.14

Isochron Age

Isochron age (Ma)	±2σ w/o J	±2σ w/J	n	MSWD	p	^{40}Ar/^{36}Ar$_{(i)}$	±2σ
3.452051	0.332355	0.334585	8	1.383	0.217	297.6	7.8

BT4-2 Raw Data

Plateau Age

Run_ID	^{36}Ar/^{39}Ar	^{37}Ar/^{39}Ar	Ca/K	Cl/K	^{38}Ar/^{39}Ar	^{40}Ar/^{39}Ar	^{40}Ar*/^{39}Ar	^{40}Ar* (%)	Age (Ma)	±2σ (Ma)	^{39}Ar (×10^{-17} mol)
92988-2A	0.0527141	-0.421662	-0.826654	0.1226189	0.0644483	21.22367	5.452549	25.69931	18.87	32.87	0.02
92988-2B	0.0551966	1.350572	2.649169	0.0024611	0.0234024	17.08846	0.7157909	4.184986	2.49	0.27	3.38
92988-2C	0.0458845	2.068624	4.059901	0.0018498	0.0214078	14.256	0.7207167	5.048525	2.51	0.16	6.53
92988-2D	0.0370811	3.350294	6.581462	0.0012141	0.019479	11.68564	0.8811166	7.523079	3.06	0.11	8.27
92988-2E	0.0290978	4.988583	9.8112	0.000758	0.0177529	9.151966	0.8614625	9.380981	2.99	0.10	8.67
92988-2F	0.0217647	6.555033	12.90622	-0.000270	0.0159564	6.954412	0.978689	14.01028	3.40	0.09	7.35
92988-2G	0.015789	8.091577	15.94874	0.0000145	0.0148676	5.090134	1.021373	19.95575	3.55	0.16	6.06
92988-2H	0.0111651	9.499624	18.74257	0.0000598	0.0139566	3.60564	1.029825	28.37866	3.58	0.13	6.59
92988-2I	0.0090203	10.63185	20.99311	0.0004631	0.0136463	2.767685	0.9218327	33.06954	3.20	0.15	5.47
92988-2J	0.008541	11.65108	23.0221	-0.000812	0.01308	2.491242	0.8693403	34.62335	3.02	0.20	4.42
92988-2K	0.0105099	13.06166	25.83495	-0.000509	0.0135004	3.034296	0.9376423	30.62827	3.26	0.15	4.49
92988-2L	0.0160619	16.70832	33.13262	0.0019086	0.0152299	4.220859	0.7554306	17.69275	2.63	0.26	2.85
92988-2M	0.0303089	34.60417	69.49509	0.0090834	0.0196272	7.292788	1.005254	13.45403	3.49	0.50	1.67
92988-2N	0.0841107	131.4715	283.5968	0.0075823	0.0253274	14.85256	0.1560416	0.9546503	0.54	1.30	0.71
92988-2O	0.1134837	211.3782	485.6462	0.0116079	0.0288007	18.43081	1.491774	6.905086	5.18	1.92	0.41
92988-2P	0.0899875	201.957	460.4664	-0.050574	0.006331	15.33874	5.175296	29.00547	17.91	6.81	0.15
Plateau calculation											
Steps	N	Ca/K		MSWD	^{39}Ar (%)	^{39}Ar (mol)			Age (Ma)	±2σ (Ma)	
F-K	6	20.41 ± 5.11		1.8	51.3	3.44 × 10^{-16}			3.38	0.12	
Composite plateau age (BT4 (1) and BT4 (2))											
E-L	14	24.88 ± 6.29		1.3	100	6.59 × 10^{-16}			3.39	0.10	

Isochron Age

Isochron age (Ma)	±2σ w/o J	±2σ w/J	n	MSWD	p	^{40}Ar/^{36}Ar$_{(i)}$	±2σ
3.248622	0.252808	0.2554	6	1.886	0.11	301.5	5.2
Composite isochron age (BT4 (1) and BT4 (2))							
3.321689	0.199338	0.202762	14	1.397	0.159	300.2	4.3

BO5 Raw Data

Plateau Age

Run_ID	^{36}Ar/^{39}Ar	^{37}Ar/^{39}Ar	Ca/K	Cl/K	^{38}Ar/^{39}Ar	^{40}Ar/^{39}Ar	^{40}Ar*/^{39}Ar	^{40}Ar* (%)	Age (Ma)	±2σ (Ma)	^{39}Ar (×10^{-17} mol)
92992-1A	0.0780306	-1.67149	-3.27275	-0.220058	-0.048990	3.654477	-19.75662	-541.3505	-69.36	141.64	0.00
92992-1B	0.0792178	1.832411	3.595666	-0.003660	0.0258044	23.17029	-0.337247	-1.453708	-1.16	0.56	1.16
92992-1C	0.0584008	3.083689	6.056572	-0.000088	0.0230612	17.88548	0.6940597	3.872418	2.39	0.15	4.31
92992-1D	0.0377706	5.083475	9.998497	-0.000846	0.0188334	11.76776	0.8955753	7.583996	3.08	0.13	6.82
92992-1E	0.0234773	6.87139	13.53211	-0.000681	0.0161258	7.459	0.9972875	13.3077	3.43	0.13	7.04
92992-1F	0.016624	8.283079	16.32839	-0.003252	0.0138977	5.217372	0.9139203	17.41846	3.14	0.11	6.31
92992-1G	0.0129791	9.339673	18.42492	0.000022	0.0142919	4.133387	1.003068	24.11418	3.45	0.22	5.69
92992-1H	0.013155	10.20501	20.14425	-0.003390	0.0131232	4.079368	0.9652584	23.49831	3.32	0.23	4.76
92992-1I	0.0167022	11.03295	21.79123	0.000668	0.0151491	4.989446	0.8817741	17.53982	3.03	0.25	3.79
92992-1J	0.0281551	12.18589	24.08791	-0.001501	0.0165218	8.373794	0.9391196	11.12097	3.23	0.14	3.96
92992-1K	0.0495712	15.33765	30.38526	0.001983	0.0216271	14.40399	0.8255903	5.670865	2.84	0.40	2.76
92992-1L	0.0898799	31.14255	62.38932	-0.003222	0.0268496	25.1817	0.8282425	3.217968	2.85	0.48	1.72
92992-1M	0.1577856	85.81776	178.8708	-0.008278	0.0359322	40.69946	0.4039925	0.9334362	1.39	1.28	0.79
92992-1N	0.2007575	152.2417	333.7015	-0.004600	0.0426891	48.83804	1.055962	1.933423	3.63	1.67	0.45
92992-1O	0.2011963	163.359	361.1909	-0.043382	0.0305286	46.95935	-0.210422	-0.397226	-0.72	2.86	0.35
92992-1P	0.1845891	155.6785	342.1487	-0.032557	0.0309447	43.40111	0.6795159	1.396286	2.34	3.63	0.27

Plateau calculation

Steps	N	Ca/K	MSWD	^{39}Ar (%)	^{39}Ar (mol)	Age (Ma)	±2σ (Ma)
D-P	13	93.35 ± 92.66	1.0	89	4.47×10^{-16}	3.21	0.12

Isochron Age

Isochron age (Ma)	±2σ w/o J	±2σ w/J	n	MSWD	p	^{40}Ar/^{36}Ar$_{(i)}$	±2σ
3.374803	0.207218	0.211337	13	0.785	0.655	296.5	2.2

BO14-1 Raw Data

Plateau Age

Run_ID	^{36}Ar/^{39}Ar	^{37}Ar/^{39}Ar	Ca/K	Cl/K	^{38}Ar/^{39}Ar	^{40}Ar/^{39}Ar	^{40}Ar*/^{39}Ar	^{40}Ar* (%)	Age (Ma)	±2σ (Ma)	^{39}Ar (×10^{-17} mol)
92991-1A	0.0241445	0.9717999	1.905576	0.2036962	0.0869047	12.40656	5.281662	42.54529	18.16	46.46	0.01
92991-1B	0.0412039	2.381874	4.675775	-0.004742	0.0182438	12.32898	0.215102	1.741901	0.74	0.46	1.89
92991-1C	0.0287441	4.176727	8.209777	0.0012996	0.0179041	8.843901	0.5935089	6.692011	2.05	0.26	6.40
92991-1D	0.0221675	7.70703	15.18668	0.0024655	0.0169258	6.767212	0.7620433	11.2017	2.63	0.12	7.28
92991-1E	0.0192103	13.20166	26.11441	0.0022374	0.0160736	5.435468	0.7507387	13.68695	2.59	0.15	5.47
92991-1F	0.0181687	19.99416	39.74035	0.0068913	0.0171922	4.662325	0.8307256	17.57296	2.87	0.24	3.73
92991-1G	0.0197311	26.27619	52.45891	0.0014304	0.0153838	4.36153	0.5590369	12.58545	1.93	0.47	2.69
92991-1H	0.0207961	30.75926	61.60468	-0.000818	0.0146502	4.335493	0.5716973	12.90668	1.97	0.56	2.12
92991-1I	0.0226919	33.89625	68.03907	0.0082788	0.0179492	4.518902	0.4355073	9.411907	1.50	0.70	1.61
92991-1J	0.0244356	36.55409	73.51319	0.0050747	0.0170927	5.350035	0.9706863	17.68497	3.35	1.16	1.73
92991-1K	0.0352738	46.35997	93.89026	0.0168625	0.022677	7.708877	0.8732009	10.96325	3.01	1.19	1.01
92991-1L	0.0638253	85.1731	177.4426	0.0151513	0.0258407	13.44074	1.194062	8.358447	4.12	2.92	0.58
92991-1M	0.1202307	211.16	485.0584	0.0026547	0.0274477	22.9489	4.405396	16.37978	15.16	5.05	0.32
92991-1N	0.1825619	366.5338	963.9679	0.0295871	0.0399869	26.96918	1.962978	5.424552	6.77	7.39	0.23
92991-1O	0.1833377	403.9994	1100.968	0.0901002	0.0534193	22.20295	-0.7922904	-2.56653	-2.74	9.01	0.17
92991-1P	0.1660851	436.86	1229.562	-0.055053	0.0133259	20.16831	7.38723	25.50767	25.35	15.70	0.13
Plateau calculation											
Steps	N	Ca/K		MSWD	^{39}Ar (%)	^{39}Ar (mol)			Age (Ma)	±2σ (Ma)	
C-L	10	66.74 ± 30.47		1.3	92.7	3.26×10^{-16}			2.55	0.17	

Isochron Age

Isochron age (Ma)	±2σ w/o J	±2σ w/J	n	MSWD	p	^{40}Ar/^{36}Ar$_{(i)}$	±2σ
2.848959	0.651962	0.652847	10	1.401	0.19	293.8	11.1

BO14-2 Raw Data

Plateau Age

Run_ID	^{36}Ar/^{39}Ar	^{37}Ar/^{39}Ar	Ca/K	Cl/K	^{38}Ar/^{39}Ar	^{40}Ar/^{39}Ar	^{40}Ar*/^{39}Ar	^{40}Ar* (%)	Age (Ma)	±2σ (Ma)	^{39}Ar (×10^{-17} mol)
92991-2A	0.0988185	1.12224	2.200867	-0.007334	0.0282613	15.35972	-14.06662	-91.51417	-49.27	35.67	0.04
92991-2B	0.0386162	2.304493	4.523612	-0.004522	0.0178346	12.03849	0.6918335	5.73799	2.39	0.33	3.18
92991-2C	0.0281198	3.874356	7.6138	0.0019754	0.0180307	8.872048	0.7845534	8.819894	2.71	0.19	4.81
92991-2D	0.0235043	6.569861	12.93555	0.0036655	0.0176345	7.198835	0.7037502	9.732236	2.43	0.23	5.27
92991-2E	0.0202108	10.14477	20.0245	0.0017665	0.0162214	6.028871	0.8023304	13.2159	2.77	0.20	4.59
92991-2F	0.0187278	14.86661	29.44232	0.0026789	0.0160677	5.219658	0.8122165	15.40208	2.80	0.25	3.53
92991-2G	0.0188719	20.30426	40.36552	0.0011961	0.0153761	4.673126	0.6536779	13.79276	2.26	0.21	2.71
92991-2H	0.0199502	26.31148	52.53066	-0.000732	0.0146916	4.530247	0.6670966	14.4584	2.30	0.42	2.74
92991-2I	0.0211735	30.80851	61.70548	0.0021849	0.0157327	4.652321	0.7843904	16.50172	2.71	0.46	2.24
92991-2J	0.0224979	33.94697	68.14333	0.009493	0.0183193	4.786355	0.7729478	15.77033	2.67	0.64	1.71
92991-2K	0.0272927	38.33119	77.18492	0.0033267	0.0169735	5.860866	0.7647858	12.70294	2.64	0.91	1.75
92991-2L	0.039723	52.30772	106.3904	0.0142889	0.0224056	8.990332	1.316601	14.11334	4.54	1.48	0.89
92991-2M	0.1119799	141.1641	306.7791	-0.023737	0.0204482	20.0794	-2.423575	-10.88614	-8.39	2.45	0.42
92991-2N	0.1813549	345.5709	891.41	0.076128	0.0529158	28.07769	1.676935	4.53815	5.79	4.28	0.27
92991-2O	0.1943406	421.2258	1167.344	-0.022365	0.0270261	23.25856	-2.033181	-6.182653	-7.04	8.95	0.21
92991-2P	0.1917987	441.7912	1249.591	-0.114944	0.0037372	20.40183	-2.756566	-9.363006	-9.55	16.14	0.11
Plateau calculation											
Steps	N	Ca/K		MSWD	^{39}Ar (%)	^{39}Ar (mol)			Age (Ma)	±2σ (Ma)	
A-L	12	50.80 ± 20.91		0.9	16	3.35×10^{-16}			2.58	0.18	
Composite plateau age (BO14 (1) and BO14 (2))											
A-L	22	59.15 ± 17.02		1.0	22	6.61×10^{-16}			2.56	0.13	

Isochron Age

Isochron age (Ma)	±2σ w/o J	±2σ w/J	n	MSWD	p	^{40}Ar/^{36}Ar$_{(i)}$	±2σ
2.514022	0.502632	0.503526	12	0.946	0.489	299.5	7.3
Composite isochron age (BO14 (1) and BO14 (2))							
2.598601	0.384887	0.386133	22	1.074	0.369	298	6

APPENDIX C

Table C-1: A summary table show lists of accepted and rejected flows for palaeointensity experiment. Types of thermomagnetic curves are given in “Therm. Type” column. Type 1 curve shows low Ti content in the sample and Type 2 curve shows titanomaghemite samples. Type 3 and Type 4 are reversible and irreversible Fe-rich titanomagnetite samples. Type 5 shows 2-phase magnetic mineral samples. Degrees of inversion are marked in “Note” column. T, P and Th stand for thermomagnetic, pilot palaeointensity run and thermal demagnetisation. Weighting scores were given to thermomagnetic curves (35%), pilot palaeointensity runs (40%) and thermal demagnetisation runs (25%). If individual sites met 65% of the maximum score (100%), they were selected for the production palaeointensity runs. The sites yielded successful results after the production runs are also given in “success?” column.

Site	Therm. Type	Note	T	P	Th	%	Select?	Success ?	Site	Therm. Type	Note	T	P	Th	%	Select?	Success ?
VA1	Type 1		No	No	No	0	No	-	VA15	Type 2	Low degree inversion	Yes	Yes	No	75	Yes	Yes
VA2	Type 2	Low degree inversion	Yes	Yes	Yes	100	Yes	Yes	VA16	Type 2	High degree inversion	No	No	No	0	No	-
VA3	Type 2	Low degree inversion	Yes	Yes	Yes	100	Yes	Yes	VA17	Type 2	Low degree inversion	Yes	No	No	35	No	-
VA4	Type 2	High degree inversion	No	No	No	0	No	-	VA18	Type 2	High degree inversion	No	No	No	0	No	-
VA5	Type 2	Low degree inversion	Yes	Yes	No data	75	Yes	Yes	VA19	Type 2	Low degree inversion	Yes	Yes	Yes	100	Yes	No
VA6	Type 2	Low degree inversion	Yes	Yes	No	75	Yes	Yes	VA20	Type 1		No	No	No	0	No	-
VA7	Type 4		Yes	Yes	No data	75	Yes	Yes	VA21	Type 2	Low degree inversion	Yes	Yes	No	75	Yes	No
VA8	Type 3		Yes	No	No data	35	No	-	VA22	Type 1		No	No	No	0	No	-
VAB9	Type 2	High degree inversion	No	No	No	0	No	-	VA23	Type 2	High degree inversion	No	No	Yes	25	No	-
VAO9	Type 4		Yes	No	Yes	60	No	-	VA24	Type 1		No	No	Yes	25	No	-
VA10	Type 2	High degree inversion	No	No	Yes	25	No	-	VA25	Type 2	High degree inversion	No	No	Yes	25	No	-
VA11	Type 2	Low degree inversion	Yes	Yes	Yes	100	Yes	Yes	VA27	Type 2	High degree inversion	No	No	Yes	25	No	-
VA12	Type 2	Low degree inversion	Yes	Yes	Yes	100	Yes	Yes	VA28	Type 5		Yes	Yes	No	75	Yes	Yes
VAD13	Type 2	High degree inversion	No	No	No	0	No	-	VA29	Type 4		Yes	No	Yes	60	No	-
VA14	Type 2	High degree inversion	No	No	Yes	25	No	-	VA30	Type 2	Low degree inversion	Yes	Yes	Yes	100	Yes	Yes

…continue from previous page…

Site	Therm. Type	Note	T	P	Th	%	Select?	Success ?
VA31	Type 4		Yes	Yes	Yes	100	Yes	Yes
VA32	Type 4		Yes	No	No	35	No	-
VA33	Type 2	Low degree inversion	Yes	Yes	Yes	100	Yes	No
VA34	Type 2	High degree inversion	No	No	Yes	25	No	-
VA35	Type 2	Low degree inversion	Yes	Yes	Yes	100	Yes	Yes
VA36	Type 4		Yes	Yes	Yes	100	Yes	No
VA37	Type 2	High degree inversion	No	No sample	No	0	No	-
HS1	Type 2	High degree inversion	No	No	No	0	No	-
HS3	Type 2	Low degree inversion	Yes	Yes	Yes	100	Yes	Yes
HS4	Type 5		Yes	Yes	Yes	100	Yes	Yes
HS5	Type 4		Yes	Yes	Yes	100	Yes	Yes
HS6	Type 2	High degree inversion	No	No	No	0	No	-
HS7	Type 2	Low degree inversion	Yes	Yes	Yes	100	Yes	Yes
HS8	Type 2	Low degree inversion	Yes	Yes	No	75	Yes	Yes
HS9	Type 2	High degree inversion	No	No	No	0	No	-
HS10	Type 3		Yes	Yes	No	75	Yes	No
HS11	Type 3		Yes	Yes	Yes	100	Yes	Yes
HS12	Type 2	High degree inversion	No	No	No	0	No	-
HS13	Type 2	Low degree inversion	Yes	Yes	Yes	100	Yes	Yes
HS14	Type 2	High degree inversion	No	No	No	0	No	-
HS15	Type 4		Yes	No	No	35	No	-
HSB15	Type 2	High degree inversion	No	No	No	0	No	-
HS16	Type 2	High degree inversion	No	No	No	0	No	-
HS17	Type 2	High degree inversion	No	No	No	0	No	-
HSB18	Type 4		Yes	Yes	No	75	Yes	Yes
HSJ18	Type 4		Yes	Yes	No	75	Yes	Yes
HS19	Type 2	High degree inversion	No	No	No	0	No	-
HS20	Type 4	Show high degree inversion	No	No	Yes	25	No	-
HS21	Type 2	Low degree inversion	Yes	Yes	No	75	Yes	No
HS22	Type 2	High degree inversion	No	No	No	0	No	-
HS23	Type 2	High degree inversion	No	No	No	0	No	-
HS24	Type 4	High degree inversion	No	No sample	No data	0	No	-
GS1	Type 4		Yes	Yes	Yes	100	Yes	Yes
GSA2	Type 3		Yes	No	No	35	No	-
GSB2	Type 1		No	No	No	0	No	-
GS3	Type 2	Low degree inversion	Yes	Yes	Yes	100	Yes	Yes
GR1	Type 1		No	No	No	0	No	-
GR2	Type 2	High degree inversion	No	No	No	0	No	-

…continue from previous page…

Site	Therm. Type	Note	T	P	Th	%	Select?	Success ?	Site	Therm. Type	Note	T	P	Th	%	Select?	Success ?
GR3	Type 2	High degree inversion	No	No	No	0	No	-	GR20	Type 2	Low degree inversion	Yes	Yes	Yes	100	Yes	No
GR4	Type 4		Yes	Yes	Yes	100	Yes	Yes	GR21	Type 4		Yes	No sample	Yes	60	No	-
GR5	Type 2	High degree inversion	No	No	Yes	25	No	-	GR22	Type 4		Yes	Yes	Yes	100	Yes	Yes
GR6	Type 1	High degree of inversion	No	No	No	0	No	-	GRA23	Type 4		Yes	Yes	Yes	100	Yes	No sample
GR7A	Type 3		Yes	No	No data	35	No	-	GRB23	Type 4		Yes	Yes	Yes	100	Yes	No
GRB7	Type 2	High degree inversion	No	No	No	0	No	-	GR24	Type 4		Yes	Yes	Yes	100	Yes	Yes
GRC7			No data	No	No	0	No	-	GRA25	Type 4		Yes	Yes	Yes	100	Yes	Yes
GR8	Type 4		Yes	No	No data	35	No	-	GRB25	Type 5		Yes	Yes	Yes	100	Yes	No
GR9	Type 4		Yes	No	No	35	No	-	GR26	Type 4		Yes	No sample	Yes	60	No	-
GR10	Type 2	High degree inversion	No	No	Yes	25	No	-	GR27	Type 4	High degree of inversion	No	No	No	0	No	-
GR11	Type 3		Yes	Yes	Yes	100	Yes	No	GR28	Type 2	Low degree inversion	Yes	No	No	35	No	-
GR12	Type 1		No	No	Yes	25	No	-	GR29	Type 4		Yes	Yes	Yes	100	Yes	Yes
GR13	Type 2	High degree inversion	No	No	Yes	25	No	-	GR30	Type 2	Low degree inversion	No	No	No	0	No	-
GR14	Type 2	High degree inversion	No	No	No	0	No	-	GR31	Type 4		Yes	Yes	Yes	100	Yes	No samples
GR15	Type 2	High degree inversion	No	No	Yes	25	No	-	GR32			No data	Yes	Yes	65	Yes	Yes
GR16	Type 2	High degree inversion	No	No	No	0	No	-	GR33	Type 4		Yes	Yes	Yes	100	Yes	Yes
GR17	Type 4		Yes	No	No	35	No	-	GRA33	Type 4		Yes	Yes	Yes	100	Yes	Yes
GR18	Type 2	Low degree inversion	Yes	No	No	35	No	-	GRB33	Type 4	High degree of inversion	No	No	Yes	25	No	-
GR19	Type 2	Low degree inversion	Yes	Yes	Yes	100	Yes	Yes	GR34	Type 4		Yes	Yes	Yes	100	Yes	No

…continue from previous page…

Site	Therm. Type	Note	T	P	Th	%	Select?	Success ?	Site	Therm. Type	Note	T	P	Th	%	Select?	Success ?
LF0	Type 4		Yes	Yes	Yes	100	Yes	Yes	TO9	Type 5		Yes	Yes	Yes	100	Yes	Yes
LF1	Type 4		Yes	Yes	Yes	100	Yes	Yes	TOA10	Type 4	High degree of inversion	No	No	Yes	25	No	-
LF2	Type 4		Yes	Yes	Yes	100	Yes	Yes	TOB10	Type 4	High degree of inversion	No	No	Yes	25	No	-
LF3	Type 4	High degree of inversion	No	No	No	0	No	-	TO11	Type 3		Yes	Yes	Yes	100	Yes	Yes
LF4	Type 4		Yes	Yes	Yes	100	Yes	Yes	TO12	Type 3		Yes	Yes	Yes	100	Yes	Yes
LF5	Type 1		No	No	No	0	No	-	TO13	Type 4	High degree of inversion	No	No	Yes	25	No	-
LF6	Type 1		No	No	Yes	25	No	-	TOA14			No data	No	Yes	25	No	-
LF7	Type 4		Yes	Yes	Yes	100	Yes	Yes	TOD14	Type 4		Yes	No	No	35	No	-
LF8	Type 4	High degree of inversion	No	No	Yes	25	No	-	BT1	Type 4	High degree of inversion	No	No	Yes	25	No	-
LF9	Type 5		Yes	Yes	No	75	Yes	Yes	BT2	Type 4	High degree of inversion	No	No	Yes	25	No	-
TOM3	Type 4		Yes	Yes	Yes	100	Yes	Yes	BT3	Type 4	High degree of inversion	No	No	Yes	25	No	-
TOM2	Type 4	High degree of inversion	No	No	No	0	No	-	BT4	Type 1		No	No	Yes	25	No	-
TOM1	Type 4		Yes	Yes	Yes	100	Yes	Yes	BT5	Type 1		No	No	No	0	No	-
TO0	Type 4		Yes	No	No data	35	No	-	BO6	Type 4	High degree of inversion	No	No	No	0	No	-
TO1	Type 4		Yes	Yes	Yes	100	Yes	Yes	BO7	Type 4	High degree of inversion	No	No	Yes	25	No	-
TO2	Type 5		Yes	No	Yes	60	No	-	BO8	Type 4	High degree of inversion	No	No	No	0	No	-
TO3	Type 4		Yes	Yes	Yes	100	Yes	Yes	BO9	Type 4	High degree of inversion	No	No	Yes	25	No	-
TO4	Type 4		Yes	No	No	35	No	-	BO10	Type 4		Yes	Yes	Yes	100	Yes	Yes
TO5	Type 4		Yes	Yes	Yes	100	Yes	Yes	BO11	Type 4	High degree of inversion	No	No	No	0	No	-
TO6	Type 4		Yes	Yes	Yes	100	Yes	Yes	BO12	Type 4		Yes	Yes	Yes	100	Yes	Yes
TO7	Type 4		Yes	Yes	Yes	100	Yes	Yes	BO13	Type 3		Yes	Yes	Yes	100	Yes	Yes
TO8	Type 3		Yes	Yes	Yes	100	Yes	Yes	BO14	Type 5		Yes	No samples	No data	35	No	-